Stanford Geothermal Program
Interdisciplinary Research
in Engineering and Earth Sciences
Stanford University
Stanford, California

LABORATORY STUDIES OF STIMULATED GEOTHERMAL RESERVOIRS

by
A. Hunsbedt
P. Kruger
A. L. London

December 1975

This research was carried out under
Research Grant NSF-AER-72-03490 by
the National Science Foundation

Abstract

Improved recovery of geothermal energy from artificially stimulated systems by in-place flashing was studied experimentally. The laboratory model used produces steam, either with or without simulated geofluid recharge, from initial pressures and temperatures up to 800 psia (54.4 bar) and 500 °F (260 °C). The rock geometry parameters and the bulk porosities of the two high permeability systems tested were measured to allow extrapolation of the experimental results to other systems. The first rock system consisted of gabbro rocks with mean equivalent diameter of about 1 inch and 44 percent porosity. The second consisted of granite rocks with mean equivalent diameter of 2.65 inches and 35 percent porosity. Thermocouples were used to measure the steam temperature and the center temperature of rocks at various points in the rock matrix. Analytic solutions were derived for the rock thermal transients for comparison to measurements. Analytic models were developed for the model pressure and temperature transients based on mass and energy balances assuming uniform axial temperature distribution. The thermal characteristics of the laboratory model were determined from heatup and cooldown calibration experiments and from fluid production experiments with water only in the model. Results show that thermal energy stored in fractured rock can be extracted effectively by reducing system pressure to allow in-place flashing. The energy extracted from the rock was 75 percent or rnore of the thermal energy stored in the rock between the temperature limits of the experiments. The fraction of rock energy extracted decreased with lowering of the liquid level because rocks in the superheated zone which developed above the vapor-liquid interface did not reach the lower temperature limit. The rock energy extraction fraction also decreased with increasing rock size and cooldown rate. Recovery of energy from the laboratory

model systems studied ranged from 1.25 to 2.57 times the energy extractable by flashing the fluid alone. The recovery factors depended on the initial pressure, the rock porosity, the rock energy extraction fraction, the external heat transfer parameter, and the enthalpy of the recharge fluid. Measured and predicted rock/steam temperature differences were generally within experimental uncertainties. Surface heat transfer coefficients evaluated for rocks in vapor environment were a factor of about 3 greater than the predicted based on packed bed results. The predicted pressure and temperature transients using the analyses developed for the model agreed well with the observed transients for most conditions. The effect of the superheated zone on the model steam pressure behavior could be accounted for. However, the effect of the subcooled zone which developed at the bottom of the model with low enthalpy fluid recharge could not be predicted adequately by the one-dimensional analyses. The analytic techniques developed and verified were used to extrapolate the experimental results to a highly fractured real size system. It appears that the thermal energy stored in rock segments with characteristic size on the order of 200 ft or greater can be extracted effectively by pressure reduction and flashing provided the water circulation is not restricted within the rock matrix. The maximum rock size depends on the depletion time and the steam production characteristic assumed for the real size system. Practical aspects of proposed artificial stimulation techniques and operation of the reservoir were not evaluated. Although improved geothermal energy recovery from stimulated reservoirs by in-place flashing appears promising, the feasibility of this extraction scheme cannot be assessed until practical and economic issues are investigated.

ACKNOWLEDGEMENTS

The support by the National Science Foundation under Grant No. NSF-AER-72-03490 during both the construction phase and early experimental phase of this program is gratefully acknowledged.

TABLE OF CONTENTS

NOMENCLATURE

English Letter Symbols

A = area (ft^2)

a = length dimension of rock (in)

a = coefficient (hr^{-1})

B = Biot number (dim. less)

b = breadth dimension of rock (in)

b = coefficient (hr^{-1})

C = specific heat capacity ($Btu/lb_m\ ^oF$)

C_1, C_2 = constants - defined in text

C_F = orifice flow factor ($lb_m/hr\ in^{1/2}$)

c = thickness dimension of rock (in)

d = rock equivalent diameter (in)

E = internal energy (Btu)

e = specific internal energy (Btu/lb_m)

e = 2. 71.. .basis of natural logarithm (dim. less)

F = Fourier number (dim. less)

FP = fraction produced (dim. less)

FR = fraction recharged (dim. less)

H = height dimension (in)

h = heat transfer coefficient ($Btu/hr\ ft^2\ ^oF$)

h = height of rock matrix (in)

i = specific enthalpy (Btu/lb_m)

k = thermal conductivity ($Btu/hr\ ^oF\ ft$)

ℓ = half thickness of rock (plate) (ft)

ℓ = recharge head tank liquid level (ft)

M = mass (lb_m)

M* = mass fraction - normalized to initial mass (dim. less)

m = mean value of measurement

n = statistical sample size (dim. less)

P = pressure (psia)

P_{so} = initial saturation pressure (psia)

P* = pressure parameter - normalized to initial saturation pressure (dim. less)

ΔP = orifice pressure drop (psi)

Q = energy transfer (Btu)

Q_m = external heat transfer parameter (Btu)

q_m = specific external heat transfer parameter (Btu/lb_m)

R = thermal resistance ($hr\ ^oF/Btu$)

R = result of measurement

R = recovery factor - defined in text (dim. less)

Re = $\rho ud/\mu$ = Reynolds number (dim. less)

r = radius or radial coordinate (in)

S = magnitude of axial temperature gradient (^oF)

St = $h/c\rho u$ = Stanton number (dim. less)

s^2 = statistical parameter - variance (ft^2)

T = temperature (^oF)

t = time (hr)

t* = nondimensional time - defined in text (dim. less)

$t_c = M_o/\dot{M}_p$ = reservoir characteristic time (hr)

U = overall heat transfer coefficient ($Btu/hr\ ft\ ^oF$)

u = velocity (ft/hr)

V = volume (ft^3)

v = variable

v = specific volume (ft^3/lb_m)

w = uncertainty interval

X = rock mass fraction (dim. less)

X = steam quality (dim. less)

x = coordinate

Z = z/h = dimensionless distance from top of chimney (dim. less)

z = distance from top of chimney (in)

Greek Letter Svmbols

α = void fraction (dim. less)

α = thermal diffusivity (ft^2/hr)

β = defined in text (dim. less)

y = recharge parameter (dim. less)

δ = conduction path length (dim. less)

η = rock energy extraction fraction (dim. less)

ϵ = emissivity (dim. less)

ϕ = drainage porosity of rock matrix (dim. less)

ψ = sphericity parameter (dim. less)

μ = cooldown rate ($^{o}F/hr$)

μ = dynamic viscosity ($lb_f\ hr/ft^2$)

ρ = density (lb_m/ft^3)

σ = standard deviation

τ = rock time constant (hr)

$\theta = T - T_\infty$ = excess temperature (^{o}F)

Subscripts

C = cool side of heat exchanger

c = chimney

c = condenser

cs = center of sphere

cp = center of plate

d = drainage from outlet line

e = end conditions

f = saturated liquid

fg = vaporization

g = saturated vapor

H = hot side of heat exchanger

i = injection or recharge

i = inlet line

in = inlet of heat exchanger

ℓ = local

1 = large size rock

'm = metal or steel

m = medium **size** rock

o = initial conditions (t=0)

o = outlet line

o = outside

out = outlet of heat exchanger

p = production

p = plate

pτ = for plate time constant

r = rock

rc = rock center

s = sphere

s = small size rock

s = start of computations

sτ = for sphere time constant

SC = steam cap

SG = sight glass

T = total

T/C = thermocouple

t = based on theory

v = void

w = wall

∞ = surroundings

Special Symbols

$\bar{\ }$ = mean value

( )' = derivative with respect to pressure

$\dot{\ }$ = quantity on a rate basis

A = indicates a definition

CHAPTER 1

INTRODUCTION

1.1 The Geothermal Resource

Geothermal energy in the earth's crust has been utilized on a limited scale for centuries. For example, natural hot water springs have been used for thousands of years for recreational, religious, and medical purposes. Local use of natural geothermal water for various heating purposes is older than recorded history, and has expanded notably in recent years. Prospects for more intensified local utilization of low-temperature geothermal waters for various non-electric purposes appears promising throughout the world in view of the increasing cost of conventional energy sources.

The first demonstration of large-scale commercial use of geothermal steam for electricity production began at Larderello, Italy in 1913. Development of the Wairakei geothermal area in New Zealand began in about 1950. In the United States the only commercial production of geothermal power is at The Geysers in California, where the generation of electricity began in 1960. In 1975 the total capacity was increased to 502 MWe, making it the largest geothermal power station in the world. Geothermal plants are also in operation at Cerro-Prieto, Mexico, Matsukawa, Japan and in several other countries. The total world-wide electric power generating capacity of about 1265 MWe from geothermal sources is not significant in comparison to conventional sources, equivalent to the power output of a single modern nuclear power station. However, rapid expansion of the electric generating capacity is considered likely in the future, for example, the generating capacity at The Geysers is scheduled to reach 1200 MWe by 1981.

The characteristics of geothermal resources have been described by Elder (1965) and by White (in Kruger and Otte, 1973). Vapor-dominated systems are by far the most economically attractive geothermal resource at this time. The major electric generating facilities at Larderello and at The Geysers are operated with superheated steam from vapor-dominated systems'. Hot water from liquid-dominated systems which is flashed into steam at the surface is used for electric power generation at Wairakei and at Cerro-Prieto.

Liquid-dominated systems are believed to occur far more frequently than vapor-dominated systems. However,, the extent of the hydrothermal resource is small compared to the hot, "dry" rock resource which is broadly distributed in the earth's crust, These systems do not produce economic amounts of either steam or hot water due to a lack of permeability and porosity, or of ground water supply. Extraction of energy from these systems at competitive cost has not yet been demonstrated. However, this energy resource is so vast and widespread that it is now being given serious technical attention both here and abroad.

Estimates of the geothermal resource of the! United States and the impact of its utilization on the Nation's energy needs were made by White (1965), Muffler and White (1972), Kilkenney (1972), Grossling (1972) and by Rex and Howell (in Kruger and Otte, 1973). An assessment of the geothermal resources of the United States edited by White and Williams was completed recently (1975).

There is wide variation in the resource estimates which reflects a number of factors including different assumptions about technological developments and cost factors, and a different meaning of the term "resource". However, the major cause of the broad spread in estimates appears to be a lack of factual knowledge about the resource itself,

It is generally agreed that technological breakthroughs that will permit the economic development of resources that are clearly not economic at the present time are necessary. The required breakthroughs include the development of artificial resource stimulation techniques to increase the productivity of hydrothermal geothermal reservoirs, and the introduction of artificial circulation systems to tap the energy stored in hot, dry rock.

1.2 Reservoir Stimulation

A variety of stimulation techniques such as explosive fracturing by nuclear or conventional explosives, hydraulic fracturing using high pressure water, and thermal stress cracking have been proposed for stimulation of submarginal geothermal resources. Hydraulic fracturing is a very common stimulation technique used in oil and gas fields to improve reservoir flow characteristics by creating a set of cracks in the producing formations adjacent to the wellbore. This is normally done by inserting temporary seals in the wellbore above and below the zone to be fractured, and then using a high-pressure pump at the surface and a high-pressure line extending through the upper seal to produce hydraulic pressure (Howard and Fast, 1970). The theory and practice of hydraulic fracturing is well developed. It is believed that the required fracture system for geothermal application can be produced without difficulty using standard techniques. Hydraulic fracturing has also proven to be a relatively inexpensive procedure in oil reservoir stimulation.

Extraction of energy from rock penetrated by the hydraulic fracture creates thermal contraction stresses that may eventually be sufficient to extend the initial crack system in three dimensions. This secondary fracturing process is referred to as thermal stress cracking. The secondary fracturing may increase both the heat transfer surface

area and the total amount of energy transferred to the circulating fluids as energy is withdrawn from the geothermal reservoir. This process has been simulated analytically by Harlow and Pracht (1972).

A research and development program on hydraulic fracturing techniques and the economics of hot, dry rock systems is presently underway at Los Alamos Scientific Laboratory. Details of this program have been reported by Smith et al. (in Kruger and Otte, 1973) and by Smith et al. (1975). The program is aimed at first creating a large hydraulic fracture in a hot, dry rock formation. Forced circulation of surface water under high pressure will then be used to transport the energy transferred from the hot rock to the water in a closed circulation loop.

The program at Los Alamos is concerned with hot, dry rock formations only. Research and Development on stimulation of geothermal wells in hydrothermal systems with low permeability or inadequate ground water supply appears to be lacking at this time.

Another stimulation technique referred to as the Plowshare concept has been considered in the past (Carlson, 1959, and Kennedy, 1964). The basis of this concept is the use of nuclear explosives to fracture large volumes of the hot rock. Two geologically different geothermal systems are amenable to energy extraction by nuclear explosives.

One is the hydrothermal field with sufficient hot ground water supply but with inadequate permeability to sustain. steam production at economic rates. The large wellbore (chimney) and the fractures created by the explosion might increase steam production for economic development of such marginal hydrothermal fields. This situation is similar to stimulation of natural gas reservoirs via nuclear explosives which has been successfully conducted on an experimental basis (Holzer, 1970).

Explosive stimulation of hydrothermal systems has been discussed by Ramey, Kruger, and Raghaven (in Kruger and Otte, 1973). The energy associated with a hydrothermal system consists of two parts: (1) thermal energy stored in the rock medium, and (2) thermal energy stored in the hot water. The ratio of the magnitudes of these two components depends principally on the rock porosity. Ramey, Kruger, and Raghaven demonstrated that: the amount of energy extracted from hydrothermal reservoirs can be greatly enhanced by operating the reservoir such that boiling takes place in the rock formation. As fluids are produced and the reservoir pressure declines, the water temperature also declines because the saturated system follows the vapor pressure/temperature curve. Temperature gradients are then set up in the rock medium resulting in heat transfer from the rock to the fluids.

The second geothermal system where the Plowshare concept may prove useful consists of hot, dry rock at moderate depths. The rock is fractured using nuclear explosives and the energy is extracted from the hot rock by piping cool water to the periphery of the region as illustrated in Fig. 1. 1. The water is heated as it percolates through the fractured rock medium to the chimney zone where either vapor or liquid is withdrawn. The principal energy source involved is the thermal energy originally stored in the rock plus some thermal energy derived from the nuclear detonation. The water in this case serves as the energy transport medium only as opposed to the hydrothermal system where a significant quantity of thermal energy is originally stored in the in-place fluids.

A detailed study of technical and economic aspects of a large-scale power plant using thermal energy from fractured hot, dry rock was reported by Burnham and Stewart (in Kruger and Otte, 1973). This study indicates that Plowshare stimulation would appear to be economical if large yield nuclear explosives (in the MT range) can be used.

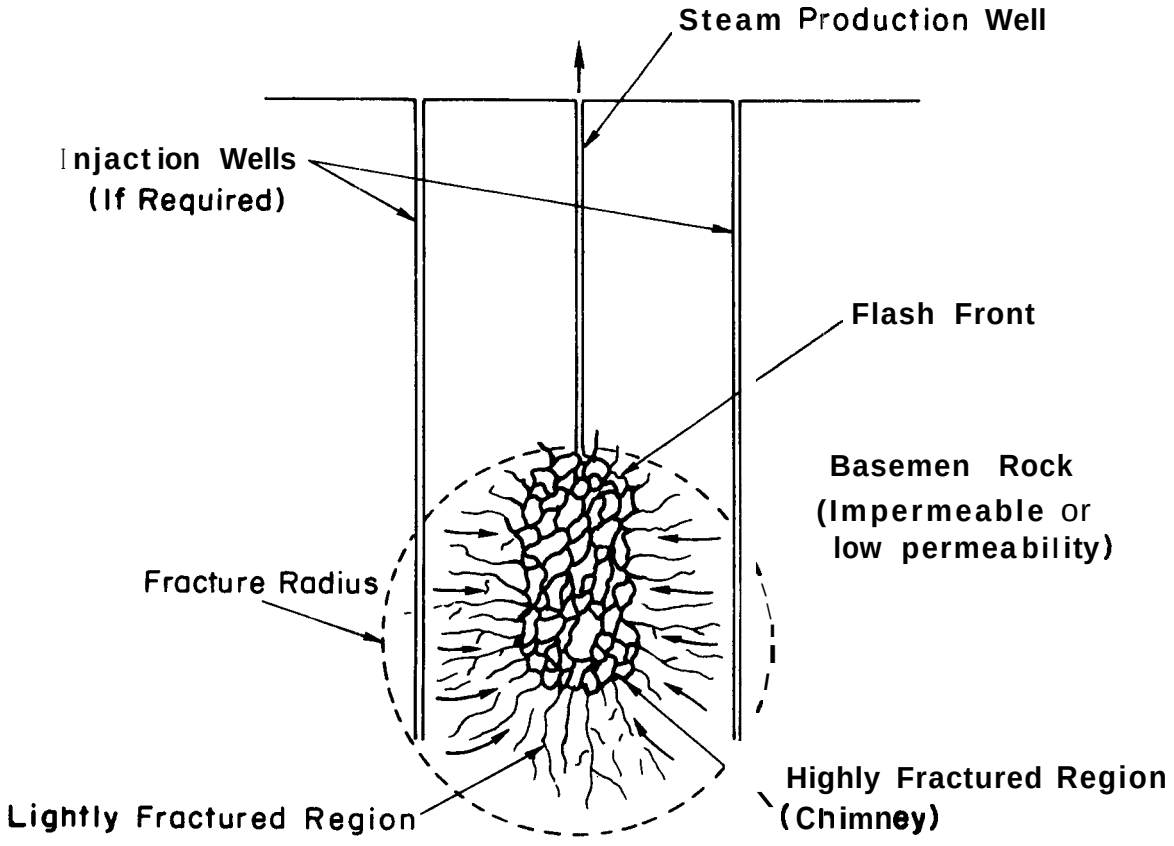

Figure 1.1 Stimulated Geothermal Reservoir

Considerable emphasis has been placed on development of relatively low temperature dry geothermal resources in the USSR (Diadkin and Pariisky, 1975) for use in the mining industry. It would appear that large-scale stimulation experiments using nuclear explosives are imminent in the USSR. Such experiments are not planned in the US at the present time. Other hot, dry rock energy extraction systems for low temperature applications have been described by Diadkin et al. (1973). These systems are created by using a combination of new drilling techniques, chemical explosives, and naturally occurring fractures.

The use of chemical explosives to stimulate geothermal wells in hydrothermal regions has been described by Austin and Leonard (in Kruger and Otte, 1973). Chemical explosives are used to enlarge the wellbore diameter in a producing zone or to fracture minerals deposited around the wellbore. The stress waves from the explosion may also result in permeability increases in the formation at some distance away from the wellbore. The required technology for stimulation using chemical explosives appears to be available, but there is no large scale field experience with geothermal application.

1.3 Experimental Study

The state of the art of geothermal reservoir engineering has not developed to a satisfactory level, due primarily to a lack of experimental data on the many physical phenomena occurring with two-phase fluid flow in hot porous media. Although field well testing may provide useful information about the character of the geothermal reservoir, such tests are often impractical or expensive. Inexpensive bench scale experiments under controlled laboratory conditions are often used to provide the necessary experimental input to analytic models.

Several laboratory experiments with flow in porous media have been conducted in the past. The steady flow of two-phase, single component fluids in unconsolidated sand was studied by Miller (1951). The fluid production from an unconsolidated sand/water system was studied by Cady (1969) and a similar study with consolidated sandstone was conducted by Chicoine (1975). A study of unsteady non-isothermal single and two-phase flow through artificial consolidated sandstone was reported by Arihara (1974).

Although there are many common characteristics between the artificially stimulated reservoir and the systems studied above, particularly those studied by Cady and Chicoine, the results are not generally applicable to stimulated reservoirs. Prediction of the fracture-stimulated reservoir flow patterns requires knowledge about the distribution of the permeability and extent of the fractures. Moreover, the rock size distribution and the fracture geometry are essential for determining the degree of rock energy extraction.

Experimental data on permeability distributions resulting from underground nuclear explosions have been reported by Boardman (1970). Data on the size distributions of the highly fractured rock media within the chimney have been reported by Rabb (1968), Rodean (1965), and Boardman (1966). Results from hydraulic fracturing experiments have been reported by Smith et al. (1975).

The experimental efforts reported here are oriented towards the study of the thermal, heat transfer, and reservoir engineering aspects of fracture-stimulated geothermal reservoirs. The key areas of study include, (1) conditions for optimum energy extraction, (2) rock heat transfer characteristics, (3) moving flash fronts, (4) fluid withdrawal/reservoir pressure behavior, (5) effects of cool and hot water recharge, (6) steam/rock temperature distributions and (7) cyclic production/recharge operation. The study was conducted using a large-scale

laboratory model of a rock-rubblized reservoir. The study was part of a broad experimental program on stimulation and reservoir engineering of geothermal reservoirs conducted at Stanford University under the Stanford Geothermal Energy Program.

To establish the feasibility of the experimental approach, the initial efforts were directed at simulating the highly fractured region of a geothermal area stimulated by explosive fracturing as indicated in Fig. 1.1. It is visualized that the stimulated geothermal area could originally be either a hot, dry rock region in which case surface water injection is required, or the area could be a low permeability hydrothermal field in which case injection of surface water is not required. Laboratory simulation of the much larger, lightly fractured region surrounding the chimney in Fig. 1.1 is more difficult. However, experimental data on such a system is considered to be of more general interest and it is intended, therefore, that later efforts will be directed towards the study of such systems.

The main objectives of the study reported here were:

(1) Construction, checkout and calibration of the experimental system to establish the adequacy of the experimental approach.

(2) Acquisition of detailed experimental data on the laboratory model reservoir behavior for a range of relevant reservoir parameters and steam production/fluid recharge conditions.

(3) The development of analytic techniques based on the observed laboratory model reservoir behavior to predict the performance of similar real size reservoirs.

Experiments have been run with two rock loadings with characteristics similar to the highly fractured, high porosity, region of a rubble chimney, with and without recharge and at pressures and temperature conditions found in geothermal systems. Since the efficiency of the energy extraction from the rock was a major objective of the study, fluid

recharge was limited so that energy addition by fluid recharge was less than the energy extraction from the rock.

The results of the efforts under item (1) and preliminary evaluations of detailed experimental results under item *(2)* have been reported previously (Hunsbedt, Kruger, and London, 1975 and 1976). The preliminary results indicated that the experimental approach was well within expectations. Important aspects of that work are repeated here to provide continuity in the current presentation of detailed evaluations of the efforts under items (2) and **(3).**

CHAPTER 2

DESCRIPTION OF TEST SYSTEM

2.1 Chimney Model System

To create an environment for the rock/water system under study which simulates a postulated prototype system, considerations were given to the design of the steel containment vessel. Since it was desired to run the tests at pressures and temperatures occurring in geothermal systems, a high integrity pressure vessel involving substantial steel mass was required. The thermal energy storage and the heat loss effects associated with the steel vessel--referred to as the chimney model in this report--were of particular importance for the proper interpretation of the experimental results.

The use of an external loop with an electric circulation heater was determined to be the best method to quickly bring the rock/water system to desired initial temperature and pressure conditions. A detailed description of the test system is given in Appendix A, and only a summary is given here. Descriptions of the design efforts have been given in earlier project progress reports (Kruger and Ramey, 1973; Kruger and Ramey, 1974).

A schematic diagram of the chimney model system in the "heat-up mode" is given in Fig. 2.1. The system operating parameters are summarized in Table 2.1. The steel containment vessel, approximately 5 feet high and about 2 feet inner diameter, is filled with the fractured rock/water system under study. The vessel is well insulated to reduce heat losses and has electric tape heaters wrapped around the steel shell (see Fig. 2.1). Tape heater power control is provided such that energy can be added to the system to compensate for heat losses.

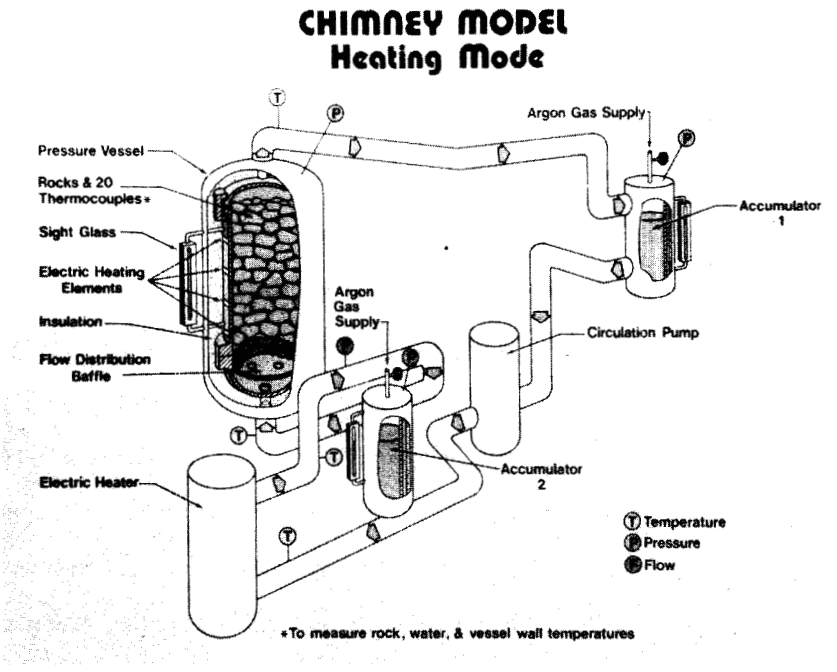

Figure **2.1** Diagram of Chimney Mode1 System - Heating Mode Operation

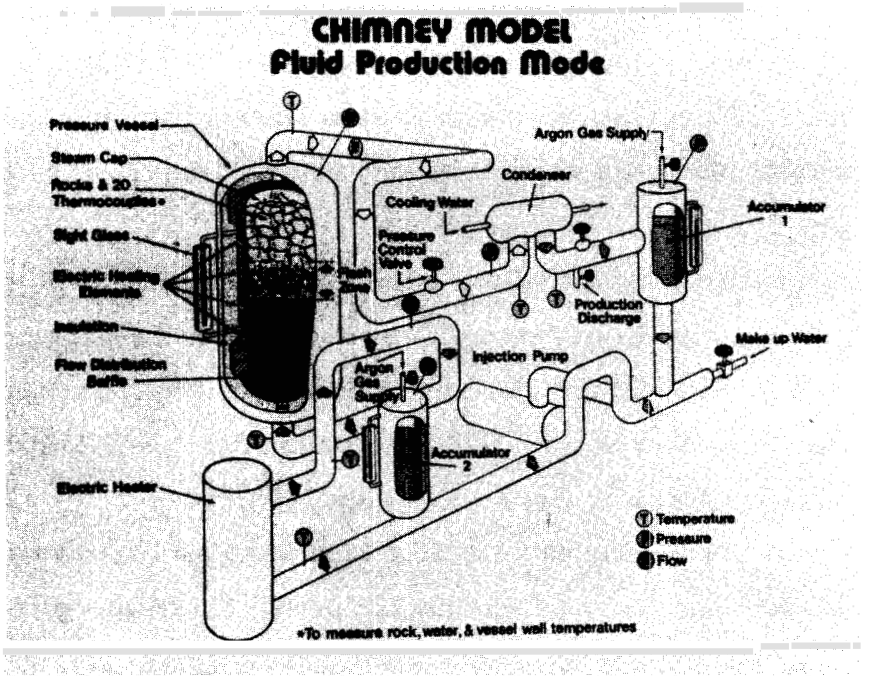

Figure 2.2 Diagram of Chimney Model System - Fluid Production Mode Operation

TABLE 2.1

Chimney Model System Operating Parameters

Operating pressure (max)	800 psig
Operating temperature (max)	500 °F
Chimney water/rock inventory	~17 ft^3
Total system water/rock inventory	~19 ft^3
Average heating rate	~40 °F/hr
Condenser cooling flow rate (max)	~7 gpm
Circulation flow rate during heatup (max)	15 gpm
Recharge flow rate (continuous)	0-1 gpm
Electric heater capacity	23 kW
Tape heater capacity (chimney)	4 kW
Tape heater capacity (water inlet line)	2 kW

A description of the heatup mode with reference to Fig. 2. 1 is useful to explain the system's operation. The system is filled with untreated tap water through a make-up water line (not shown in Fig. 2. 1). To avoid corrosion in the carbon steel system, oxygen scavenging is required, and hydrazine or sodium sulfite is added immediately following the water-fill. Pressurization of the system to avoid flashing is accomplished by addition of argon gas to accumulators 1 and 2.

The circulation pump directs the flow of water through the electric heater which produces approximately 10°F increase in water temperature. The water from the heater circulates through the chimney where some of its energy is transferred to the steel vessel and the rock. Water at the chimney water mixture temperature is then returned via accumulator 1. Heatup circulation is continued until the desired temperature and pressure conditions are achieved and temperature equilibrium of the rock/water/steel system is established. Heatup from

room temperature to about 480 °F is normally accomplished in about 10 hrs.

A schematic diagram of the system fluid production mode is given in Fig. 2.2. Steam production is initiated by opening the flow control valve. The produced steam is condensed in the water-cooled condenser and the mass of condensate is measured as a function of time. Recharge of fluids at the desired temperature and rate is accomplished using the injection pump and the electric heater for preheating. An automatic control system on the heater is used to provide recharge water with approximately constant, linearly decreasing, or linearly increasing fluid enthalpy/time characteristics at the exit of the heater.

Heat losses in the inlet line between the heater and the chimney inlet are compensated for by energy addition using the electric tape heaters on the inlet line. The recharged fluid enters at the lower section of the chimney and is distributed uniformly by the flow distribution baffle (see Appendix A for details). In the postulated prototype system, the recharge fluids are thought to enter mostly along the sides of the chimney. Thus, the laboratory model does not simulate completely the recharge mechanism of a prototype system in this respect.

Instrumentation for measurement of temperatures at various points in the chimney and in the heating loop are iindicated in Fig. 2.1 and 2.2. A summary of the parameters and conditions measured are given in Table 2.2. Details of the instrumentation are given in Appendix A and descriptions of the internal chimney temperature measurements are discussed in the section on rock instrumentation.

Most instrumentation readings were recorded automatically using multipoint recorders. Recordings were also macle of the mass of fluids produced, the injection head tank level to obtain mass of fluids recharged, and the pressure measured by a test gage was recorded to check the electronic pressure transmitter measurement. Electric power inputs to the tape heaters on the chimney and on the inlet line

TABLE 2.2

Summary of Measured Parameters and Conditions

Temperature	Terminal temperatures for chimney model, electric heater, condenser
	Water temperature distribution in chimney
	Rock temperature distribution
	Metal temperature distribution
Pressures	Chimney
	Accumulators
	Condenser
Flow Rates	Circulation
	Condenser cooling water
	Recharge (head tank water level measurement)
	Production (gravimetric measurement)

were measured and recorded as a function of time. A sight glass installed on the chimney covering about 60 percent of the chimney height was used to observe the approximate chimney liquid level during the steam production transient.

2.2 Rock Characteristics

Tests have been run with two different rock loadings. The first rock consisted of a gabbro rock sieved through a 1.5 inch square mesh screen. The rock was purchased as "granite" but closer examination revealed that an appropriate designation was hornblende quartz gabbro. The geographical origin of the rock was not established definitely but is believed to be the Logan area on the San Andreas fault northeast of Monterey, California. The rock is very hard and has a relatively high density.

The second rock loading consisted of a granitic rock with sizes of individual rocks about three times larger than that of the first rock loading. The rock was obtained from a quarry located at Rocklin east of Sacramento, California. The major elements of the two rock types were determined by chemical analysis as given in Table 2. 3

Major Elements of the Two Experimental Rock Types

Element	First Rock Loading (gabbro)	Second Rock Loading (granite)
SiO_2	62.9	73.0
TiO_2	0. 58	0.35
Al_2O_3	15. 7	14. 6
Fe_2O_3	1.4	0. 87
FeO	4.4	0. 84
MnO	0.12	0. 05
MgO	2.5	0. 50
CaO	5.1	2.5
Na_2O	3.5	4.7
K_2O	1.0	1.7
H_2O	1.57	0.74
P_2O_5	0. 19	0. 18
CO_2	0.07	0.08

To extrapolate the experimental thermal results to other systems it is necessary first to characterize the geometries of the rocks used in the experiments. The rock characteristics that appear to be significant for the present study include linear length dimensions and shape factors derived from these, volume, surface area, and the surface area/volume ratio.

The determination of a rock's geometry requires a large number of measurements, but for a large assembly of similar rocks, a practical scheme is based on measurement of the three orthogonal axes (Zingg, 1935; Krumbein, 1941, and Griffiths, 1967). These measurements are indicated in the upper portion of Fig. 2. 3. A classification scheme commonly used (Zingg, 1935) based on these measurements is shown in the lower portion of Fig. 2. 3.

From these length measurements and the measured mass of individual rocks, several parameters useful for the characterization of a rock are obtained. The volume of a rock is given approximately by the rock mass divided by the mean solid density of the rock loading measured as discussed later. The equivalent diameter of a rock is defined as the diameter of a sphere having volume equal to that of the rock, or

$$d \triangleq (6V/\pi)^{1/3} \qquad (2.\ 1a)$$

A measure of the sphericity of a rock is obtained as the cube root of the ratio of the rock volume to the volume of the circumscribing sphere. When the volume of the rock is approximated by a triaxial ellipsoid, the sphericity parameter becomes (Zingg, 1935; Krumbein, 1941)

$$\psi \triangleq (bc/a^2)^{1/3} \qquad (2.\ 1b)$$

Other parameters computed for individual rocks included the breadth/length ratio (b/a) and the thickness/length ratio (c/a). The surface area of a triaxial ellipsoid cannot be determined in closed form, but can be approximated by the following expression:::

*The bracketed term is the exact surface area of a prolate spheroid. The multiplier is an approximation to the ratio of the circumference of an ellipse to that of a circle.

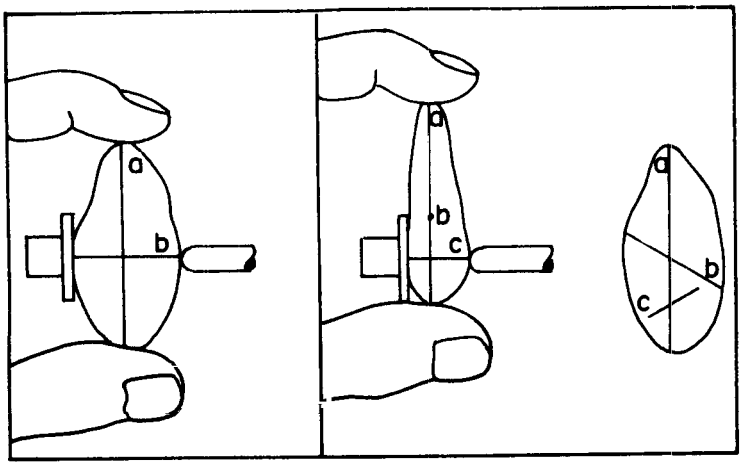

a = length
b = breadth
c = thickness

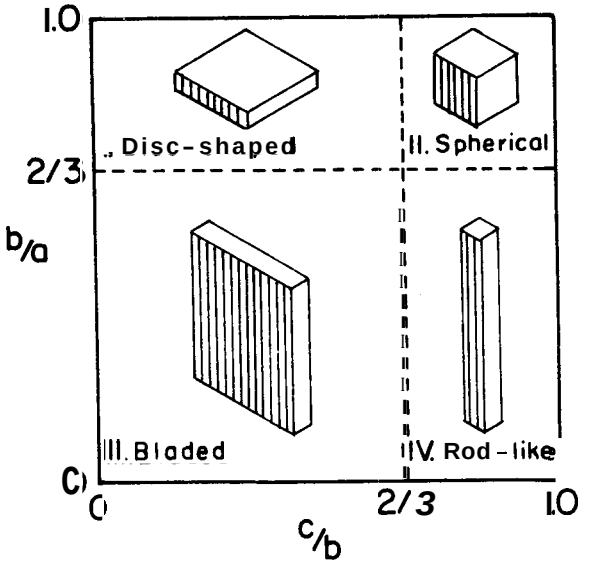

Figure 2.3 Zingg's Classification System for Rock Shapes

$$A = \frac{\pi}{2}\left[b^2 + \frac{ab}{\sqrt{1-(b/a)^2}}\sin^{-1}\sqrt{1-(b/a)^2}\right]\frac{b+c}{2b} \qquad (2.1c)$$

It is expected that the above equation is a fair approximation to the surface area of rocks with few sharp corners such as was generally the case with the rocks used here. The surface area/volume ratio (SVR = A/V) was computed for each rock contained in the sample. For comparison, this parameter was also computed by treating the rock as a sphere with equivalent diameter d and a plate of thickness c. The surface area/volume ratio for a sphere is

$$SVR_s = 6/d \qquad (2.1d)$$

and for a plate it is

$$SVR_P = 2/c \qquad (2.1e)$$

It is noted by comparison of Eqs. (2.1d) and (2.1e) that the surface area/volume ratio for a sphere is three times that of a plate. Moreover, with equal characteristic length (i.e., with d = c) these ratios decrease as the characteristic lengths d and c increase.

Statistical samples of the two rock loadings were obtained and analyzed. Details of the sampling techniques used and of the statistical analysis are given in Appendix B. Two different sampling techniques were used to determine the most efficient method. First, a large sample consisting of 1978 rocks (about 8 percent of the population) from the first rock loading was obtained (referred to subsequently as sample 1-1). No particular emphasis was placed on assuring randomness.

A second much smaller sample (168 rocks) of the first rock loading (sample 1-2) was then obtained by a method referred to as point counting, It involved placing all rocks--the entire population--on a large flat surface. To obtain a random sample, a coarse square grid of wires was layed out above the rocks and rocks immediately under the

grid points were picked for the sample, The point counting method was also used to obtain a sample of the second rock loading (sample 2-2) consisting of 156 rocks.

The three orthogonal axes (a, b, and c, see Fig. 2. 3) and the rock mass of individual rocks of these samples were measured and analyzed statistically. The probability density function, cumulative distribution function, and the statistical parameters mean, variance, and standard deviation as defined in Appendix B were calculated for the measured quantities, the shape factors, and other derived parameters for each sample.

The distribution functions were first plotted on linear paper. However, since it is often found that size distributions arising from crushing processes are lognormal (Herdan, 1960, and Rodean, 1964), the distribution functions were also plotted on semilog paper. The log-normal distribution function has been derived by Epstein (1947) for certain postulated breakage mechanisms as

$$f(x) = \frac{1}{\sigma_{\ln x}\sqrt{2\pi}} \exp\left[-\frac{1}{2\sigma^2_{\ln x}}(\ln x - \overline{\ln x})^2\right] \qquad (2.2)$$

It is noted that this is simply the normal distribution with x replaced by $\ln x$ on the right hand side.

Evaluation and comparison of results from samples 1-1 and 1-2 (both samples from the first rock. loading) showed some discrepancies between details of the distributions, but the difference between the mean and standard deviations of the derived parameters was less than 18 percent. Therefore, the point counting sampling procedure is preferred since it is much quicker.

Evaluation of the results, presented in detail in Appendix B, showed that the distributions of the measured and derived dimensional

quantities for the first rock loading approached lognormal behavior while the distributions for the derived nondimensional parameters approached the standard normal distribution.

An example of a lognormal parameter is given in Fig. 2.4 where the cumulative and probability density functions are plotted for the rock equivalent diameter on semilog paper. The computed lognormal distribution using Eq. (2. 2) is also included in the figure for comparison. It is observed that the sample contains more fine particles than the lognormal distribution would predict and there are fewer large particles which is characteristic of distributions obtained in practice. For example, the data and predictions for particle size distributions obtained from contained underground nuclear explosions are shown in Fig. 2.6 as presented by Lombard (in Kruger, 1966). Comparison of the probability distributions of Figs. 2.4 and 2. 6 shows a remarkable resemblance between these completely independent data.

The probability distribution and cumulative distribution functions for dimensional parameters of the second rock loading were not lognormal. This is indicated in Fig. 2. 5 which gives the distribution functions for the equivalent diameter. The nondimensional parameters were found to have some resemblance to the normal distribution but they were not nearly as normal as the corresponding parameters of the first rock loading. It may be concluded, therefore, that the population constituting the second rock loading was not generated by a large scale mechanical crushing process.

The means and standard deviations of the geometry parameters for both rock loadings (from samples 1-1 and 2-2) are given in Table 2.4. When considering the irregular distributions of the second rock loading, it is not surprising that the standard deviations are large compared to the means. Standard deviations are meaningful only for distributions which are normal or near normal. Therefore, only limited significance can be placed on the magnitudes of the standard deviations for dimensional

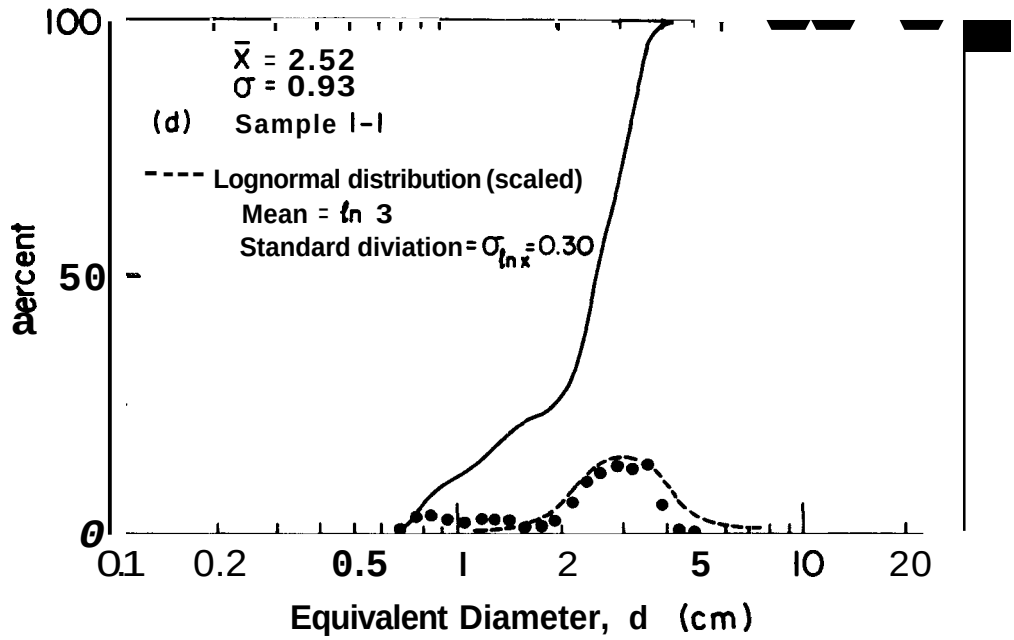

Figure 2.4 Cumulative and Probability Density Distribution Functions for Rock Equivalent Diameter - First Rock Loading

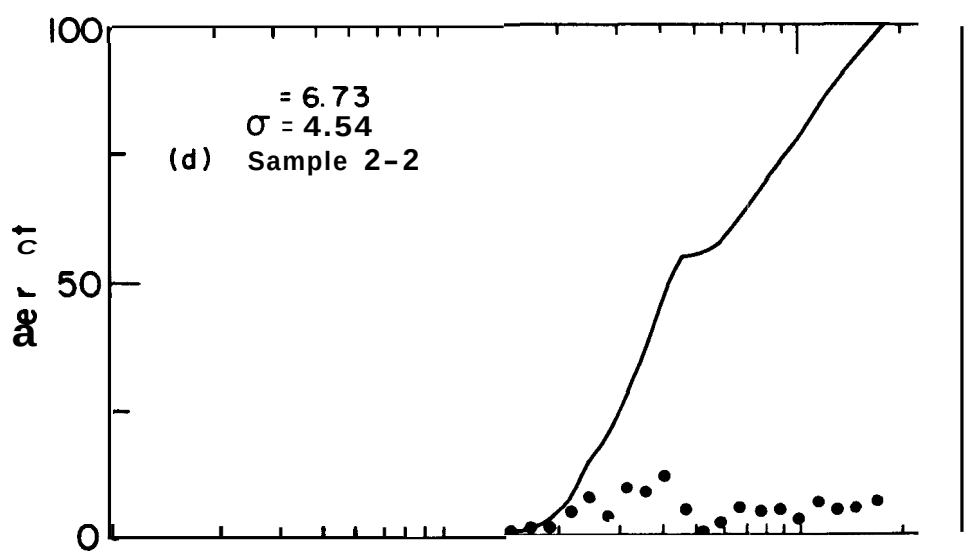

Figure 2. 5 Cumulative and Probability Density Distribution Functions for Rock Equivalent Diameter - Second Rock Loading

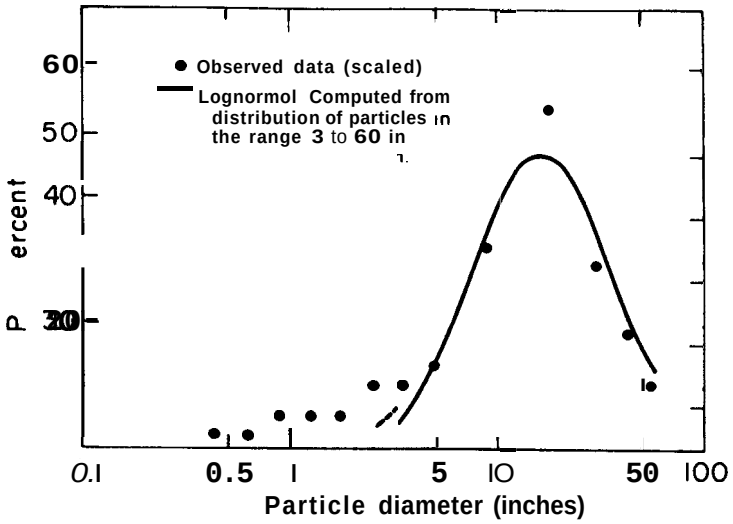

Figure 2.6 Probability Density Distribution Function for Particle Size (from Lombard, in Kruger 1966)

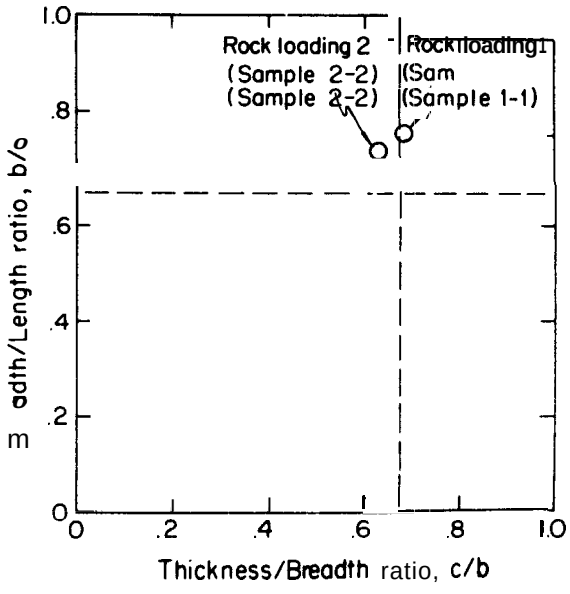

Figure 2.7 Classification of **Rock** Shapes Based on Zingg

parameters. The mean values, however, are used in the rock thermal analysis.

From the sphericity parameter data in Table 2.4, it appears that the rocks of the first rock loading are slightly more spherical than those of the second rock loading. It is seen from Fig. 2.7 that the rocks of the first rock loading are barely classified as spherical while those of the second rock loading are more disc-shaped.

The mean size of the rocks, as given by the equivalent diameter, is almost a factor of three greater for the second as compared to the first rock loading. Comparison of the computed surface area/volume ratio parameters in Table 2.4 (SVR) shows that these are almost identical to those based on the sphere approximation (SVR_S). However, the surface area/volume ratios based on the plate approximation (SVP_P) are lower than either of the above. This suggests that the heat transfer behavior of the rocks might be closer to that of spheres than to that of plates.

To measure the thermal behavior of individual rocks, thermocouples were inserted into rocks distributed throughout the chimney. The means of several geometry parameters for these "instrumented rocks" (six for each rock loading) are compared to the corresponding means for the two rock loadings in Table 2.5. It is noted that the mean size of the instrumented rocks in each case are considerably greater than the mean for the rock loadings (factors of approximately 3 and 6), but the mean shapes as given by the parameters b/a, c/a and ψ do not differ substantially. To attempt to obtain reliable rock/water temperature difference measurements, it was necessary to instrument relatively large rocks. Scaling laws based on mathematical models for these rocks were used to extrapolate the results to other rock sizes. Details of the instrumented rock geometries and photographs of a few of the rocks are given in Appendix B.

TABLE 2.4

Mean and Standard Deviations of Rock Geometry Parameters

Parameter	First Rock Loading (Sample 1-1)		Second Rock Loading (Sample 2-2)	
	Mean	Standard Deviation	Mean	Standard Deviation
Length, a (cm)	3.83	1.44	10.9	7.9[illegible]
Breadth, b (cm)	2.82	1.08	7.41	5.07
Thickness, c (cm)	1.88	0.77	4.11	2.32
Mass, M_r (g)	32.6	26.5	1093	179[illegible]
Equivalent Diameter, d (cm)	2.52	0.93	6.73	4.5[illegible]
Sphericity Parameter, ψ (dim. less)	0.71	0.09	0.67	0.1[illegible]
Breadth/length ratio, b/a (dim. less)	0.74	0.13	0.71	0.1[illegible]
Thickness/length ratio, c/a (dim. less)	0.50	0.12	0.44	0.1[illegible]
Surface Area, A (cm^2)	28.78	17.48	245	292
Volume, V (cm^3)	11.68	9.48	419	688
Surface Area/Volume Ratio, S+R (cm^{-1})	2.96	1.74	1.31	0.80
Surface Area/Volume Ratio, $S+R_s$ (cm^{-1})	2.96	1.74	1.40	0.8[illegible]
Surface Area/Volume Ratio, $S+R_p$ (cm^{-1})	1.41	0.94	0.68	0.4[illegible]

TABLE 2.5

Comparison of M an Rock Geometry Parameters

(Mean for:	M_r (g)	d (cm)	b/a (dim.less)	c/a (dim.less)	ψ (dim.less)	SVR (cm^{-1})
First Rock Loading (Sample 1-1)	32.6	2. 52	0.75	0. 50	0. 71	2. 96
Instrumented Rocks for First Rock Loading	85. 2	3. 88	0.75	0. 54	0. 73	1. 77
Second Rock Loading (Sample 2-2)	1093	6.73	0. 71	0. 44	0. 67	1. 31
Instrumented Rocks for Second Rock Loading	6696	16.0	0.63	0. 33	0. 59	0. 52

The bulk parameters such as total rock mass:, mean rock solid density, rock matrix volume, * volume of void, and the drainage porosity were determined for each rock loading by weighing the chimney rock prior to loading and by water displacement (for details see Appendix B). These parameters are listed in Table 2. 6.

Parameter	First Rock Loading	Second Rock Loading
Total Rock Mass (lb_m)	1640	1818
Mean Solid Density (g/cm^3)	2.79	2. 61
Rock Matrix Volume (ft^3)	16.57	16. 57
Volume of Void (ft^3)	7. 25	5. 72
Drainage Porosity (dim.less)	0.44	0. 35

* Rock matrix volume refers to the total chimney volume occupied by rock.

The permeabilities of both rock loadings were very large resulting in virtually zero flow pressuredrop in the chimney for the low flow velocities of these experiments. The intrinsic porosities of the hard rocks used are considered to be negligible compared to that based on the void space between the rocks.

2.3 Rock Instrumentation.

The center temperature of the instrumented rocks located at various points in the rock matrix (indicated in Figs. 2.8, 2.9, and 2.10) were measured during the transients. The procedure used to locate the thermocouple for the rock center temperature is illustrated in Fig. 2.11. A 1/8-inch diameter hole was first drilled to the approximate rock center in most cases along the c-axis. The 1/16-inch diameter thermocouple was then cemented in place using a high temperature cement. To avoid! direct contact between the cement and the steam, a sealer was applied near the surface.

To measure rock/steam temperature differences, thermocouples were located in the steam next to the instrumented rocks as indicated in Figs. 2.8, 2.9 and 2.10. These were also used to measure the axial steam temperature distribution and to check if radial or circumferential non-uniformities existed in the chimney during the production transient. With a total of 18 thermocouples available for all functions, the chimney thermocouple arrangement shown in Fig. 2.8 was selected for the first rock loading.

Evaluation of the first test results (Hunsbedt, Kruger, and London, 1975) showed that there were no radial or circumferential temperature non-uniformities in the liquid region, but non-uniformities in the superheated region above the liquid level existed.. Therefore, the thermocouples were rearranged as indicated in Fig. 2.9 for the second rock loading. Three instrumented rocks of different sizes to measure the

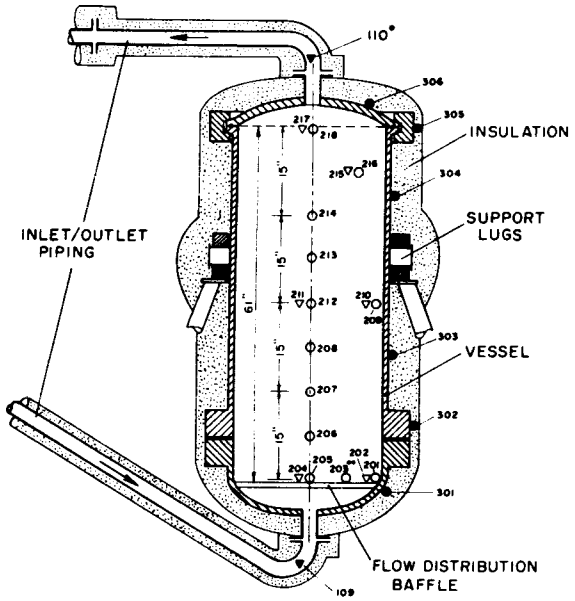

Figure 2.8 Chimney Thermocouple Locations - First Rock Loading

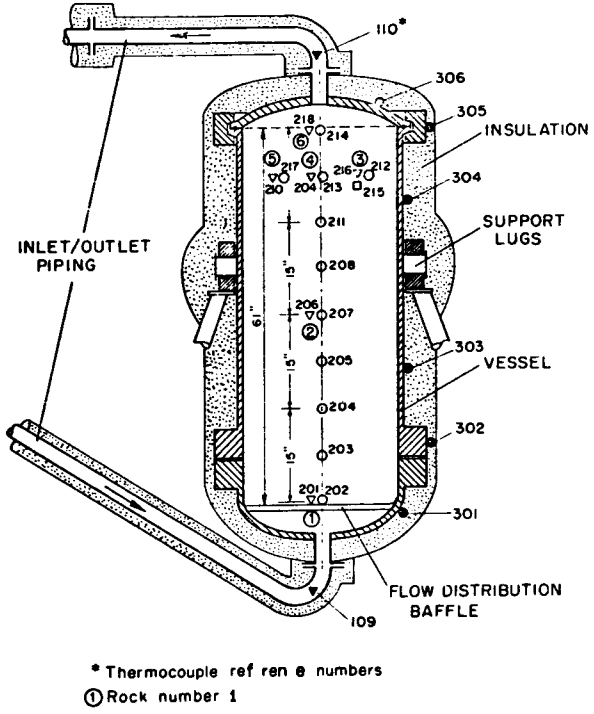

Figure 2 9 Chimney Thermocouple Locations - Second Rock Loading

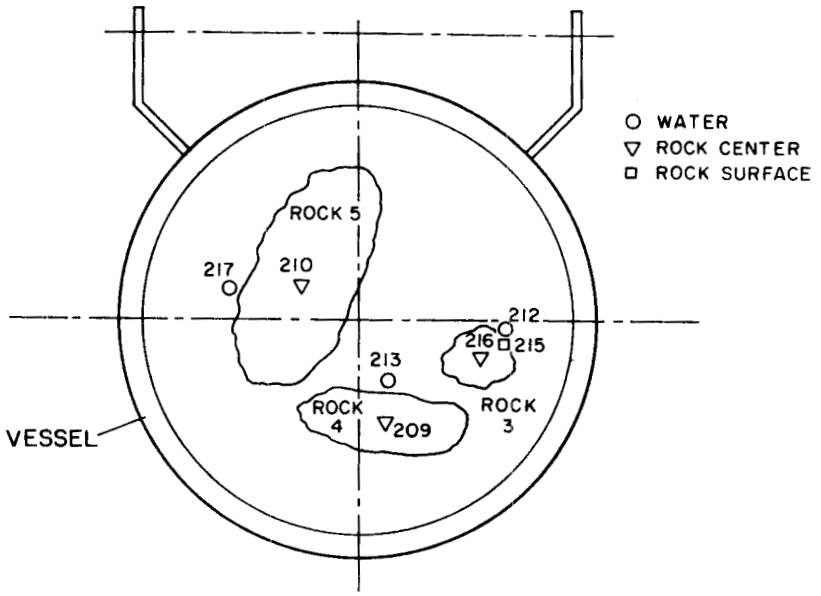

Figure 2. 10 Orientation of Thermocouples in Plane Next to the Top for the Second Rock Loading

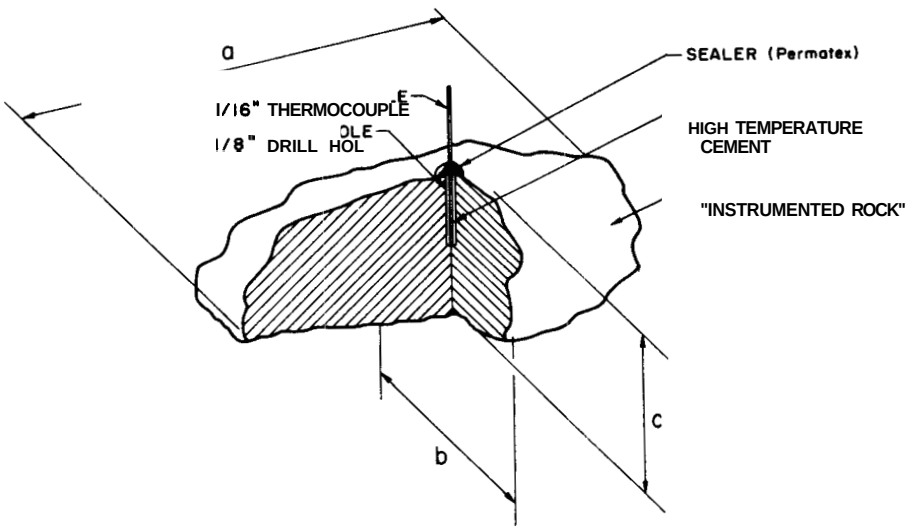

Figure 2. 11 Details of Thermocouple in an Instrumented Rock

effect of rock size on rock/steam temperature differences were located in the plane next to the top as indicated in Figs. 2.9 and 2.10.

The test results with the first rock loading also indicated that reflux of condensed steam from the outlet line might occur. In an attempt to investigate this possibility further, a thermocouple was cemented in a hole drilled completely through instrumented rock 3 such that the thermocouple junction was flush with the rock surface (see Figs. 2.9 and 2.10). If water droplets strike the thermocouple junction, its temperature should be lower than that of the surrounding superheated steam.

CHAPTER 3

ANALYSIS

3.1 Thermal Analysis of Rocks

To compute the rate of rock energy extraction, it is necessary to formulate a mathematical model for the thermal transient of the rock. Several parameters should affect its thermal behavior, such as; (1) a size parameter or a characteristic dimension as its equivalent diameter or thickness, (2) the shape of the rock as described mainly by its surface area/volume ratio, (3) rate of cooldown of the surroundings, and (4) the state of the surrounding steam, i.e., vapor or liquid phase.

Since it is difficult to analyze mathematically a rock with arbitrary shape, it becomes necessary to consider idealized rocks with regular geometry such as a sphere and a plate, The observed rock thermal behavior is then compared to the analysis to determine if either the sphere or the plate idealization is adequate to describe the rock thermal behavior.

3.1.1 Analytic Solutions

Analytic solutions may be obtained in closed form for rocks submerged in a medium which cools according to some continuous function, e.g., an exponential or a linear function. The analysis was carried out for linear cooldown because it appeared to be the best approximation to the real system behavior.

The energy extracted from a rock is related to its mean temperature, which is less than the center temperature when the rock is being cooled. Solutions for the mean and center temperatures are derived in Appendix C for a rock shaped as a sphere of radius r_o and a plate of thickness 2ℓ. Based on one-dimensional analysis, these solutions are given in the following:

Exact solution for mean temperature of sphere:

$$\frac{\bar{T}_r - T}{\mu r_o^2/\alpha} = (1/5 + 1/B)/3 - \sum_{n=1}^{\infty} \frac{6B^2 e^{-\beta_n^2 F}}{\beta_n^4[\beta_n^2 + B(B-1)]} \qquad (3.1a)$$

Exact solution for center temperature of sphere:

$$\frac{T_{rc} - T}{\mu r_o^2/\alpha} = (1/2 \text{ t } 1/B)/3 - \sum_{n=1}^{\infty} \frac{2Be^{-\beta_n^2 F}}{\beta_n[\beta_n^2 + B(B-1)]\sin\beta_n} \qquad (3.1b)$$

Exact solution for mean temperature of plate:

$$\frac{\bar{T}_r - T}{\mu \ell^2/\alpha} = (1/3 + 1/B) - \sum_{n=1}^{\infty} \frac{2B^2 e^{-\beta_n^2 F}}{\beta_n^4[B(B+1) + \beta_n^2]} \qquad (3.1c)$$

Exact solution for center temperature of plate:

$$\frac{T_{rc} - T}{\mu \ell^2/\alpha} = (1/2 + 1/B) - \sum_{n=1}^{\infty} \frac{2Be^{-\beta_n^2 F}}{\beta_n^2[B(B+1) + \beta_n^2]\cos\beta_n} \qquad (3.1d)$$

In these equations μ is the cooldown rate, F is the Fourier number and B is the Biot number (see Appendix C for details).

The infinite sums in the above equations require considerable numerical evaluations. Since one-lump approximations are usually accurate enough for our purposes, these approximations, erived in Appendix C in terms of the mean heat conduction path lengths (δ's), are given in the following:

$$\frac{\bar{T}_r - T}{\mu r_o^2/\alpha} = \frac{(\delta_s + 1/B)}{3}\left[1 - e^{-3F/(\delta_s + 1/B)}\right] \tag{3.2a}$$

One-lump solution for center temperature of sphere:

$$\frac{T_{rc} - T}{\mu r_o^2/\alpha} = \frac{(\delta_{cs} + 1/B)}{3}\left[1 - e^{-3F/(\delta_{cs} + 1/B)}\right] \tag{3.2b}$$

One-lump solution for mean temperature of plate

$$\frac{\bar{T}_r - T}{\mu \ell^2/\alpha} = (\delta_p + 1/B)\left[1 - e^{-F/(\delta_p + 1/B)}\right] \tag{3.2c}$$

One-lump solution for center temperature of plate

$$\frac{T_{rc} - T}{\mu \ell^2/\alpha} = (\delta_{cp} + 1/13)\left[1 - e^{-F/(\delta_{cp} + 1/B)}\right]1 \tag{3.2d}$$

Comparisons of **Eqs. (3.** 1) to **Eqs. (3.** 2) show that the values of the δ's for quasi-steady state conditions (time dependent terms go to zero) are:

For sphere: $\delta_s = 1/5$, $\delta_{cs} = 1/2$

For plate: $\delta_p = 1/3$, $\delta_{cp} = 1/2$ (3.3)

The rock/steam temperature difference characteristics predicted by the one-lump and exact solutions are given in Fig. 3.1 for B = 10.* It is observed that the sphere attains quasi-steady state rock/steam temperature differences sooner than the plate mainly because the sphere has the larger surface area/volume ratio (by a factor of 3). Moreover, the rock/steam temperature differences are higher for the plate than for the sphere which is also related to the different surface area/volume ratios for the two geometries. It is further observed that the one-lump solutions are in reasonable agreement with the exact solutions, particularly for the body mean temperatures.

The one-lump solutions may be employed to estimate Biot numbers (and heat transfer coefficients) from experimental1 data. Rock/steam temperature differences are measured for rocks of various known sizes both in vapor and liquid environments. Since the cooldown rate is fairly constant, it may be acceptable to use local cooldown rates μ_a to evaluate approximate values of the Biot number based on the sphere idealization, When time dependent terms are neglected, Eq. (3.2b) gives

$$B \triangleq \frac{hr_o}{k} \cong \frac{1}{\dfrac{3(T_{rc}-T)}{\mu_\ell r_o^2/\alpha} - \dfrac{1}{2}} \qquad (3.4)$$

where all quantities on the right hand side are known from temperature measurements, the instrumented rock geometry, and the rock thermal properties.

*This value of B corresponded to a rock with characteristic length L, r_o, $\ell \cong 6$ inches submerged in liquid.

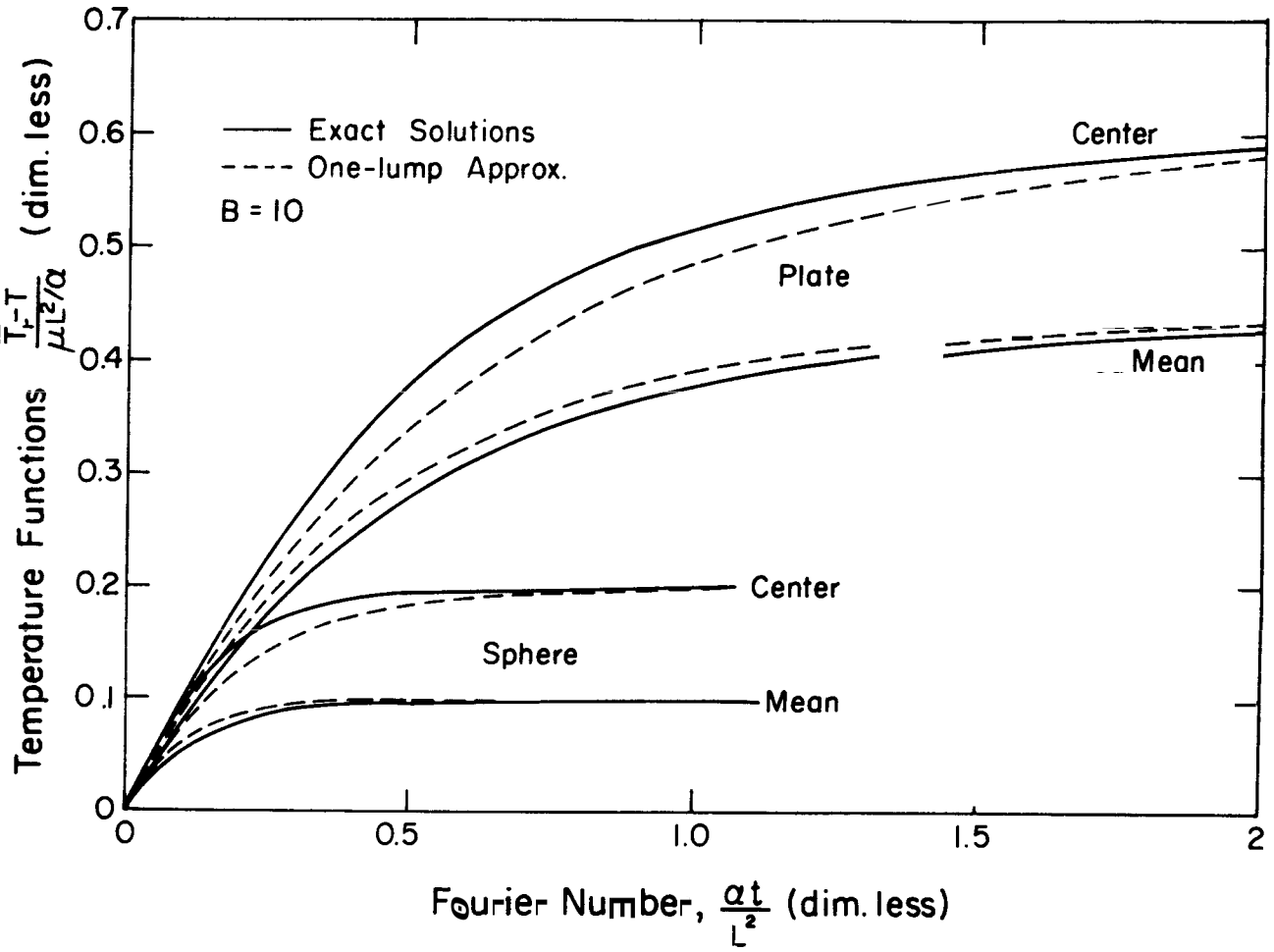

Figure 3.1 Predicted Temperature Functions Using Exact and Approximate Theory.

3.1.2 Time Constants

The thermal characteristics of the idealized rock shapes considered are closely related to their "time constants". The physical meaning of the term "time constant" is best illustrated by an example. Suppose a body is in thermal equilibrium with its surroundings and then the surrounding temperature is suddenly changed to a different temperature. A certain period of time is required for the body to reach the new equilibrium temperature. The time required for the body mean temperature to reach 63.2 percent of the temperature change is defined as the time constant.

The time constants for spheres and plates can be obtained from temperature charts (Jaeger and Clarke, 1947; and Schneider, 1955). Temperatures are generally given in nondimensional form in terms of the Fourier and Biot numbers. A more convenient method based on a one-lump parameter approach, derived from these temperature charts, is given in Appendix C. The time constants for the sphere and the plate are given by the following equations:

$$\tau_s = \frac{r_o^2}{3\alpha}(\delta_{s\tau} + 1/B) \qquad \text{(sphere)} \qquad (3.5)$$

$$\tau_p = \frac{\ell^2}{\alpha}(\delta_{p\tau} + 1/B) \qquad \text{(plate)} \qquad (3.6)$$

The δ's used in these equations are functions of the Biot number as shown in Fig. C.3 in Appendix C.

Time constants for spheres (Eq. (3.5)) for a range of diameters and Biot numbers ranging from 0.1 to infinity are given in Fig. 3.2.

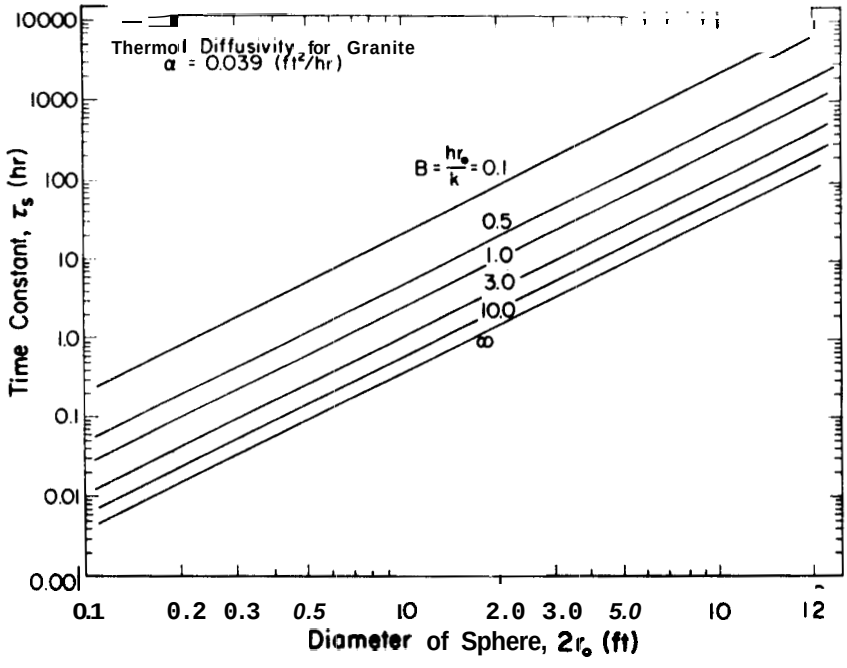

Figure 3.2 Time Constants for **Spheres**

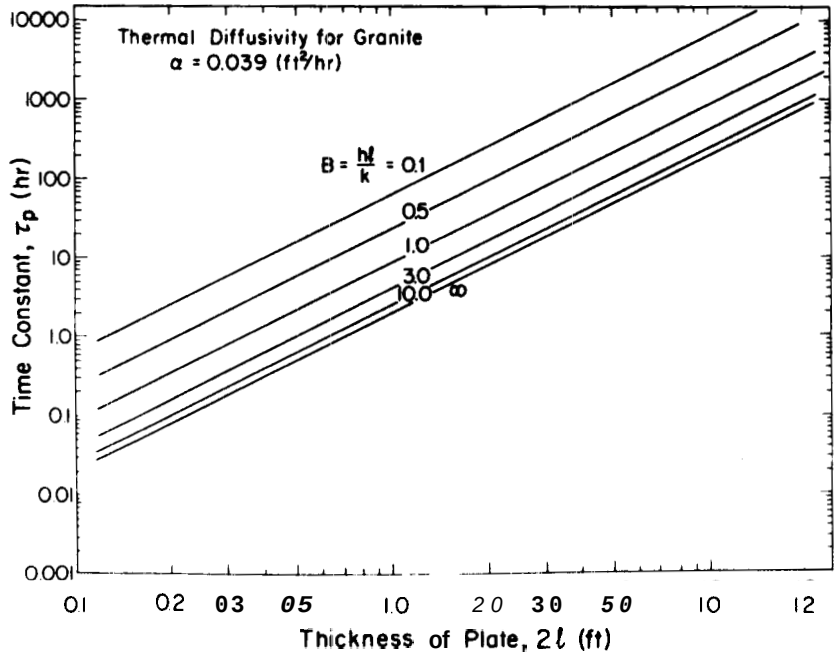

Figure 3.3 Time Constants for **Plates**

Time constants for plates (Eq. (3.6)) are given in Fig. 3. 3. The thermal diffusivity of granite:: at a mean temperature of 400 ^{o}F was used to compute these time constants.

The time constants for spherical rocks are estimated from Eq. (3. 5) with $2r_o$ = d = equivalent diameter for the rock. If the thickness c of a rock is small compared to the other **two** rock dimensions (a and b), Eq. (3. 6) is used to estimate the time constant with 2ℓ = c.

Most rocks have shapes which are different from these two limiting cases. To estimate the time constants of suc'h rocks, the following formula is proposed

$$\tau = (1 - \psi^{1/n})\tau_P + \psi^{1/n}\tau_S \qquad (3.7)$$

where n is evaluated empirically and where ψ is the sphericity parameter defined in Chapter 2. The limits of the above equation corresponds to the limits discussed above since ψ approaches; 1 when the rock becomes spherical and τ approaches 0 when the one rock dimension is small in comparison to the other **two.** Experimental data to determine n in Eq. (3. 7) directly are not available, but evaluation of the surface area/volume ratios for the rocks in Chapter 2 indicated that the thermal behavior might be close to that of spheres. It would appear, therefore, that the exponent of ψ should be selected so that the estimated rock time constants are heavily weighed towards those of spheres. **A** relatively large value of n is required to achieve this. Since there are no experimental data on which the choice of n can be based, an arbitrary value of n = **4** is tentatively proposed for the present analysis.

The time constants calculated from Eqs. (3. 5) and (3. 6) depend on the Biot number (see Figs. **3.** 2 and 3. 3). The convective heat transfer coefficient in liquid and vapor environments may vary by more

*See Appendix D for detailed evaluation of rock thermal properties.

than an order of magnitude. Since the Biot number is proportional to the surface heat transfer coefficient, the rock time constants will in turn depend on the rock environment. The heat transfer coefficient in liquid environment is relatively high so that the surface thermal resistance is small in comparison to the internal thermal resistance (i.e., high Biot number). In that case the magnitude of the heat transfer coefficient does not affect the time constant significantly. For the purpose of estimating the time constants, a heat transfer coefficient of 50 Btu/hr ft^2 ^{0}F was assumed.

It is more difficult to estimate the heat transfer coefficient in saturated or slightly superheated vapor environment due to a possible reflux of condensed steam droplets from the outlet line region. Under these conditions re-evaporation of water droplets which encounter a rock surface may seriously affect the apparent surface heat transfer coefficient due to mass associated energy transport from the surface superimposed on the convective heat transfer mechanism.

If mass associated energy transport is neglected, one may obtain a rough estimate of the heat transfer coefficient for superheated steam flow using the correlation by Meek (1961) for gas flow in a packed bed of uniform diameter spheres. This correlation is

$$St = 2.02\ Re^{-0.38} \qquad (3.8)$$

The Reynolds number (Re) and the Stanton number (St) are based on the "approach" flow velocity which is the flow velocity corresponding to the chimney flow area without rock.

The heat transfer coefficient for the average conditions of these experiments was estimated to be 1.1 Btu/hr ft^2 ^{0}F. The actual heat transfer coefficient may be considerably higher due to the possible reflux effect, It is assumed for the purpose of estimating the time constants that the heat transfer coefficient is 3 Btu/hr ft^2 ^{0}F. The estimated

time constants for the mean size rock of each roclk loading are given in Table 3. 1. Time constant data :for the instrumented rocks of the two rock loadings are given in Appendix C (Table C. 2).

TABLE 3. 1

Geometry Data and Es mated Time Constants for Mear Size Rocks

Idealization	Symbol*	First Rock Loading	Second Rock Loading
Sphere	d (inches)	0.99	2. 65
	τ_{sL} (hr)	0.014	0.044
	τ_{sG} (hr)	0. 18	0.46
Plate	c (inches)	0.74	1. 62
	τ_{pL} (hr)	0.034	0.085
	τ_{pG} (hr)	0. 39	0. 92
Combined Sphere and Plate Eq. (3. 7) (n=4)	τ_L (hr)	0.016	0.048
	τ_G (hr)	0.197	0.49

'Subscript "L" refers to liquid environment (h = 50 Btu/hr ft^2 °F) and "G" to vapor environment (h = 3 Btu/hr ft^2 °F)

Examination of the magnitudes of the time constants in Table 3. 1 shows that the sphere approximation results in time constants which are roughly about half of those for the plate approximation, Closer examination of Table 3. 1 also shows that the time constants for rocks in vapor environment, where the Eliot number is small in this case,

increase approximately as the characteristic length d. However, the time constants increase more as the lengtlh squared for rocks in liquid environment where the surface heat transfer resistance is of less importance (large Biot number).

A relationship for estimating the mean rock/steam temperature differences in terms of the time constant and the local cooldown rate μ_ℓ is derived. For the quasi-steady state approximation the rock/steam temperature difference for a sphere becomes

$$\frac{\overline{T}_r - T}{\mu_\ell r_o^2/\alpha} = \frac{(\delta_s + 1/B)}{3} \qquad (3.9)$$

The magnitude of δ_s is approximately equal to $\delta_{s\tau}$ (0.20 vs. −0.18) for B greater than about 1. Therefore, one can set δ_s t 1/B $\simeq \delta_{s\tau}$ t 1/B. Combining Eqs. (3.6) and (3.9) then gives

$$\overline{T}_r - T = \mu_\ell \tau_s . \qquad (3.10)$$

3.1.3 Numerical Formulation of Rock Thermal Transient

The rocks are cooling down in a steam environment with a temperature that depends on the chimney pressure. The chimney steam pressure in turn is largely a function of the steam production/recharge characteristics. Thus, there is a coupling effect between steam production/recharge and the rock cooldown rate which largely determines the rock energy extraction rate. This coupling effect cannot be adequately described for the entire transient by the analytic solutions derived for constant cooldown rate. A numerical computation procedure

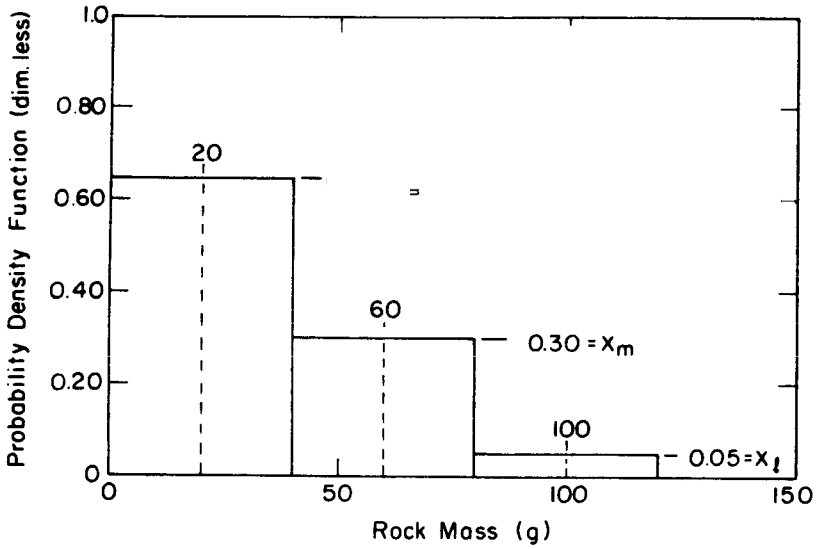

Figure 3.4 Assumed Distribution of Rock Mass for the First Rock Loading

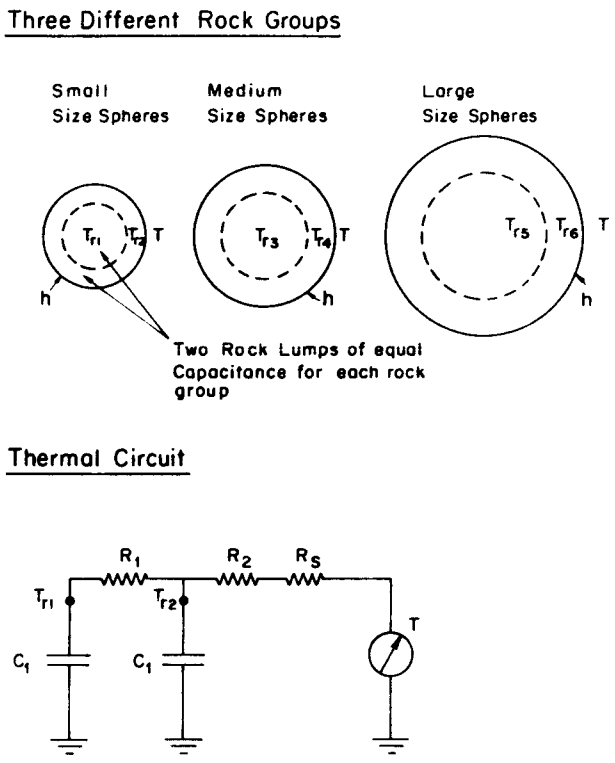

Figure 3 5 Idealized Rock Model for Numerical Solution

for the rock thermal transients which is coupled to the actual variation in the surrounding temperature is required.

To formulate a numerical procedure, an idealized physical model which adequately represents the gross thermal behavior of the complete rock loading is needed. In view of the rock geometry data presented in Chapter 2 it would appear that the rocks can be represented by spheres. However, the number of sphere sizes in the idealized model must be limited such that acceptable numerical computation time results.

Considering Fig. B. **4** for the distribution of rock mass it would appear that three different rock size groups is sufficient. The distribution of sizes used to represent the first rock loading is shown in Fig. **3.4.** **A** similar grouping (with different mass fractions) was used for the second rock loading. Comparison of the one-lump and exact analytic solutions for linear cooldown showed that a fair prediction of the thermal transient was possible with the one-lump approach. However, to improve the prediction further it was decided to subdivide each rock size group into **two** equal thermal capacitance (equal volume) lumps as indicated in the upper portion of Fig. 3.5,

Each sphere is analyzed with the help of the analog thermal circuit shown in the lower portion of Fig. 3.5. The thermal resistances R_1, R_2, and R_s represent, respectively, the thermal conduction resistance between inner and outer lumps, thermal conduction resistance from the outer lump to the surface of the sphere, and the convection resistance at the rock surface. To reduce computation time it is assumed that the rock thermal properties and the surface heat transfer coefficient are constant.

An energy balance on each lump leads to one first order, linear differential equation with constant coefficients. The derivations of the equations given below are presented in Appendix C.

$$\frac{dT_{r1}}{dt} = a'_{11}T_{r1} + a'_{12}T_{r2} + \cdots + a'_{16}T_{r6} + b'_1 T$$

$$\vdots \qquad \vdots$$

$$\frac{dT_{r6}}{dt} = a'_{61}T_{r1} + a'_{62}T_{r2} + \cdots + a'_{66}T_{r6} + b'_6 T \qquad (3.11)$$

Here the mean rock lump temperatures are represented by T_{ri} ($i = 1, 2, \cdots, 6$) and the temperature of the surrounding steam is T which represents the coupling (or driving) mechanism between the rock and its surroundings. The formulation of the equations governing the steam temperature T in terms of the steam production/recharge characteristics and the simultaneous solution (integration) of the equations are presented later.

Once each mean rock lump temperature has been determined at a given time t, the spatial mean temperature of the rock loading is computed as follows:

$$\bar{T}_r = [(T_{r1} + T_{r2})X_s + (T_{r3} + T_{r4})X_m + (T_{r5} + T_{r6})X_l]/2M_r \qquad (3.12)$$

where the X's are the assumed rock mass fractions (see Fig. 3.4), and where M_r is the total rock loading mass. The rate of rock energy extraction is then computed from

$$Q_r = M_r \bar{C}_r \frac{d\bar{T}_r}{dt} \qquad (3.13)$$

where $\bar{C}_r$ is the time averaged specific heat capacity of the rock.

3.2 Laboratory Model Reservoir Analysis

3.2.1 Analysis on a Rate Basis

In this section an analysis is presented for the pressure and temperature transients of the model. The analysis, once verified, becomes a tool which can be used to predict the behavior of other similar systems within the limitations of the analysis,

It is necessary first to make certain idealizations regarding the physical system under consideration. Since there is no flow pressure drop in the rock matrix, the fluids can circulate freely by natural convection within the rock matrix. There is a small static head of only 2 psi in the model, For these conditions the fluids may be at nearly uniform temperature equal to the saturation temperature corresponding to the average steam pressure.

The idealized system under consideration is shown in Fig. 3.6. Steam with enthalpy i_p is produced at a rate M_p and fluids with enthalpy i_i are recharged at a rate M_i. There is heat transfer at a rate Q_r from the rock and at a rate Q_m from the steel vessel to the two-phase liquid/vapor mixture in the control volume. The control volume considered is the void space bounded by the rock surfaces and the chimney steel wall. Derivations of the governing equations using the conservation of mass and energy principles are given in Appendix C. The resulting differential equation for the time derivative of pressure is

$$\frac{dP}{dt} = \frac{\dot{Q}_m + \dot{Q}_r + \left(i_i + v_f \frac{e_{fg}}{v_{fg}} - e_f\right)\dot{M}_i - \left(i_p + v_f \frac{e_{fg}}{v_{fg}} - e_f\right)\dot{M}_p}{\left[(e_f)' + \frac{V\phi}{M}\left(\frac{e_{fg}}{v_{fg}}\right)' - \left(v_f \frac{e_{fg}}{v_{fg}}\right)'\right]M} \qquad (3.14)$$

Analytic formulations for the parameters, referred to as the boundary parameters, Q_m, $\dot{Q}_r$, $\dot{M}_i$, i_i, M_p, i_p, and M as well as for the steam

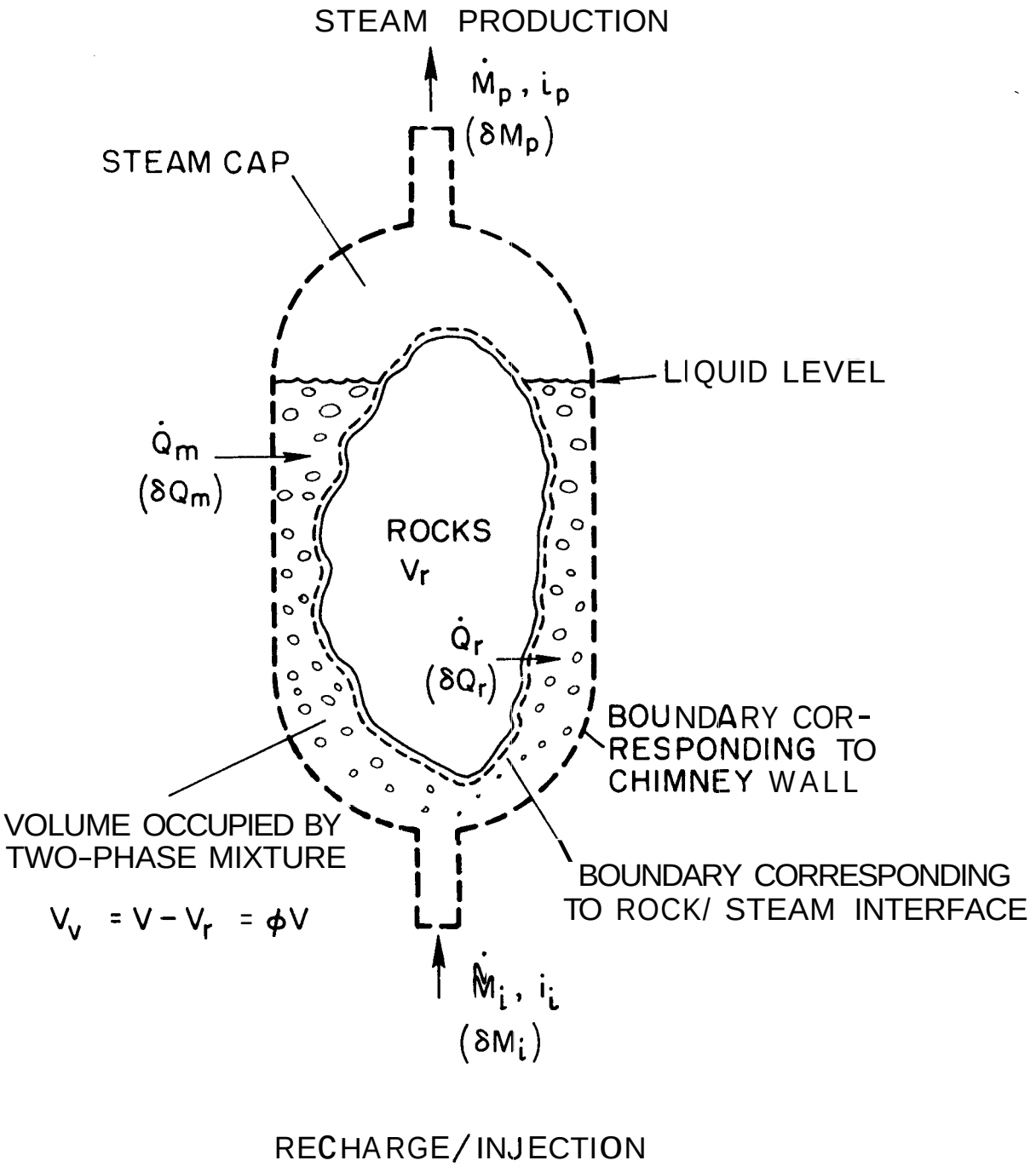

Figure 3.6 Control Volume for Chimney Model Analysis

properties are required in Eq. (3. 14). 111 this analysis the experimental data will provide the basis for obtaining these formulations.

An expression for Q_m based on an energy balance on the steel vessel is given by

$$\dot{Q}_m = \dot{Q}_m - M_m \frac{d(C_m \theta_m)}{dt} - UA\theta_m \qquad (3.15)$$

The first term on the right: represents energy addition by the electric tape heaters on the vessel. The second term represents energy release from the steel as the chimney cools down during the steam production process, The last term is the heat losses to the environment from the chimney. The temperature difference θ_m is measured as a function of time for each experiment. The numerical1 values of M_m and UA were determined from heatup and cooldown experiments as described previously (Hunsbedt, Kruger, and London, 1975).

The rate of energy extraction from 'the rock as given by Eq. (3. 13) is established by simultaneous solution of Eqs. (3. 11) and (3. 14). Details of the solution procedure are given later in this section.

The recharge and steam production rates are determined from the slope of the measured cumulative recharge and steam production-time data. These data were also used to compute M, the mass of fluids in the chimney at time t used in Eq. (3.14), from a mass balance on the chimney which gives

$$M = M_o + M_i - M_P \qquad (3.16)$$

where M_o is determined from the known void volume and measured initial water temperature.

The enthalpy of the recharged fluids at the chimney inlet is computed from the following expression based on an energy balance on the inlet line

$$i_i = i_H \; t \; (\dot{Q}_i - U_i A_i \theta_i / \dot{M}_i \qquad (3.17)$$

where i_H is the enthalpy measured at the exit of the electric circulation heater. The rate of energy addition by the tape heaters for the inlet line Q_i is measured as a function of time and the line heat losses are estimated using conventional procedures.

The enthalpy of the produced steam at the chimney exit was computed using a similar procedure to obtain

$$i_p = i_c - U_o A_o \theta_o / \dot{M}_p \qquad (3.18)$$

where i_C is the steam enthalpy at the condenser inlet evaluated from a heat balance on the condenser as a function of time. Details of this procedure has been given previously (Hunsbedt, Kruger, and London, 1975).

Thermodynamic properties of steam are available in tables (Meyer et al., 1967). and as FORTRAN subroutines (McClintock and Silvestri, 1968). These subroutines:: were used in the numerical solution procedure.

3.2.2 Numerical Solution Procedure

To simplify the numerical solution of the differential equations, it is convenient to introduce nondimensional variables. The variables found to be useful for this particular problem are stated below (see the Nomenclature for explanation of dimensional quantities):

Computer programs were made ;available by the Nuclear Energy Division of the General Electric Company, San Jose, California.

$$
\begin{aligned}
P^* &\triangleq P_s/P_{so} && = \text{chimney pressure parameter}\\
t^* &\triangleq t/t_c && = \text{nondimensional production time}\\
M_P^* &\triangleq M_P/M_o && = \text{cumulative steam production parameter}\\
\dot{M}_P^* &\triangleq \dot{M}_P/\bar{\dot{M}}_P && = \text{steam production rate parameter}\\
M_i^* &\triangleq M_i/M_0 && = \text{cumulative recharge parameter}\\
\dot{M}_i^* &\triangleq \dot{M}_i/\bar{\dot{M}}_p && = \text{recharge rate parameter}\\
M^* &\triangleq M/M_o && = \text{chimney mass fraction}
\end{aligned}
\qquad (3.19)
$$

where t_c is the reservoir characteristic time defined as the initial in-place fluid mass, M_o, divided by the mean steam production rate, $\bar{\dot{M}}_p$.

The previous equations required to describe the reservoir transients (rock temperature, steam temperature, and pressure) in terms of these non-dimensional variables are summarized below:

Rock Lump Temperatures (rewritten Ea. (3.11)):

$$
\begin{aligned}
\frac{dT_{r1}}{dt^*} &= a_{11}T_{r1} + \cdots a_{16}T_{r6} + b_1 T\\
&\vdots \qquad\qquad \vdots \qquad\quad \vdots\\
\frac{dT_{r6}}{dt^*} &= a_{61}T_{r1} + \cdots a_{66}T_{r6} + b_6 T
\end{aligned}
\qquad (3.20a)
$$

Rock Mean Temperature (Eq. (3.12)):

$$
\bar{T}_r = [(T_{r1} + T_{r2})X_s + (T_{r3} + T_{r4})X_m + (T_{r5} + T_{r6})X_1]/2M_r \qquad (3.20b)
$$

Rate of **Rock** Energy Extraction (rewritten **Eq. (3. 13)**):

$$\dot{Q}_r = M_r \bar{C}_r \frac{d\bar{T}_r}{dt^*} t_c \qquad (3.20c)$$

Pressure (rewritten **Eq. (3. 14)**):

$$\frac{dP^*}{dt^*} = \frac{\dot{Q}_m/\bar{M}_p + \dot{Q}_r/\bar{M}_p + \left(i_i + v_f \frac{e_{fg}}{v_{fg}} - e_f\right)\dot{M}_i^* - \left(i_p + v_f \frac{e_{fg}}{v_{fg}} - e_f\right)\dot{M}_p^*}{\left[(e_f)' + \frac{1}{M^*}\frac{V\phi}{M_o}\left(\frac{e_{fg}}{v_{fg}}\right)' - \left(v_f \frac{e_{fg}}{v_{fg}}\right)'\right] M^* P_{so}} \qquad (3.20d)$$

Stearn Temperature:

$$T = f(P^*, P_{so}) \qquad \text{(from steam tables)} \qquad (3.20e)$$

Parameters:

$$M^* = 1 + M_i^* - M_p^* \qquad (3.20f)$$

$$\dot{M}_i^* = \frac{dM_i^*}{dt^*} \qquad (3.20g)$$

$$\dot{M}_p^* = \frac{dM_p^*}{dt^*} \qquad (3.20h)$$

and $\dot{Q}_m$, i_i, and i_p from **Eqs.** (3.15) through (3.18).

Initial Conditions:

$T_{r1}, T_{r2} \cdots T_{r6}$, T and P* are specified at the start of integration (time = t_s^*)

A fourth order numerical integration procedure* was used to solve the system of equations. The starting time for the computation

* The procedure used is referred to as the Runge-Kutta method. For a description see, e. g. , Carnaharn, Luther and Wilkens (1969).

t_s^* was selected such that saturated water conditions had been reached in the chimney. The system was generally slightly subcooled when steam production was initiated (at $t^* = 0$) due to argon gas pressurization during heatup, but saturated steam conditions were normally reached in the chimney after about 5 to 10 minutes of steam production. The temperature of the rock lumps at time t_s^* were specified to be equal to the measured water temperature at this time. The pressure was set equal to the measured pressure at time t_s^*.

Details of the analysis and considerations regarding the maximum time step size to assure stability are given in Appendix C. The limiting factor in determining the maximum time step is the minimum rock lump time constant. When the rocks are small, the maximum time step is also small and the integration procedure is slow and expensive. It was possible, however to reduce the number of steam property evaluations in the coefficients on the right hand side of Eq. (3. 14) because these changed only slightly over a few time steps. Thus, evaluation of the steam properties every 20th time step was sufficient. The computation time was reduced by a factor of about one third with no apparent effect on the numerical solution using this approach.

To verify the numerical formulation and solution procedure for the rock thermal transients, a run was made with conditions such that constant cooldown rate resulted. The numerical results for the mean temperature of a sphere given by Eq. (3. la) are compared in Fig. 3. 7. The solid lines are the exact solutions for B = 1 and 10. The broken lines are the numerical results with the geometry factors r_1^* and r_2^* from Johnson (1955) as described in Appendix C.

It is seen from Fig. 3. 7 that the numerical predictions do not agree well with the exact solution. It was suspected that the geometry factors derived by Johnson for hollow spheres with large outer to inner radii ratio were not strictly applicable to the solid sphere geometry with surface heat transfer :resistance. The magnitudes of the geometry

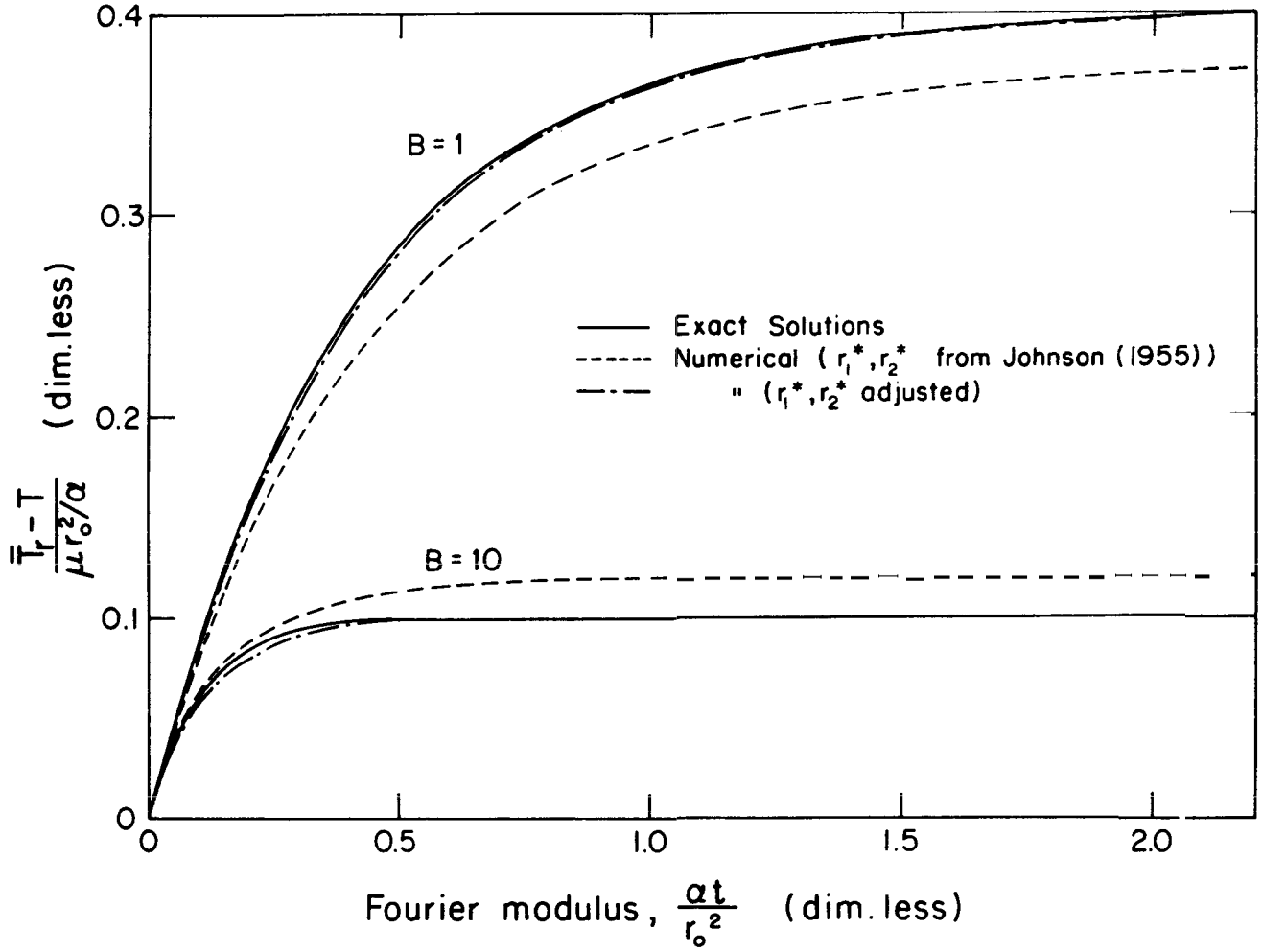

Figure 3.7 Comparison of Numerical and Exact Rock Thermal Transients

factors were therefore adjusted until reasonable agreement between the numerical and exact results was achieved for the adjusted r_1^* and r_2^* values listed in Table 3.2. The adjusted data in the table indicate that the geometry factors depend on the Biot number (relative importance of surface thermal resistance). The geometry factors were found to vary approximately linearly with the Biot number. Therefore, linear interpolation is used to estimate the geometry factors for other values of the Biot number from the adjusted data,

TABLE 3.2

Geometry Factors for the Two-Lump Parameter Description of A Sphere

Source	Geometry Factor	B = 1	B = 10
Johnson (1955)	r_1^*	0.5092	0.5092
	r_2^*	0.8992	0.8992
Adjusted (This study)	r_1^*	0.4339	0.5725
	r_2^*	0.8626	0.9298

3.2.3 Analysis on a Time Interval Basis

The analysis on a rate basis in the previous section gave the reservoir pressure and temperature histories as functions of time. There may be cases, in which only the end conditions rather than the complete transients are required. The initial conditions of the reservoir are known from temperature and pressure measurements prior to starting steam production. It is desired to determine how much of the original reservoir fluids can be produced for a specified end pressure, reservoir volume, porosity, recharge, and degree of rock energy extraction.

The idealized system shown in Fig. 3.6 is analyzed. At the start of steam production, it is assumed that the system contains saturated liquid only. Furthermore, it is assumed that a uniform temperature two-phase mixture is maintained in the system during the steam production transient. This assumption is usually made to simplify the analysis as was the case in the analysis by Whiting and Ramey (1968). A later analysis by Brigham and Morrow (1974) assumed uniform temperature conditions in the liquid phase and a vapor/rock temperature distribution in the vapor zone that remained constant with time. The present analysis accounts for the possibility that not all of the thermal energy stored in the rock is extracted by introducing the rock energy extraction fraction concept. An outline of the present analysis is given below. Details of the derivations are given in Appendix C.

Conservation of mass for the control volume containing the two-phase steam mixture in Fig. 3.6 gives on a time interval basis

$$M_e = M_o + M_i - M_P \tag{3.21}$$

where the subscripts "e" and "o" refer to mass in the system at the end and initial conditions, respectively. The two last quantities represent cumulative mass recharge and steam production at the end state, respectively.

It is assumed that the enthalpies of the recharged and produced fluids do not vary significantly in the time interval from the initial to the end state considered. Conservation of mass and energy for the control volume then leads to an approximate expression for the mass of fluids in the system at the end state which is

$$M_e = \left[(i_p - e_o)M_o + (i_p - i_i)M_i - Q_m - \rho_r V(1-\phi)\bar{C}_r(T_o - T_e)\eta_e\right] \Big/ (i_p - e_e) \tag{3.22}$$

The enthalpy of the produced steam i_P and the recharge enthalpy i_i are the average of the initial and end state enthalpies. The last term in Eq. (3.22) represents energy extraction from the rock. The parameter η_e is a measure of the fraction of the thermal energy contained in the rock media extracted between the temperature limits. Methods to estimate η_e for highly fractured systems are discussed later.

The internal energy and specific volume of the saturated liquid at the start of production are obtained from the steam tables. The initial mass of liquid in the system is

$$M_o = v_o V\phi \tag{3.23}$$

An iterative procedure proposed by Van Wylen (1964) is used to compute the conditions at the end state as follows. A rough estimate of M_e is made and then the specific volume of the two-phase mixture at the end state is computed from

$$v_e = \frac{\phi V}{M_e} = v_{fe} + x_e v_{fge} \tag{3.24a}$$

or solving for the steam quality

$$X_e = \frac{v_e - v_{fe}}{v_{fge}} \tag{3.24b}$$

The internal energy at the end state is then estimated using steam table data from the relation

$$e_e = e_{fe} + X_e e_{fge} \tag{3.25}$$

This value of e_e is used in Eq. (3.22) with the other specified data to estimate a new value of M_e and the process is continued until convergence is obtained.

Equation (3. 22) can be written in terms of the parameters defined by:

$$\begin{aligned} &\text{Fraction Produced} && FP \triangleq M_p/M_o \\ &\text{Fraction Recharged} && FR \triangleq M_i/M_o \\ &\text{Specific External Heat Transfer Parameter} && q_m \triangleq Q_m/M_o \end{aligned} \qquad (3.26)$$

These parameters with Eqs. (3.21.) and (3.22) result in the following expression for the predicted fraction produced

$$FP_t = \left[(e_o - e_e) - (i_i - e_e)FR - q_m - \rho_r V(1-\phi)\bar{C}_r(T_o - T_e)\eta_e/M_o\right] \Big/ (i_p - e_e) \qquad (3.27)$$

The above equation is used to evaluate the :fraction produced based on the theory (hence the subscript "t") using actual experimental data for the parameters on the right hand side, By comparing FP_t to the experimental fraction produced FP (without subscript), checks on the consistency of the experimental procedure and the analysis are obtained.

3. 3 Liquid Level Analysis

It is assumed that the upper section of the chimney is filled with vapor (steam cap) and that the lower section contains liquid with entrained vapor bubbles as indicated in Fig. 3. 8. It would appear that the degree of vapor bubble entrainment depends on the boiling rate. For low rates, evaporation will occur mostly from the liquid-vapor interface with few entrained vapor bubbles while higher boiling rates will result in more entrained vapor bubbles. Therefore, at high boiling rates the liquid tends to expand and the liquid-vapor interface tends to become less distinct.

The described behavior is postulated based on the observed behavior of water boiling in a kettle. However, the analogy between the chimney and the kettle is not complete as boiling in a kettle takes place at constant pressure while in the chimney the pressure is declining. Furthermore, the rocks act as uniformly distributed heat sources and the rock surfaces with the many crevices and faults provide a large number of nucleation sites for vapor bubbles. These factors should enhance bubble formation in the chimney liquid as compared to in the kettle. It is believed, therefore,, that evaporation from the interior of the liquid is dominant for the conditions of these experiments.

3. 3. 1 Liquid Level Correction

The indicated liquid level z', measured from the top flange as shown in Fig. 3. 8, is different from the nominal liquid level z in the chimney because the liquid in the partially insulated sight glass is cooler than the liquid inside the chimney. A method is given for correcting the indicated liquid level to obtain the nominal level. It is assumed that the specific volume of the chimney liquid above point "1" in Fig. 3. 8 is that of saturated liquid; thus, vapor bubble entrainment is neglected. The effect of this assumption is that the estimated nominal liquid level is slightly lower than the actual by the amount of liquid expansion due to entrained vapor bubbles. The assumption, therefore, is best for relatively low liquid levels.

Neglecting flow pressure drop in the rock matrix, the static head of the liquids in the sight glass and in the chimney are equal at point "1". An expression for the estimated nominal liquid level in terms of the indicated liquid level and other parameters given in Fig. 3. 8 is derived in Appendix C. This expression is

$$Z = \left(1 - \frac{v_f}{v_{SG}}\right)\frac{H}{h} + \frac{v_f}{v_{SG}} Z' \qquad (3.28)$$

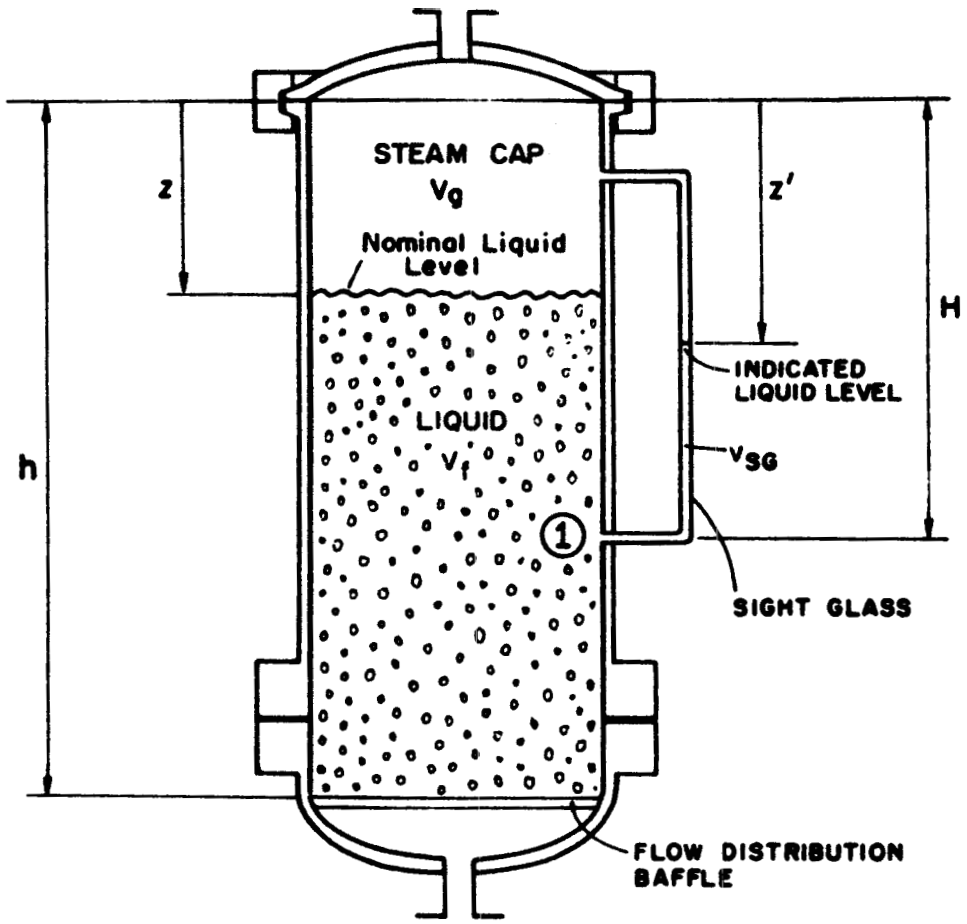

Figure 3.8 Model for Chimney Liquid Level Analysis

The specific volume of the sight glass liquid v_{SG} was evaluated from the steam tables using measured sight glass temperature data.

3. 3. 2 Void/Steam Quality Relationship

During fluid production testing the 1x0-phase mixture contained inside the chimney will pass through a series of states on a P-i diagram.* To determine the production path **two** independent state variables are required. One state variable readily available is the chimney steam pressure. **A** second state variable is the chimney bulk steam quality which can be determined from liquid level measurements. The chimney bulk steam quality is defined by (see the Nomenclature for explanation of symbols)

$$X \triangleq \frac{M_g}{M_g + M_f} = \frac{M_g}{M} = 1 - \frac{M_f}{M} \quad . \tag{3.29}$$

Also, the chimney bulk void fraction is defined by

$$\alpha \triangleq \frac{V_g}{V_g + V_f} = \frac{V_g}{V_T} = 1 - \frac{V_f}{V_T} \quad . \tag{3.30}$$

An expression for α in terms of the nominal liquid'level Z, derived in Appendix C, is given by

$$\alpha = (V_d + V_{sc} + V\phi Z)/V_T \quad . \tag{3.31}$$

*P-i diagram refers to the pressure-enthalpy diagram

Since the sight glass does not cover the total chimney height (see Fig. 3. 8), the nominal liquid level Z computed from Eq. (3. 28) is not available during the early part of the production transient. Consequently, the void fraction (and the steam quality) cannot be evaluated for the entire transient. However, an approximate expression for the liquid level in terms of the mass fraction M* is derived in Appendix C for the case of saturated vapor and liquid phases. This approximate liquid level, called the "effective" Liquid level, is given by

$$Z_t = \left[\left(\frac{V_d}{V\phi} + \frac{V_{sc}}{V\phi}\right)\frac{1}{v_g} + \left(1 + \frac{V_i}{V\phi}\right)\frac{1}{v_f} - \frac{M^*}{V\phi/M_o}\right]\frac{v_f}{1 - \frac{v_f}{v_g}} . \quad (3.32)$$

The subscript "t" is used to distinguish the effective liquid level Z_t from the nominal liquid level Z. It is expected that Z_t is slightly lower than Z because liquid expansion due to vapor bubble entrainment is neglected completely in Eq. (3. 32). The effective liquid level is used in Eq. (3. 31) to give the void fraction for the entire transient. The chimney bulk steam quality is then computed from the void/steam quality relationship, derived in Appendix C, given by

$$X = 1 - \frac{V_T}{v_f M_o M^*}(1 - \alpha) , \quad (3.33)$$

3.4 Data Reduction Procedures

The experimental data recorded throughout the experiment using the two multipoint recorders included all temperatures, the chimney

steam pressure, condenser flow rate (orifice pressure drop), and the chimney electric heater tape power.

Other data obtained by frequent observation were mass produced, chimney liquid level, injection head tank liquid level (used for determining mass recharged) and inlet line heater tape power. Data for the chimney steam pressure and the chimney lheater tape power voltage were also observed to serve as an independent check on the corresponding recorded quantities.

After each experiment, the data were read from the recorder charts at discrete times when observed data were available. All data were tabulated and keypunched for computer processing. Numerous constants such as the chimney volume, porosity, chimney steel mass fractions, heat transfer loss conductances, inlet/outlet line geometry data, rock sizes, rock thermal properties, instrumentation, conversion factors, and integer constants used for program control were also added as input.

The data reduction computer programming was combined with the reservoir transient analysis programniing presented in Chapter 3. The data reduction part is executed first. Several parameters such as the boundary parameters discussed in section 3. 2, normalized chimney pressure, fraction produced, fraction recharged, liquid level, and other parameters discussed in section 3. 3 are computed from the experimental data.

Other parameters included the external heat transfer parameter representing net heat transfer to the water/rock system. The expression for this parameter, obtained by integrating Eq. (3. 15) from the initial to the end state of the transient, is

$$Q_m = \int_o^e \dot{Q}_E dt \; t \; M_m \left[(C_m e_m)_o - (C_m e_m)_e \right] - \int_o^e UA\theta_m dt \qquad (3.34)$$

The specific external heat transfer parameter, q_m is defined as the net heat transfer to the water/rock system per unit mass of water in the system initially as defined by Eq. (3.26). Positive values of q_m indicates heat transfer to the water/rock system and negative values represent heat transfer from the system.

The ratio of energy addition by recharge to the thermal energy of the initial in-place fluids between the temperature limits of the process is a measure of the importance of recharge. This ratio, referred to as the recharge parameter, can take on negative values as in the case of recharge of cool water, it can be zero as in the case of no recharge, and it can be positive as in the case of hot water recharge. The recharge parameter is

$$\gamma_w \triangleq \frac{\int_o^{M_i} (i_i - e_{fe}) dM_i}{M_o(e_{fo} - e_{fe})} \qquad (3.35)$$

Note that the recharge energy is referenced to the internal energy of saturated liquid at the end state. A similar equation for the ratio of energy addition by recharge to energy available in the rock media is

$$\gamma_r \triangleq \frac{\int_o^{M_i} (i_i - e_{fe}) dM_i}{M_r \bar{C}_r (T_o - T_e)} \qquad (3.36)$$

The data from all fluid production experiments were processed using the data reduction routine. Selected parameters were plotted directly from the printouts. Upon completion of the data reduction computations, the reservoir transient analysis was executed as needed.

3.5 Measurement Accuracy

3.5.1 Instrumentation Calibration

A comparison of chimney steam pressure data measured by the pressure gage and the pressure transmitter has been given previously (Hunsbedt, Kruger and London, 1'975). The maximum discrepancy between the two independent pressure measurements was found to be about 5 psi. The measured steam temperature (saturation temperature) was compared to the saturation temperature corresponding to the pressure measured by the transmitter. The maximum difference between the two measurements was 3 ^{o}F. Checks of this type were made at periodic intervals during the testing to insure continuous calibration,

Thermocouples used for rock/steam and metal temperature measurements were calibrated relative to each other by turning the heater off and letting the circulation pump run. All thermocouple responses converged to one reading on the recorders which indicated that temperature equilibrium was achieved and that the relative errors between the thermocouples were less than about 2 ^{o}F.

The injection head tank level was observed through a sight glass on the tank. The distance between major subdivisions on the glass was 0.5 inch, but it was possible to read the tank level to within 0.25 inch. Changes in head tank water temperature between fillings resulted in an estimated density change of about 0.6 percent. The indicated chimney liquid level could be read to within 0.25 inch on a steel ruler attached to the chimney sight glass. The mass of fluids produced could be measured to within 1 lb using a bench scale.

3.5.2 Uncertainty Analysis

An evaluation of the accuracy and reliability of these results was attempted. Often experiments are repeated a sufficient number of

times or with different measurement techniques so that the reliability of the results can be statistically assessed. However, in many large-scale engineering experiments, such as the present, repetition is not practical due to the high costs involved. Experiments of this type are referred to as single-sample experiments.

The theory of uncertainty analysis for single-sample experiments has been treated by Kline and McClintock (1953) and systematic techniques for use in design have been presented by Wilson (1955). The "uncertainty" means a possible value of the error which is the difference between the true and observed values. Whereas, the error is a certain fixed (unknown) number the uncertainty may vary considerably depending on the particular circumstances of the experiment.

To estimate the uncertainty in a result which depends on several variables observed directly in the laboratory, engineering estimates must first be made for the uncertainties in each of the observed variables. Kline and McClintock choose to describe the uncertainty in each variable as follows

$$m \pm w \quad (b \text{ to } 1) \tag{3.37}$$

where m is the reading with all known corrections applied, w is the uncertainty interval, and b is the odds selected by the experimenter such that he is willing to bet b to 1 that the error is less than $\pm w$. The uncertainty interval is established by the experimenter based largely on experience and judgment. The odds chosen are generally 10 or 20 to 1.

When the n variables v_i affecting a result R are independent the uncertainty interval for the result w_R is estimated from

$$w_R = \left[\left(\frac{\partial R}{\partial v_1} w_1\right)^2 + \left(\frac{\partial R}{\partial v_1} w_2\right)^2 + \cdots + \left(\frac{\partial R}{\partial v_n} w_n\right)^2\right]^{1/2} \tag{3.38}$$

where the w_i's are the estimated uncertainty intervals (each with equal odds b to 1) for the n variables. The value of w_R found this way will be based on essentially the same odds as the uncertainty interval for the variables.

The above procedure was applied to the present experimental system. The uncertainty interval and percent uncertainty interval for variables and parameters were estimated for odds 20 to 1 and recorded as shown in Table C. **4** in Appendix C. These intervals were then used to estimate the uncertainties in the results with the formulas listed in Table C. 5 and Eq. **(3. 38).** Details of the computations are given in Appendix C. The estimated undertainty intervals for the major results of these experiments are presented in Table **3. 3.**

A few uncertainty intervals expressed in percent (relative uncertainty intervals) varied significantly from start to the end of the transient. In these cases the uncertainty analysis was carried out for both extremes as indicated in the table.

It is noted from Table **3. 3** that relatively large uncertainties are associated with some results. In particular, the fluid recharge and production rates have large uncertainties towards the end of the transient when these rates were the lowest. This effect along with a substantial uncertainty in the line heat loss term propagated into the uncertainty for the enthalpy of the recharged fluids.

Table **3. 3** shows the uncertainty intervals for Q_m and $\mathbf{q}_m$ in dimensional form because the magnitude of Q_m itself varied widely making it difficult to find an appropriate basis for the percent uncertainty interval. The uncertainty interval for q_m is approximately equal to the uncertainty interval for Q_m divided by the initial system fluids. Therefore, the uncertainty interval in $\mathbf{q}_m$ is given for each value of the porosity ϕ. The magnitude of the uncertainty interval for FP_t depend on whether there is recharge or not. The: uncertainty is caused by the

TABLE 3.3

Estimated Uncertaintv Intervals for the Chimney Model Experiments

Result	Symbol	Percent Uncertainty Interval 20 to 1
Rock Matrix Drainage Porosity	ϕ	3. 0
Solid Density of Rock	ρ_r	3. 3
Mass of Fluids Recharged	M_i	5.2
Mass Recharge Rate	$\dot{M}_i$	4.4 to 17*
Mass of Fluids Produced	M_p	5.0 to 0. 7
Mass Production Rate	$\dot{M}_p$	1.4 to 14
Initial System Steam Mass	M_o	2. 5
Fraction Recharged	FR	5. 8
Fraction Produced - Experimental	FP	5.6 to 2. 6
Fraction Produced - Predicted	FP_t - ϕ=1. 0, no recharge	10.2
	ϕ=. 35, recharge	14.2
Liquid and Vapor Mass in System	M	2.8 to 5. 7
System Mass Fraction	M*	3.8 to 6. 2
Chimney Steam Pressure	P*	1.2 to 10
Recharge Steam Enthalpy	i_i	2 to 20
Produced Steam Enthalpy	i_p	2.4 to 7.4
Rock Energy Extraction Fraction	η_e	3. 5
Observed Chimney Liquid Level	Z	5. 0
Predicted Chimney Liquid Level	Z_t	5.7
Chimney Bulk Steam Void Fraction	α	8.7
Chimney Bulk Steam Quality	X	49
Chimney Bulk Steam Enthalpy	i	2.5
External Heat Transfer Parameter	Qm	10,800 (Btu)
Specific Q_m	q_m for ϕ=1. 0	12.6 (Btu/lb_m)
	for ϕ=0.44	26.4 (Btu/lb_m)
	for ϕ=0. 35	32. 5 (Btu/lb_m)
Measured Rock/Steam AT	T_{rc}-T	3. 0 (°F)
Predicted Rock/Steam AT	T_{rc}-T	4.0 (°F)

*First figure refers to start of transient and the second refers to end of transient. If only one figure is given it is an average value and only slight deviations occurred.

uncertainties in the parameters used to compute FP_t particularly in the recharge fluid enthalpy and in $q_{m'}$

The uncertainty interval for Q_m corresponded to approximately 20 percent of the thermal energy stored in the initial in-place fluids between the temperature limits of the experiment. This comparison shows that the thermal effect (wall effect) caused by the pressure vessel is not a limitation to obtaining meaningful experimental data with the chimney model. However, attempts should be made to reduce the uncertainties in Q_m and in other parameters in future experiments.

CHAPTER 4

RESULTS

4. 1 Description of Experiments

Detailed tabulations of the test conditions and parameters for the 29 experiments are given in Table 4. 1. During the early phases of the experimental program, the heat transfer from the chimney metal to the rock/steam system (the wall effect) represented by q_m was determined from heatup and cooldown experiments (Hunsbedt, Kruger and London, 1975). To verify these results, additional experimental data were desired. Such data were provided by the three first fluid production experiments (runs 1 through 3) without rock in the chimney (100 percent porosity).

The next 22 experiments (runs 4 through 25) were with the first rock loading described in Chapter 2 (44 percent porosity). These tests were conducted to study the effects of such system parameters and conditions as, (1) initial pressure and temperature, (2) end pressure and temperature, (3) external heat transfer parameter, (4) hot or cool fluid recharge, (5) steam production rate, and (6) cyclic production/recharge operation.

The final four experiments (runs 26 through 29) were with the second rock loading (35 percent porosity). These tests were conducted to study the effect of rock porosity and the effect of the rock size at various cooldown rates.

The test conditions were varied over as great a range as was practical to provide the broadest possible basis for analytic model verification. The maximum initial steam pressure was limited by the system design pressure of 800 psig. .Most experiments were run at initial pressures of about 550 to 600 psia with a few runs above and below.

TABLE 4.1

Experimental Conditions and Parameters

Run	Drainage Porosity ϕ (percent)	Initial Temperature T_o (°F)	Initial Pressure P_o (psia)	Initial Pressure P_{so} (psia)	End Temperature T_e (°F)	End Pressure P_e (psia)
1	100	499	745	675	360	136
2	100	501	767	687	309	76
3	100	500	796	681	263	37
4	44	477	604	550	252	31
5	44	386	255	210	215	16
6	44	486	659	599	235	23
7	44	484	647	588	325	96
8	44	486	647	599	288	56
9	44	485	647	593	249	29
10	44	486	687	599	304	72
11	44	477	596	550	298	65
12	44	477	600	550	300	67
13	44	480	584	566	268	40
14	44	478	599	556	307	74
15	44	481	583	572	289	56
16	44	478	579	556	287	55
17	44	482	577	577	255	32
18	44	479	585	560	264	38
19	44	478	596	556	282	51
20	44	481	584	572	285	53
21	44	480	584	566	302	69
22	44	480	579	566	261	36
23	44	482	581	577	260	36
24	44	481	583	572	292	60
25	44	403	287	256	269	41
26	35	483	591	582	229	20
27	35	484	592	588	267	40
28	35	483	586	582	263	37
29	35	484	581	588	264	38

TABLE 4. 1 (Continued)

Run	Duration of Experiment t_e (hr)	Mean Cooldown Rate $\bar{\mu}$ (°F/hr)	Mass Produced M_p (lb_m)	Mean Steam Production Rate $\bar{\dot{M}}_p$ (lb_m/hr)	Characteristic Time t_c (hr)
1	20.10	6. 9	127.9	6.4	135. 1
2	47.30	4. 1	113.6	2.4	357.1
3	23. 70	10.0	118.3	5.0	172.4
4	17. 30	13. 0	125. 0	7. 2	56. 8
5	18. 0	9. 5	101.0	5. 6	79.4
6	18.60	13. 5	142.6	7.7	53.2
7	16. 50	9.6	159. 7	9.7	42.2
8	23. 0	8. 6	212.5	9.2	44. 1
9	17.07	13. 8	226.6	13. 3	30. 7
10	25.00	7. 3	373.2	14.9	27. 3
11	24.00	7. 5	236.4	9.9	41. 7
12	28.00	6. 3	258. 7	9.2	44.4
13	26.00	8. 2	283.0	10.9	37. 6
14	15. 50	11.0	235.3	15. 2	27. 0
15	19. 50	9. 8	267.9	13. 7	29. 8
16	18.00	10.3	257. 8	14. 3	28. 7
17	18. 50	12. 3	241.6	13. 1	31. 3
18	11.00	19. 5	236.6	21.5	19. 1
19	9. 50	20.6	248. 1	26. 1	15. 7
20	10. 50	18. 7	277. 7	26. 5	15. 5
21	10.00	17. 8	297.8	29. 8	13. 7
22	11.00	19. 9	236.0	21. 5	19. 1
23	8. 00	27. 8	201.7	25. 2	16. 2
24	12.00	15. 8	301.2	25. 1	16. 3
25	6. 00	22. 3	139.0	23. 2	18. 9
26	8. 50	29. 9	201.3	23. 7	14. 0
27	13.00	16. 7	178.0	13. 7	24. 2
28	3. 50	62. 7	196. 0	56.0	5. 9
29	8. 50	25. 9	277.8	32.7	10. 1

TABLE 4.1 (Continued)

Run	Mass Recharged M_i (lb_m)	Mean Recharge Rate $\bar{\dot{M}}_i$ (lb_m/hr)	Initial Mass M_o (lb_m)	Fraction Produced FP (dim. less)	Fraction Recharged FR (dim. less)	Ratio FR/FP [dim.less]
1	0.0	0.0	858.8	0.15	0.0	0.0
2	0.0	0.0	857.0	0.13	0.0	0.0
3	0.0	0.0	858.3	0.14	0.0	0.0
4	0.0	0.0	410.7	0.30	0.0	0.0
5	0.0	0.0	444.0	0.23	0.0	0.0
6	0.0	0.0	407.0	0.35	0.0	0.0
7	0.0	0.0	407.8	0.39	0.0	0.0
8	0.0	0.0	406.9	0.52	0.0	0.0
9	118.5	6.9	407.4	0.56	0.29	0.55
10	446.7	17.9	407.1	0.92	1.10	1.21
11	106.7	4.5	410.7	0.58	0.26	0.45
12	123.4	4.4	410.7	0.63	0.30	0.48
13	94.3	3.6	409.3	0.69	0.23	0.33
14	222.8	14.4	410.3	0.57	0.54	0.95
15	177.0	9.1	408.9	0.66	0.43	0.65
16	250.3	13.9	410.2	0.63	0.61	0.97
17	240.1	21.8	408.4	0.59	0.59	1.0
18	0.0	0.0	409.8	0.58	0.0	0
19	236.9	24.9	410.2	0.60	0.58	0.97
20	263.8	25.1	408.9	0.68	0.64	0.94
21	281.0	28.1	409.3	0.73	0.69	0.95
22	0.0	0.0	409.3	0.58	0.0	0.0
23	0.0	0.0	408.4	0.49	0.0	0.0
24	200.9	16.7	408.9	0.74	0.49	0.66
25	0.0	0.0	438.3	0.32	0.0	0.0
26	0.0	0.0	332.0	0.61	0.0	0.0
27	0.0	0.0	331.7	0.54	0.0	0.0
28	0.0	0.0	332.0	0.59	0.0	0.0
29	331.7	39.0	331.6	0.84	1.00	1.19

TABLE 4. 1 (Continued)

Run	Recharge Parameter y_w (dim. less)	Recharge Pararneter y_r (dim. less)	Heat Transfer Parameter q_m (Btu/lb_m)	Mean Slope in Superheated Zone S_e (^oF)
1	0.0	0.0	--	--
2	0.0	0.0	--	--
3	0.0	0.0	-126.7	--
4	0.0	0.0	-102.0	130
5	0.0	0.0	-100.3	118
6	0.0	0.0	-104.7	159
7	0.0	0.0	36.7	27
8	0.0	0.0	65.7	102
9	-0.16	-0.20	68.9	65
10	-1.32	-1.45	203.2	--
11	-0.44	-0.59	125.3	0
12	-0.12	-0.15	101.2	0
13	-0.04	-0.05	110.5	119
14	-0.09	-0.12	115.9	0
15	0.14	0.19	143.5	0
16	0.06	0.08	140.4	0
17	-0.39	-0.52	202.9	38
18	0.0	0.0	151.1	145
19	-0.25	-0.31	198.5	36
20	0.20	0.27	181.0	57
21	0.69	0.87	157.5	33
22	0.0	0.0	153.9	143
23	0.0	0.0	48.4	159
24	0.45	0.60	200.5	96
25	0.0	0.0	22.8	92
26	0.0	0.0	84.2	224
27	0.0	0.0	75.3	188
28	0.0	0.0	143.9	190
29	0.57	0.56	110.3	0

With argon gas pressurization during heatup, the fluid was slightly subcooled (compressed) when steam production was initiated as shown previously (Hunsbedt, Kruger, and London, 1975).

The experiments were discontinued at pressures ranging from 16 to 136 psia. The steam production rates, determined largely by the flow control valve setting, were varied to give a wide range of rock cooldown rates and pressure depletion tirnes as indicated in Table **4.** 1. The maximum steam production rate was determined by the condenser capacity.

During the early runs with the first rock loading, attempt was made to maintain approxirnately constant steam production rate by adjusting the flow control valve. However, due to operation difficulties, subsequent runs were made with constant valve setting, resulting in decreasing steam production rate with chimney pressure decline.

The fluid recharge rate was maintained about the same as the steam production rate. Initial difficulties with the injection pump controls resulted in runs with recharge during only part of the transient. The recharge for a few **runs** exceeded the steam production substantially resulting in subcooled reservoir conditions and production of liquid during part of the transient.

Experiments 1 through 6 were made without energy addition by the chimney tape heaters, Also, the steam production transients were long resulting in substantial cumulative heat losses and negative values of q_m (heat transfer away from the rock/water system). Most of the subsequent experiments were with energy addition and shorter steam production transients resulting in positive q_m.

The proper amount of energy addition by the tape heaters to give a desired value of q_m could not be estimated accurately in advance since computer processing of the temperature transient data was required. Therefore, its value was not available immediately following

the test. Initially the energy addition was overestimated resulting in runs with q_m's larger than desired. However, the energy addition by the tape heaters was estimated more precisely for subsequent runs based on the experience gained.

To check the reproducibility of the experiments, run 22 was made for conditions as close as practical to those of run 18. Almost identical initial and end conditions, fluids produced, and other parameters were achieved for the two runs (see Table 4. 1). Examination of the measured internal temperature distributions also showed that characteristic features were reproduced closely,.

4. 2 Results and Predictions

4. 2. 1 Temperature Distributions

The measured chimney temperature distributions for representative experiments are given to illustrate several characteristics of the results which are discussed in detail in later sections. The temperature distributions for runs 23, 26 and 28 are given in Figs. 4. 1 through 4. 3. The rock/steam temperatures at various times are shown as functions of the non-dimensional distance from tap of the rock matrix. * The steam production rates of these experiments gave mean cooldown rates $\bar{\mu}$ as indicated in the figures. The runs had no recharge (FR = 0).

It is observed that the rock/steam temperature distributions are uniform initially (t = 0) and that the temperatures are slightly lower than the saturation temperature for the: chimney pressure (slightly subcooled conditions). Saturated steam conditions are established in the chimney by pressure reduction as a result of initiating steam production. When this occurs, the steam pressure and the steam temperature decline resulting in rock/steam temperature differences and initiation of heat transfer from the rock to the two-phase steam mixture.

* Refer to Figs. 2. 8, 2. 9, and 2. 10 for thermocouple locations.

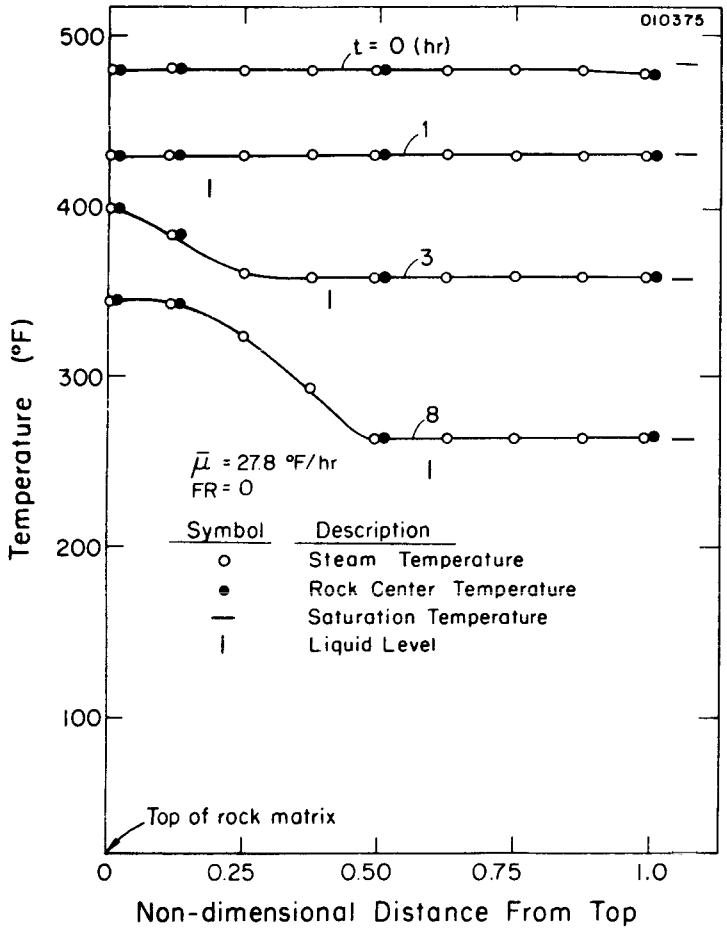

Figure 4.1 Chimney Rock/Steam Temperature Distribution for Run 23

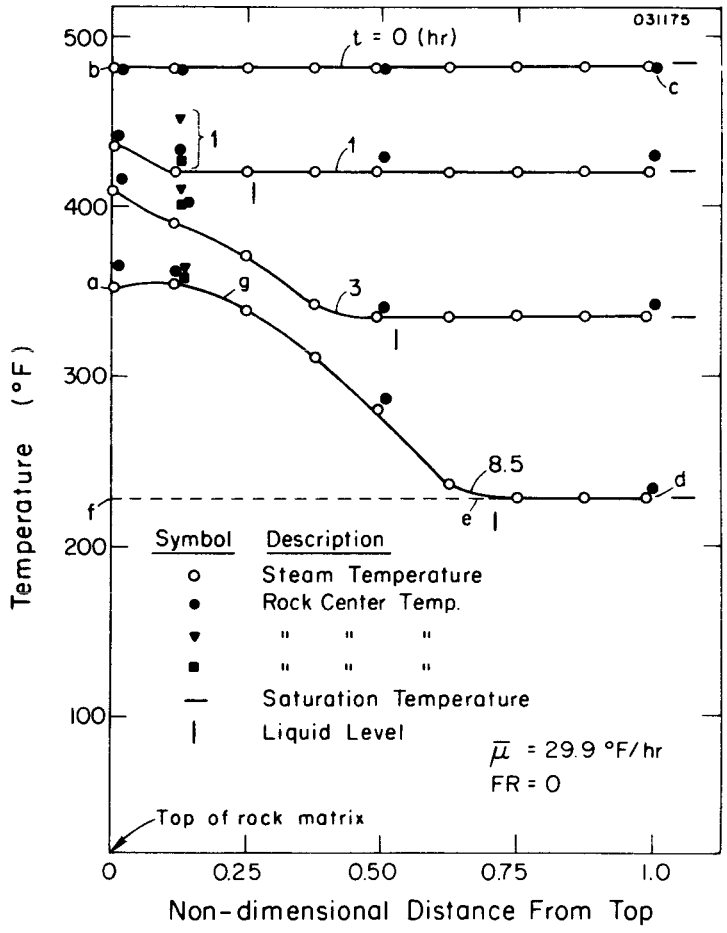

Figure 4.2 Chimney Rock/Steam Temperature Distribution for Run 26

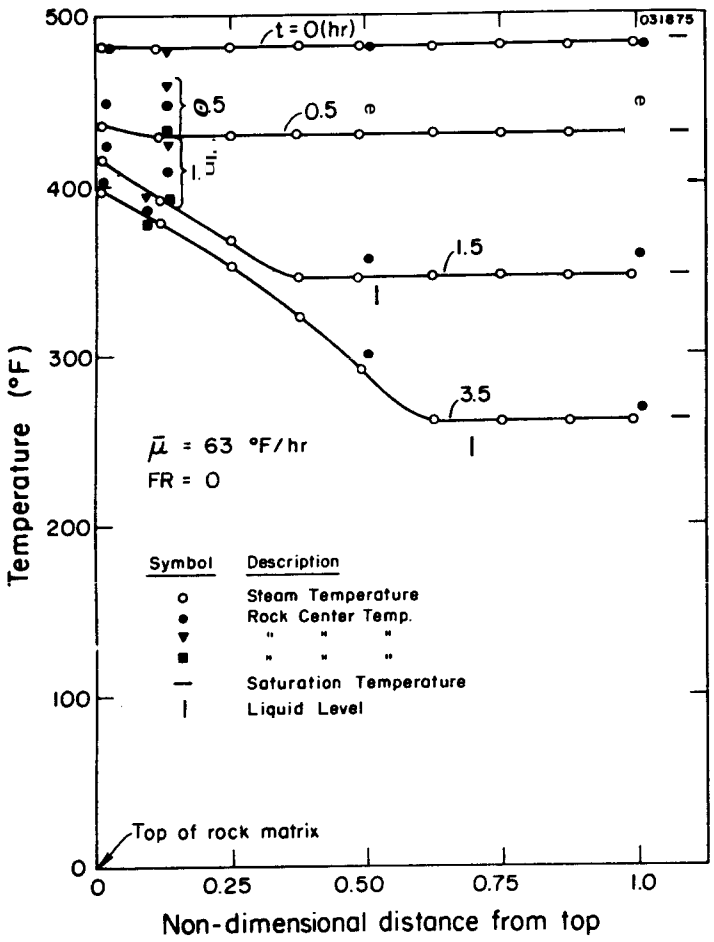

Figure 4.3 Chimney Rock/Steam Temperature Distribution for Run 28

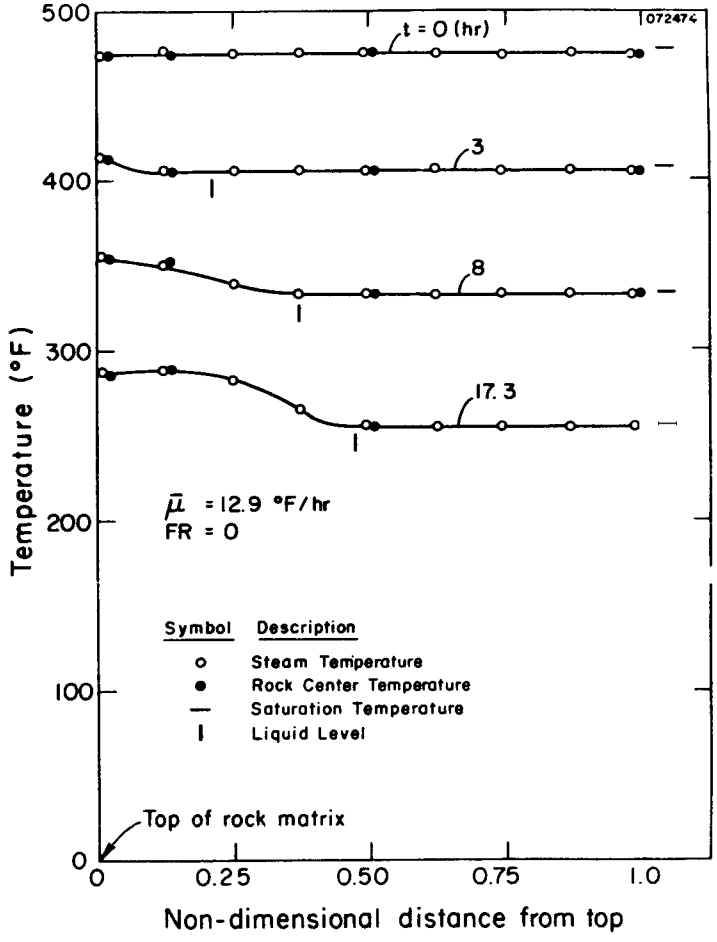

Figure 4.4 Chimney Rock/Steam Temperature Distribution for Run 4

It is seen that for the small rocks of run 23 (Fig. **4.** *1)* the rocks are essentially in thermal equilibrium with the surrounding steam. This is not the case for runs 26 and 28 (Figs. 4.2 and **4.** *3)* with the large rocks. Preliminary evaluation of these results shows that the rock/steam temperature differences are proportional to the local cool-down rates and the square of the rock dimensions as the rock thermal analysis in Chapter *3* indicated. Further evaluation of the rock/steam temperature differences is given in a later section.

It is also observed in Figs. **4.** 1 through **4. 3** that later in the transient the liquid level drops within the rock matrix and a superheated vapor zone develops above the liquid level. Note that the temperature in the liquid region below the vapor-liquid interface is uniform and that it appears to be equal to the saturation temperature indicating that boiling may occur throughout the liquid region.

The degree of superheat appears to increase approximately linearly with distance above the vapor-liquid interface for much of the transient period. Towards the end of the transient, however, the slope changes near the top (exit) for runs 23 and 26. This "desuperheat" effect is believed to be caused by reflux of condensed steam originating mostly in the outlet line. Note that the effect is not apparent with run 28 which had about twice as high mean steam production rate as runs 23 and 26. Results for run **4** with steam production rate of **7.** 2 lb_m/hr (vs 56 lb_m/hr for run 28) given in Fig. **4.4** show that the desuperheat effect is more severe for low steam production rates.

The desuperheat effect can be explained by noting that condensation and reflux of condensed steam depend mainly on heat losses in the outlet line region which is approximately constant from run to run. The reflux ratio, defined as the reflux rate divided by the steam production rate, therefore decreases with increasing steam production rate. For example, the reflux ratio for run 28 (highest mean steam production rate) was estimated to be 0. 027 while for run **4** (lowest mean steam

production rate) it was 0. 21. An energy balance on the rock and vapor in the upper section of the chimney shows that the desuperheat effect will be more severe when the reflux ratio is high.

A desuperheat effect was noted by Cady (1969) in his experiments with unconsolidated sand cores. There are, however, some apparent differences between characteristics of his results and the present. Cady found that the temperature profile in the superheated zone did not change substantially with time once superheated conditions were reached. This is in contrast to the present experiments which showed large changes in the rock/vapor temperature in the superheated zone for all cases, particularly for runs with large reflux ratios. It would appear, therefore, that the assumption of constant superheated zone temperature profile with time made by Brigham and Morrow (1974) may not be applicable to the present system.

The temperature distribution for run 25 which was for almost the same conditions as for run 23, but with lower initial temperature and pressure, is shown in Fig. 4. 5. It is seen that the superheated zone is relatively small because the liquid level was higher. In fact, if the liquid level is maintained high enough, a superheated zone cannot develop. This is illustrated in Fig. 4.6 which gives the temperature distribution for run 29 with recharge of hot water (FR = 1.0 and y_w = 0. 57). For this run the recharge was greater than production (FR/FP = 1.19) resulting in an approximately stationary liquid level located at the very top of the rock matrix.

The temperature distribution for run 17 with recharge of cool water:: (FR = 0. 59 and y_w = -0. 39) is shown in Fig, 4.7. The recharge

---

Cool water recharge means that no external preheating was used except for an initial heating effect from the small transfer of thermal energy stored in the inlet piping from the initial heatup process. The inlet water temperature dropped off very rapidly to near room temperature.

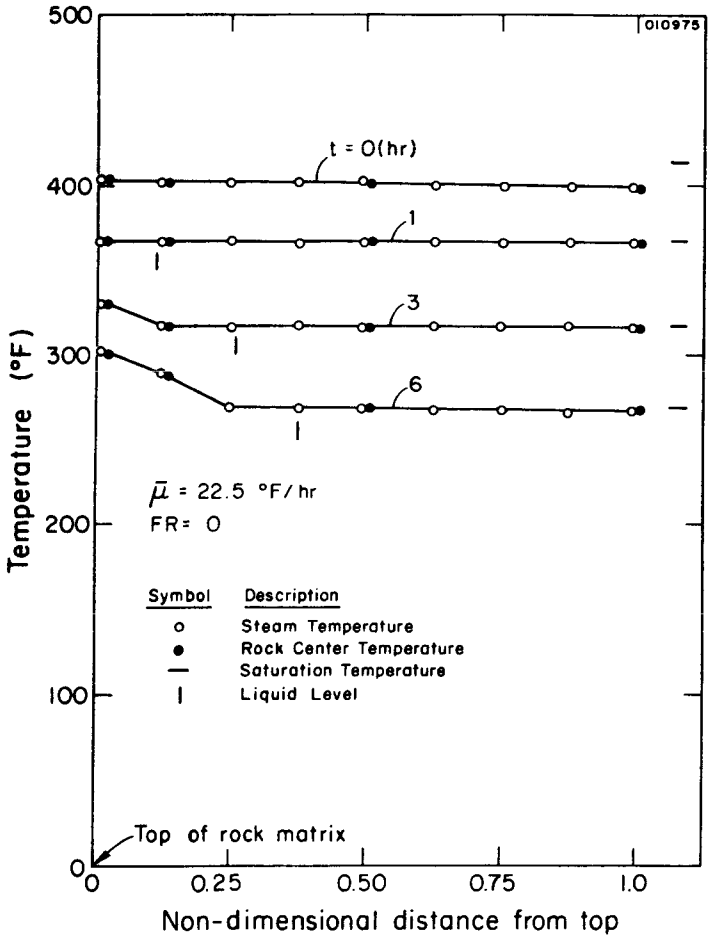

Figure 4.5 Chimney Rock/Steam Temperature Distribution for Run 25

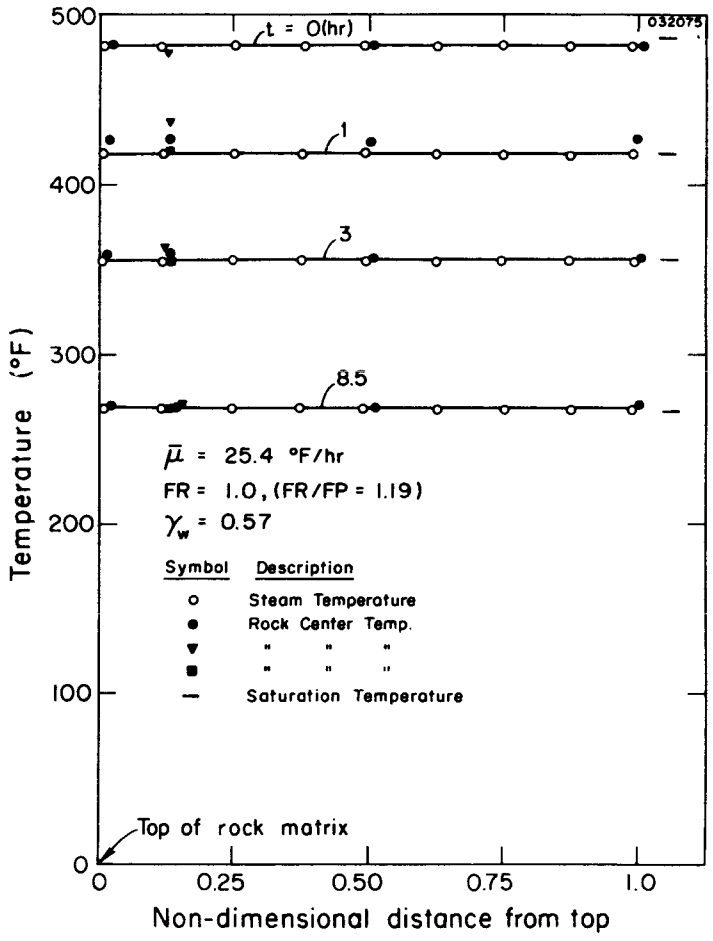

Figure 4.6 Chimney Rock/Steam Temperature Distribution for Run 29

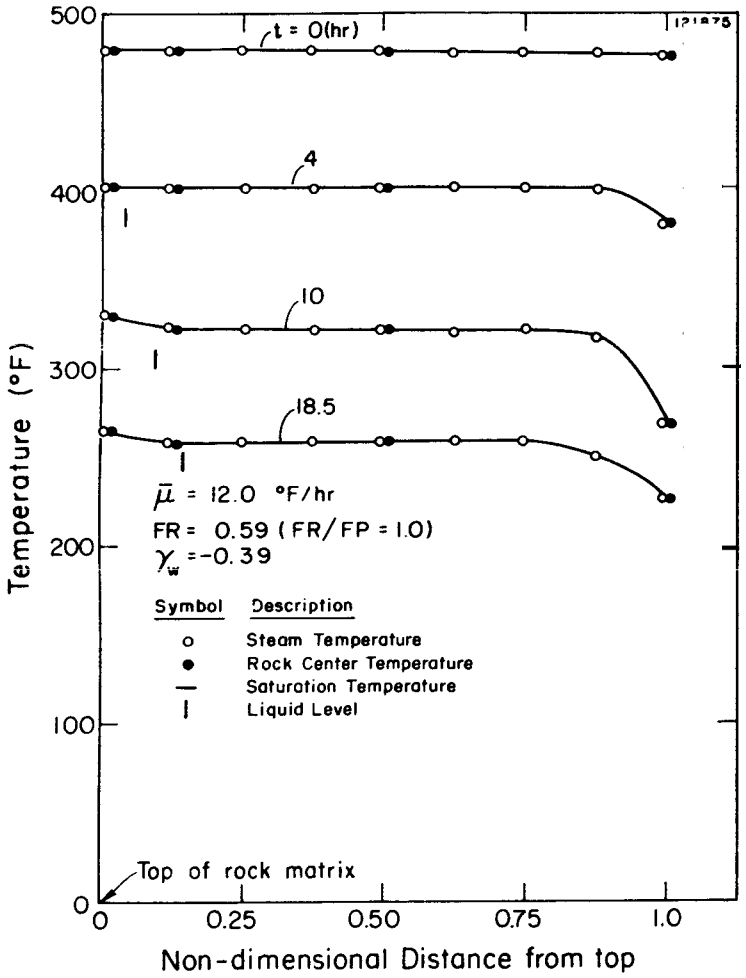

Figure 4.7 Chimney Rock/Steam Temperature Distribution for Run 17

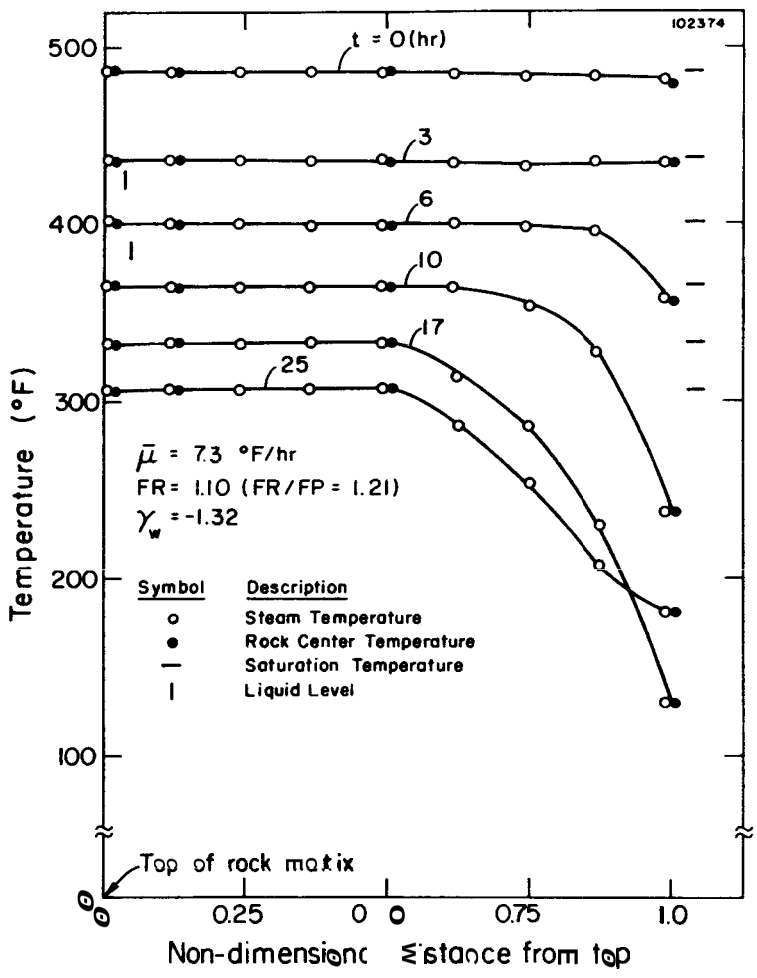

Figure 4.8 Chimney Rock/Steam Temperature Distribution for Run 10

was such that the liquid level dropped within the rock matrix (FR/FP = 0.99) and a slight superheated zone developed. Furthermore, a subcooled zone developed at the bottom as a result of cool fluid recharge. This indicates a density stratification effect and that the cool fluid does not mix with the hotter liquid in the upper section of the chimney. Since the system pressure is determined by the liquid temperature in the upper section, it is expected that the subcooled zone will have little influence on the reservoir pressure behavior except for the effect of the additional rock energy extraction from the top and bottom parts of the rock matrix.

The density stratification phenomenon is demonstrated more clearly in Fig, 4. 8 for run 10 in which the recharge of cool water (FR = 1. 10 and y_w = -1. 32) was greater than the steam production (FR/FP = 1. 20). Note that the temperature profiles at times t = 17 and 25 hr overlap each other, The reason for this behavior is energy supply to the subcooled liquid zone by heat transfer from the chimney metal and by axial heat transfer and diffusion in the liquid when recharge was discontinued at about t = 21 hr.

4. 2. 2 Rock Energy Extraction Fraction

The thermal energy extracted from the rock at the end of the transient is, except for a small rock/steam temperature difference correction, proportional to the area indicated by a-b-c-d-e-g-a in Fig. 4.2. The maximum thermal energy extraction for this run is proportional to area a-b-c-d-e-f-a. The ratio of extracted rock energy to the maximum rock energy extraction possible between the temperature limits defines the rock energy extraction fraction η as

$$\eta \triangleq \frac{Q_r}{Q_{r,max}} = \frac{Q_r}{M_r \bar{C}_r (T_o - \bar{T})} \qquad (4.1)$$

where the upper temperature limit T_o is the initial rock/steam temperature and where the lower temperature limit T is the saturation temperature corresponding to the steam pressure at time t. The rock energy extraction fraction is normally less than unity, but it can be greater than unity for runs with cool water recharge.

The temperature distributions in Figs. 4.1 through 4.8 show that the rock energy extraction fraction η varies from run to run depending on several parameters including time. In particular, the rock energy extraction fraction at the end of the transient η_e depends on the liquid level because it largely determines the magnitude of the superheated zone (proportional to area a-g-e-:€-ain Fig. 4.2). For example, from the data in Fig. 4.6 (liquid level near the top) it is noted that η_e is close to unity. In comparison, from the data in Fig. 4.3 (liquid level 70 percent down) it appears that η_e is about 0.7 to 0.8.

It was shown earlier that the magnitude of the superheated zone was reduced with increasing reflux ratio. Consequently, the rock energy extraction fraction η_e is also affected by the reflux ratio. This effect is difficult to describe quantitatively, but it can be assessed qualitatively by comparing the magnitude of the superheated zones. For example, the superheated zone for run 28 in Fig. 4.3 with reflux ratio 0.027 is larger than for run 4 in Fig. 4.4 with reflux ratio 0.21. The energy extraction fraction is therefore greater for run 4 than for run 28.

It is observed that the rock/steam temperature difference existing at the end of the transient (indicated clearly in Fig. 4.3) results in a decrease in extracted rock energy and in η_e. This effect was not significant with the small rocks of the first rock loading because the rocks were essentially in thermal equilibrium with the steam as indicated in Fig. 4.1. A 4 percent effect was noted with the larger rocks of the second rock loading, but the rock/steam temperature differences may be significant with larger rocks which are cooled rapidly.

A measure of the effect of the rock/steam temperature difference on η_e is obtained by forming the ratio of mean rock/steam temperature difference at the end of the transient to total liquid temperature drop for the experiment. This ratio is given by

$$\beta_e \triangleq \frac{\bar{T}_r - T_e}{T_o - T_e} = \frac{\mu_e}{\bar{\mu}} \frac{\tau}{t_e} \qquad (4.2a)$$

where $\mu_e/\bar{\mu}$ is the ratio of local cooldown rate at the end of the transient to the mean cooldown rate for the complete transient, τ is the time constant for the mean size rock and where t_e is the transient time. The relationship between β_e and η_e in the absence of any of the other factors affecting η_e is obtained by combining Eqs. (4. 1) and (4. 2a) to give

$$\eta_e = \frac{Q_r}{M_r \bar{C}_r (T_o - T_e)} = \frac{T_o - \bar{T}_r}{T_o - T_e} = 1 - \beta_e \qquad (4.2b)$$

From Eq. (4. 2a) it is noted that β_e, and consequently η_e by Eq. (4. 2b), depends on the product of the $\mu_e/\bar{\mu}$ and τ/t_e ratios. If the magnitude of either ratio is small, the effect on η_e is also small. The maximum τ/t_e ratio for these experiments was about 0. 1. The $\mu_e/\bar{\mu}$ ratios for these experiments were about 0. 3 to 0. 5. The maximum β_e was estimated for run 28 to be 0. 04 indicating 4 percent reduction in the rock energy extraction fraction. This effect is small in comparison to the superheated zone effect.

Estimated rock energy extraction fractions η_e for runs 4 through 29 are given in Table 4. 2. The previous discussion showed that η_e depends on several parameters of which the liquid level appeared the most important. The levels at the end of the transient Z_e are therefore included in the table.

TABLE 4.2

Rock Energy Extraction Fractions

Run	End Liquid Level Z_e (dim. less)	Rock Energy Extraction Fraction η_e (dim. less)
4	0.41	0.95
5	0.29	0.97
6	0.47	0.93
7	0.48	0.98
8	0.62	0.90
9	0.38	0.98
10	0.0	1.18
11	0.41	1.0
12	0.42	1.0
13	0.56	0.91
14	0.12	1.0
15	0.32	1.0
16	0.12	1.0
17	0.13	0.99
18	0.68	0.80
19	0.13	0.99
20	0.14	0.99
21	0.14	0.99
22	0.68	0.81
23	0.60	0.87
24	0.35	0.97
25	0.38	0.95
26	0.72	0.77
27	0.65	0.78
28	0.70	0.75
29	0.0	0.99

The largest η_e obtained was 1.18 for run 10 which had a sub-cooled zone at the bottom as indicated in Fig. 4.8. The lowest η_e was 0.75 for run 28 which had the largest β_e parameter (β_e = 0.04) and the lowest reflux ratio.

To illustrate further the liquid level dependence, the η_e data are given as a function of Z_e in Fig. 4.9. The scatter in the data indicates that η_e depends on other parameters as well, in particular, reflux of condensed steam is believed to be a major cause of the scatter. It is noted from Fig. 4.9 that η_e changes rather slowly for Z_e values less than about 0.4 and then drops off more rapidly. This behavior indicates that η_e may vary approximately as the square of the liquid level,

An expression for η in terms of the liquid level squared is derived on the basis of the chimney temperature distribution shown in Fig. 4. 10. A space averaged value of the axial steam temperature gradients in the superheated region is defined as

$$S = \left| \frac{dT}{dZ} \right| \qquad (4.3)$$

where Z is the nondimensional distance from the top. Application of Eq. (4.1) leads to an expression for η which is

$$\eta = 1 - \frac{S Z^2}{2(T_o - T)} \qquad (4.4)$$

The values for S_e given in Table 4,1 were evaluated from Eq. (4.4) using experimental η_e, Z_e, T_o, and Te data. The Se data and Eq.. (4.4) are used to modify the model transient analysis to account for the incomplete energy extraction in the superheated zone,

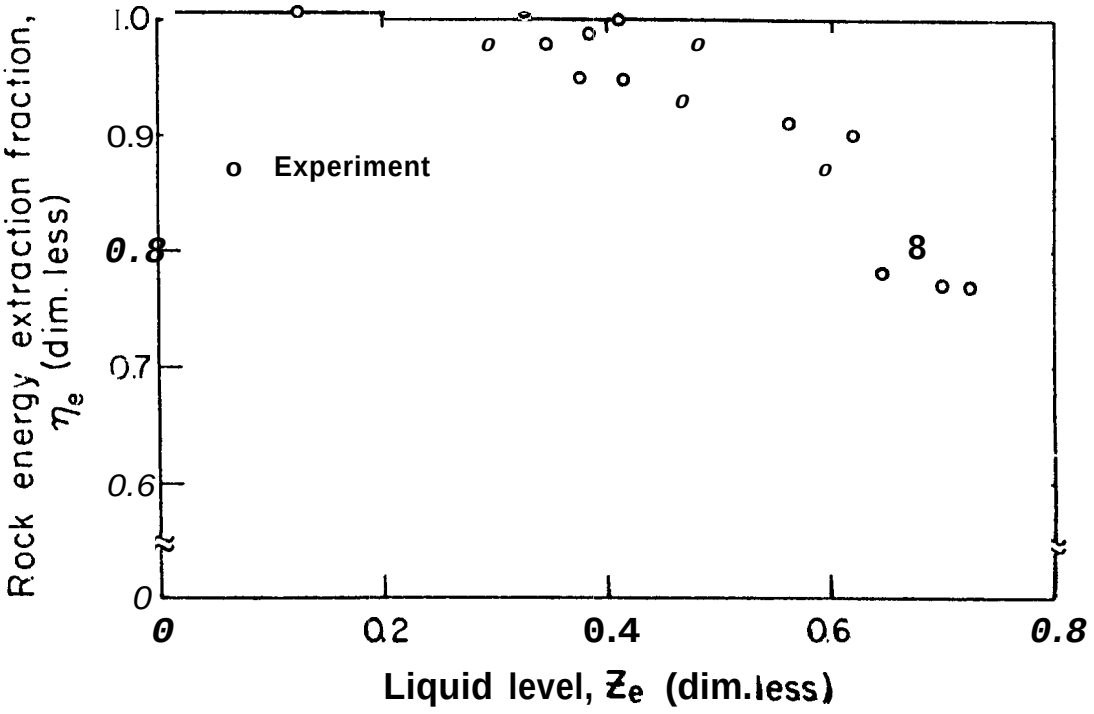

Figure 4. 9 Experimental Rock Energy Extraction Fractions

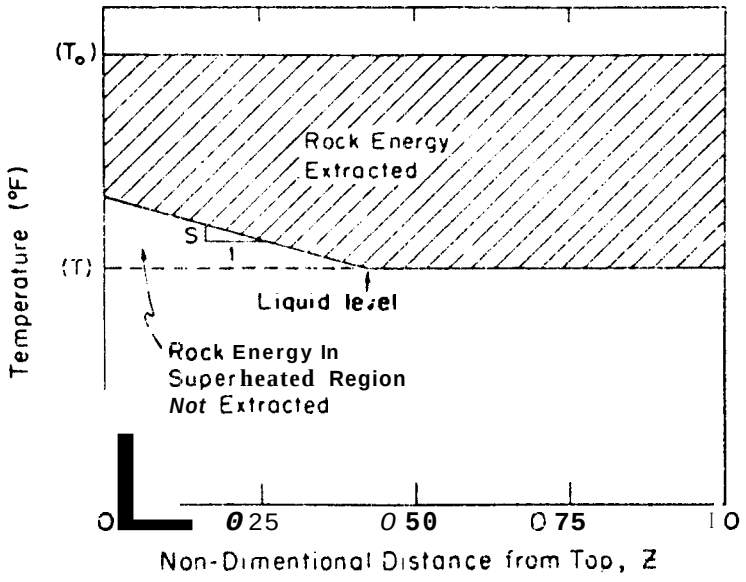

Figure 4. 10 Idealized Model for Rock Energy Extraction Fraction Concept

4.2.3 Rock/Steam Temperature Differences

Measured chimney temperature transients for run 26 are shown in Fig. 4.11 to illustrate how the rocks cool in vapor and liquid environments. The lower set of curves represent the center temperature of the instrumented rock located at the bottom of the chimney (rock 1 in Fig. 2.9) and the temperature of the surrounding saturated liquid. The upper set of curves show the center temperatures of the three instrumented rocks located in the plane next to the top of the chimney (rocks 3, 4, and 5 in Fig. 2.9) and the temperature of the surrounding superheated vapor.*

The liquid temperature is the saturattion temperature corresponding to the steam pressure which is declining as a result of steam production. The steam production rate of run 26 decreased with time resulting in a liquid cooldown characteristic as shown in Fig. 4.11 (lowest curve). Observe that the liquid cooldown rate (slope of the liquid cooldown curve) is also declining with time resulting in a $\mu_e/\bar{\mu}$ ratio of about 0.4 for this run. All rocks below the liquid-vapor interface tend to cool at approximately the same rate as the liquid as indicated for rock 1 in Fig. 4.11.

The temperature of the superheated vapor above the liquid-vapor interface depends primarily on the energy supply from the rock and is essentially independent of the pressure. The temperature of the vapor surrounding instrumented rocks 3, 4, and 5 after about 2 hr follows a path that is different from that of the liquid as indicated in Fig. 4.11. The rocks surrounded by vapor appear to cool at a nearly constant, considerably lower rate than rocks in liquid.

---

*The vapor temperature measurements in the superheated zone indicated about 10 °F radial variation. The lowest of these (measured by T/C 215) is given in Fig. 4.11,

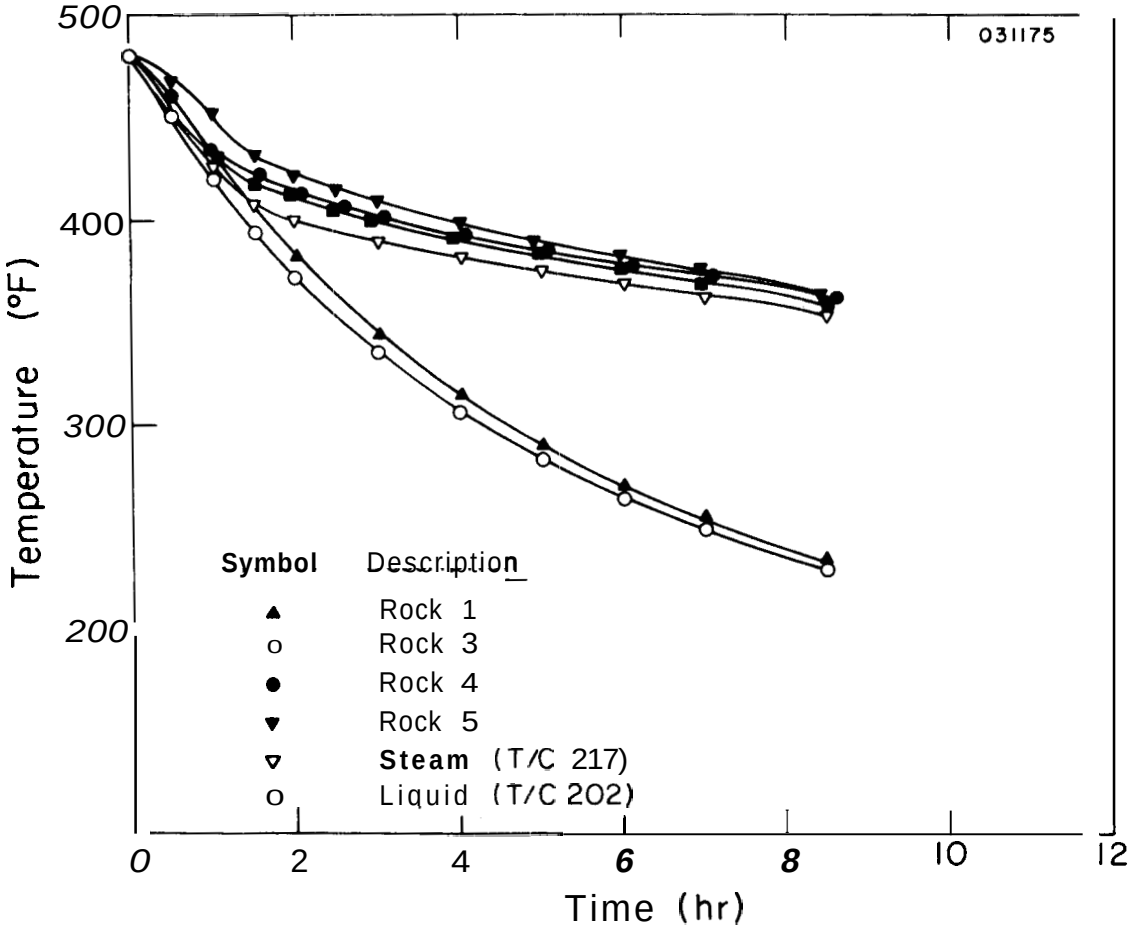

Figure 4. 11 Experimental Rock/Steam Temperature Transients for Run 26

The cooldown characteristics shown in Fig. 4. 11 were representative of experiments with no recharge. When the liquid level was maintained at the top by fluid recharge, as was the case for run 29, the superheated zone could not develop. Consequently, all rocks were in a liquid environment and cooled approximately as rock 1 in Fig. 4. 11.

The validity of treating a rock as a sphere or a plate is assessed by comparing the predicted rock/steam temperature differences to measurements. The experimental rock center/steam temperature difference data for instrumented rocks 1 and 5 obtained for runs 26, 28 and 29 are compared to predictions in Table **4.** 3. The rock center/steam temperature differences were predicted using Eq. **(3.** 2b) for the sphere idealization and Eq. (3.2d) for the plate idealization. The comparisons shown in Table **4.3** were made at times in the transients such that time dependent terms in the above equations were negligible (quasi-steady state conditions). The local cooldown rates derived from the liquid and vapor cooldown curves were used in the predictions.

Rock **1** was always submerged in liquid for which a surface heat transfer coefficient of h ▫ 50 Btu/hr ft^2 ^oF was assumed. Rock 5 was submerged in liquid initially and then in superheated vapor for runs 26 and 28. **A** vapor heat transfer coefficient of h = 3 Btu/hr ft^2 ^oF was assumed for the prediction. Rock 5 was submerged entirely in liquid during run 29. The environment and the Riot numbers corresponding to the assumed heat transfer coefficients and the rock geometry are listed in Table **4. 3.**

The results in Table **4,** 3 found to be representative of the experimental results show the following trends:

(1) In liquid the predicted rock center/steam temperature differences based on the sphere and plate approximations are nearly equal.

(2) In vapor the plate approximation results in substantially higher predicted temperature differences than do the sphere approximation.

TABLE 4.3

Comparison of Measured and Predicted Rock Center/Steam Temperature Differences

Run	Time (hr)	Description	Environment	Rock Center/ Steam Temp. Difference for Rock 1 (°F)	Environment	Rock Center/ Steam Temp. Difference for Rock 5 (°F)
28	3	Measurement	Liquid	7	Vapor	17
		Predicted (Sphere approximation)	(B=9.6)	12.9	(B=0.82)	20.1
		Predicted (Plate approximation)	(B=5.2)	12.8	(B=0.45)	28.4
28	3.5	Measurement	Liquid	7	Vapor	14
		Predicted (Sphere approximation)	(B=9.6)	12.4	(B=0.82)	11.4
		Predicted (Plate approximation)	(B=5.2)	12.1	(B=0.45)	10.2
29	4	Measurement	Liquid	5	Liquid	8
		Predicted (Sphere approximation)	(B=9.6)	8	(B=13.6)	15
		Predicted (Plate approximation)	(B=5.2)	7.9	(B=7.4)	14.8

(3) In liquid the predicted rock center/steam temperature differences are substantially higher than the measured.

(4) In vapor the predicted rock center/steam temperature differences based on the sphere approximation are close to the measurements.

(5) In vapor the plate approximation results in rock/steam temperature differences which are always higher than the measured.

Evaluation of the surface heat transfer coefficients in the following is based on the sphere idealization.

4.2.4 Heat Transfer Coefficients

The predicted rock center temperature difference is insensitive to the heat transfer coefficient in liquid environments (Biot number high) while the prediction is sensitive to the heat transfer coefficient in superheated vapor environments (Biot number low). This suggests that evaluation of the heat transfer coefficient frorn Eq. (3.4) using the liquid environment experimental data would lead to poor accuracy in the heat transfer coefficient, but better results would be expected from the superheated vapor data,

The variation with time of the averatge heat transfer coefficient for rocks 3, 4, and 5 in superheated vapor environments for runs 26 and 28 are given in Figs. 4.12 and 4.13. The heat transfer coefficients were evaluated from Eq. (3.4) for each rock using experimental rock center/steam temperature difference and cooldown rate data. The rock thermal property data in Appendix D and the rock geometry data in Table B.3 were also used for the evaluation. The average vapor temperature (average of temperatures measured by T/C 212, 216, and 217 in Fig. 2.10) was used to compute the rock center/steam temperature difference. The heat transfer coefficients computed from the correlation by Meek (1961) as given by Eq. (3.13) are included in the figures for comparison. In evaluating these heat transfer coefficients, the Reynolds number based on the mean rock equivalent diameter for the three rocks was

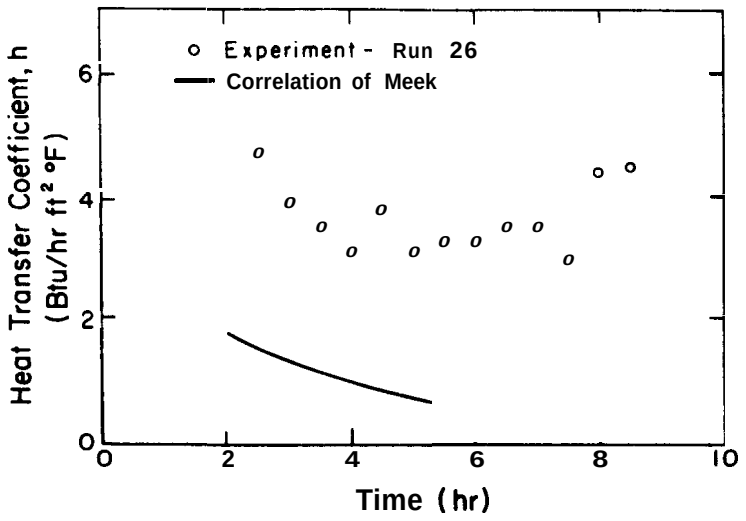

Figure 4. 12 Variation of Mean Heat Transfer Coefficient in Superheated Vapor Environment for Run 26 (Reflux ratio ~ 0. 064)

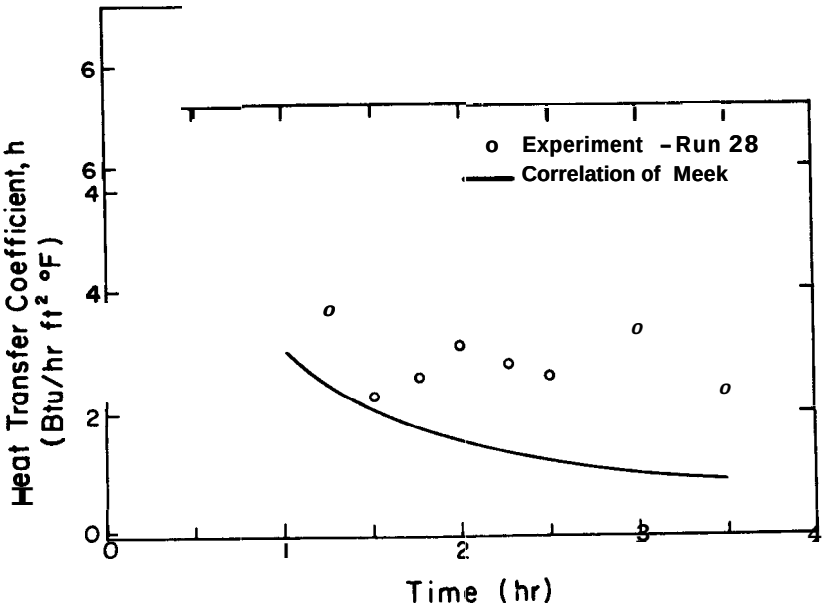

Figure 4. 13 Variation of Mean Heat Transfer Coefficient in Superheated Vapor Environment for Run 28 (Reflux ratio —0. 027)

used. The vapor flow velocity used in the Reynolds and Stanton numbers was the "approach" flow velocity or the flow velocity in the chimney without the rock present.

It is seen from Fig. 4. 12 that the experimental heat transfer coefficient for run 26 is as much as 10 times higher than the prediction. A similar trend is obseved for run 28 in Fig. 4. 13, but the experimental heat transfer coefficients are higher than the predicted by a factor of only about 1 to 3 in this case. The improved heat transfer is believed to be caused by reflux of condensed steamfrom the outlet line region with subsequent re-evaporation of water droplets striking the rocks. It appears to be of less significance for run 28 with more than a factor of two lower mean reflux ratio as compared to run 26 (reflux ratio ~0. 027 for run 28 vs. −0. 064 for run 26). Moreover, the improvement in the heat transfer appears to increase as the reflux ratio increases towards the end of the transients. This is indicated in Fig. 4. 14 which shows a sharply increasing Stanton number with decreasing Reynolds number or increasing reflux ratio. It is now known, however, whether reflux accounts for all of the rise since other factors such as low Reynolds number effects may also affect the heat transfer results.

It appears from Fig. 4. 14 that the experimental data approach the Meek correlation as the Reynolds number increases to between 100 to 200. For the present experimental conditions, this is equivalent to saying that the experimental data approach the prediction when the reflux ratio approaches zero.

4. 2. 5 Fraction Produced

The ratio of mass of steam produced to the total fluids originally in the system--referred to as the fraction produced FP--is of considerable interest in reservoir evaluation studies. For the present system it is expected from energy considerations that the reservoir pressure vs fluid withdrawal behavior will depend on such parameters as

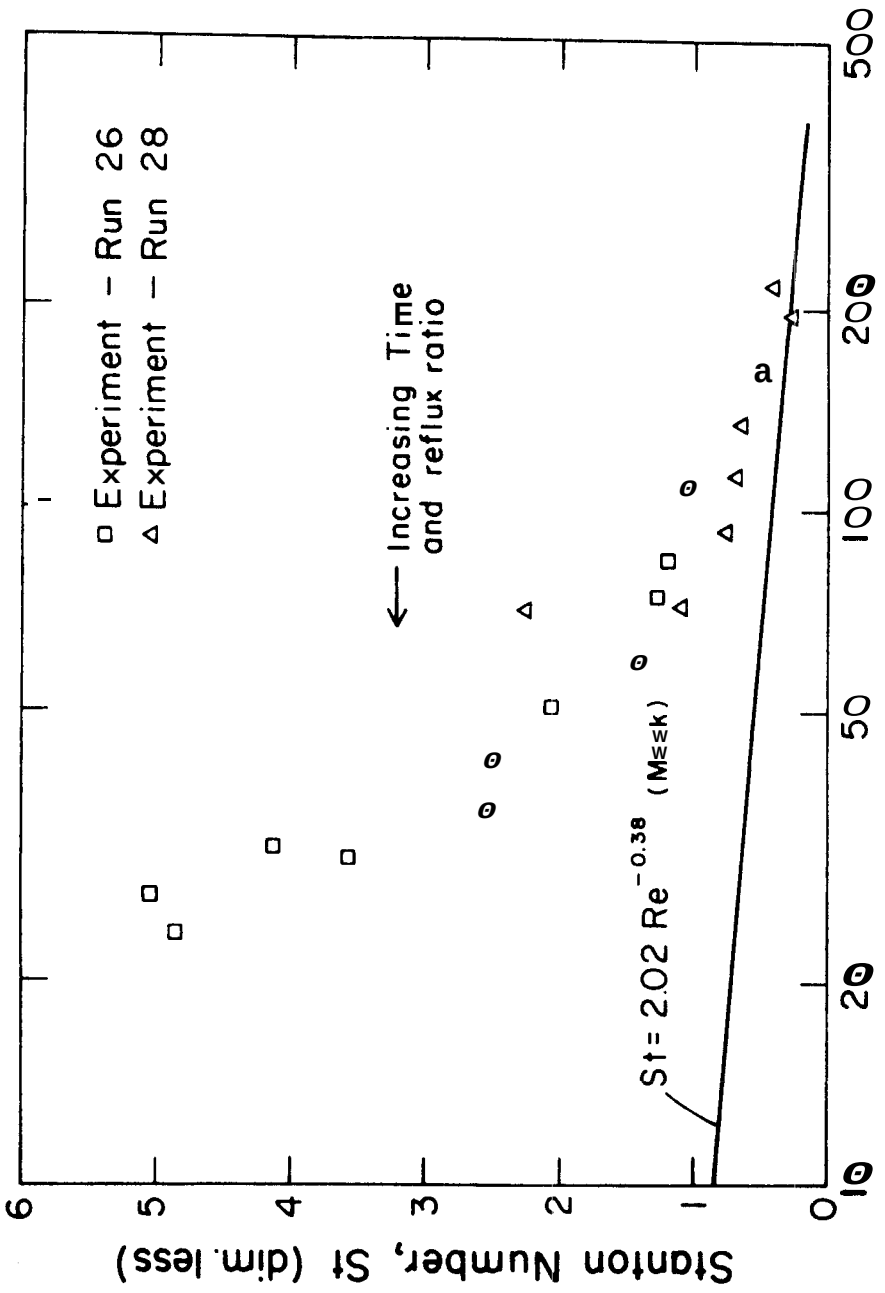

Figure 4.14 Stanton Number vs Reynolds Number for Rocks in Superheated Vapor Environment

(1) initial pressure and temperature, (2) external heat transfer parameter, (3) rock porosity, (4) rock energy extraction fraction, and (5) fluid recharge.

The effect of the initial temperature and pressure on the reservoir pressure vs fluid withdrawal for runs 23 and 25, both with no recharge and the first rock loading, is shown in Fig. 4. 15. The reservoir pressure normalized to the saturation pressure corresponding to the initial reservoir temperature is plotted vs the fraction produced. Parameters and conditions for the runs are tabulated in the figure. It is confirmed in Fig. 4. 15 that higher initial pressure (and temperature) results in higher fractions produced.

The effect of the external heat transfer parameter on the reservoir pressure vs fluid withdrawal is shown in Fig, 4. 16. The tabulation in Fig. 4. 16 shows that q_m is negative for run 4 indicating energy removal from the rock/water system. In contrast, q_m is positive for run 18. The net result is a pressure vs production characteristic which is almost a factor of two higher for run 18 as compared to run 4.

The normalized pressure vs fraction produced for three runs with different porosities and no recharge is given in Fig. 4. 17. The effect of energy extraction from the rock is seen by comparing run 3 (no rock) to runs 23 and 26. This effect, however, is overemphasized due to the large negative value of q_m for run 3 as compared to positive values for the other runs. Equation (3.27) was used to adjust the fraction produced for run 3 such that q_m = 48 Btu/lb_m (same as for run 23) which gave the dashed curve shown as run 3' in Fig. 4. 17. The remaining tabulated parameters in Fig. 4. 17 show no significant differences. Therefore, a qualitative assessment of the effect of porosity is obtained by comparing runs 3', 23 and 26. It is noted that energy extraction from the rock increases the fraction produced as the porosity is lowered.

The improved recovery of fluids from the model reservoir caused by heat transfer from the rock is considered in more detail. A recovery

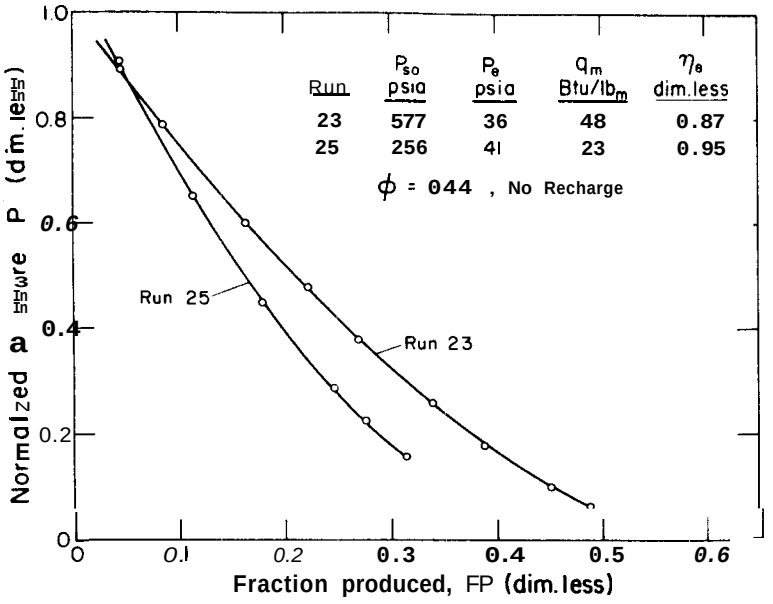

Figure 4. 15 Effect of Initial Pressure on Reservoir Pressure vs Fluid Withdrawal Behavior

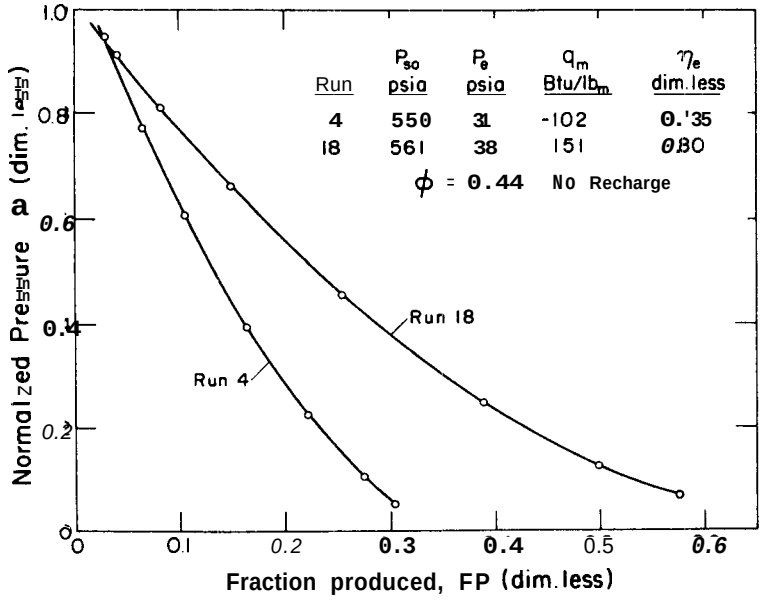

Figure 4. 16 Effect of the Specific External Heat Transfer Parameter on the Reservoir Pressure vs Fluid Withdrawal Behavior

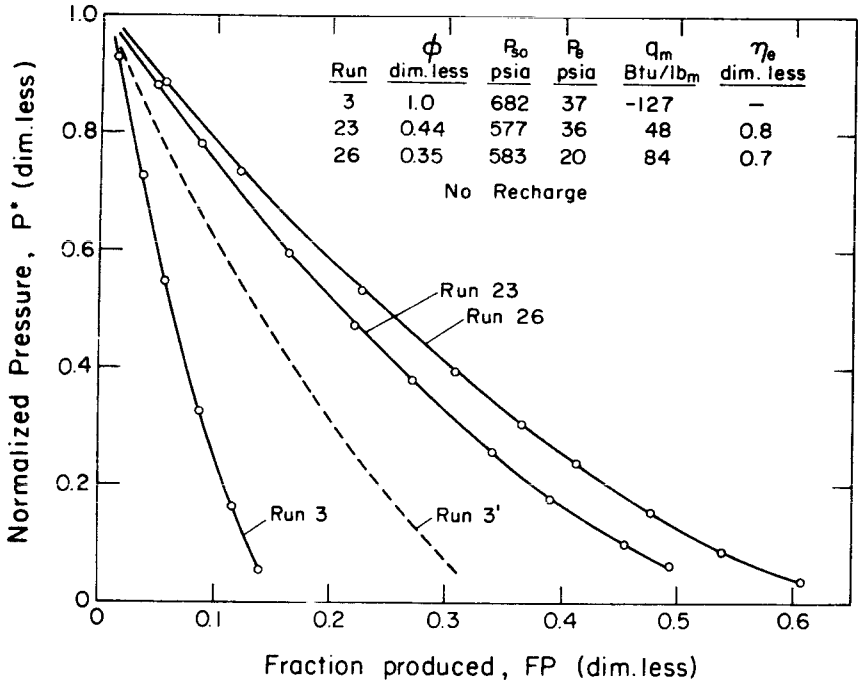

Figure 4.17 Effect of Rock Porosity on the Reservoir vs Fluid Withdrawal Behavior

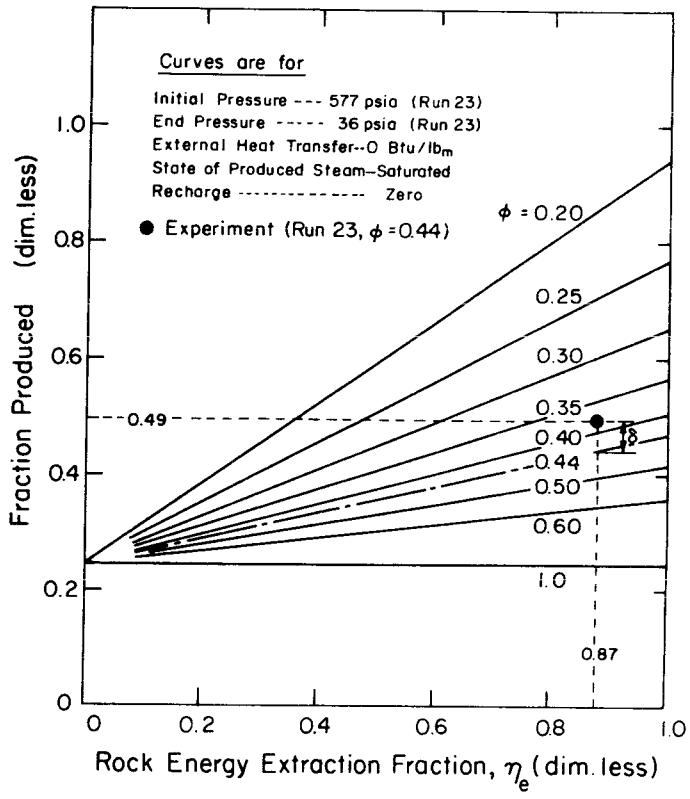

Figure 4.18 Fraction Produced vs the Rock Energy Extraction Fraction for Conditions of Run 23

factor is defined as

$$R \triangleq \frac{FP}{FP_o} = \frac{\text{Experimental Fraction Produced with Rock}}{\text{Fraction Produced without Rock}} \qquad (4.5)$$

The fraction produced in the denominator is estimated using a simplified version of Eq. (3.27) as

$$FP_o = (e_o - e_e)/(i_p - e_e) \qquad (4.6)$$

Thus, the experimental fraction produced FP is compared to the recovery achieved by flashing the fluids only and producing steam with enthalpy equal to the experimental.. In evaluating; FP_o, the experimental initial and end states were also used.

The experimental fractions produced and the specific external heat transfer parameters are given in Table 4.4 for runs without recharge. Also given are the predicted fractions produced without rock FP_o and the recovery factors obtained according to Eq. (4.5).

TABLE 4.4

Recovery Factors for Experiments without Recharge

Run	Experiment (with rock) FP(dim. less)	Experiment (with rock) q_m(Btu/lb$_m$)	Computed (no rock, q_m=0) FP_o(dim. less)	Recovery Factor $R=FP/FP_o$(dim. less)
4	0.30	-102	0.24	1.25
5	0.23	-1.00	0.17	1.35
6	0.35	-105	0.26	1.35
7	0.39	37	0.19	2.05
8	0.52	66	0.22	2.36
18	0.58	151	0.23	2.52
22	0.58	I.54	0.23	2.52
23	0.49	48	0.23	2.13
25	0.32	23	0.15	2.13
26	0.61	84	0.26	2.35
27	0.54	75	0.22	2.45
28	0.59	I.44	0.23	2.57

The recovery factor is seen to range between 1.25 for run 4 with a negative q_m to 2.57 for run 28 with a positive q_m. The large range in R is caused mainly by the significant variation in q_m which largely overshadows the effect of such parameters as the rock porosity, the rock energy extraction fraction, and the initial pressure.

The relationship between the fraction produced, the rock porosity, and the rock energy extraction fraction is illustrated in Fig. 4.18. The fraction produced computed from Eq. (3.27) is plotted vs η_e for different values of the porosity 8 for initial and end conditions of run 23, but with $q_m = 0$. It is seen that the fraction produced increases with η_e. Also, the fraction produced increases with decreasing rock porosity for a given η_e.

The magnitude of the recovery factor R is seen by comparing the fraction produced with rock ($\phi < 1.0$) and without rock ($\phi = 1.0$) at a given η_e. The recovery factor is seen to vary over a wide range depending on η_e and 8. The experimental fraction produced for run 23 is also shown in Fig. 4.113 It is higher than the calculated (for a porosity of 44 percent) by an amount δ because of the positive q_m (48 Btu/lb_m) for the experiment as opposed to the calculated where $q_m = 0$.

The effect of fluid recharge on the reservoir pressure behavior is shown in Fig. 4.19. Run 18 had no recharge (FR = 0) while runs 19, 20 and 21 had recharge of fluids with varying mean enthalpies as indicated by the range of the recharge parameter y_w (range -0.25 to 0.69). Because external heating was applied, these runs had relatively high q_m's ranging from 151 to 199 Btu/lb_m.

Comparison of runs 18 and 19 indicates that recharge of low enthalpy water tends to increase the fraction produced slightly. However, examination of the magnitudes of η_e and q_m shows that both these parameters are lower for run 18 than for run 19 (0.80 vs 0.99 and 151 vs 1199). Therefore, the effect of low enthalpy water recharge appears to be negligible, On the other hand, recharge of higher enthalpy

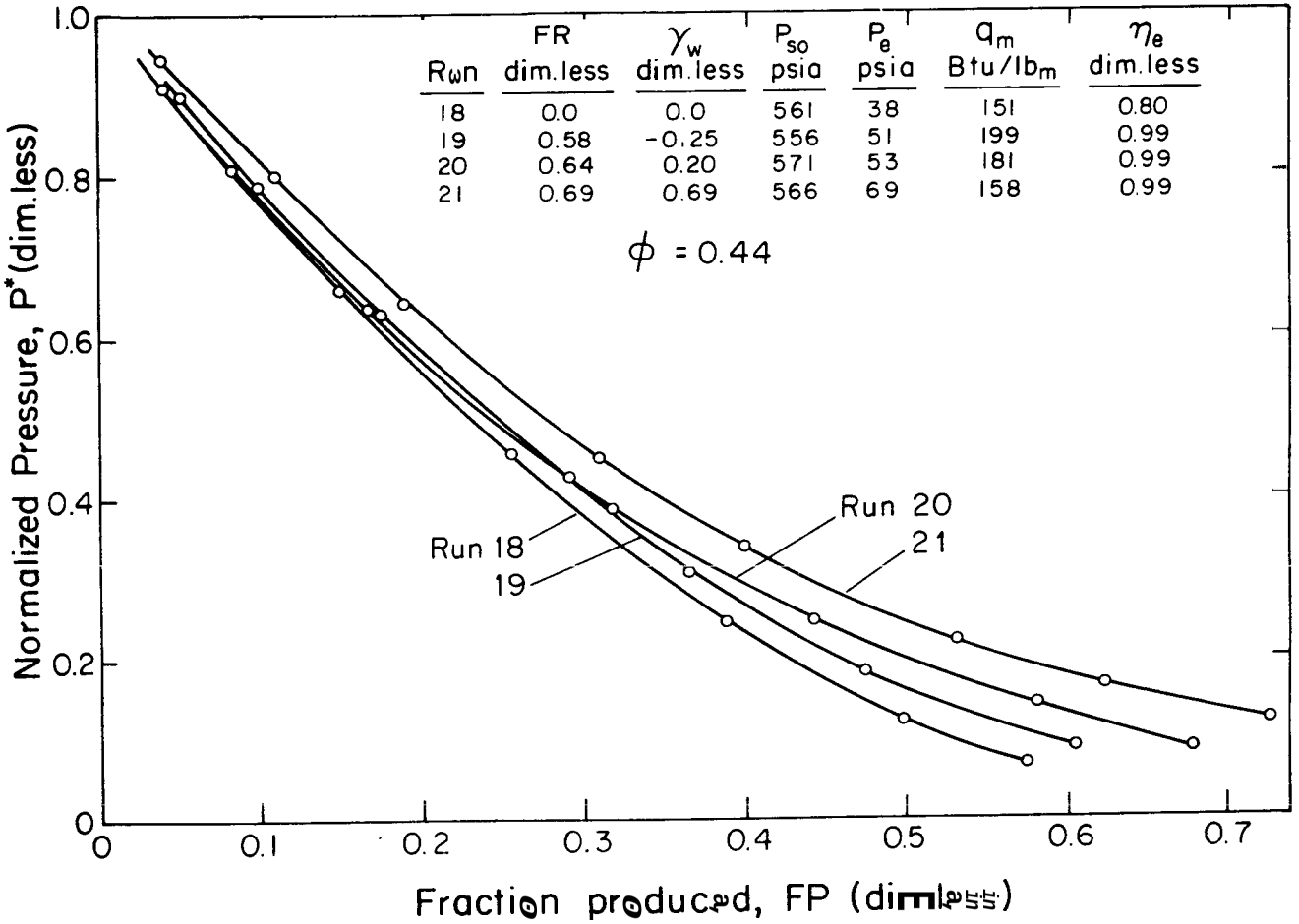

Figure 4.19 Effect of Fluid Recharge on the Reservoir Pressure vs Fluid Withdrawal Behavior

water has a significant effect on the pressure vs steam production behavior as seen by comparison of runs 18 and 21.

A major object of the investigation was to develop analytic techniques and determine their usefulness and limitations. A comparison of experimental and predicted fractions produced is given in Table 4.5 for 27 of the 29 experiments.* The predicted fractions produced were evaluated from Eq. (3.27) using data given in Table 4.1.

TABLE 4.5

Experimental and Predicted Fractions Produced at the End Condition

Run	Experiment (FP)	Prediction (FP_t)	Deviation $(FP-FP_t)/FP_t$ (Percent)
3	0.14	0.13	± 6.9
4	0.30	0.32	- 7.5
5	0.23	0.21	± 9.5
6	0.35	0.36	- 2.8
7	0.39	0.41	- 7.3
8	0.52	0.46	±13.0
9	0.56	0.49	±14.8
10	0.92	0.40	±130
11	0.58	0.47	+23.4
12	0.63	0.45	±39.0
13	0.69	0.52	±33.6
14	0.57	0.47	+21.9
15	0.66	0.58	±13.9
16	0.63	0.55	±14.5
17	0.59	0.52	±13.1
18	0.58	0.54	± 8.2
19	0.60	0.59	+ 1.9
20	0.68	0.64	± 6.7
21	0.73	0.68	± 8.1
22	0.58	0.54	± 8.2
23	0.49	0.44	+10.5
24	0.74	0.73	± 1.4
25	0.32	0.28	±13.9
26	0.61	0.56	± 8.4
27	0.54	0.51	+ 5.9
28	0.59	0.57	± 3.5
29	0.84	0.76	+10.1

*Adequate experimental data for the first two runs were not available.

The percentage difference between experimental and predicted fractions produced in the right hand column show that the experimental fractions produced were higher than the predicted by 1.4 to 130 percent in 24 experiments and lower by 2. 8 to 7. 5 percent in 3 experiments.

4. 2.6 Liquid Level

The measured and predicted effective liquid levels for runs 8 and 26 are given in Figs. **4.** 20 and 4. 21 as functions of time. The ordinate represents the liquid level measured from the top of the rock matrix normalized to the rock matrix height (see Fig. 3. 8). The data points represent the nominal liquid level. computed from the observed sight glass liquid level using Eq. (3. **28).** The effective liquid level was computed from Eq. (3. 32) with saturated vapor and liquid phases and measured fluid recharge/production data.

It is noted from these figures that the nominal liquid levels are higher than the computed effective levels by about 1 to 5 percent of the chimney height (61 inches). The data given above were representative of runs with no recharge. For comparison, the liquid levels for runs 12 and 24, both with recharge, are given in Figs. 4.22 and 4. 23. Run 12 was with recharge of cool water during the first part of the transient. Run 24 had recharge of hot water during most of the transient, but steam production was discontinued for a period of time to allow the chimney to be recharged with hot fluids (cyclic steam production). This accounts for the bump in the liquid level characteristic in Fig. **4.** 23. It is seen that the agreement between predictions and observations is better for run 12 with cool water recharge than for runs without recharge such as runs 8 and 26 in Figs. **4.** 20 and 4.21. Results for other runs with cool water recharge also showed better agreement between observed and predicted liquid levels.

The estimated uncertainty interval for the predicted liquid level given in Table **3.** *3* is 5. 7 percent of the rock matrix height. The

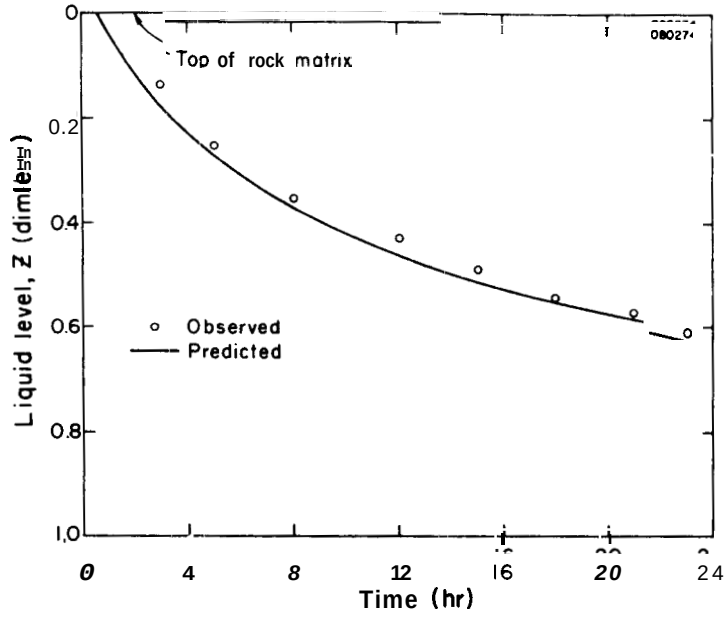

Figure 4.20 Liquid Level Characteristic for Run 8 with No Recharge

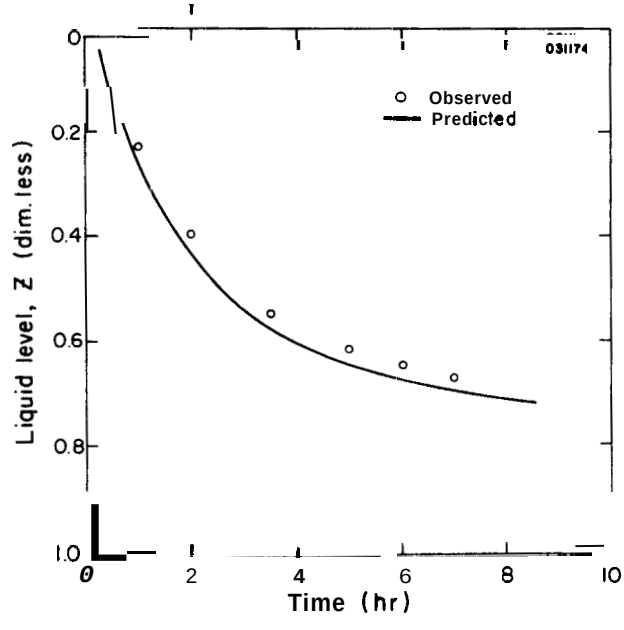

Figure 4.21 Liquid Level Characteristic for Run 26 with No Recharge

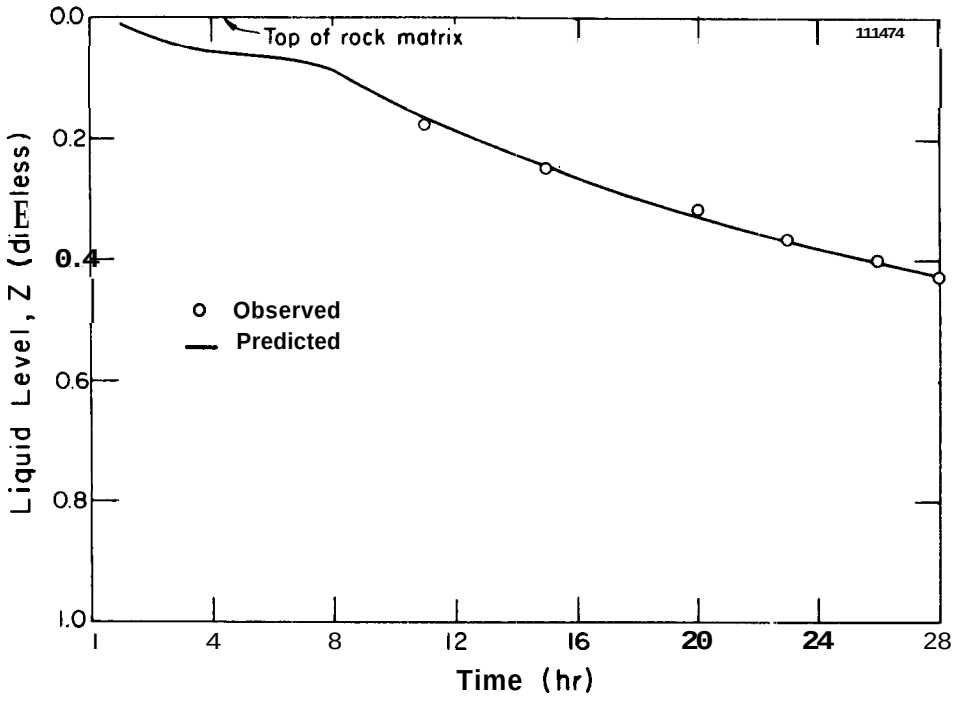

Figure 4.22 Liquid Level Characteristic for Run 12 with Partial Recharge

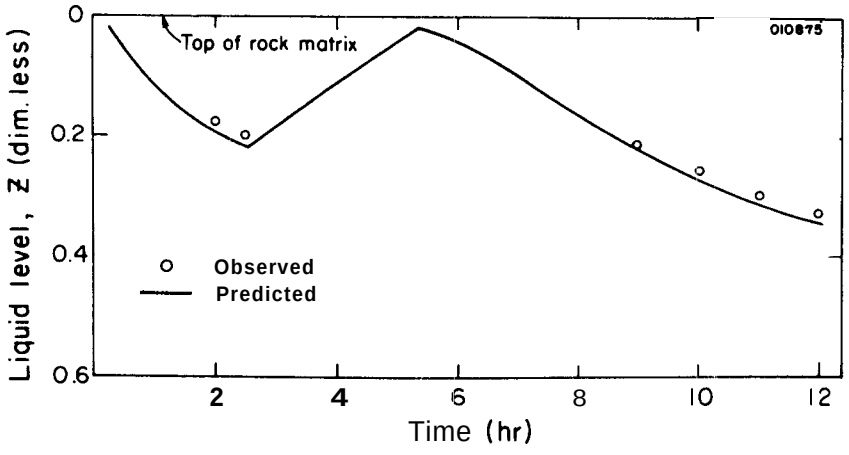

Figure 4.23 Liquid Level Characteristic for Run 24 with Cyclic Recharge

estimated uncertainty interval for the nominal liquid level is 5 percent of the rock matrix height. The difference between the nominal and effective liquid levels appears to be well within the estimated uncertainty intervals.

It appears from the data in Figs. 4.20 and 4.21 that the predicted liquid level is consistently lower than the observed for runs without recharge. Two possible causes of this trend are, (1) settling of the rock matrix with time which changes the assumed steam cap volume, and (2) expansion of the liquid due to vapor bubble entrainment not accounted for in Eq. (3.32).

The rock matrix had settled about 1.5 inches (about 2.5 percent of the rock matrix height at the conclusion of the tests with the first rock loading. Since the time dependence of the amount of settling was not known, the small settling effect was corrected for in an approximate manner. Negligible settling was observed with the second rock loading.

The liquid level rise due to possible entrained vapor bubbles was investigated further by running a special experiment. The liquid level was observed at frequent intervals while steam production was started and discontinued as indicated in Fig. 4.24. The chimney pressure was relatively high at first (the system consisted of superheated steam and subcooled liquid initially) resulting in a relatively high initial steam production rate. When saturated system conditions were reached, the rate of pressure depletion and the steam production rate leveled off. At the same time there was a rise in the observed liquid level. The liquid level dropped immediately by about 4 percent (2.4 inches) when steam production was discontinued (at about 25 min). The liquid level rose by about the same arnount when steam production was resumed at time 40 min. Steam production was discontinued a second time (at about 55 min) producing an immediate drop in the liquid level as before.

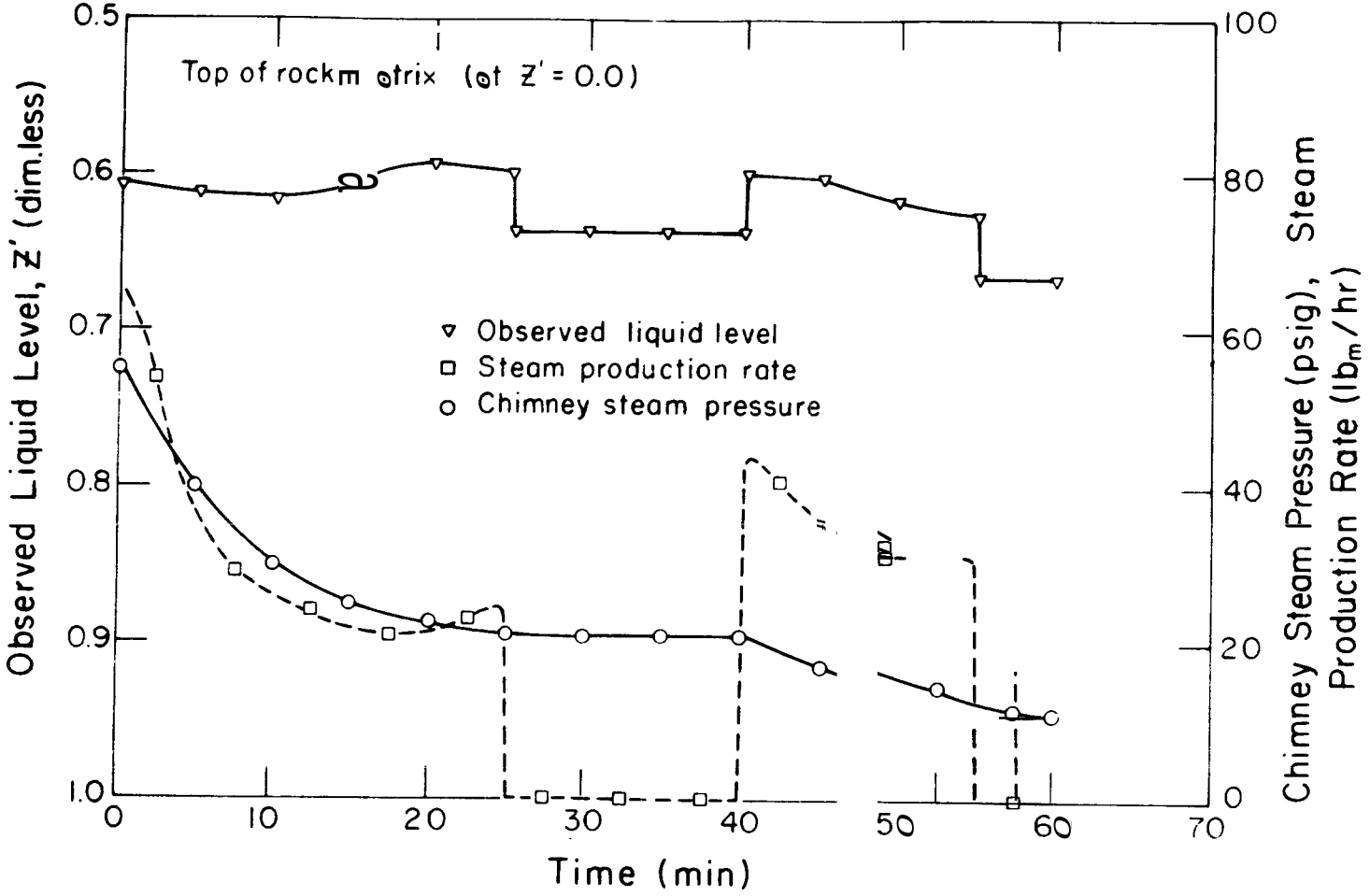

Figure 4.24 Liquid Level Characteristic with Varying Steam Production and No Recharge

The observed liquid level fluctuations in Fig. 4.24 could possibly be caused by a flow friction pressure drop in the rock matrix as well as liquid expansion from entrained vapor bubbles. However, if the pressure drop was important, the level would have dropped slightly instead of rising as the steam flow rate and the flow velocity:: through the matrix was reduced in the time period 5 to 15 min. Consequently, the observed rise in the liquid level is believed to be caused by increased expansion of the liquid as the volume of the entrained vapor bubbles increased with lowering of the steam pressure.

As soon as steam production was discontinued, the bubble formation (boiling')in the liquid was suppressed. Since the rock/steam temperature difference (and heat transfer from the rocks to the liquid) does not go to zero immediately, it would appear that the boiling was suppressed because the pressure was constant with zero steam production.

4.2.7 Recharge and Production Characteristics

The cumulative fluid recharge and production characteristics and the enthalpies of the recharged and produced fluids largely determine the reservoir transients. These quantities are the basis for determining five of the six boundary parameters, namely $\dot{M}_i$, i_i, $\dot{M}_p$, i_p, and M, required in the reservoir transient analysis discussed in Chapter 3. In a real geothermal system perhaps only two of these parameters, the steam production rate $\dot{M}_P$ and the enthalpy of the produced fluids i_p, can be determined relatively easily by measurements at the surface. The remaining parameters, $\dot{M}_i$, i_i, and M are determined by analysis in which numerous assumptions are required concerning such parameters as the aquifer and reservoir geometries, porosity, permeability, initial

---

Flow friction pressure drop is proportional to some power of the flow velocity.

state, and temperature distribution. This situation is simplified considerably for the laboratory model reservoir because the boundary parameters are determined relatively accurately from laboratory measurements.

The cumulative steam production characteristics for runs 23, 25 and 26 are given in Fig. 4. 25 (refer to Table 4. 1 for test conditions). The corresponding liquid level characteristic for run 26 was given in Figs. 4. 21. The runs given in Fig. 4. 25 are representative of experiments with constant flow control valve setting (constant discharge flow area). It is noted that as the chimney steam pressure declined the steam production rates, which are proportional to the slope of the production characteristics, also declined. Run 25 was for much lower initial pressure than the two other runs resulting in somewhat less total steam produced.

Cumulative recharge and steam production characteristics for run 12 are given in Fig. 4.26. It is o'bserved that the recharge was discontinued at a time of about 8 hr which is also apparent from the liquid level characteristic in Fig. 4. 22. The recharge was discontinued in this case because problems developed with the injection pump during the experiment. The cumulative fluid recharge and production characteristics for run 19 are given in Fig. 4.27. It is observed that fluid recharge was maintained just below steam production in this case.

The recharge and production characteristics for run 24 are given in Fig. 4. 28. The corresponding liquid level characteristic is given in Fig. 4.23. The recharge rate was somewhat lower than the production rate initially. Steam production was discontinued at about 2. 5 hr while rechargeing the chimney with hot fluids having a mean enthalpy of about 516 Btu/lb_m (see Table 4. 1). Steam production was resumed at about 5. 5 hr when the liquid level was close to the top as seen from Fig. 4. 23.

The enthalpy of the fluids recharged at the chimney inlet (specified as the location of T/C 109 in Fig. 2. 9) vs tirne for run 19 with

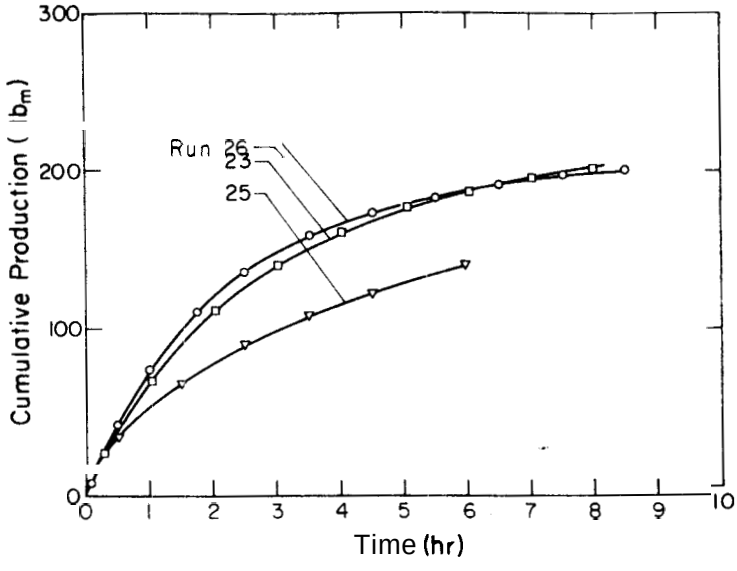

Figure 4.25 Steam Production Characteristics for Runs 23, 25 and 26 with No Recharge

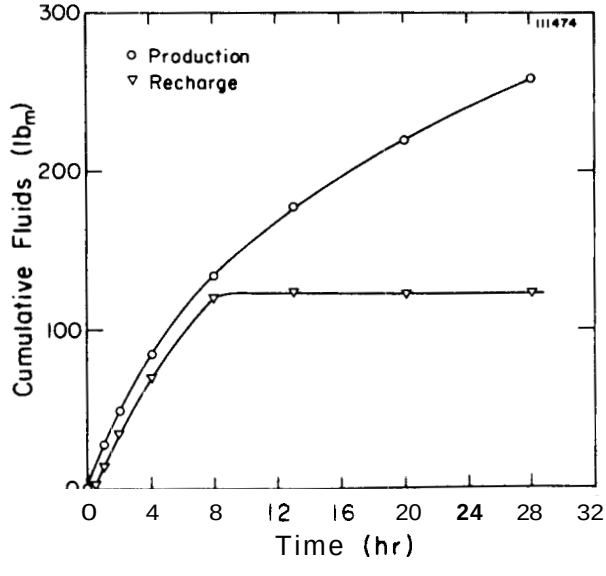

Figure 4. 26 Recharge and Production Characteristics for Run 12 with Partial Recharge

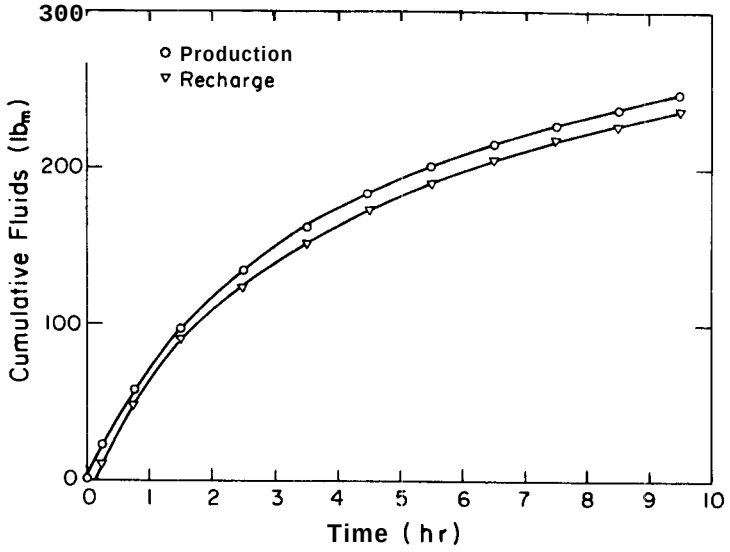

Figure 4.27 Recharge and Production Characteristics for Run 19 with Continuous Recharge

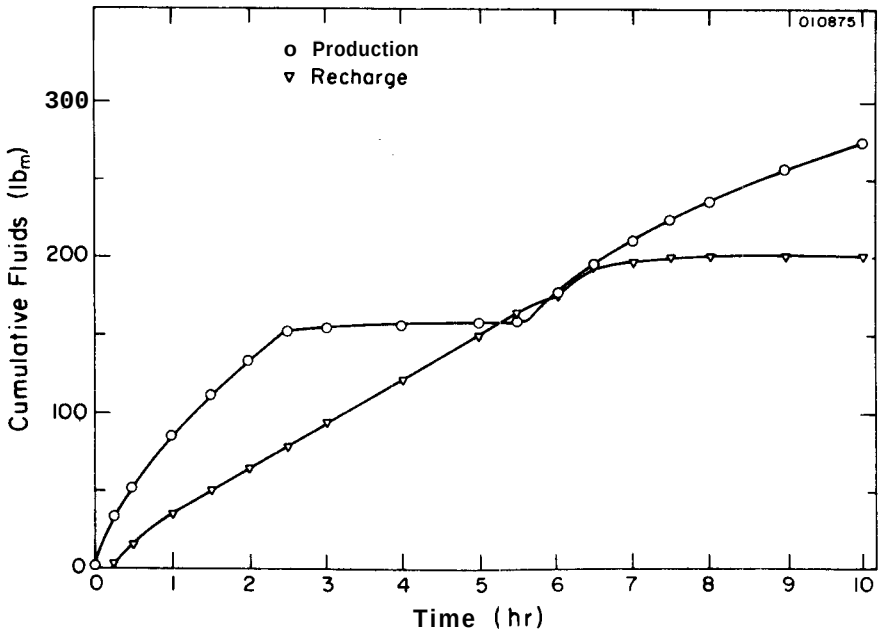

Figure 4. 28 Recharge and Production Characteristics for Run 24 with Cyclic Steam Production

cool water recharge is given in Fig. 4. 29 relative to the enthalpy of saturated liquid corresponding to the chimney steam pressure. One set of data points were derived from temperature measurements at the chimney inlet. It is seen that the enthalpy dropped off very rapidly during the first 2 hr of the transient and then leveled off. At the start of the transient, the fluids in the inlet piping and the steel in the piping were at about the same temperature as the chimney interior because the heatup operation was discontinued immediately prior to initiating the experiment. Since there was no preheating in the electric heater or by the inlet line tape heaters, except for heat transfer from the piping steel, heat losses from the inlet line resulted in cooling of the fluids contained in the line before it reached the chimney inlet. The result was a decreasing enthalpy characteristic as indicated in Fig. 4. 29.

At lower temperatures, line heat losses become negligible and the enthalpy characteristic leveled off as fluids recharged by the injection pump, originally at room temperature, reached the chimney inlet. The recharge enthalpy changed only slowly thereafter, the change being caused mostly by diminishing residual heating effect from the steel. The predicted inlet fluid enthalpy is also given in Fig. 4. 29. These data points represent computations based on Eq. (3. 17) in which the measured enthalpy at the electric heater exit, the measured power input to the line tape heater, the estimated line heat losses, and the recharge rate are required as input.

The recharge enthalpy characteristic computed from Eq. (3. 17) for run 21 with hot water recharge vs the enthalpy of saturated liquid is given in Fig. 4. 30. The recharge fluid enthalpy is rising with time and the fluid is a mixture of liquid and vapor (steam quality of 29 percent at the end of the transient). The uncertainty analysis in Chapter 3 showed that the estimated uncertainty interval for the computed recharge enthalpy is from 2 percent at the beginning to a5 high as 40

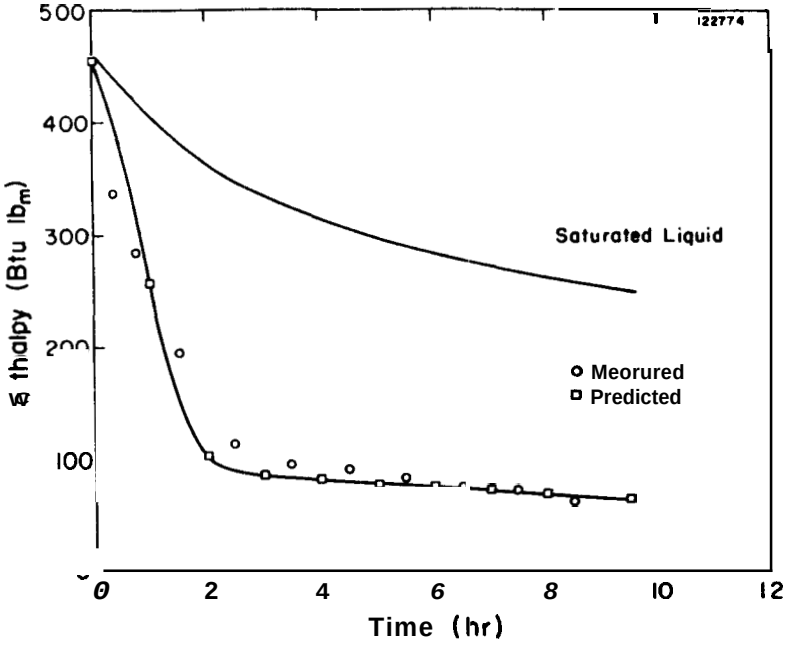

Figure 4. 29 Recharge Fluid Enthalpy for Run 19 - Cool Water Recharge

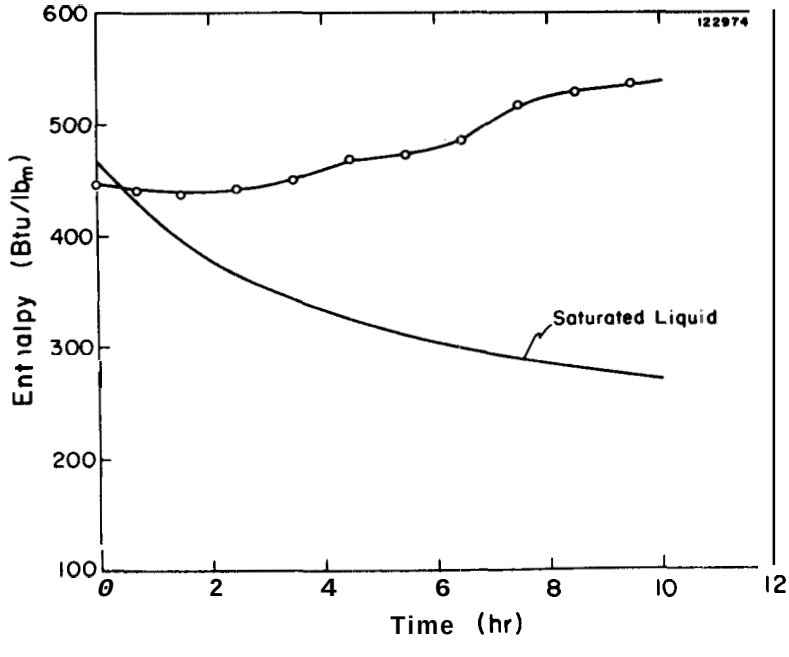

Figure 4. 30 Recharge Fluid Enthalpy for Run 21 - Hot Water Recharge

percent at the end of the transient. Therefore, the actual recharge fluid enthalpy is uncertain towards the end.

The mean enthalpy of the recharge fluids is defined as

$$\bar{i}_i = \frac{1}{M_i} \int_0^{M_i} i_i \, dM_i \qquad (4.7a)$$

which is written in terms of the fraction recharged FR and the recharge parameter γ_w as

$$\bar{i}_i = \left[\gamma_w (e_{fo} - e_{fe})/FR\right] + e_{fe} \qquad (4.7b)$$

Examination of the mean. enthalpy data given in the second column of Table 4.6 shows that the range of $\bar{i}_i$ is 40 Btu/lb_m for run 10 to 517 Btu/lb_m for run 24.

The measured temperature characteristic of the produced steam at the exit of the chimney (specified as the location of T/C 110 in Fig. 2.9) is given in Fig. 4.31 for run 18 with no recharge. The saturation temperature corresponding to the chimney steam pressure is also given for comparison. The difference between these curves represents the degree of superheat at this location. It is observed that the degree of superheat remains fairly constant during the last half of the transient for this run because reflux of condensed steam limited increase in the degree of superheat.

In cases with or without recharge where the degree of superheat was small, the measured temperature at the chimney exit corresponded to the saturation temperature. Occasionally, the measured temperature fluctuated between the saturation temperature and a slightly higher temperature, The observed fluctuation is believed to be caused by droplets cooling the thermocouple junction.

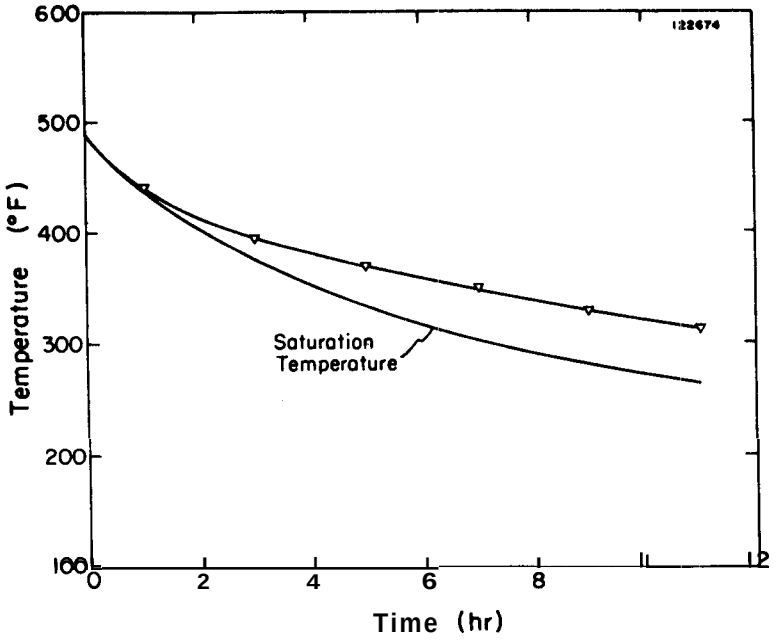

Figure 4. 31 Steam Temperature Characteristic at the Chimney Exit for Run 18

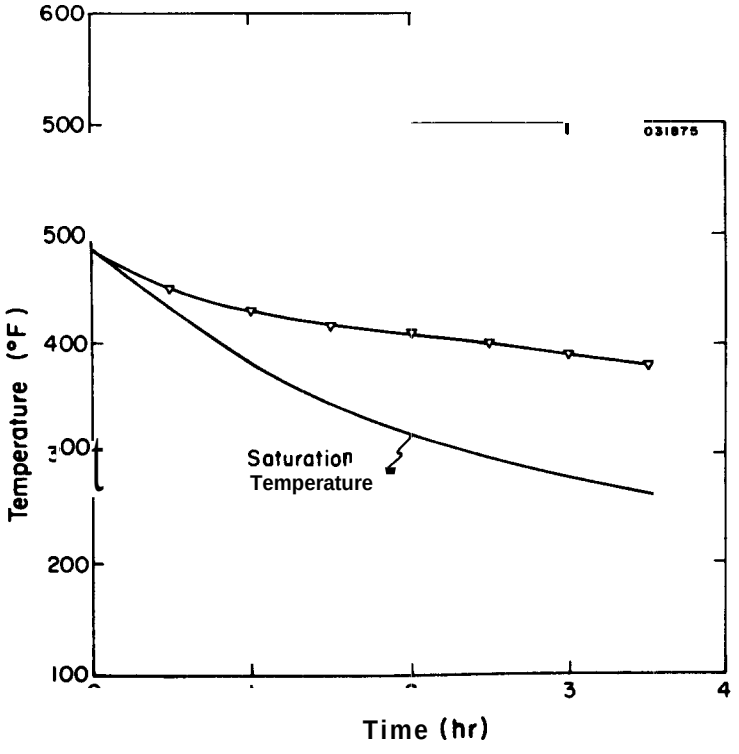

Figure 4. 32 Steam Temperature Characteristic at the Chimney Exit .for Run 28

The desuperheat effect was not significant for runs with higher steam production rates as: indicated in Fig. 4. 32 for run 28. The degree of superheat at the chimney exit is seen to increase with time and reached about 120 ^{o}F at the end of the transient. The corresponding degree of superheat at: the top of the rock matrix given in Fig. **4.** 3 was about 130 ^{o}F which was also the maximum achieved for any of the experiments.

The enthalpy characteristic of the produced steam at the chimney exit for run 18 is given in Fig. **4. 33.** The corresponding steam enthalpy parameter* defined by

$$X_P \triangleq (i_P - i_f)/i_{fg} \qquad (4.8)$$

is also given. It is noted that the enthalpy of the produced steam at first increases slightly. The enthalpy then decreases as the steam pressure declines which is also the trend for the saturated vapor enthalpy. The steam enthalpy parameter X_P remains fairly constant for the last half of the transient as did the degree of superheat in Fig. 4. 31.

The estimated mean enthalpy and the steam enthalpy parameters for all runs are given in the last **two** colums of Table 4.6. The mean values were evaluated at points approximately half way through the transients. The range of the mean exit enthalpy was 1098 to 1234 Btu/lb_m and the corresponding range for the steam enthalpy parameter was 0.88 to 1. 043.

The steam exit enthalpy was also computed based on energy balances on the condenser and on the outlet line as explained in Chapter 3.

*The term "steam enthalpy parameter" is a useful index to describe the state of the fluid. For example, if $X < 0$ the fluid is in the subcooled or compressed state, if $0 < X < 1$ the fluid is a two-phase mixture in which case X is referred to as the steam quality, and **if** $X < 1$ the fluid is superheated.

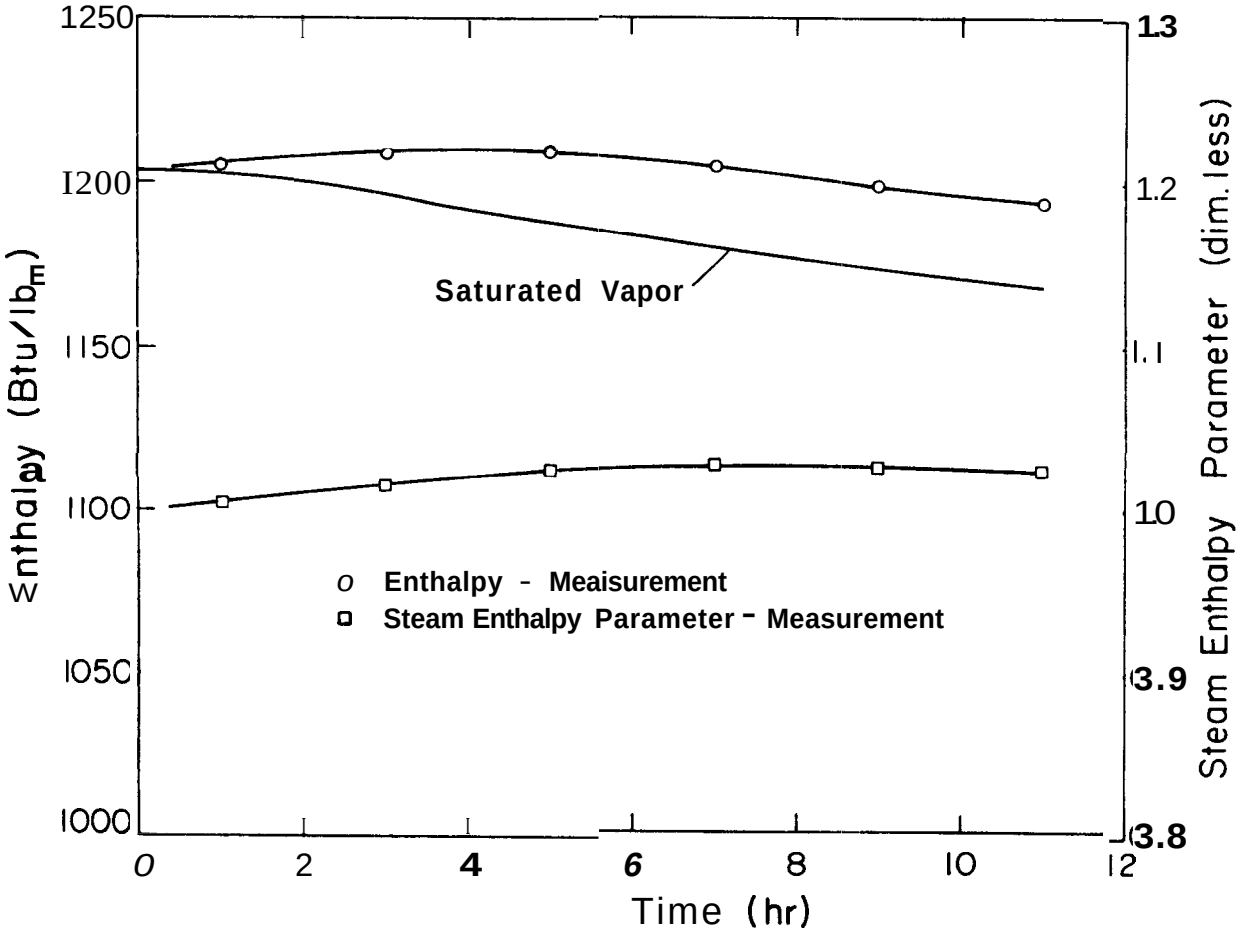

Figure 4. 33 Enthalpy and Steam Enthalpy Parameter Characteristics for Run 18

Table 4.6

Mean Recharge and Production Fluid Enthalpy Data

Run	Mean Recharge Fluid Enthalpy $\bar{i}_i$ (Btu/lb$_m$)	Mean Steam Enthalpy $\bar{i}_P$ (Btu/lbm)	Enthalpy Parameter $\bar{X}_P$ (dim. less)
1	--	--	--
2	--	--	--
3	--	1192	1
4	--	1202	1.007
5	--	1186	1.006
6	--	1204	1.011
7	--	1205	1.004
8	--	1209	1.012
9	149	1198	1.002
10	40	1098	0.88
11	136	1204	1.006
12	194	1193	1
13	198	1198	1.002
14	246	1198	1
15	325	1200	1.001
16	276	1200	1.002
17	64	1197	1.002
18	--	1225	1.033
19	194	1196	1
20	319	1200	1.002
21	462	1202	1.003
22	--	1224	1.033
23	--	1225	1.033
24	517	1197	1
25	--	1192	1.003
26	--	1224	1.035
27	--	1224	1.033
28	--	1234	1.043
29	366	1199	1.002

However, there were large scatter in the computed steam enthalpy parameters which made its use impractical for iinput to the transient analysis as originally intended. Therefore, a correlation based on the general shape of the measured steam enthalpy parameter was substituted. The general form of the correlation for the steam enthalpy parameter used was

$$X_P = C_1 + C_2 t \tag{4.9}$$

where C_1 is a constant of magnitude near 1 and C_2 was estimated for each case from the mean steam enthalpy parameter data in Table 4.6 to approximate measured characteristics. The enthalpy of the produced steam i_P at time t for use in the transient analysis was computed from Eq. (4. 8) which is rearranged to give

$$i_P = i_f + X_p i_{fg} \tag{4. 10}$$

with X_P from Eq. (4. 9).

4.2. 8 Reservoir Thermodynamics

The reservoir fluids as a whole as well as the liquid and vapor components go through a series of thermodynamic states as the reservoir is produced. A convenient illustration of these thermodynamic paths is given by the pressure-enthalpy diagram for water as shown in Fig, 4. 34. The envelope curves denoted by saturated liquid and saturated vapor meet at the critical point as indicated in the figure. To the left of the saturated liquid curve the fluid is subcooled or compressed and to the right of the saturated vapor curve the fluid is superheated. Between the envelope curves the fluids consist of a mixture of saturated liquid and vapor.

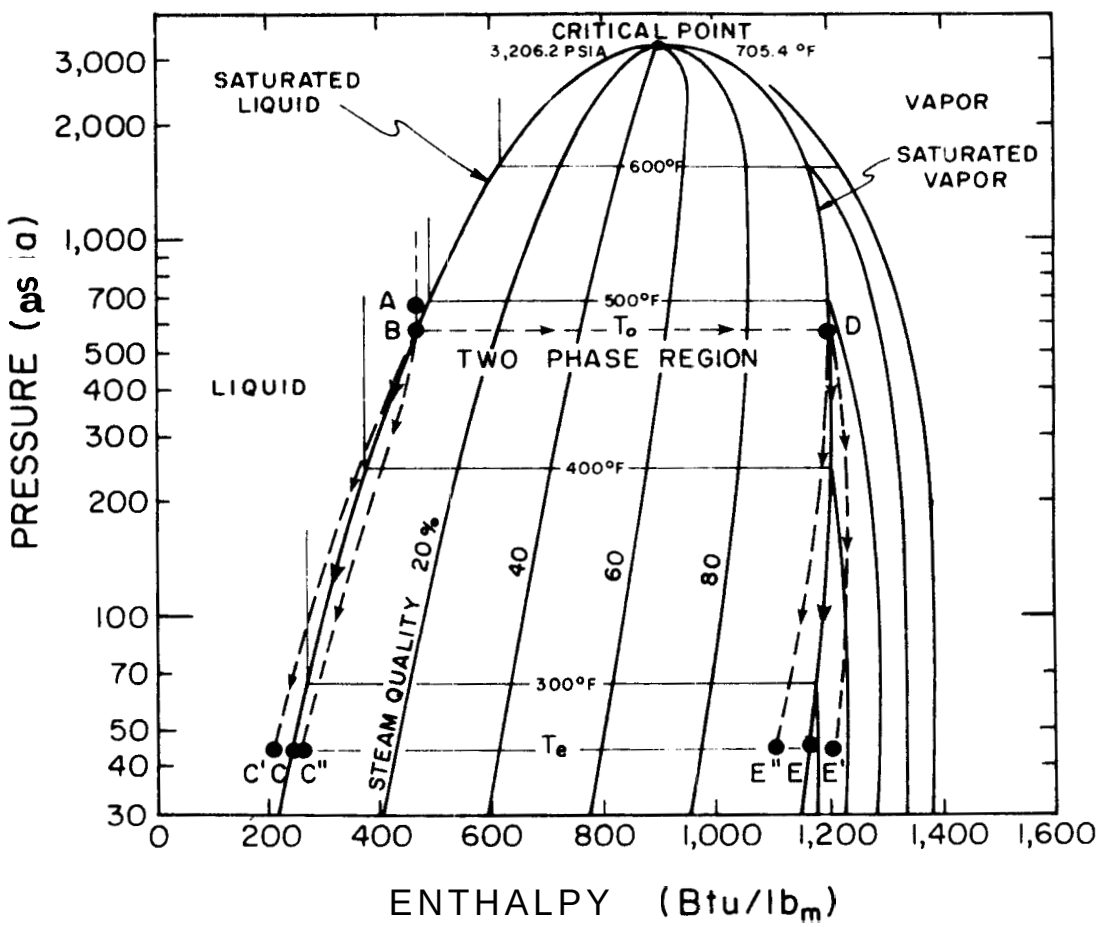

Figure **4. 34** Pressure–Enthalpy Diagram for Water

A number of initial reservoir states are possible. For example, if the reservoir consists entirely of liquids at pressures higher than the saturation pressure corresponding to the reservoir temperature the reservoir state is subcooled and would be denoted by a point "A" in Fig. 4.34. If the reservoir consists initially of a mixture of liquid and vapor, the reservoir state would lie somewhere between the envelope curves for example between points "B" and "D". Finally, the initial state could be superheated vapor in which case the state would be denoted by a point to the right of "D".

The above description is simplified in that nonuniformities of temperature and pressure, existing to some degrees in all reservoirs, have not been accounted for. Frequently, there is considerable temperature variation from the lower portion to the top of the reservoir. Moreover, the vapor and liquid phases are often segregated with the vapor phase at the top and the liquid phase at the bottom, and the liquid and vapor may not be in thermodynamic equilibrium. For example, the present experiments show that it is possible to have a superheated vapor phase and a liquid phase that is saturated or even partially subcooled in the reservoir (see, e.g., Fig. 4.1 and 4.7). Care is therefore needed when referring to a reservoir state which lies between the envelope curves. One would normally associate this two-phase region with saturated vapor and liquid phases. However, in the present discussion the reservoir bulk enthalpy indicates the weighted mean of the actual liquid and vapor components. The mean state of each of these components is not necessarily saturated liquid or vapor.

The initial reservoir state for the present experiments are represented by point "A" in Fig. 4.34. The degree of liquid compression (distance between A and B) differed somewhat from run to run as did the initial temperature T_o. Upon initiating steam production from the reservoir, saturated liquid conditions (point "B" in Fig. 4.34) was

reached after a few minutes. At that point boiling started and each phase followed separate thermodynamic paths.

The liquid phase normally followed a path similar to curve B-C in Fig. **4.34.** However, in cases with cool water recharge the liquid followed a path similar to curve B-C'. The mean state of the liquid in several runs are noted from the temperature distribution histories in Figs. **4.** 1 through **4.** 8. The state of the vapor phase normally followed paths similar to curve D-E or D-E' in Fig. **4.34.** In some cases with low steam production rate or high recharge rate, the path followed was more like curve D-E" because some moisture was entrained in the vapor.

Since the steam production occurred from the top of the reservoir, the state of the produced steam was close to the mean for the vapor in the reservoir. When vapor only is produced, the reservoir is often referred to as liquid dominated. It would appear, therefore, that the term "vapor" or "liquid" dominated reservoirs do not accurately characterize a geothermal reservoir in which the phases are segregated. Rather, the terms characterize the reservoir conditions locally around the wellbore producing sections.

The reservoir fluids (liquid and vapor) as a whole followed a production path which was very close to that of the liquid phase because the mass of liquid was much greater than that of vapor. The reservoir bulk steam quality and enthalpy for run 26 with no recharge are given in Fig. **4.35.** The reservoir bulk steam quality was evaluated from liquid level measurements and saturated fluid properties discussed in Chapter **3.** The reservoir bulk enthalpy was computed from the bulk steam quality and saturated steam properties, although, the phases were not always completely saturated.

The bulk steam quality is seen from Fig. **4.** 35 to increase to about 0. 5 percent, but then decreases, The bulk steam quality reached only about 0, 1 percent for some runs with hot water recharge because of the

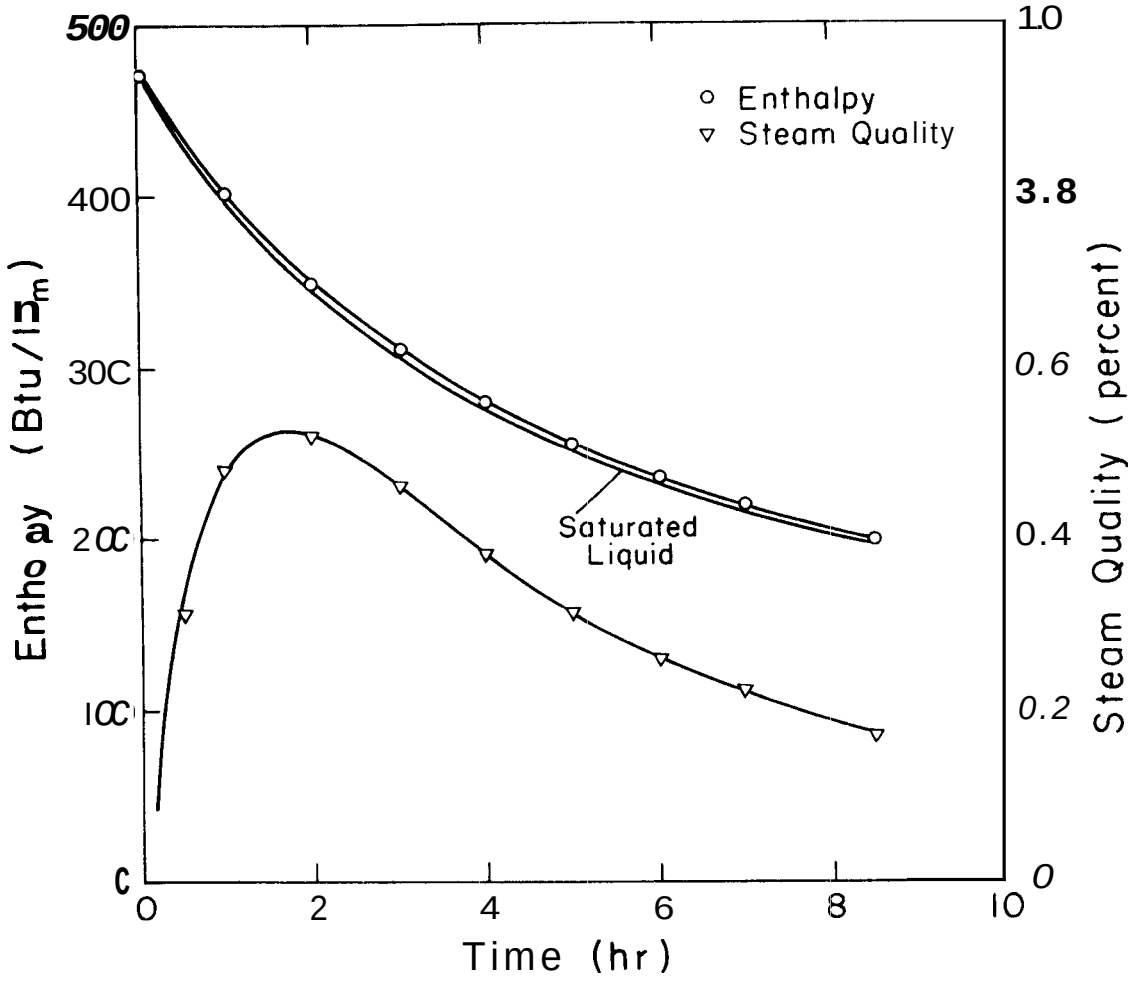

Figure 4.35 Bulk Steam Quality and Enthalpy Characteristics of the Reservoir Fluids for Run 26 with No Recharge

smaller void space above the liquid. The bulk steam enthalpy is also given in Fig. 4.35 vs the saturated liquid enthalpy. The thermodynamic path for the reservoir fluids as a whole for most of the present experiments was similar to curve B-G" in Fig. 4.34.

Reservoir production paths distinctly different from the present would appear possible. For example, if the reservoir had rock porosity less than 20 percent and no recharge such that all liquids could be evaporated, the reservoir state would follow a path similar to curve B-C" initially, but as the liquid evaporated completely the path would turn to the right and end near point E'. Further experiments are desirable to demonstrate the variety of different production path characteristics that might occur in a real system.

4.2.9 Predicted Pressure and Temperature Transients

The predicted pressure and temperature transients were compared to the experimental data for representative experimental conditions to evaluate the validity of the transient analysis developed in Chapter 3. Two changes to the original analysis were necessary. The results in this chapter showed that only a fraction of the thermal energy in the rock is extracted. An approxirnate expression €or the rate of energy extraction from the rock was obtained by multiplying Eq. (3.13) by the rock energy extraction fraction η given by Eq. (4.4). The correlation for the steam enthalpy parameter given by Eq. (4,9) was used in Eq. (4.10) to compute the enthalpy of the produced steam.

Experimental and predicted results for the pressure transients of runs 3, 18 and 26, all with no recharge, are given in Fig. 4.36 in which the chimney steam pressure is plotted vs time. Run 3 was with water only in the chimney, run 18 was with the first rock loading, and run 26 was with the second rock loading. Reference is made to Table 4.1 for details of the experimental1 conditions.

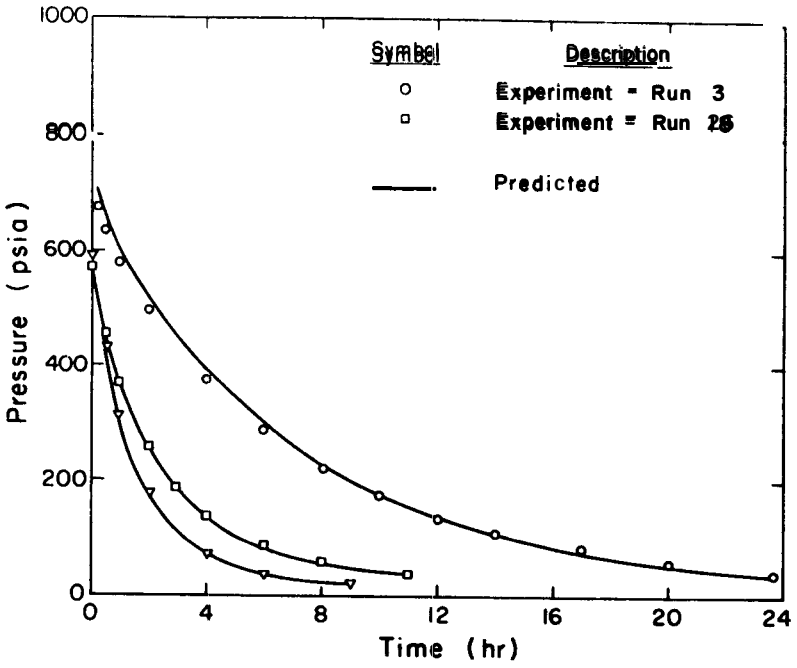

Figure 4.36 Experimental and Predicted Pressure Transients for Runs 3, 18 and 26 - Dimensional Coordinates

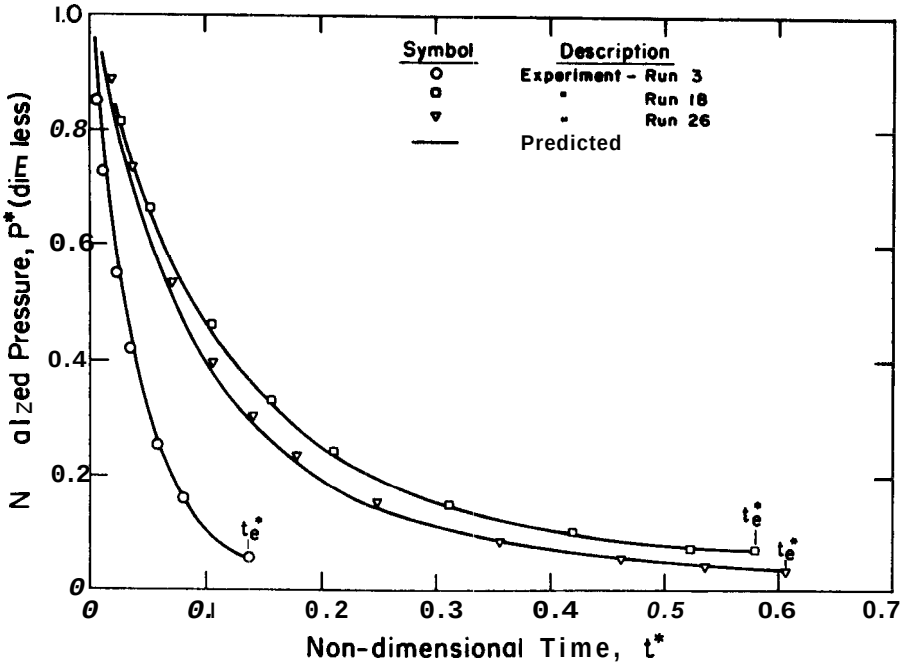

Figure 4. 37 Experimental and Predicted Pressure Transients for Runs 3, 18 and 26

The same transients data are given in Fig. 4.37 in terms of the nondimensional pressure and time variables defined by Eq. (3.19). These curves resemble the P* - FP curves in that the end points along the absissa (i.e., t^*_e) correspond to the fraction produced at the end of the transient. This is seen from the definition of t* which is

$$t^* = t/t_c = \bar{M}_p t/M_o \qquad (4.11a)$$

At time t_e the numerator is $\bar{M}_p t_e = M_P$ and therefore

$$t^*_e = M_p/M_o = FP \qquad (4.11b)$$

If the steam production rate is constant, t* and FP are equal at the same instant and the P* - t* curves are identical to the P* - FP curves.

The nondimensional P* - t* curves are preferred over the standard dimensional curves of Fig. 4.36 in the following because the ranges of the nondimensional variables change less from run to run than do the dimensional variables. The P* - t* curves also give some indication as to what fraction of fluid is produced. Moreover, with certain assumptions the P* - t* curves may be used as modeling parameters to extrapolate the present results to other systems.

Further comparisons of predicted and experimental pressure transients for runs without recharge are given in Fig. 4.38, Run 25 was initiated at a lower pressure than run 23 (287 psia for run 25 vs 581 psia for run 23). The experimental and predicted pressure transients for run 28, also with no recharge, are given in Fig. 4.39. It is noted from Table 4.1 that run 28 had about twice as high cooldown rate as any of the other runs compared in Figs. 4.37 through 4.38. It is observed that the predicted pressure is higher or lower than the measured pressure depending on which run is considered and on the time in the transient. However, reasonable agreement between measurement and prediction for the entire transient is noted in a majority of cases. The

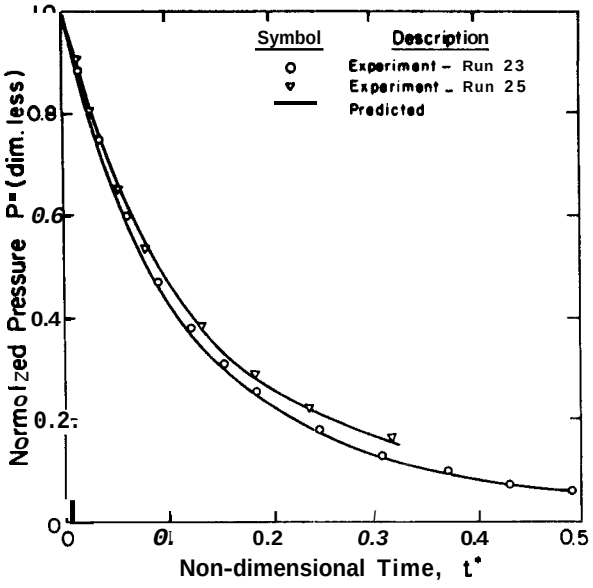

Figure **4. 38** Experimental and Predicted Pressure Transients for Runs 23 and 25

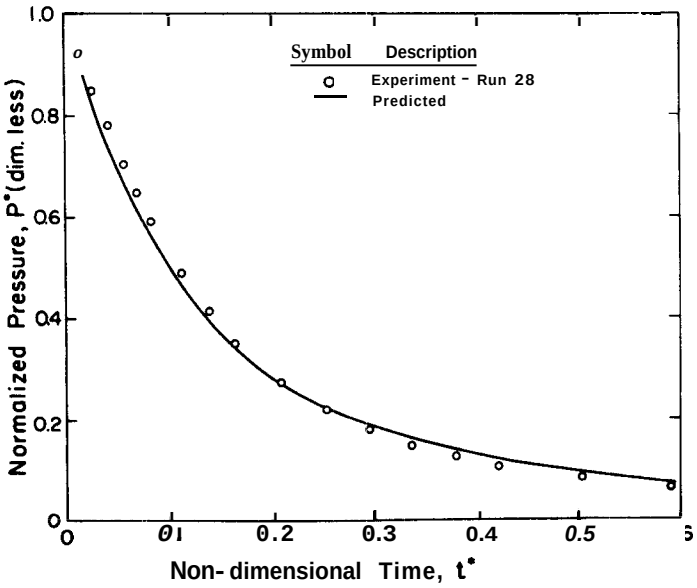

Figure **4.** 39 Experimental and Predicted Pressure Transients for Run 28

maximum deviation occurred for run 28 where the predicted pressure was about K5 percent higher than the measured near the end of the transient which exceeded the uncertainty interval of ±10 percent estimated for the pressure measurement. However, in all other cases with no recharge the predicted pressure near the end of the transient was well within the estimated uncertainty interval.

The predicted pressure was about 8 percent higher than the measured for run 3 during the early part of the transient. This was the maximum deviation noted at early times for these runs. The corresponding uncertainty interval for the measured pressure was 1.2 percent. The difference between the measured and predicted pressures exceeded the estimated uncertainty interval during the early part of the transient in a few cases.

Comparison of predicted and experimental results for runs 19 and 21 with recharge are given in Fig. 4.40. Run 19 was with cool water recharge indicated by the negative γ_w tabulated in the figure. The mass and enthalpy recharge characteristics for run 19 are given in Figs. 4.27 and 4.29. Run 21 was with hot water recharge, The recharge enthalpy characteristic for run 21 is given in Fig. 4. 30.

The agreement between predicted and experimental results is seen to be excellent for run 21 with hot water recharge. However, for run 19 with (coolwater recharge the predicted pressure was lower than the measured by about 22 percent during the last part of the transient while the agreement was reasonable during early times. The same trend is noted in Fig. **4.** 41 which gives the predicted and measured pressure transients for run 12 also with cool water recharge. In this case the predicted pressure is lower than the measured by about 66 percent at the end of the transient. It appears from these results that relatively latrge differences between predictions and experiments are associated with runs where cool water is recharged.

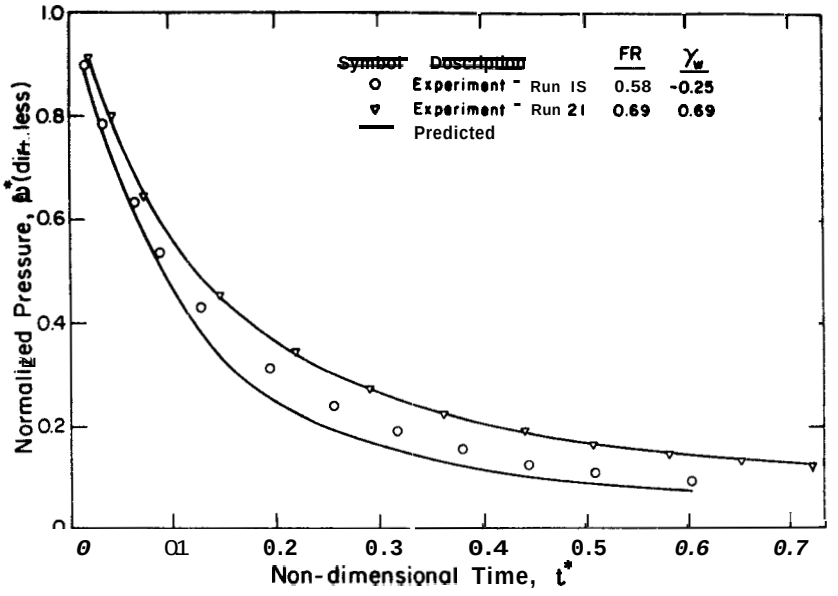

Figure 4.40 Experimental and Predicted Pressure Transients for Runs 19 and 21

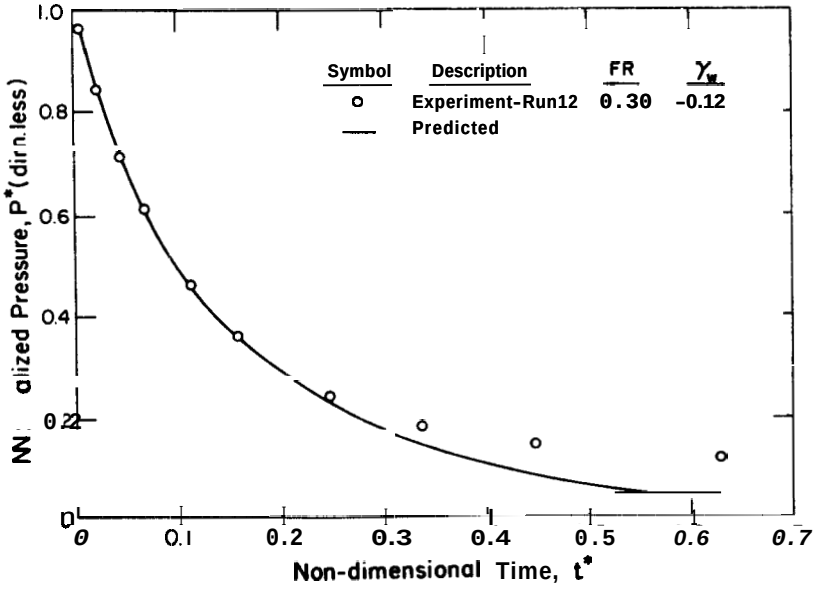

Figure 4.41 Experimental and Predicted Pressure Transient for Run 12

The predicted pressure transient for run 24 with cyclic production and continuous recharge of hot water is compared to the measured transient in. Fig. 4.42. The mass recharge and production characteristics for run 24 are given in Fig. 4. 28 and the variation of the liquid level with time is given in Fig. 4. 23. It is noted that the analytic model can predict the observed 'behavior to within ±9 percent.

During the recharge period extending from t* values of about 0. 15 to 0. 34, approximately 70 lb_m of fluids with mean enthalpy of about 500 Btu/lb_m was added to the system. The recharged fluid mass corresponded to about 18 percent of the original in-place fluids. The pressure rise resulting from the fluid recharge was about 30 psi.

The predicted liquid and the mean rock temperature transients for run 23 with the first rock loading (small rock) are given in Fig. 4.43. The measured temperatures of the liquid and of instrumented rock 2 are also given. It is noted that the predicted and measured rock temperatures are essentially in thermal equilibrium with the liquid. Finite rock/liquid temperature differences are predicted and measured for run 26 with the second rock loading (large rock) as shown in Fig. 4.44.

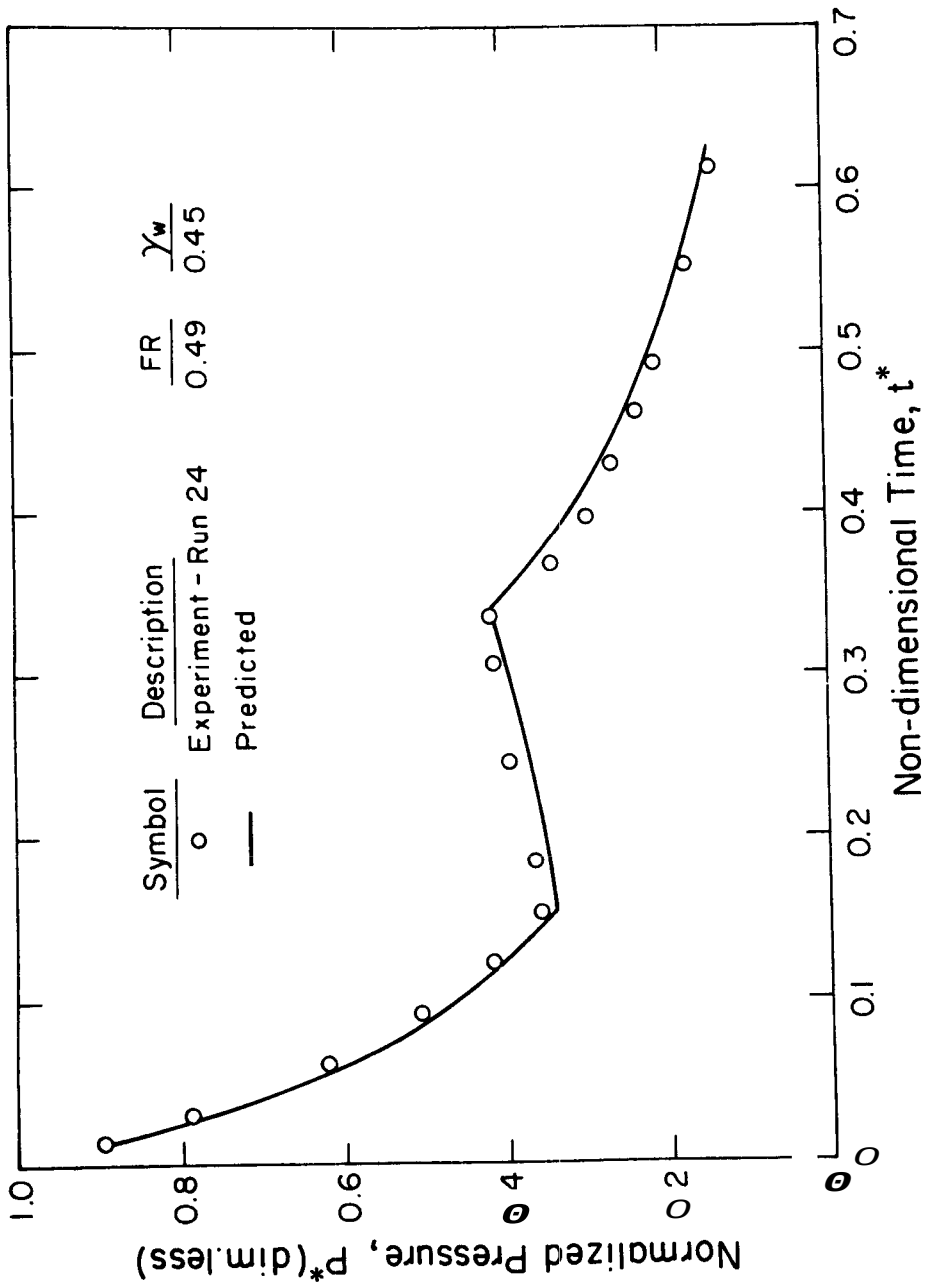

Figure 4.42 Experimental and Predicted Pressure Transient for Run 24

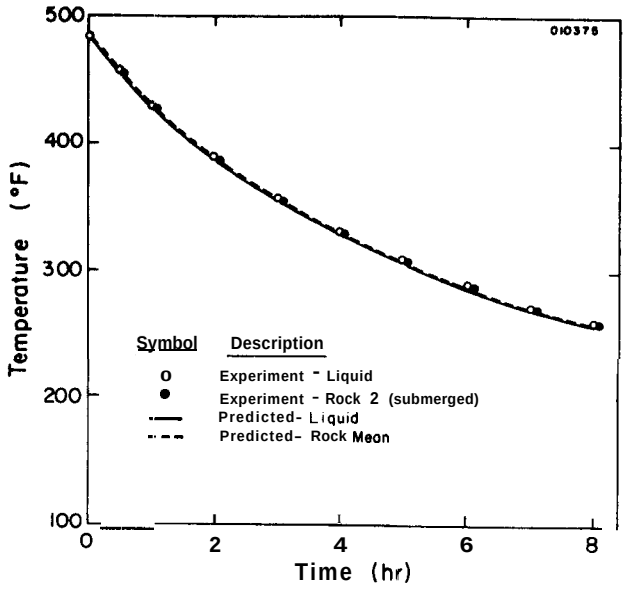

Figure **4.43** Experimental and Predicted Liquid and **Rock** Temperature Transients for Run 23

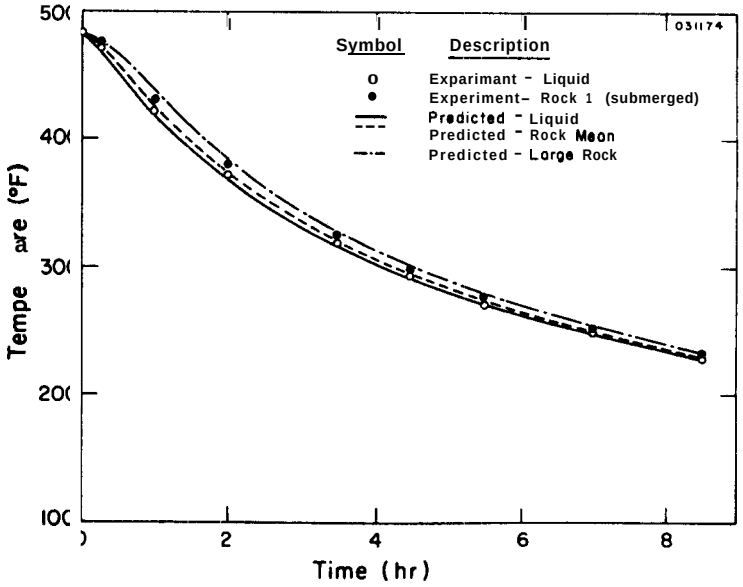

Figure **4.44** Experimental and Predicted Liquid and Rock Temperature Transients for Run 26

CHAPTER 5

DISCUSSION

5. 1 Experimental Results

The experimental results show that the thermal energy stored in the fractured rock used in these experiments can be extracted effectively. The energy extraction was achieved by lowering the system pressure by steam production so that boiling was initiated within the rock matrix. Since the two-phase saturated steam mixture follows the vapor pressure/temperature curve, thermal gradients were set up in the rock resulting in heat transfer from the rock to the steam.

The rock energy extraction fraction is defined as the ratio of the extracted rock energy to the available energy between the measured initial temperature and the saturation temperature corresponding to the pressure at the end of the experiment. The range of rock energy extraction fractions evaluated from rock temperature measurements was 0. 75 to 1. 18. The estimated uncertainty interval for these results is ±3, 5 percent. The highest rock energy extraction was achieved with the smaller rock (gabbro) and cool water recharge while the lowest was with the larger rock (granite) and no recharge.

The parameters and conditions that determined the magnitude of the rock energy extraction fraction were; (1) the position of the liquid level in the chimney, (2) reflux rate of condensed steam from the outlet line region relative to the steam production rate (reflux ratio), (3) recharge of cool water at the bottom of the chimney, and (4) the magnitude of the temperature difference between the rock and the steam.

A superheated zone developed above the liquid level in experiments with zero or low recharge relative to steam production. The existence of the superheated zone resulted in incomplete energy extraction from

the rock in this zone relative to rock subrnerged in saturated liquid, The corresponding reduction in the energy extraction fraction depended on the degree of superheat at the exit which was as high as 120 ^{o}F in some experiments.

The extent of the superheated zone was determined by the position of the liquid level and by reflux of condensed steam from the outlet region. The liquid level was maintained in the experimental system by controling the recharge/production ratio, Lowering of the liquid level resulted in a larger super'heated zone and a correspondingly lower rock energy extraction fraction, Reflux of condensed steam, on the other hand, tended to reduce the degree of exit superheat and the extent of the superheated zone. The experimental rock energy extraction fractions therefore increased with increasing reflux ratios.

Reflux of condensed steam from the wellbore relative to the steam production, i.e., the reflux ratio, is expected to be considerably lower in a real size system as compared to the experimental system. Therefore, the desuperheat effect noted for relatively high reflux ratios in the experiments is expected to be small in a real size system. Vapor superheat of the same order as achieved in the experiments may therefore be achieved in a real size system, Higher rock energy extraction fractions and lower degrees of vapor superheat were achieved in the experimental system by increasing the liquid level, Such an increase in the rock energy extraction fraction accompanied by a lowering of the degree of vapor superheat also appears feasible in a real size system.

Recharge of cool water resulted in a cool water zone in the lower section and a hot Saturated liquid zone in the upper section of the chimney. The rocks in the subcooled water zone were cooled to temperatures less than the saturation temperature. Moreover, the recharge reduced or eliminated the superheated zone. These two factors combined gave a rock energy extraction fraction greater than unity in one case.

The rock/steam temperature difference existing at the end of the transient results in a decrease in the rock energy extraction fraction. This effect was not significant with the small rocks of the first rock loading because the rocks were essentially in thermal equilibrium with the steam. A 4 percent effect was noted with the larger rocks of the second rock loading which is negligible compared to other effects in the experimental system. However, the rock/steam temperature differences may be of considerable practical importance in real size systems with much larger rocks. This effect is therefore considered in more detail.

A measure of the rock/steam temperature difference effect on the rock energy extraction fraction η_e in the absence of other effects is given by

$$\eta_e = 1 - \beta_e = 1 - \frac{\mu_e}{\bar{\mu}} \frac{\tau}{t_e}$$

where $\mu_e/\bar{\mu}$ is the ratio of local cooldown rate at the end of the transient to the mean cooldown rate, τ is the time constant for the mean size rock, and where t_e is the transient time. The τ/t_e ratio can be reduced by either increasing the steam production transient time t_e or by decreasing the rock size by fracturing to give a smaller mean rock time constant. In a real. size system the transient time t_e is largely determined by the design life of the power generating facilities. The question of whether practical fracturing methods exist such that rock segments with a sufficiently low mean time constant; for economic utilization can be achieved was not investigated.

The $\mu_e/\bar{\mu}$ ratio may be reduced by cooling the rock more slowly (reduce steam production rate) towards the end of the transient such that $\mu_e/\bar{\mu}$ is less than unity, The $\mu_e/\bar{\mu}$ ratios of these experiments

were about 0. 3 to 0. 5. It may not be desirable to operate a real size system with such a decreasing steam production rate characteristic although more rock energy may be extracted in this way. Economic and practical. considerations are required to determine the optimum operating scheme to achieve maximum energy extraction in a given case.

Boiling was achieved without difficulties in the laboratory model by lowering the steam pressure because the operator could control the steam production/recharge ratio. In a real size system the maximum steam production is limited by the wellbore geometry. In cases where the recharge mechanism is artificial as illustrated in Fig, 1. 1, the recharge rate rnay also be controled. In that case it should be relatively easy to control the liquid level and to establish saturated reservoir conditions. Control of the liquid level may be more difficult in stimulated hydrothermal fields where the natural recharge may exceed the wellbore discharge capability.

Uniform temperature conditions in the liquid were achieved for the experiments because of boiling and natural convection in the relatively high permeability rock matrix as the pressure declined. Since a real size system is much taller, the higher pressures due to the static liquid head prevent boiling at depths. Although the axial temperature distribution in the liquid is not known for a real size system, it is expected to be close to the uniform axial distribution found in the experimental system. The potential therefore exists for achieving rock energy extraction fractions of the same order as those achieved for the experimental systern.

The axial temperature distribution is not known in the liquid zone of a relatively low permeability rock matrix with restricted natural convection such as in the lightly fractured region of Fig. 1. 1. In such cases the rock energy extraction fractions may be considerably lower than those achieved in the present experiments. Care must therefore

be exercised in extrapolating the present results to systems with finite permeabilities.

The rock energy extraction scheme tested in the chimney model to date involved the establishment of non-isothermal steam conditions. This was achieved by controling steam production and fluid recharge such that sufficient pressure reduction resulted to initiate boiling. The model can also be operated as a compressed liquid reservoir consisting of hot rock and subcooled liquid initially. Energy extraction from the rock is achieved by recharging cool water at the bottom and producing the hotter water at the top. This energy extraction scheme is similar to the one proposed for the Los Alamos dry, hot rock project.

Energy extraction from the rock resulted in fractions produced which were greater than those achieved by flashing of water alone. The fraction produced was found to increase with (1) lower end pressure, (2) higher initial pressure/temperature, (3) recharge of hot water, (4) lower rock porosity, (5) higher rock energy extraction fraction, and (6) higher values of the external heat transfer parameter. A recovery factor R is defined as the ratio of the experimental fraction produced to the fraction produced by flashing the water alone for the same initial and end pressure conditions, but with external heat transfer parameter q_m equal to zero. The recovery factor for experiments without recharge ranged between 1.25 for run 4 with a negative q_m to 2.57 for run 28 with a positive q_m. The estimated uncertainty interval for R is *15 percent. The large range in R is caused mainly by the significant variation in q_m. This effect largely overshadows the effect of other parameters such as (1) the rock porosity, (2) the rock energy extraction fraction, and (3) the initial pressure which also influence R significantly.

For real size systems q_m is positive, but to estimate its magnitude, extensive analysis is required of the lightly fractured region surrounding the chimney (see Fig, 1.1). Such an analysis was not

performed in the present investigation. The effect of energy extraction from the highly fractured rock only on the recovery factor is seen by adjusting the experimental. results such that $q_m = 0$ using Eq. (3.27). The estimated recovery factor is 1.72 for the conditions of run 23 (44 percent porosity) and 1.86 for the conditions of run 26 (35 percent porosity).

The recovery factor increases with decreasing porosity because more rock energy is available per unit reservoir volume to evaporate the liquid. Theoretically, the recovery factor with zero recharge and external heat transfer is as high as 5 for the upper pressure conditions of these experiments and rock porosity less than 20 percent. However, low porosity usually is accompanied by low permeability and reduced water circulation which almost certainly mean reduced energy extraction fractions and recovery factors.

The 35 percent porosity of the second rock loading is the lowest that may be achieved for the particular rock size distribution. However, further reduction in the porosity may be obtained by filling the void space in the present rock loading with coarse sand. It appears that a porosity of the order of 20 percent can be obtained. Test with such a system would be desirable as a first step in investigating low porosity systems with finite permeabilities.

Recharge of hot water has the effect of increasing the recovery factor because energy is added to the system and because the energy extraction fraction is increased. External heat transfer from the surrounding results in positive q_m which also has the effect of increasing the recovery factor. It is apparent that the magnitude of the recovery factor that can be achieved in a real size system depends on a number of factors which cannot be assessed quantitatively unless specific information is available about the system.

The results show that the predicted rock center/steam temperature differences based on the sphere idealization were in substantial agreement with the measurements in vapor environment. However, the experimental rock center/steam temperature differences for rocks in liquid environment were about 40 percent lower than the predicted based on either the sphere and plate idealizations. The prediction based on the plate idealization was always 'higher than the experimental for rocks in vapor environments. Conclusions regarding these results cannot be drawn until the uncertainties in the measured and predicted rock center/steam temperature differences are discussed.

The estimated uncertainty interval for the rock center/steam temperature difference measurement is about ±3 ^{o}F. There are uncertainties associated with the parameters μ_e, α, k, r_o, ℓ, and h used in Eqs. (3.2) for predicting the rock center/steam temperature differences. The uncertainty interval for the predicted temperature difference is estimated to be about ±4 ^{o}F for both liquid and vapor environments as indicated in Table 3.3.

Closer examination of the data in Table 4.3 shows that the predicted and measured rock center/steam temperature differences appear to be within the estimated uncertainty intervals (i.e., the error bands overlap) in most cases. Although the sphere approximation appears to be the best in vapor environment, the results are largely inconclusive as to which of the geometry approximations (sphere or plate) is the most appropriate for these rock shapes. Improved rock center/steam temperature difference measurement techniques, better rock thermal property data, and better heat transfer coefficient data are required.

The mass-energy balance analysis on a time interval basis developed for the chimney was used to predict the model reservoir behavior. The predicted and experimental results in most cases were in agreement for a wide range of experimental conditions. Comparison of predicted

and experimental fractions produced shows that the experimental fractions produced were higher than the predicted by 1.4 to 130 percent in 24 experiments and lower by 2. 8 to 7. 5 percent in 3 experiments.

These results have to be looked at in view of the estimated uncertainties in the data. From Table 3. 3 the uncertainty in FP is ±2. 6 percent while the uncertainty in FP_t due to uncertainties in the experimental parameters used in Eq. (3. 27) range between 10.2 to 14. 2 percent. Examination of the data in Table 4.4 shows that the data appears to be within the estimated uncertainty intervals in 22 of the 27 runs.

The experimental fraction produced for run 10 is more than a factor of two higher than the predicted. It is recalled that run 10 had cool water recharge and a large subcooled zone at the bottom as seen from Fig. 4. 8. Several of the other runs with larger than expected deviations also had some cool water recharge, Under these conditions, the uniform axial temperature distribution assumption used in deriving Eq. (3. 27) from mass-energy balances is seriously violated. Consequently, the relatively large differences between experiments and predictions are not surprising.

The observation that the experimental data were generally higher than the predictions also in cases without recharge suggests a systematic error in the data or that assumptions inherent in the analysis are violated. It was assumed in the analysis that the widely varying recharge and produced fluid enthalpies were equal to the mean of the initial and end enthalpies. Considerable uncertainties are associated with the parameters used in Eq. (3. 27) to compute FP_t. Systematic errors could be associated with any of the parameters $\bar{i}_i$, $\bar{i}_p$, q_m, M_o, ϕ, and FR.

The agreement between experiment and prediction shows that the analysis is consistent with the experimental results. Therefore, the analysis may be applied to predict the performance of real size systems

with similar characteristics as long as the assumptions inherent in the analysis are not violated. Modification of the analytic model appears feasible such that it can treat cool fluid recharge adequately. A possible approach is to apply the mass-energy balances to the hot water/steam and subcooled zones separately.

The transient analysis developed for the chimney model was used to predict its transient behavior for representative experimental conditions. The results show that the predicted pressures at the end of the transients were within the 10 percent uncertainty interval for the measured pressures in a majority of cases. The predicted pressure transient differed substantially from measurements in certain cases such as in, (1) experiments with cool water recharge, (2) experiments with the highest cooldown rate, and (3) experiments employing cyclic production/recharge.

Since the analysis was based on a uniform axial temperature distribution and saturated steam conditions, the analysis was not expected to predict the model reservoir behavior when cool water was recharged at the bottom. In that case a cool water zone developed in the lower section of the chimney which violated. the uniform temperature assumption.

The temperature non-uniformities due to the superheated zone at the top was accounted for using a simplified analysis. At the highest cooldown rates, indications are that the simplified approach may not be adequate. There is also a possibility that the computation of the rate of external heat transfer from the vessel based on the one-lump model is inadequate at the highest cooldown rates. A closer examination of the analytic techniques employed for the superheated zone and the one-lump treatment of the vessel may well show that more detailed modelling is required.

Since major improvements to the model require significant efforts and their inclusion would seriously increase the computation costs, it

is debatable whether such a task should be carried out. Modification of other existing more general codes developed for geothermal systems may be preferable.

The disagreement between prediction and experiment for the run with cyclic production/recharge is believed to be associated with the boundary parameters which were approximated by a series of step functions. These approximations may not adequately reflect the abrupt changes taking place, for example, in the steam production. It appears that this difficulty can be resolved by acquiring input data at more frequent intervals.

The excellent agreement between predicted and experimental transients in a majority of cases indicates consistency between measurements, system parameters, and the analysis. The transient analysis may therefore be applied to other similar systems with known parameters as long as the assumptions inherent in the analysis are not seriously violated.

One experiment was performed with cyclic steam production and continuous recharge of hot fluids having mean enthalpy of about 500 Btu/lb_m. With zero steam production, recharge of about 70 lb_m of fluids (corresponding to about 18 percent of the original in-place fluids) gave a chimney steam pressure rise of about 30 psi. The energy added to the system by the fluids recharge during the recharge period was used to heat, (1) the chimney rock, (2) the chimney liquid, and (3) the steel vessel. It is not unexpected, therefore, that the pressure rise was relatively moderate.

The pressure rise would increase with larger amounts of recharge and by recharge of higher enthalpy fluids. The amount of recharge is limited by the void space available in the chimney in the depleted state which for the present rock loadings was about 70 percent of the total void. The fluid enthalpy in a real size system is limited upwards to that of the fluids in the surrounding aquifer which probably will not

exceed 500 Btu/lb_m. It appears, therefore, that the energy that can be added by fluid recharge alone is not sufficient to make the recharge process a feasible and worthwhile operation for a real size system. It is possible, however, that in a real size system heat transfer from the surrounding rock may contribute somewhat to the "recharge process" over an extended period of time. This effect was not evaluated during the present investigation.

The predicted effective liquid level based on mass recharge/production data and saturated steam properties differed from the nominal liquid level based on liquid level measurements by as much as 5 percent of the rock matrix height. The estimated uncertainty intervals for the effective and nominal levels were 5. 7 and 5 percent. The agreement between the data shows that the mass recharge and production measurements and the geometry data used to compute the effective liquid level are consistent with the liquid level measurements.

The observed liquid expansion appeared to be caused by boiling in the interior of the liquid as a result of continuous lowering of the steam pressure. Boiling in the interior of the liquid appeared to be more predominant t'han evaporation at the liquid-.vapor interface. The results show that there is no distinct flash front in the chimney. However, there is a flash zone which extends from the liquid-vapor interface to the bottom of the chimney in cases without cool water recharge. It appears that there will also be a flash zone in a real system which extends from the liquid-vapor interface to some unknown depth. Its magnitude depends on the axial liquid temperature distribution which develop in the system and on the static head of the liquid.

Liquid expansion due to entrained vapor bubbles was not accounted for in predicting the! effective liquid level. Entrained vapor bubbles in the upper portion of the liquid only were neglected in computing the nominal level. The effective level is therefore expected to be lower

than the nominal for cases with hot water or no recharge when vapor bubbles occur throughout the liquid. On the other hand, with cool water recharge there are no vapor bubbles in the lower section with correspondingly reduced liquid expansion. This trend was observed in the data where the agreement between the effective and nominal liquid levels was generally better with recharge of cool water than with recharge of hot water or no'recharge.

The rock surface heat transfer coefficient evaluated from the temperature measurements for rocks in vapor environment was about 3 Btu/hr ft^2 ^oF which is three times the expected coefficient based on data for spheres. Reflux of condensed steam from the outlet line region, which subsequently evaporates, is believed to cause the increase in the heat transfer coefficient. Significant experimental uncertainties are associated with the heat transfer results. However, accurate heat transfer coefficients are not needed for a large rock since in that case the Biot number is also large such that 1/B approaches zero. The significance of this effect is that large rocks cool equally fast in liquid or vapor environments.

5.2 Extrapolation of Results

The analytic techniques and experimental results from the laboratory model are used to make predictions about a real size fracture-stimulated system. It is assumed that a fractured rock system having a total volume of 10^9 ft^3 has been generated and that several of the chimney model experimental parameters and conditions are applicable to the real size system. Thus, the average rock porosity may be assumed to be 0.35 equal to the porosity of the second rock loading. Also, the real size system may have initial pressure, end pressure, external heat transfer parameter, rock energy extraction fraction, and other conditions as given in Table 4.1 for run 26. A mean steam

production rate of 118,000 lb_m/hr may be assumed for the real size system (vs 23. 7 lb_m/hr for the laboratory model). The mass of fluid originally in the real size system was estimated to be $17 \cdot 10^9$ lb_m (vs **330** lb_m for the laboratory model).

The reservoir pressure depletion may be estimated using the P* - t* characteristic for run 26 given in Fig. 4. 37. The nondimensional time at the end state is seen from Fig. 4. 37 to be $t^*_e = 0.61$. From the definition of t* in Eq. **(4.**11a), the specified mean steam production rate. and the estimated in-place fluids the pressure depletion time is estimated to be t_e = 88,000 hr or about 10 years. The steam production rate characteristics may be assumed similar (but rates differing by a constant factor) for the real size and laboratory systems. In that case the P* - t* characteristic may also be used to determine the reservoir pressure at a given time or the time at which the pressure has reached a particular value. For example, it may be desirable to estimate the time when the reservoir pressure will reach 150 psia. From Fig. 4.37 a t* value of 0. **155** is read at P* = 150/582 = 0. 26. The time required to reach this pressure would be 2.6 years.

The magnitude of the rock/steam temperature difference at the end transient and its effect on the rock energy extraction fraction is also examined for various rock sizes. Rock sizes were estimated for the conditions of the real size system such that the estimated rock/steam temperature difference effect on the rock energy extraction fraction was 1, 2, 5, and 10 percent. The results given in Table 5. 1 show that effective rock energy extraction may be achieved for rock sizes on the order of 200 ft or more.

The largest rock size in a chimney created by nuclear explosives is on the order of 10 ft. It would therefore appear that extensive fracturing with explosive energy is not required for effective rock energy extraction. The use of hydraulic fracturing to create a series of large parallel fractures could prove to be a very effective stimulation technique.

TABLE 5.1

Estimated Effect of Rock Size on the Rock Energy Extraction Fraction for the Real Size System

Mean Rock Size d (ft)	Estimated Effect on η_e (percent)
72	1.0
102	2.0
161	5.0
227	10.0

The transient analysis developed for the chimney model in Chapter 3 was used to predict the pressure and temperature transients of the real size system considered previously. The analysis was carried out for the arbitrarily selected mean rock sizes of 26 ft and 105 ft to study the effect of the rock size on the pressure transient. The predicted pressure transients for these two cases are given in Fig. 5.1. The steam and mean rock temperature transients are given in Fig. 5.2.

It is noted from Fig. 5.1 that the reservoir steam pressure drops off more rapidly for the larger rock size. From Fig. 5.2, it is noted that the smaller rocks are nearly in thermal equilibrium with the steam for the entire transient. Relatively large rock/steam temperature differences are apparent with the larger rocks during the first part of the transient. A smaller amount of rock energy is therefore extracted with the larger rocks which results in lower reservoir pressures as noted in Fig. 5.1. The steam temperature transients in Fig. 5.2 show that the cooldown rate decreases with time because of the decreasing steam production rate characteristic assumed. The rock/steam temperature differences proportional to the cooldown rate are therefore

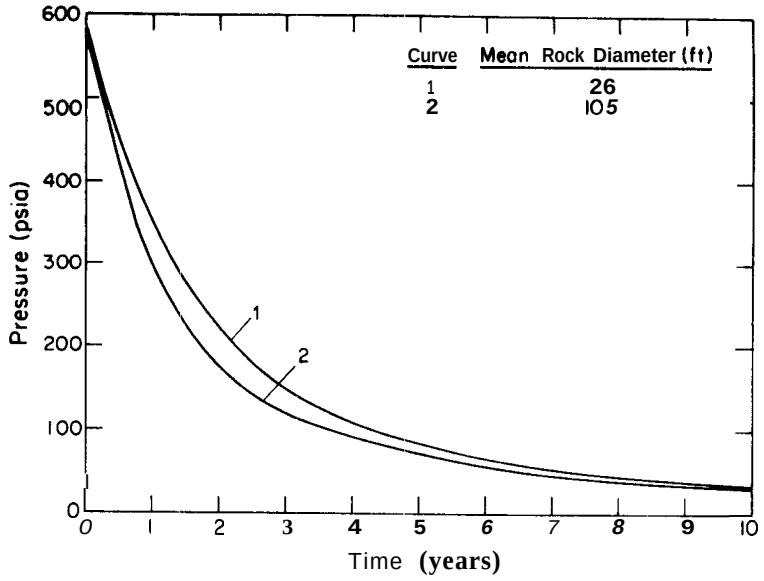

Figure 5. 1 Predicted Pressure Transients for the Real Size System with Two Different Rock Sizes

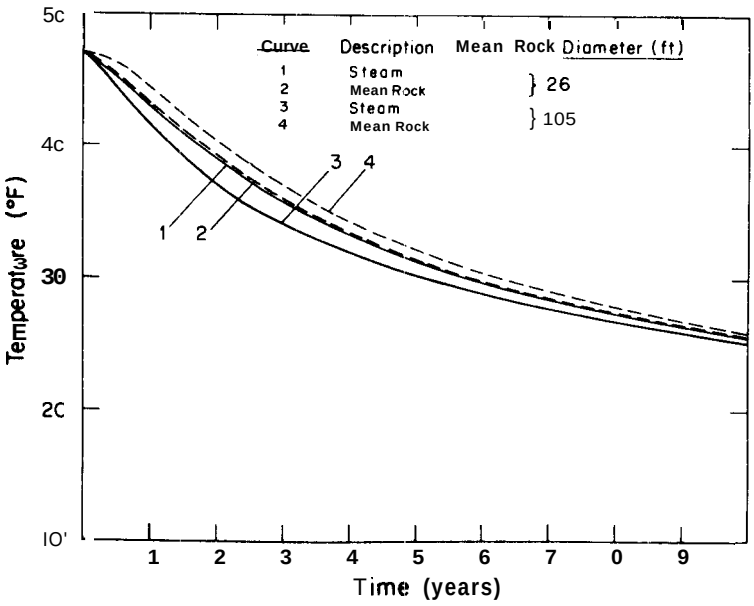

Figure 5. 2 Predicted Steam and Rock Temperature Transients for the Real Size System with Two Different Rock Sizes

lower towards the end of the transient. Consequently, the pressure transients in Fig, 5. 1 are seen to approach each other at large times.

This analysis shows that the effect of the rock size is not significant if steam production from the system is continued for about 10 years which gives a mean cooldown rate of 0. 0026 ^{o}F/hr. However, the effect of rock size is greater if steam production is discontinued earlier such that a higher mean cooldown rate results. For example, the data in Fig. 5. 1 show that at a time of 2 years the steam pressure would be about 220 psia for the smaller rock vs about 170 psia for the larger rock. The mean cooldown rate in the time period to 2 years was about twice (0. 0057 ^{o}F/hr) that for a 10 year depletion time. It is apparent, therefore, that the extent of fracturing and rock size required to achieve a desired degree of rock energy extraction depends to a large extent on the requirements of the application,

The validity of applying the transient analysis to the real size system depends largely on how the axial temperature distribution develops in this system as compared to that in the laboratory model. Whereas boiling occurred throughout the liquid zone in the laboratory model, this is not likely in the real size system because of the much higher liquid static heads. However, a fairly uniform axial temperature distribution in the liquid is likely because of natural circulation in a high permeability systern. In that case the transient analysis should give adequate performance estimates for real size systems.

5. 3 Experimental Techniques

The results show that the wall effect, represented by q_m, can be determined relatively accurately from calibration experiments and analyses. However, the rnagnitude of the wall effect was difficult to control. Improvements in the tape heater power controls such that a specific value of q_m may be preselected are therefore desirable. An

automatic control system employing the measured wall to steam temperature difference as the input signal appears feasible. The uncertainty interval for q_m may be reduced by acquiring insulation that can readily be removed and replaced without physical damage occurring to the insulation. Repeated calibration tests at various operating conditions would also be useful to determine the wall effect with greater precision.

The mass of fluids recharged and produced were determined by a head tank level measurement and by a gravimetric measurement. Improvements in the recharge system to reduce the uncertainty interval for the mass recharged are desirable. Possible improvements include the use of gravimetric measurement instead of the level measurement. Automatic control systems for the fluid recharge and production systems such that preselected production and recharge rate characteristics may be obtained would greatly enhance the usefulness of the system. The chimney steam pressure measurement instrumentation employed during the present test series is considered adequate at most operating conditions. However, at low pressures the relative uncertainties in the pressure measurements are higher than desired. Substantial improvements in the instrumentation in the low pressure range do not appear justified at this time.

At times minor operational difficulties were experienced with certain hardware components. The O-ring used for sealing the quick opening head at the top failed several times during the initial testing. Improved O-rings partially eliminated the problem, but for safety reasons it was necessary to operate the system at slightly derated maximum conditions. Whereas, the system design condition was 800 psig at 500 ^{o}F, most experiments were initiated at pressures of about 575 psig and temperatures of about 480 ^{o}F.

Operational difficulties were also experienced with the high pressure seal in the circulation pump. Silica in the fluids tended to deposit

on the seal and leaks developed such that system shut down was necessary immediately. To reduce this problem, frequent disassembly and cleaning of the seal was required. Operational difficulties experienced with the positive displacement injection pump were caused by fouling of the pump suction and discharge values. Frequent disassembly and cleaning of the valves eliminated the problem.

CHAPTER 6

CONCLUSIONS AND RECOMMENDATIONS

6. 1 Conclusions

1. Results show that therrnal energy stored in fractured rock can be extracted effectively by reducing system pressure by steam production to allow boiling to take place within the rock matrix. The range of the rock energy extraction fraction was 0. 75 to 1. 18 indicating that 75 percent or more of the thermal energy stored in the rock between the defined temperature limits of the experiments was extracted. Parameters found to affect the rock energy extraction fraction were, (1) the position of the liquid level, (2) reflux of condensed steam, (3) the recharge of cool water, and (4) rock/steam temperature differences which depended on rock size and cooldown rate.

2. Recovery of energy from the high permeability fractured rock systems tested increased by factors of 1. 25 to 2. 57 over that achieved with flashing the in-place fluid alone. The improved recovery was achieved by creating non-isothermal conditions by pressure reduction and in-place boiling. Several parameters such as, (1) external heat transfer parameter, (2) rock porosity, (3) rock energy extraction fraction, (4) initial pressure, and (5) recharge of high enthalpy fluid affected the recovery factor. These parameters are also expected to affect the recovery factor in a real size, high permeability system.

3. Comparison of predicted and measured rock/steam temperature differences for the instrumented rocks shows that these were generally within rneasurement accuracy. Since the

uncertainty intervals for both experimental and predicted rock/steam temperature differences are quite large, it was not possible to resolve completely the question of which geometry approximation (sphere or plate) was the most appropriate for these rocks. Improvements in the experimental techniques and in the thermal property data used for the prediction are required.

4. Comparison of predicted fractions produced based on mass-energy balances to experimental fractions produced shows that the experimental results can be predicted for a wide range of conditions excluding experiments with cool water recharge. In cases with significant recharge of cool water, non-uniformities in the axial. temperature distribution resulted which violated the basic assumption in the analysis. The mass-energy balance analysis could not therefore predict the performance of such systems. Improvements in the analysis to remove the uniform axial temperature assumption appears feasible.

5. The transient analysis was used to predict the chimney behavior for a wide range of conditions. Results show that the analysis predicted the observed behavior closely in most cases. However, the model could not predict the performance with cool water recharge because a subcooled liquid zone developed at the bottom which seriously violated the uniform axial temperature assumption inherent in the analysis. Improvements to the model to obtain a more versatile analysis appear feasible.

6. The results from the cyclic steam production and continuous recharge experiment show that only a moderate pressure rise was achieved during the recharge process. The feasibility of recharging a real system by fluid recharge alone to achieve

useful pressure and temperature increases is considered questionalsle. The reason is that the energy added to the system by fluid recharge alone is insufficient to heat the reservoir rock and the cool reservoir fluids to an adequate degree. It appears, however, that in a real size system heat transfer from the surrounding rock may contribute somewhat to the recharge process particularly if relatively large recharge times are involved.

7. There does not appear to be a distinct flash front near the liquid-vapor interface in the chimney model. Evaporation and vapor bubble formation occurred in the interior of the liquid with a flash zone that extended from the liquid-vapor interface to the bottom of the chimney in the absence of cool water recharge. It is anticipated that a flash zone will extend to some depth in a real size system determined by the liquid static head and the axial liquid temperature distribution which develop.

8. Scaling of the model rock heat transfer behavior to a particular real size system indicates that the energy extraction fraction does not depend significantly on the rock size. The analysis shows that the rock energy extraction fraction is reduced by only 10 percent for rock sizes up to about 200 ft. The degree of energy extraction depends on the cooldown rate and the steam production rate characteristic assumed for the real size system,

9. Practical and economic aspects of artificial geothermal resource stimulation and in-place flashing were not evaluated. Although, improved geothermal energy recovery from fractured systems by in-place flashing appears promising, field experience is required to establish its feasibility.

6.2 Recommendations

The following broad recommendations for further work are offered:

1. It is recommended that the rock thermal transient analysis for the rock/steam temperature difference for a rock of arbitrary shape be developed further. Improved rock/steam temperature measurements or different measurement techniques should be developed. Better rock thermal property and heat transfer coefficient data should be obtained to verify the analysis.
2. It is recommended that improvements in the mass-energy balance analysis be made such that the effect of cool water recharge can be predicted adequately. Also, methods to adequately account for varying production and recharge fluid enthalpies should be included in the analysis.
3. It is recommended that the costs vs benefits of significant improvements to the present transient analysis be investigated. The feasibility of utilizing more general codes being developed for the geothermal industry should be considered as an alternative to improving the present analysis.
4. A few improvements in the present chimney model system hardware should be considered. These include the installation of a control system for power control of the chimney tape heaters and the use of replaceable insulation on the chimney. Considerations should also be given to replacing the present fluid production and fluid recharge measurement systems with semi-automatic systems such that better measurement accuracy and preselected recharge and production characteristics may be achieved.
5. Additional tests to investigate the effectiveness of other rock energy extraction schemes and the reservoir characteristics

of other reservoir types are recommended. The near term effort with the second rock loading should concentrate on energy extraction from a compressed liquid reservoir with cool water recharge. Subsequent tests are recommended with steam production from an initially compressed liquid reservoir which later becomes saturated. The behavior of a reservoir consisting of superheated vapor with a small amount of subcooled liquid at the bottom should also be investigated.

6. Further testing to investigate energy extraction from low porosity, low permeability systems is recommended. As a first step in this effort, it is recommended that the void spaces in the second rock loading be filled with coarse sand which should give porosities of about 20 percent and a finite permeability. Subsequent tests with rock segments containing artificial fractures are recommended,

7. Tests with a rock loading consisting of the rock obtained from the underground Piledriver chimney are recommended. Particular emphasis should be placed on radiological and water quality aspects.

APPENDIX A

DESCRIPTION OF TEST APPARATUS

A. 1 Chimney Model System

Details of the chimney model system are described here to supplement the summary description given in Chapter 2. The chimney model is located in the Lloyd Noble Laboratory of Petroleum Engineering at Stanford University, California. The piping and instrumentation diagram of the system is given in Fig. A. l, Figure A. 2 is a photograph showing a side view of the chimney model system, while Fig. A. *3* pictures the vessel and its support structure,,

The system is constiructed primarily from low carbon steel and is designed to ASME standards. A safety relief system is installed to vent the high pressure fluid to the atmosp'here in case of accidental over-pressurization, A manually operated blowdown system is also available.

The system operates in two primary modes. The initial reservoir temperature and pressure conditions are established in the "heating mode" shown in Fig. 2. 1. The experiments are conducted in the "fluid production mode" shown in Fig. 2. 2. These operating modes were described in Chapter 2.

A. 1. 1 Chimney Model

The pressure vessel is 2 feet I. D. and approximately 5 feet high. The lower head is connected to the vessel shell by standard bolted flanges while the tap closure is a "quick opening" head. The vessel shell has several penetrations for temperature and pressure measurement instrumentation entry. A sight glass is installed on the vessel to observe water level movements.

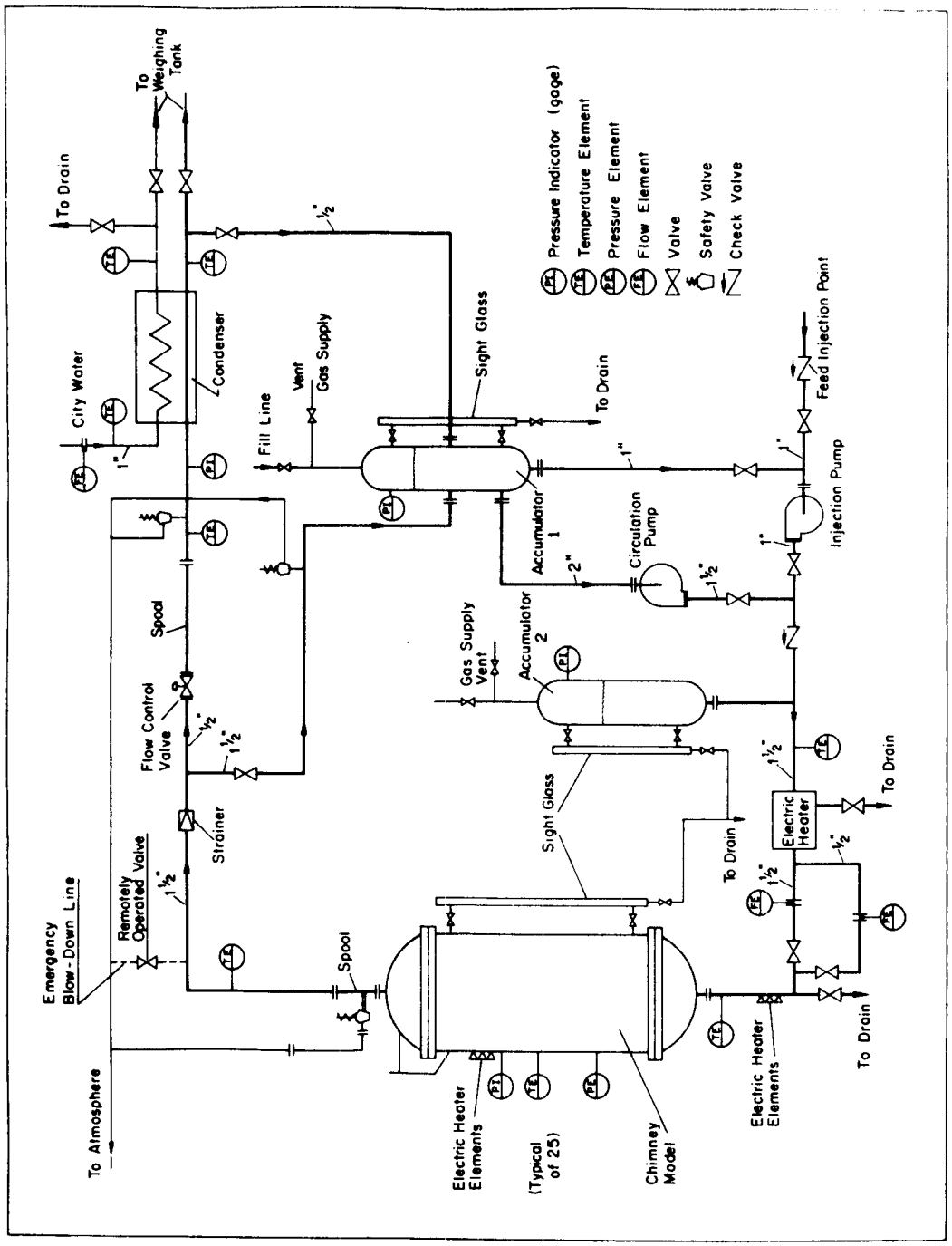

Figure A.1 Piping and Instrumentation Diagram for Chimney Model System

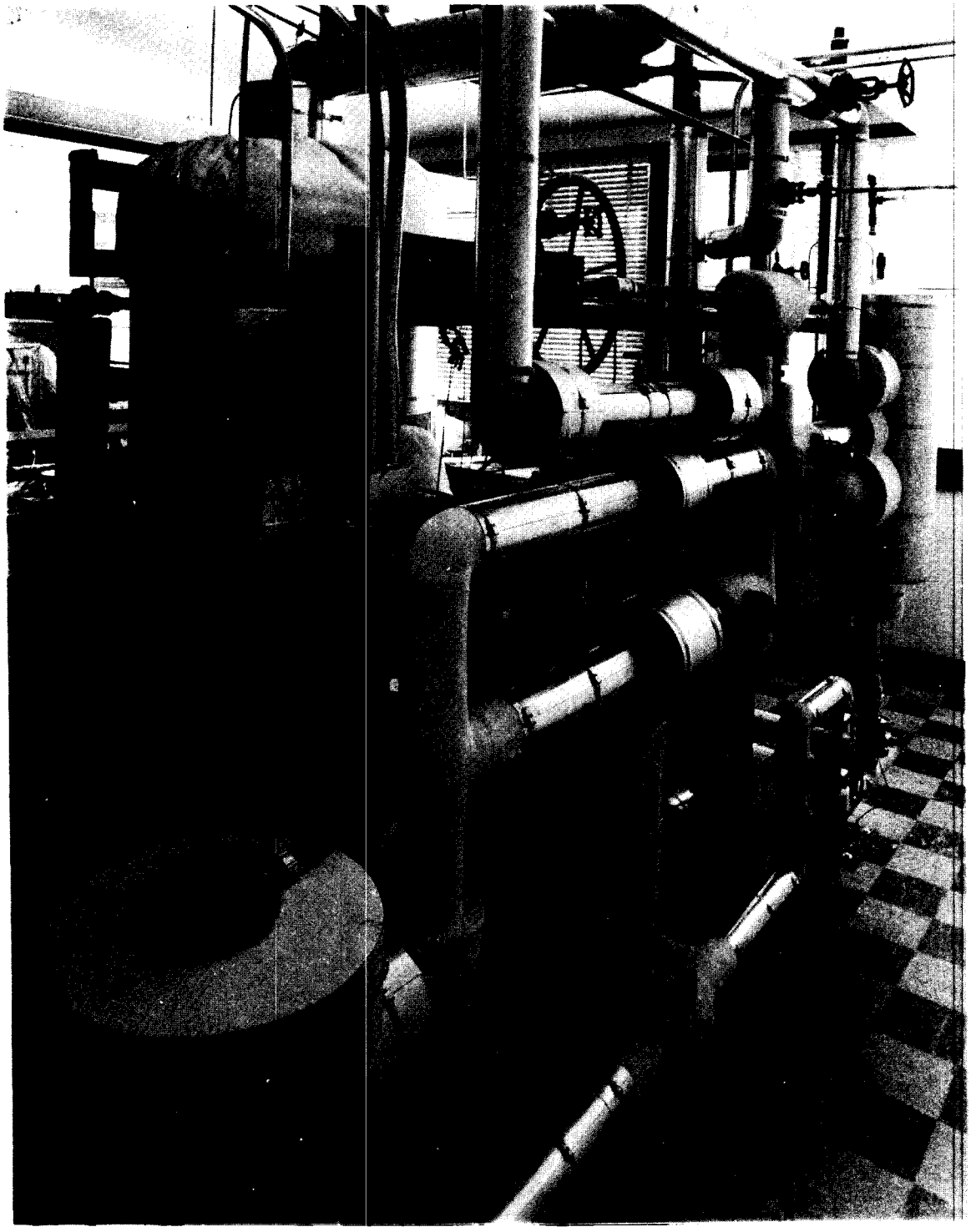

Figure A.2 Chimney Model System

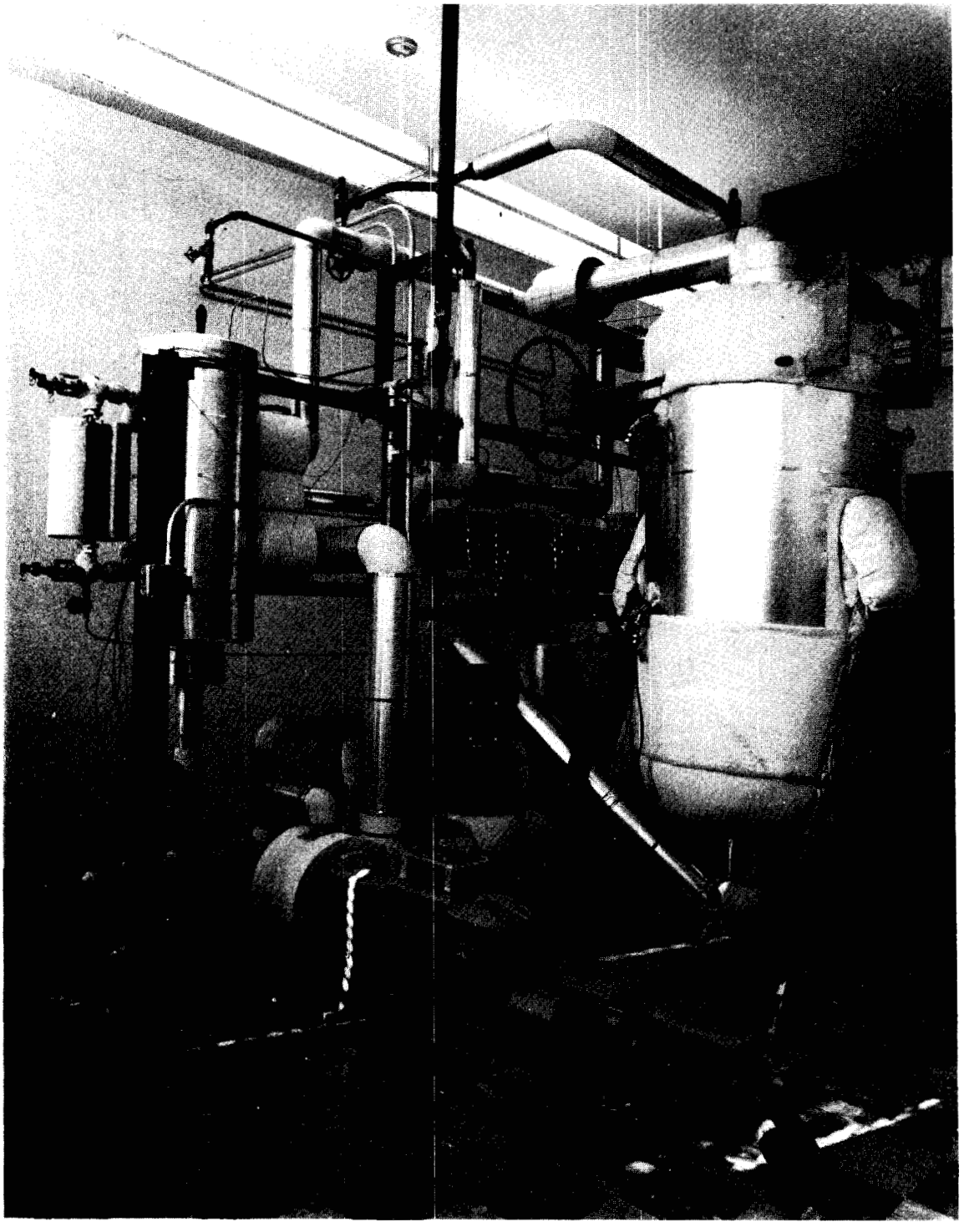

Figure A.3 Chimney and Support Structure

The vessel is supported on a horizontal axis through its approximate center of gravity by brackets. These allow the vessel to be rotated 90 degrees from a vertical position to a horizontal position after inlet and outlet piping, instrumentation, and other connections are disconnected from the vessel. This provides ready access to the lower section of the vessel during rock loading. The vessel shell has tape heaters wrapped around the outside diameter with heating power control sufficient to compensate for heat losses, or to supply energy to the water/rock system at a desired rate. The vessel is well insulated to reduce heat losses,

To assure uniform flow distribution,, a baffle is installed at the lower end of the vessel (inlet). A diagram of this flow distribution baffle arrangement is shown in Fig. A. 4. A photograph of the low side of the baffle prior to installation is shown in Fig. A. 5.

A. 1.2 Auxiliary Cornponents

A 23 KW electric heater in the circulation piping supplies the thermal energy necessary to establish the initial temperature and pressure conditions in the chimney. It is also used to preheat the recharge water to desired temperature conditions. The circulation heater, prior to installation of electrical supplies and insulation, is shown in Fig. A. 6. The heater is controlled by an on/off thermostat during heatup operation, but an automatic: power control system is used to regulate the degree of preheating of the recharge water. The control system may be set to provide recharge water with either approximately constant, linearly decreasing, or linearly increasing enthalpy as a function of time.

A 15 gpm centrifugal pump provides 9 feet head for the circulation flow. A view of this pump prior to installation of insulation is shown in Fig. A. 7. The pump housing and parts in contact with water are made

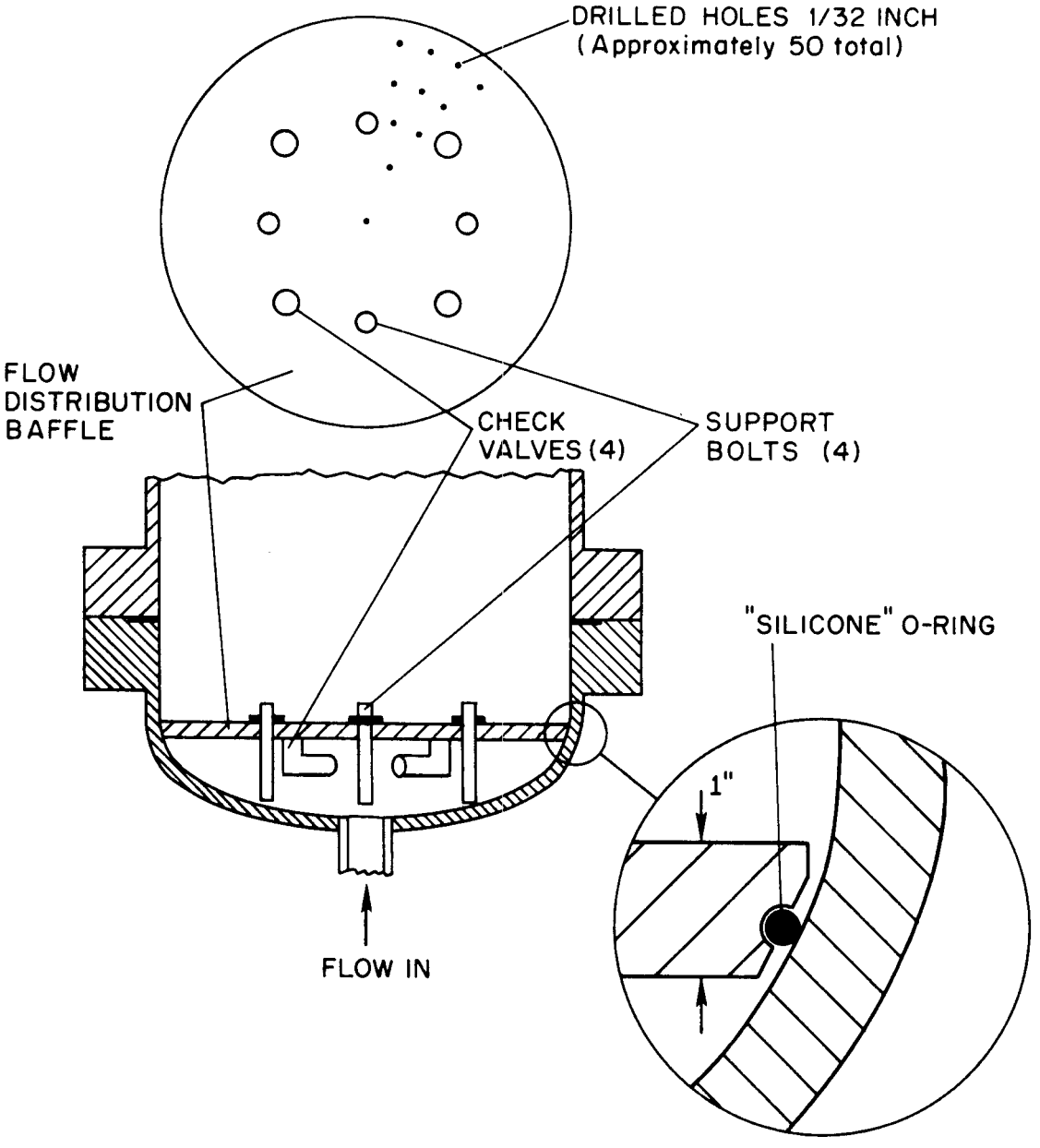

Figure A. 4 Flow Distribution Baffle Arrangement

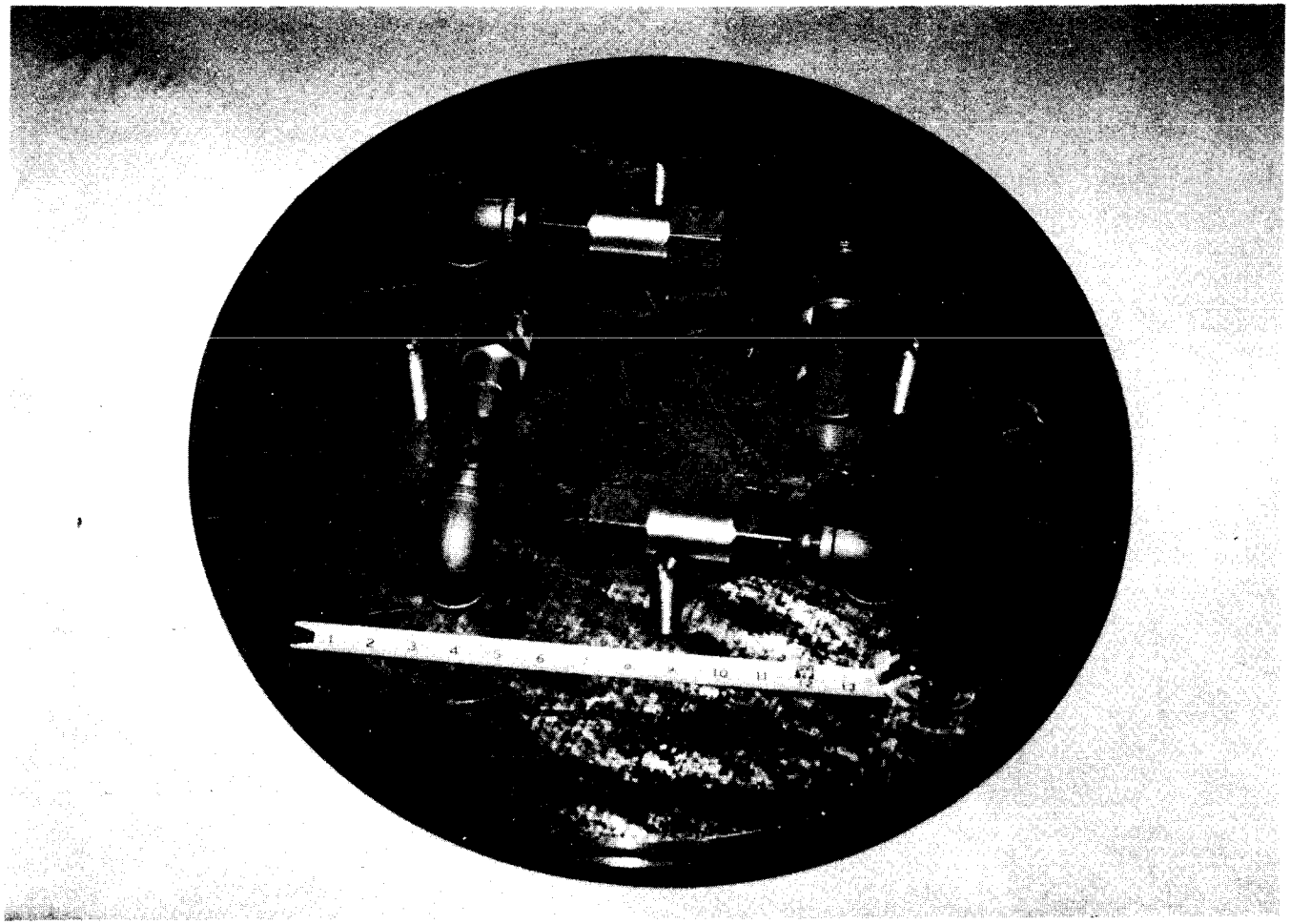

Figure A. 5 Low Side of Flow Distribution Baffle

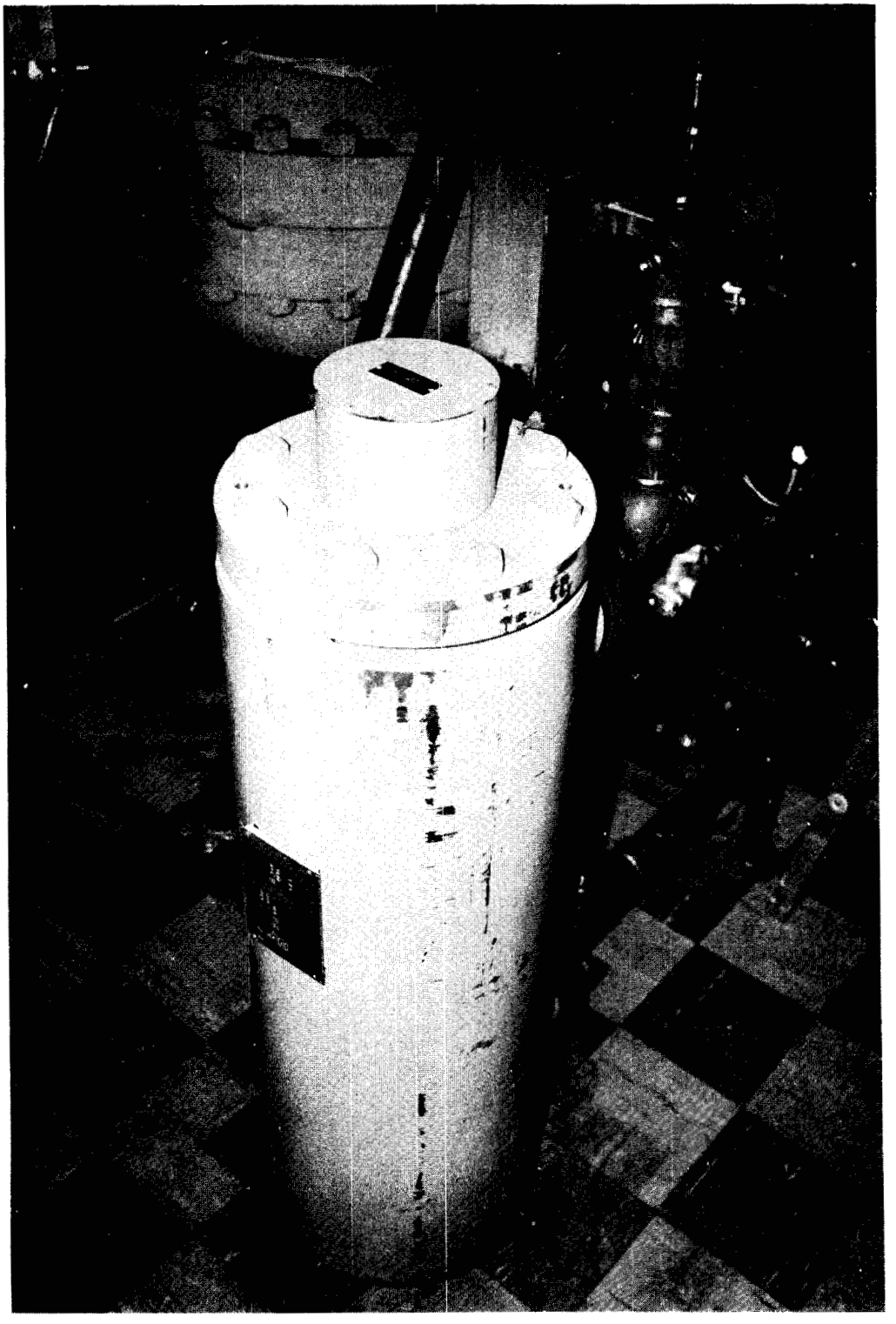

Figure A. 6 Side View of Chimney Model System with the Electric Circulation Heater in the Foreground Prior to Installation of Insulation

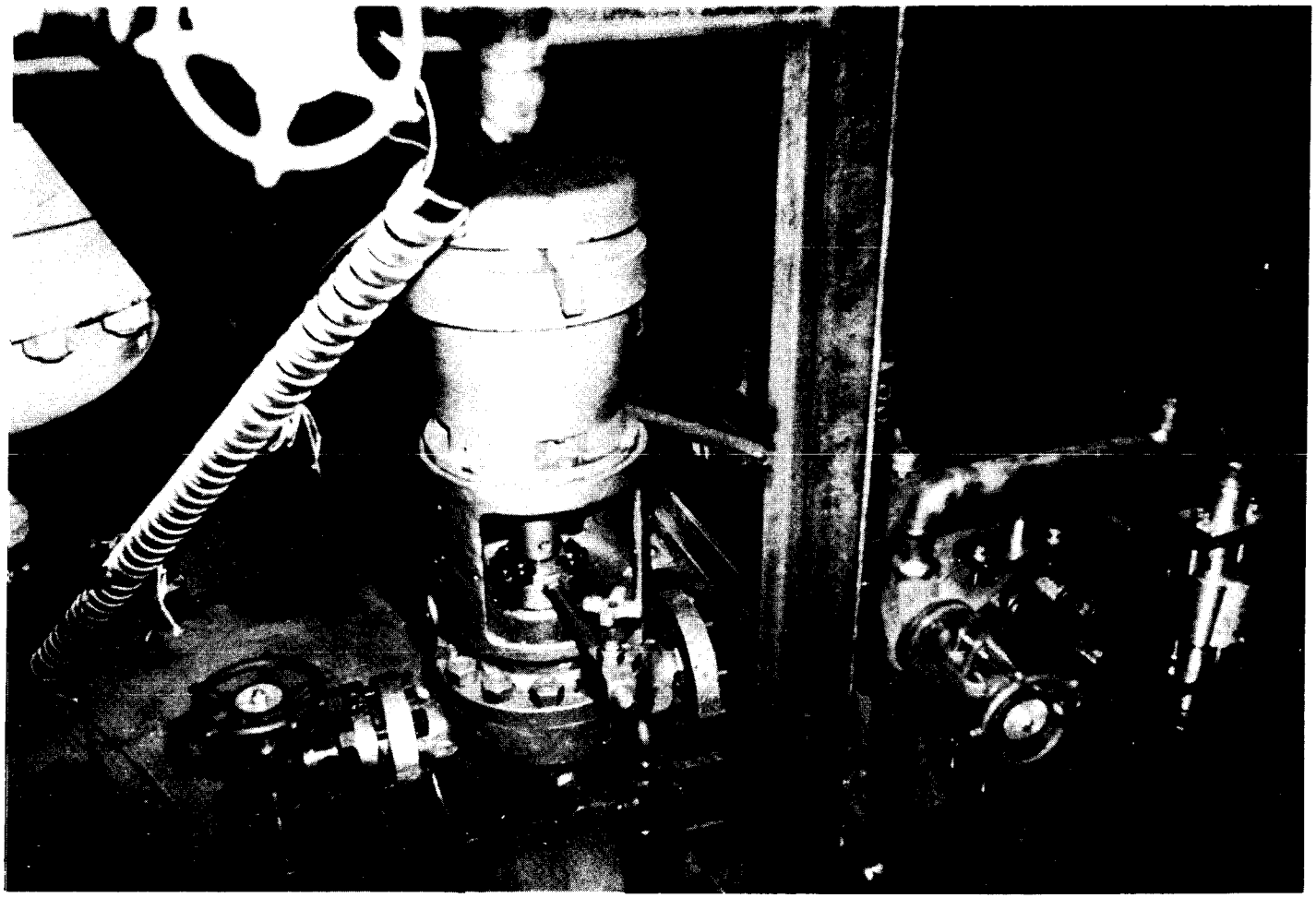

Figure A.7 Circulation Pump Prior to Installation of Insulation

from stainless steel. The 1 gpm injection pump used to recharge the chimney is a positive displacement pump delivering a maximum head of 800 psi. The injection pump is shown as the component in the foreground in Fig. **A. 3** and in the background in Fig. **A.** 7. The flow rate can be controlled continuously by adjustment of the piston displacement in the range 0-1 gpm. Parts in contact with water are made from stainless steel.

The circulation loop is constructed from schedule 80 low carbon steel piping (sizes 1/2, 1, 1-1/2, and 2 inch), Except for connections to chimney, pumps, electric heater and various other components, the piping is all welded (140 high pressure welds). The system can be emptied at two low points by the drain valves which release approximately 99 percent of the system fluids. The piping system and components are well insulated to reduce heat losses.

A. 2 Instrumentation

The parameters and conditions measured during operation of the system are summarized in Table 2. 2. The locations of the loop pressure, temperature and flow measurement sensors are indicated in Figs. **A.** 1, 2. 1 and 2.2. Pressure indicators (gages) are installed according to ASME code requirements. Sensors used for acquiring experimental data are discussed. individually in the following.

A. 2. 1 Temperature and Pressure Measurements

The thermocouples used for loop temperature measurements are 1/8 inch diameter stainless steel sheathed (grounded) iron/constantan thermocouples (type J). The positions of the thermocouples used to measure the chimney steam, rock and metal temperature conditions are shown in Figs. 2. 8 through 2. 10. The thermocouples used for

steam and rock temperature measurement are similar to the above except they are 1/16 inch diameter.

All chiimney thermocouples are inserted through the vessel wall by Conax high pressure fittings. The metal temperatures are measured using unsheathed thermocouples (type J) cemented to the outside metal surface with high temperature cement. All thermocouple measurements are recorded on multipoint recorders. The loop metal temperatures are measured at accumulators 1 and 2. The pressure in the chimney is measured with an electronic pressure transmitter employing a Bourdon-tube as the primary sensing element. Since the chimney pressure measurement is essential to these experiments, a redundant pressure measurement was provided by a 1/4 percent accuracy test gage.

A. 2. 2 Flow Measurements

The circulation flow rate during heatup is measured using a 0. 945 inch diameter orifice installed in the 1-1/2 inch line. * The measured pressure difference signal from the electronic differential pressure transmitter is fed to the multi-point recorders. The recharge flow was originally measured using a 0. 357 inch diameter orifice installed in the 1/2 inch line, but this arrangement proved to be unreliable. The recharge flow rate was therefore computed from injection head tank water level rneasurements as a function of time.

The condenser cooling water flow rate is measured using a 0. 540 inch dimater orifice installed in the 1 inch water line, The recording of this measurement is the same as for the circulation flow measurement. The produced fluid is weighed in the collection tank as a function of time. Since evaporation from the approximately 70 ^{o}F temperature liquid in the collection tank is negligible, the steam production rate is computed directly from the liquid mass measurements.

---

* Flow sections with flange taps were used for the orifice installations.

APPENDIX B

ROCK CHARACTERIZATION

B. 1 Statistical Analysis of Rocks

To compare results from the chimney model experiments, some uniform description or measurement of the rock geometries is needed. These data are also required to extrapolate the experimental rock thermal behavior to real size fracture-stimulated systems. The rock characteristics that appear to be significant were discussed in Chapter 2. The linear dimensions illustrated in the upper portion of Fig. 2. 3, the mass, and the rock density were used to calculate the shape factors discussed in Chapter 2. Details of the sampling techniques, the statistical analysis, and the results are given in the following,

B. 1. 1 Sampling Techniques and Statistics

A major object of any statistical sampling procedure is to obtain a representative or random sample of the population such that reliable statistical information are obtained. The sampling techniques used for this study include:

1. The selection of a large sample with no particular precautions taken to assure randomness.
2. Point counting, a method involving a relatively small sample where particular emphasis is on assuring randomness.

The point counting method involved spreading the rock on a plane surface. Rocks immediately under the grid points of a square grid placed over the rock population were selected for the sample.

The first method was time consuming because a large number of rocks had to be measured. Since smaller samples are required with the point counting method, it is less time consuming although more effort is required in the sampling itself. For comparison, both methods

were used for the first rock loading, but only the second method was used for the second rock loading. Each sample was numbered for later reference. These reference numbers and the number of rocks in each sample are given in Table B. 1.

TABLE B. 1

Sample Number	Rock Loading	Sampling Technique	Number of Rocks in Sample
1-1*	1	1	1978
1-2	1	2	168
2-2	2	2	156

*First number refers to rock loading and the second give the sampling technique.

The cumulative distribution functions and the probability density functions were computed for each of the original measurements and for the derived parameters, such as those given by Eqs. (2. la) through (2. lc). Initially all distributions were plotted using linear scale along the abscissa. Since particle size distributions resulting from grinding or crushing processes are often found to approach lognormal distributions, the data were also plotted on semilog paper with the logarithmic scale along the abscissa. The mean, variance, and standard deviation were computed for each parameter from the formulas,

$$\text{mean} \qquad \bar{x} \triangleq \frac{1}{n}\sum_{i=1}^{n} x_i , \tag{B. la}$$

$$\text{variance} \qquad s^2 \triangleq \frac{1}{n-1}\sum_{i=1}^{n} (x_i - \bar{x})^2 , \tag{B. lb}$$

and

$$\text{standard deviation} \qquad \sigma = (s^2)^{1/2} \tag{B.lc}$$

B. 1. 2 Analysis and Results

The cumulative distribution and probability density functions are shown in Figs. B. 1 through B. 9 for sample 1-1 using linear scales along the abscissas. The mean arid standard deviations for each parameter are listed in the figures. The units of $\bar{x}$ and σ are the same as for the parameter shown along the abscissa.

The probability density functions of Figs. B. 1 through B. 6 for a, b, c, M_r, d, and A, show that when linear abscissas are used these parameters are not normal on the low side, but they are fairly normal on the high side. It is apparent that there is a higher probability of encountering rocks with very small dimensions than very large. The probability density distribution for rock mass given in Fig. B. 4 is seen to be severely skewed.

A detailed study of these figures indicates that a rock with one relatively small dimension has two other dimensions of the same order. Additionally, a rock with one dimension near the mean has two other measurements which are substantially different from the mean. The distribution functions for the b/a and c/a ratios and for the sphericity parameter ψ are shown in Figs, B. 7 through B. 9. In contrast to the previous dimensional parameters,, the distributions for these dimensionless parameters approach the normal,

The results of the statistical analysis for the small second sample of the first rock loading (sample 1.-2) showed trends that resembled the results for the first sample (sample 1-1). As an example, a comparison:: of the probability density and cumulative distribution functions for the equivalent diameter derived from samples 1-1 and 1-2 is given in Fig. B. 10. It is observed that there are some differences between the

---

Use of normalized abscissa was required because the range of the equivalent diameters for the two samples were not identical. The normalized variable is the equivalent diameter divided by its range.

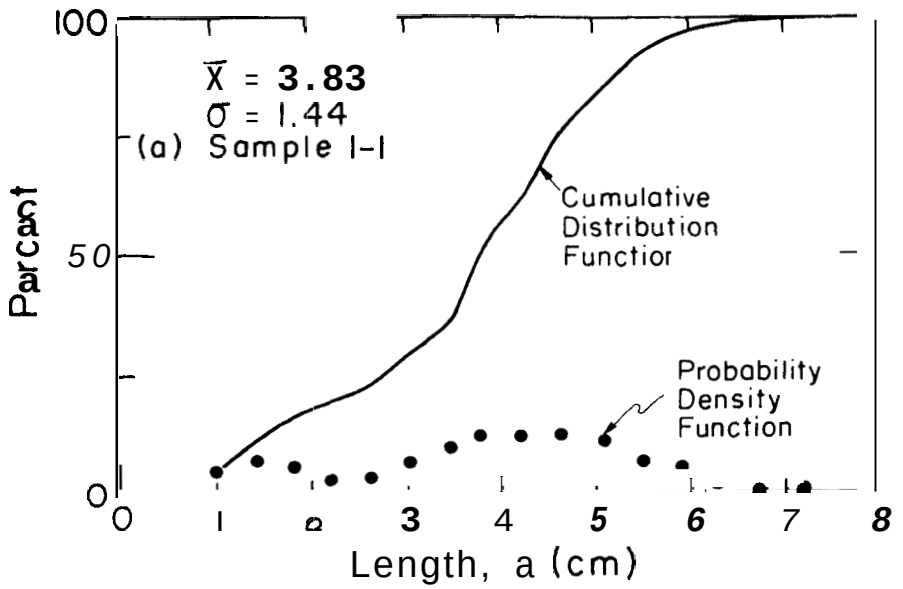

Figure B. 1 Cumulative Distribution and Probability Density Functions for **Rock** Length Dimension

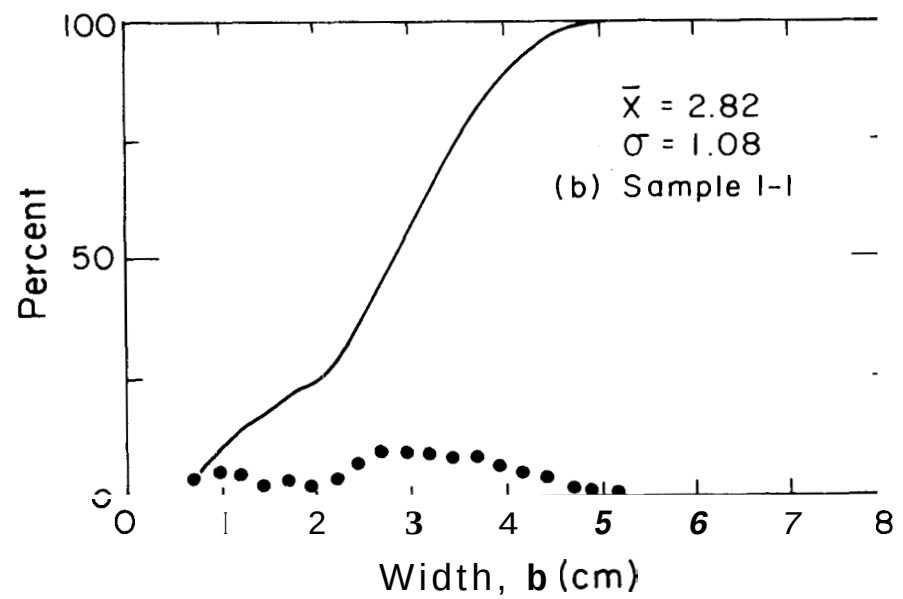

Figure B. 2 Cumulative Distribution and Probability Density Functions for **Rock** Breadth Dimension

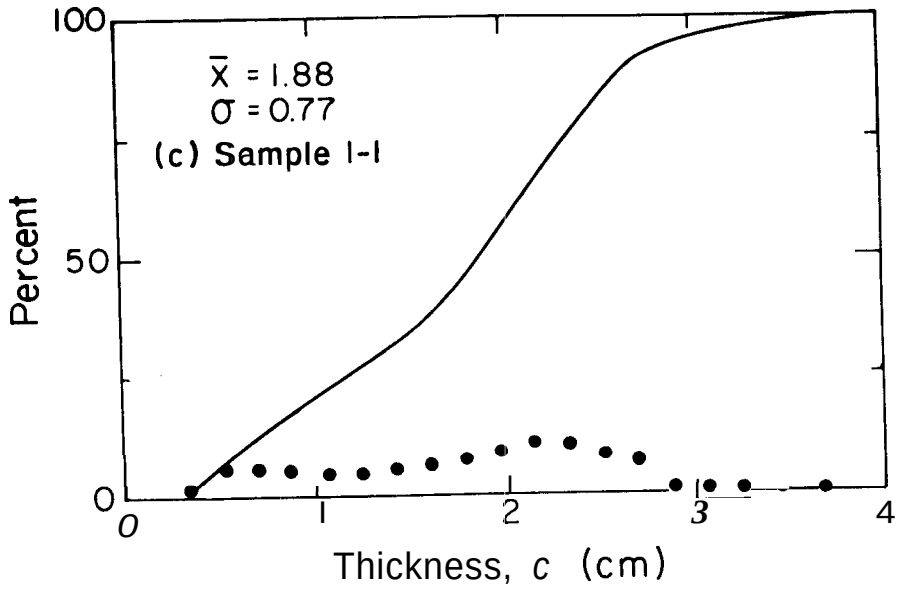

Figure E. 3 Cumulative Distribution and Probability Density Functions for Rock Tnickness Dimension

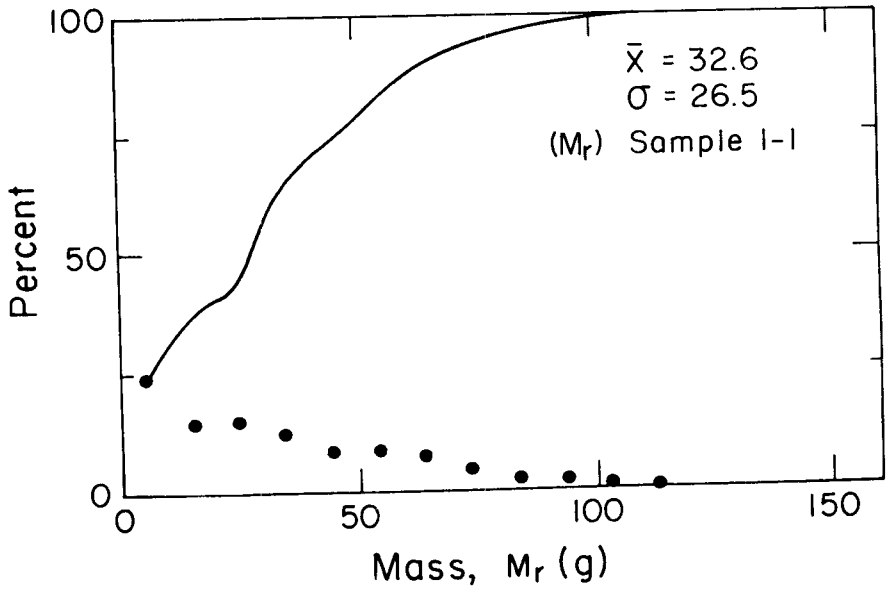

Figure B. 4 Curnulativc Distribution and Probability Density Functions for Rock Mass

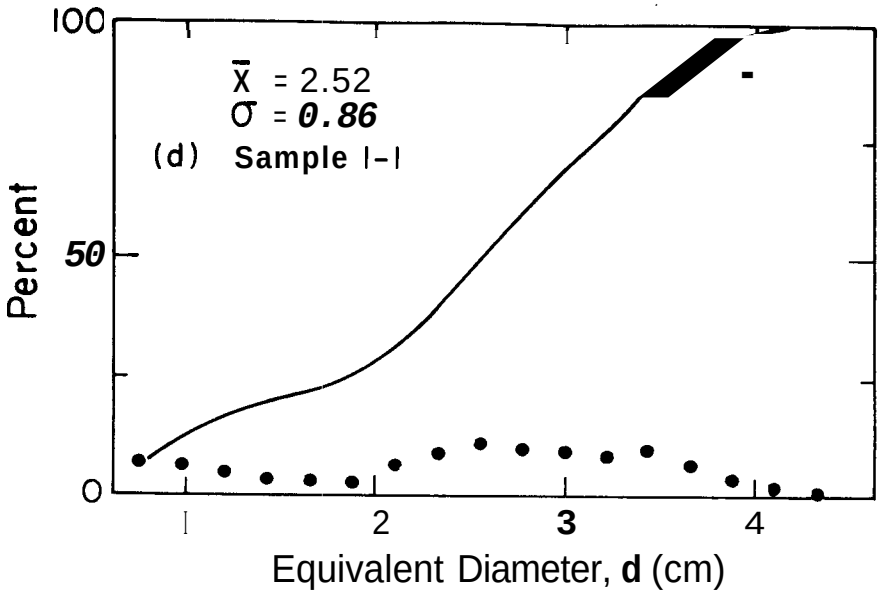

Figure B. 5 Cumulative Distribution and Probability Density Functions for Rock Equivalent Diameter

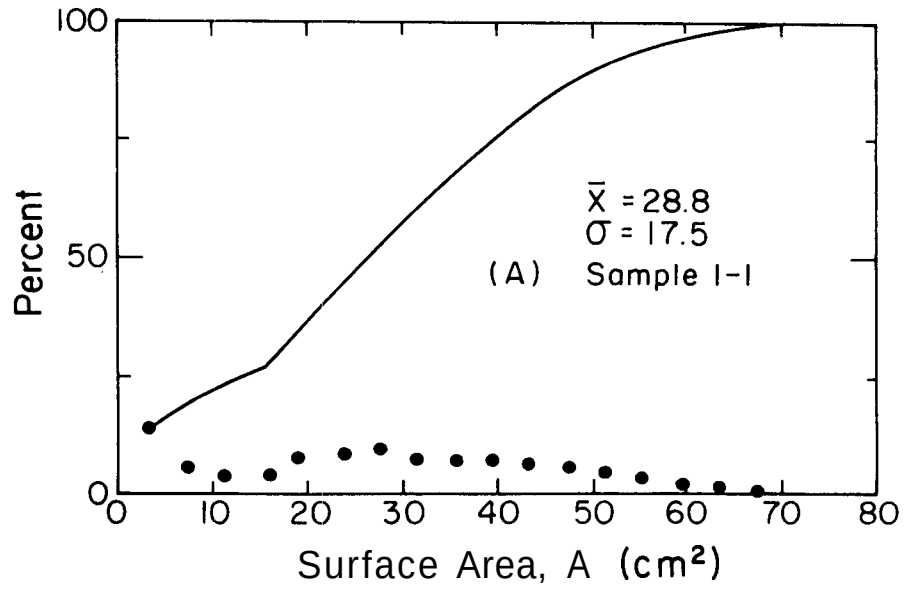

Figure 5.6 Cumulative Distribution and Probability Density Functions for Rock Area

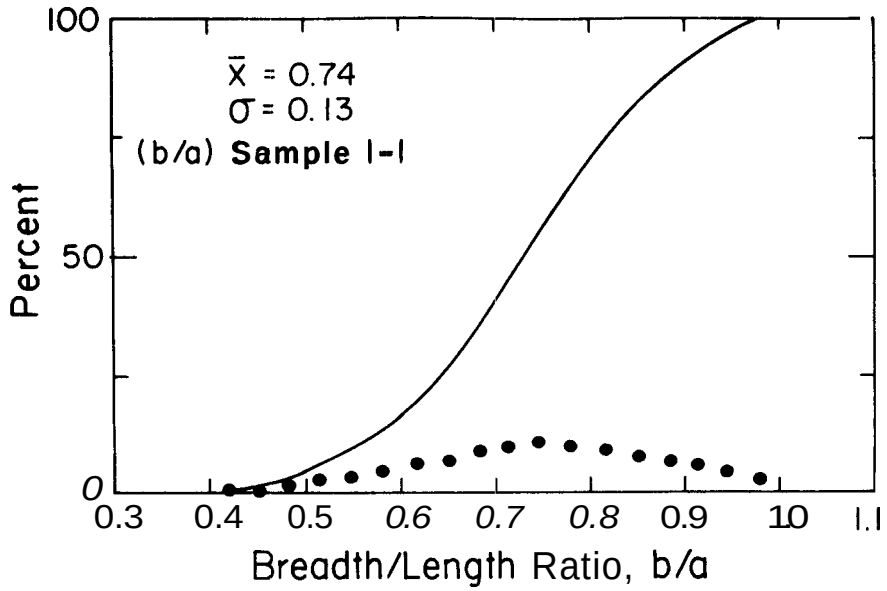

Figure B. 7 Cumulative Distribution and Probability Density Functions for Breadth/Length Ratio

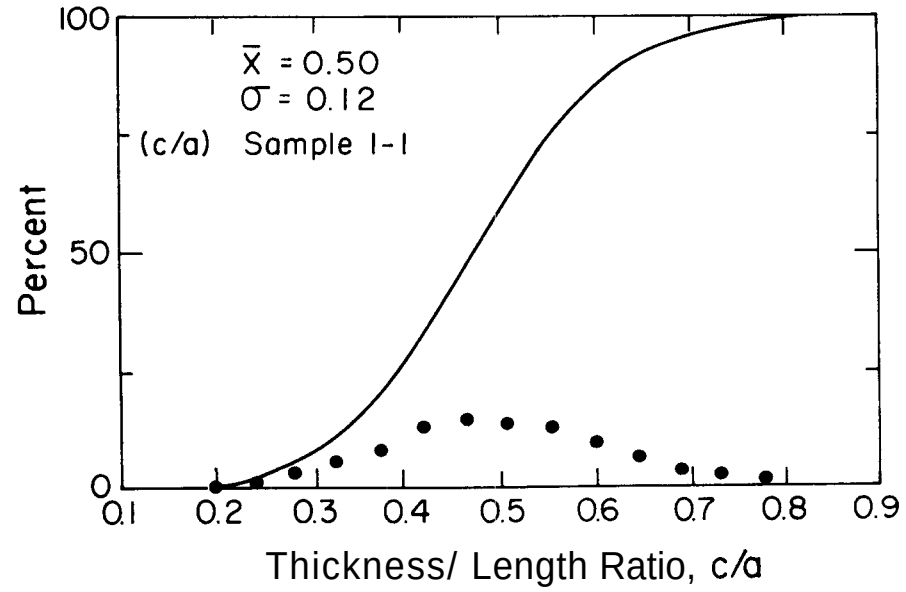

Figure B. 8 Cumulative Distribution and Probability Density Functions for Thickness/Length Ratio

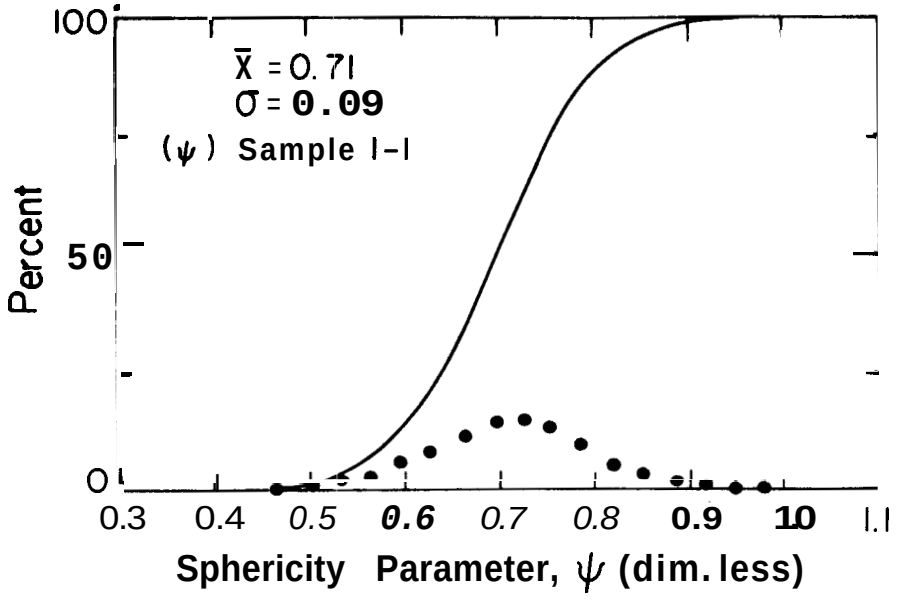

Figure B. 9 Cumulative Distribution and Probability Density Functions for Sphericity Parameter

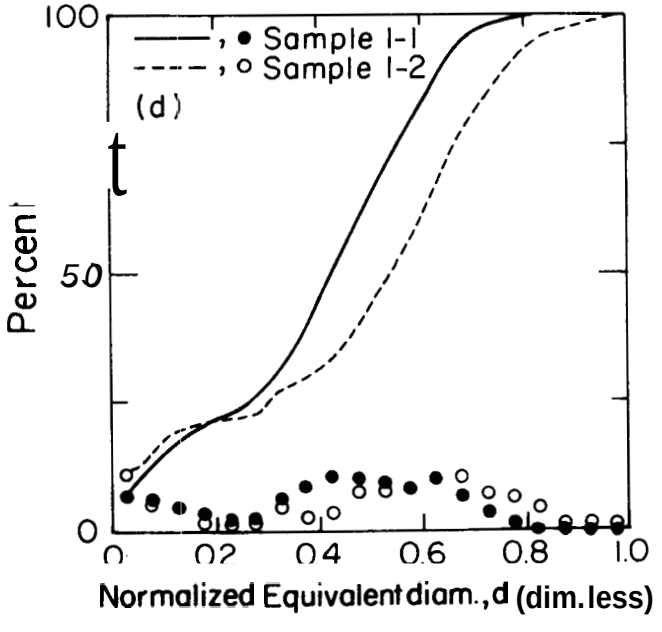

Figure B. 10 Comparison of Distribution Functions Derived from Samples 1-1 and 1-2

distribution functions derived from the two samples. However, it was found that the means, which are of major interest in this study, did not differ much for the two samples as is indicated in Table B. 2. Since the second sampling method (point counting) is the fastest, it was used for the second rock loading.

The distribution functions for the linear length dimensions and the mass for sample 1-1 were also plotted on semilog paper as shown in Figs. B. 11 through B. 14. It is seen that these distributions approach the lognormal.

The results of the statistical analysis of sample 2-2 for the mass and the linear length dimensions are shown in Figs. B. 15 through B. 18 on semilog paper. It is seen that none of these distributions appear to approach the lognormal. The explanation for the indicated behavior appears to be that the second rock loading was not a random population.

B. 2 Bulk Parameters

The term "bulk parameters" refers to such parameters as total rock mass, mean solid rock density, void volume, drainage porosity, and permeability of the rock loading. The volume of rock with associated void space is referred to as the rock matrix. The rock matrix extends from the flow distribution baffle as the bottom to the flange face at the top of the chimney (see Fig. 2. 8).

There are small spaces at the top and bottom of the chimney where there are no rocks. For this study it was found appropriate to exclude these spaces and use a porosity defined by

$$\phi \triangleq \frac{\text{Volume of void in rock matrix}}{\text{Volume of rock matrix}} \qquad \text{(B. 2)}$$

TABLE B.2

Comparison of Mean and Standard Deviations From Two Different Samples

Parameter		Sample 1-1		Sample 1-2	
		Mean	Standard Deviation	Mean	Standard Deviation
Length, a	(cm)	3.83	1.44	3.95	1.56
Breadth, b	(cm)	2.82	1.08	2.81	1.10
Thickness,	(cm)	1.88	0.77	1.92	0.84
Mass, M_r	(g)	32.6	26.5	36.5	29.7
Equivalent Diameter, $\mathcal{D}$	(cm)	2.52	0.93	2.60	1.01
Surface Area, A	(cm^2)	0.71	0.09	0.70	0.09
Sphericity Parameter, ψ	(dimensionless)	0.74	0.13	0.72	0.13
Breadth/length Ratio, b/a	(dimensionless)	0.50	0.12	0.49	0.13
Thickness/length Ratio, c/a	(dimensionless)	28.8	17.5	24.4	15.2

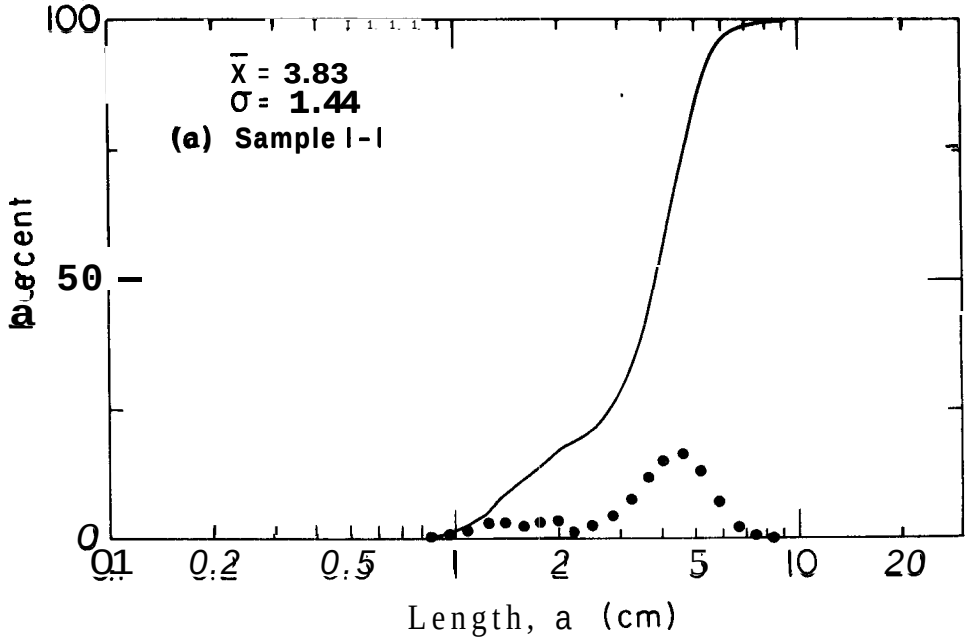

Figure B. 11 Cumulative Distribution and Probability Density Functions for Rock Length Dimension (Logarithmic Abscissa)

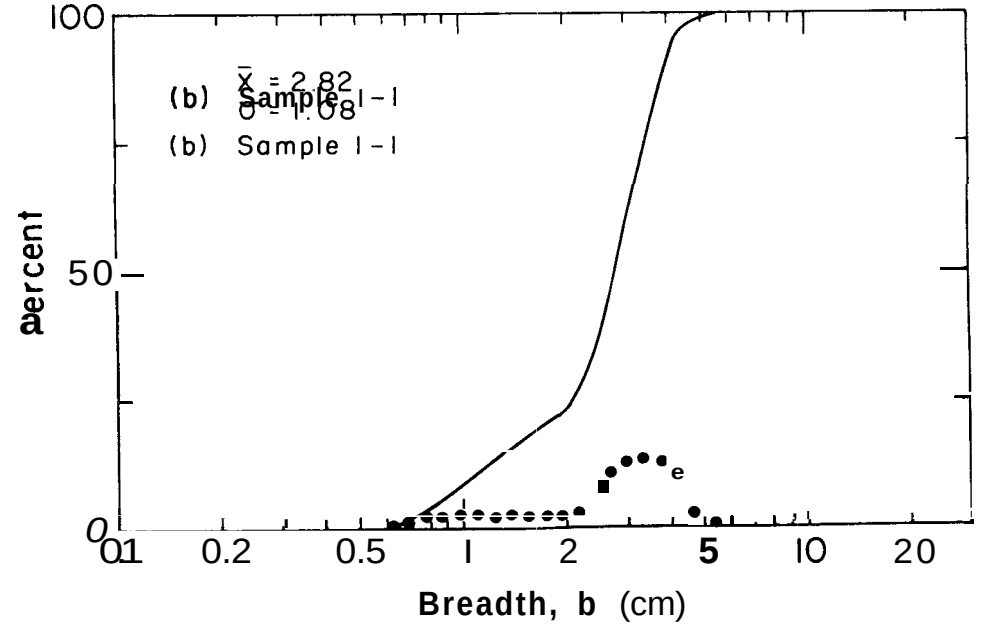

Figure B. 12 Cumulative Distribution and Probability Density Functions for Rock Breadth Dimension (Logarithmic Abscissa)

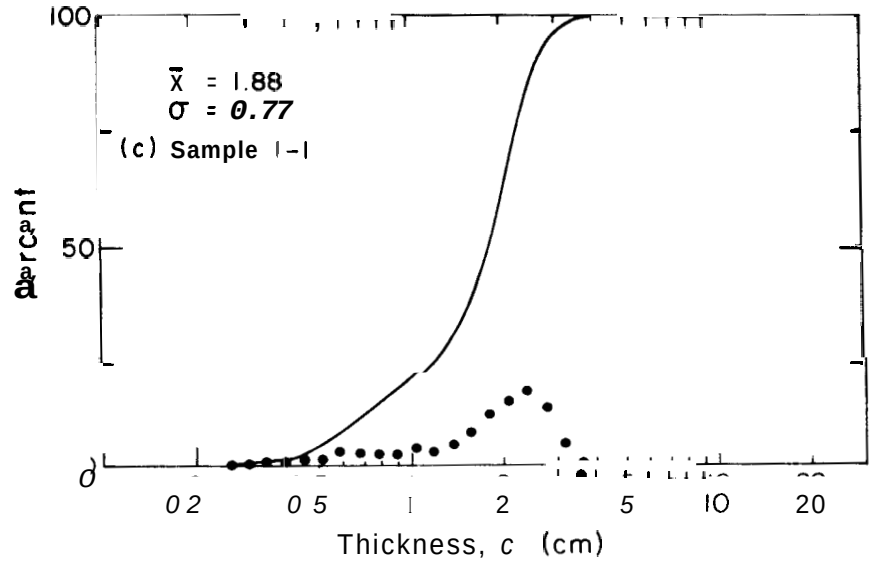

Figure B. 13 Cumulative Distribution and Probability Density Functions for Rock Thickness Dimension (Logarithmic Abscissa)

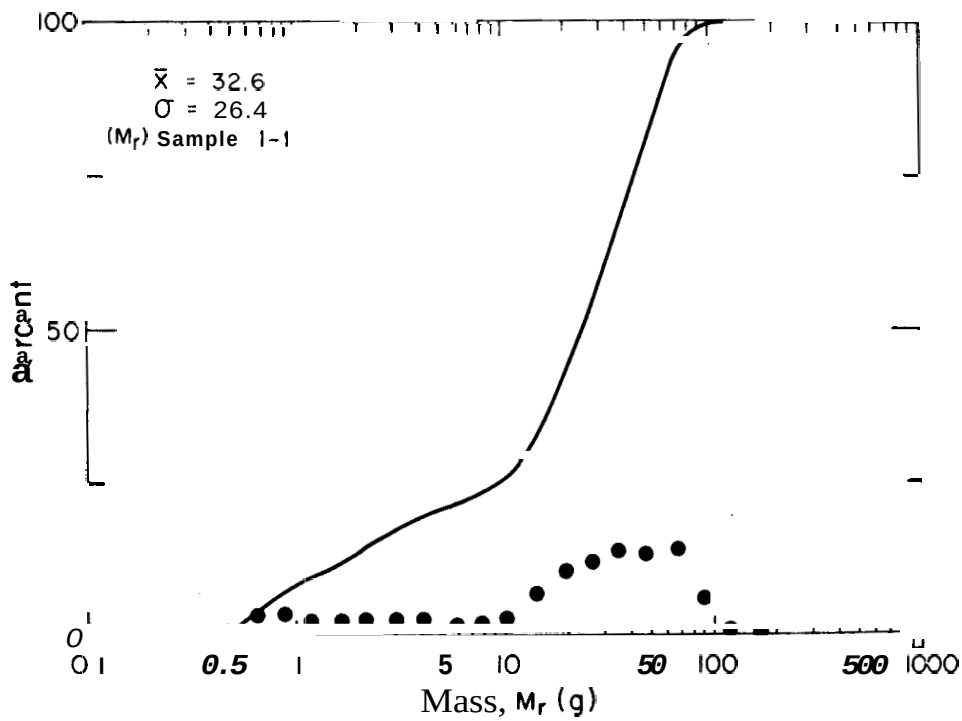

Figure B. 14 Cumulative Distribution and Probability Density Functions for **Rock** Mass (Logarithmic Abscissa)

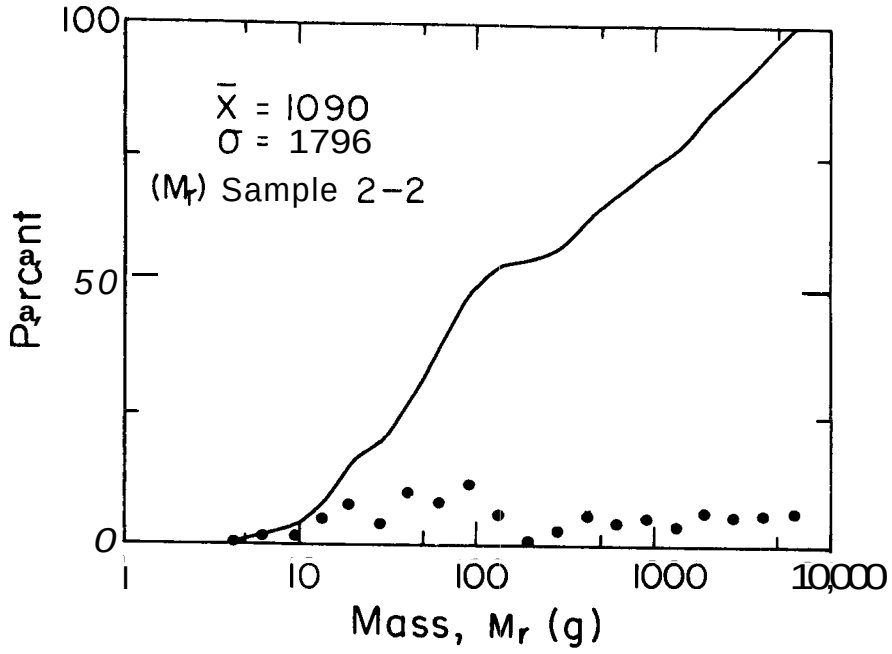

Figure B. 15 Cumulative Distribution and Probability Density Functions for Rock Mass-Second Rock Loading (Logarithmic Abscissa)

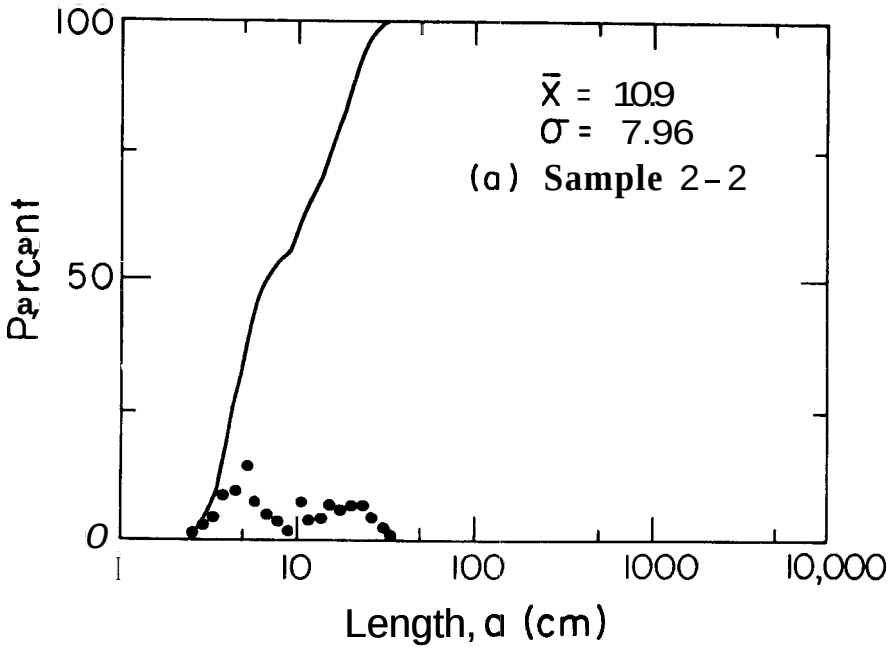

Figure B. 16 Cumulative Distribution and Probability Density Functions for Length Dimension-Second Rock Loading (Logarithmic Abscissa)

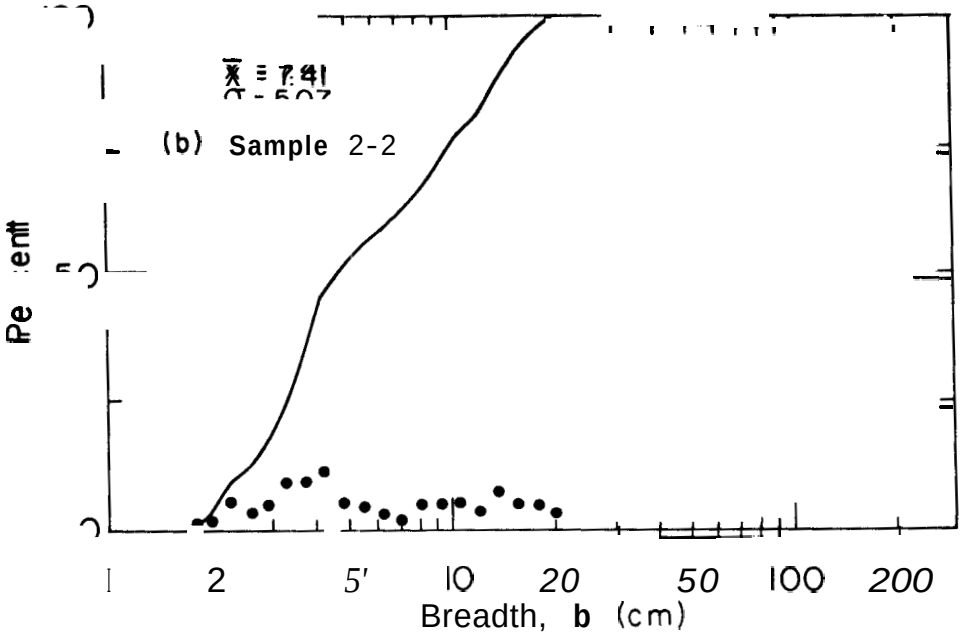

Figure B. 17 Cumulative Distribution and Probability Density Functions for Breadth Dimension-Second Rock Loading (Logarithmic Abscissa)

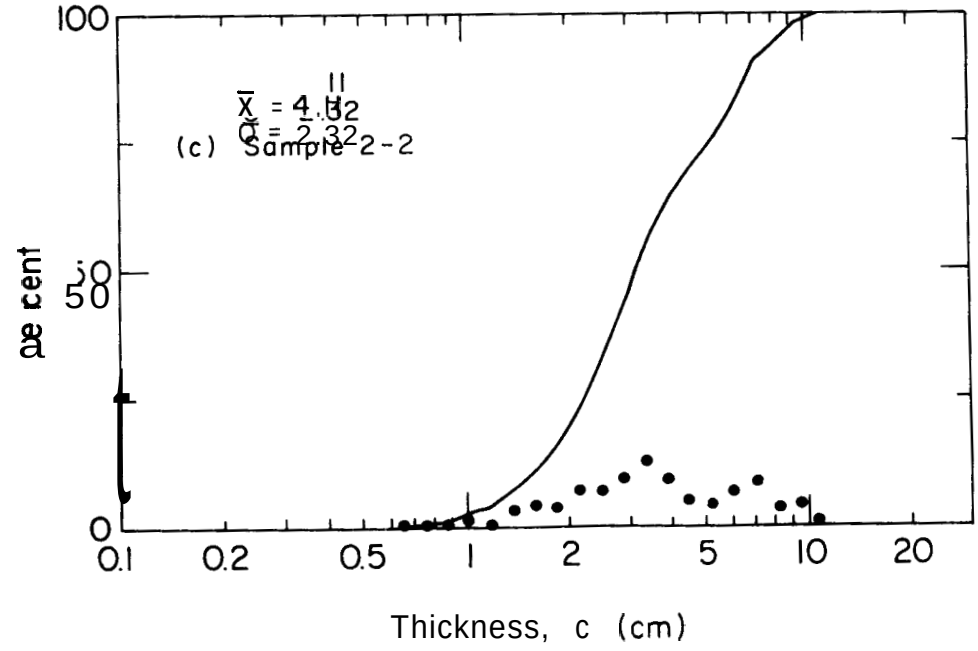

Figure B. 18 Cumulative Distribution and Probability Density Functions for Thickness Dimension-Second Rock Loading (Logarithmic Abscissa)

The following procedure was used to determine the bulk parameters:

(1) The void space between the flow distribution baffle and the inlet isolation valve (see Fig. C. 5) was determined by filling the void with water which was weighed after draining.

(2) Batches of rock were cleaned and weighed prior to loading the chimney. The total rock mass was determined from the sum of the batches.

(3) After completing the rock loading, step (1) was repeated, but this time water was filled to the top of rock matrix (top flange) and then drained. The difference between volumes determined from steps (3) and (1) is the rock. matrix void.

(4) Equation (B. 2) was used to compute the drainage porosity using the rock matrix void and the volume of the rock matrix computed from chimney geometry data. The rock mean solid density was computed from the rack volume (rock matrix volume less void space) and the measured rock mass.

A summary of the bulk parameters obtained for the two rock loadings is given in Table 2.6.

The intrinsic porosity of the solid rocks used in this study is considered negligible compared to the void space between the rocks. The high permeability of the connected voids between the rocks provides very little resistance to the: flow of fluids at the low flow velocities of these tests. Thus, the flow friction pressure drop in the rock matrix is negligible. However, there is a small pressure difference from the bottom to the top (about 2 psi) due to the static head of liquid in the chimney.

B. 3 Instrumented Rocks

Several "instrumented" rocks were positioned at various locations in the rock matrix to measure the rock temperature behavior during the

fluid production transient. The instrumentation consisted of 1/16 inch diameter thermocouples cemented into 1/8 inch diameter holes drilled in the rocks. Details of the procedure are given in Chapter 2. Geometry data for the instrumented rocks of both rock loadings are given in Table B. 3. The location of each rock in the rock matrix is given in Figs. 2. 8 through 2. 10. Photographs of several instrumented rocks of each rock loading are given in Figs. B. 19 and B. 20.

TABLE B. 3

Geome r, [illegible] for [illegible] N Rocks

Parameter		Instrumented Rock Number (First Rock Loading)						Instrumented Rock Number (Second Rock Loading)					
		1	2	3	4	5	6	1	2	3	4	5	6
Length ℓ	(cm)	6.4	4.8	5.3	5.6	6.4	4.2	24.8	26.0	15.2	31.8	41.9	24.1
Breadth, b	(cm)	3 1	4.1	7 6	4.1	3 3	3 9	19.1	14.0	13.3	14.0	26.7	12.7
Thickness, c	(cm)	2.5	2 8	3 3	3.0	3 0	2 5	8.9	8.3	5.1	8.9	12.7	8.9
Equivalent Diameter, d	(cm)	4.0	3.8	3.9	3.9	4.1	3.6	16.5	15.4	9.0	16.4	23.3	15.1
Sphericity Parameter ψ	(dim. less)	0 68	0 79	0 74	0.74	0.63	0 83	0.65	0.55	0.66	0.50	0.58	0.58
Breadth/length Ratio b/a	(dim. less)	0.80	0.84	0.67	0.73	0.52	0.94	0.77	0.54	0.87	0.44	0.64	0.53
Thickness/length ratio, c/a	(dim. less)	0.40	0.58	0.62	0.55	0.48	0.61	0.36	0.32	0.33	0.28	0.30	0.37
Rock Mass, M_r	(g)	93.6	77.6	86.3	89.1	98.3	65.6	617	4950	998	6040	17300	4680
Surface Area, A	(cm^2)	71.7	49.6	51.9	57.3	54.2	41.2	1010	787	423	957	2310	705
Volume, V	(cm^3)	34.3	27.8	30.9	31.9	25.2	23.5	2370	1890	382	2310	6650	1790
Surface area/volume ratio	SVR (cm^{-1})	2.08	1.78	1.68	1.79	1.54	1.75	0.43	0.42	1.11	0.41	0.35	0.39
Surface area/volume ratio	SVR_s (cm^{-1})	1.50	1.58	1.54	1.54	1.46	1.67	0.92	0.99	1.69	0.93	0.65	1.01
Surface area/volume ratio	SVR_p (cm^{-1})	0.8	0 71	0 61	0.67	0 67	0 80	0.22	0.24	0.39	0.22	0.16	0.22

Figure B. 19 Instrumented **Rocks** of the First **Rock** Loading

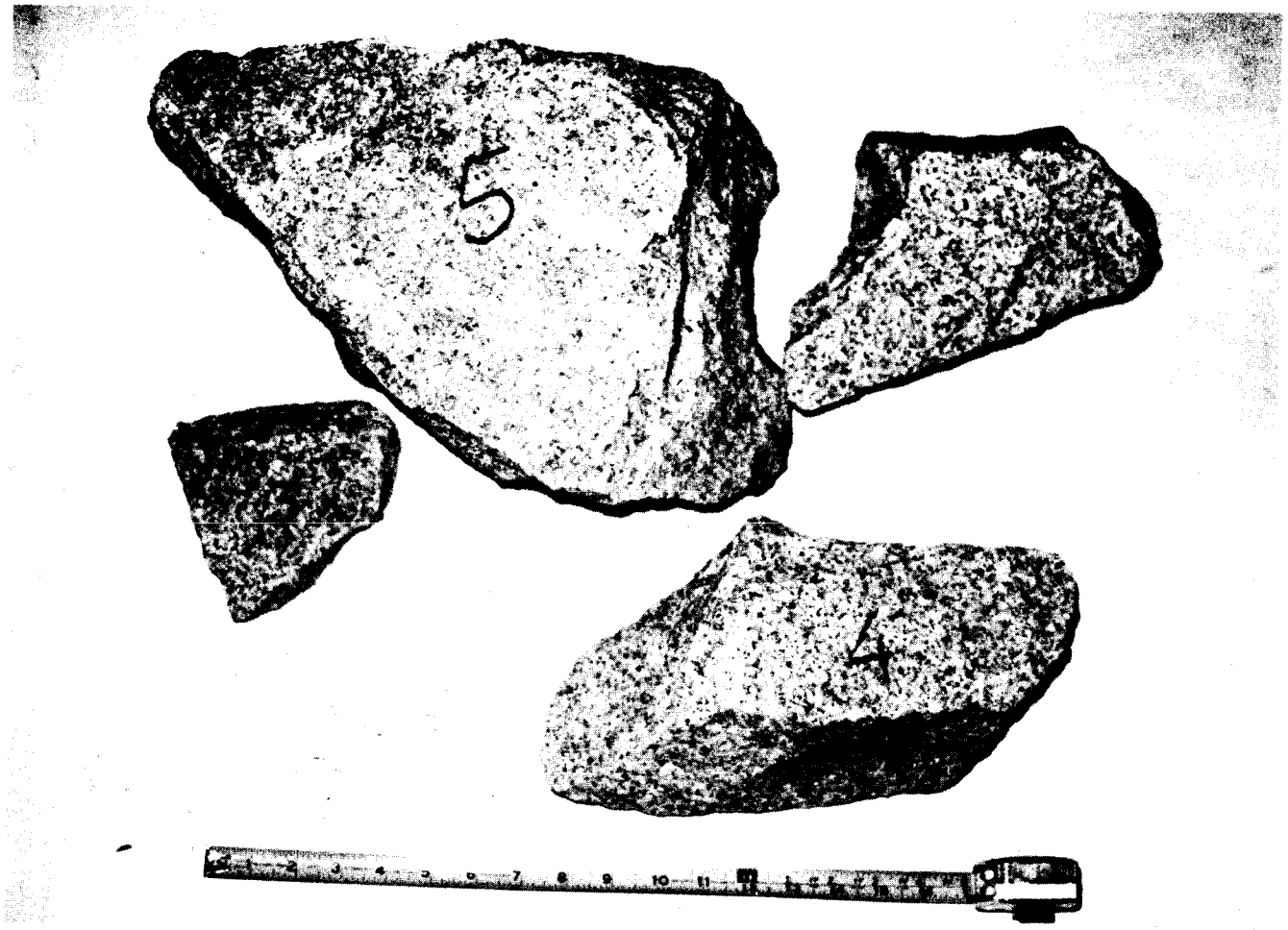

Figure B. 20 Instrumented Rocks of the Second Rock Loading

APPENDIX C

DETAILS OF ANALYSIS

C. 1 Derivations for Rock Thermal Transients

C. 1. 1 Exact Solution for Plate

When one dimension of a rock is small compared to the other two, the rock thermal behavior may be approximated by that of a plate. The exact solution for the thermal behavior of a plate in a linearly decreasing temperature environment was discussed in Chapter 3. Formulation of the boundary value prolblem and its solution is given here.

Using the notation for the plate in Fig. C. 1, the one-dimensional boundary value problem becomes':

Partial Differential Equation (PDE)	$T_t - \alpha T_{xx} = 0$	$0 \leq x \leq \ell$, $t > O$
Boundary Conditions (BC)	$T_x = 0$	at $x = 0$, $t > 0$
	$-kT_x = h(T - T_o + \mu t)$	at $x = \ell$, $t > 0$
Initial Condition (IC)	$T = T_\theta$	$0 \leq x \leq \ell$, $t = O$

Letting $u = T - T_\theta$ and $H = h/k$ the above system is transformed to

PDE	$u_t - \alpha u_{xx} = 0$	$0 \leq x \leq \ell$, $t > 0$	(C. la)
BC	$u_x = 0$	at $x = 0$, $t > 0$	(C. lb)
	$u_x + Hu = -H\mu t$	at $x = \ell$, $t > 0$	(C. lc)
IC	$u = o$	$0 \leq x \leq \ell$, $t = O$	(C. Id)

* In the following the subscripts t, x, and xx represent partial derivatives with respect to time t and the space variable. Also, the subscript "r" used to denote "rock" is neglected temporarily in order not to confuse it with derivative with respect to radius.

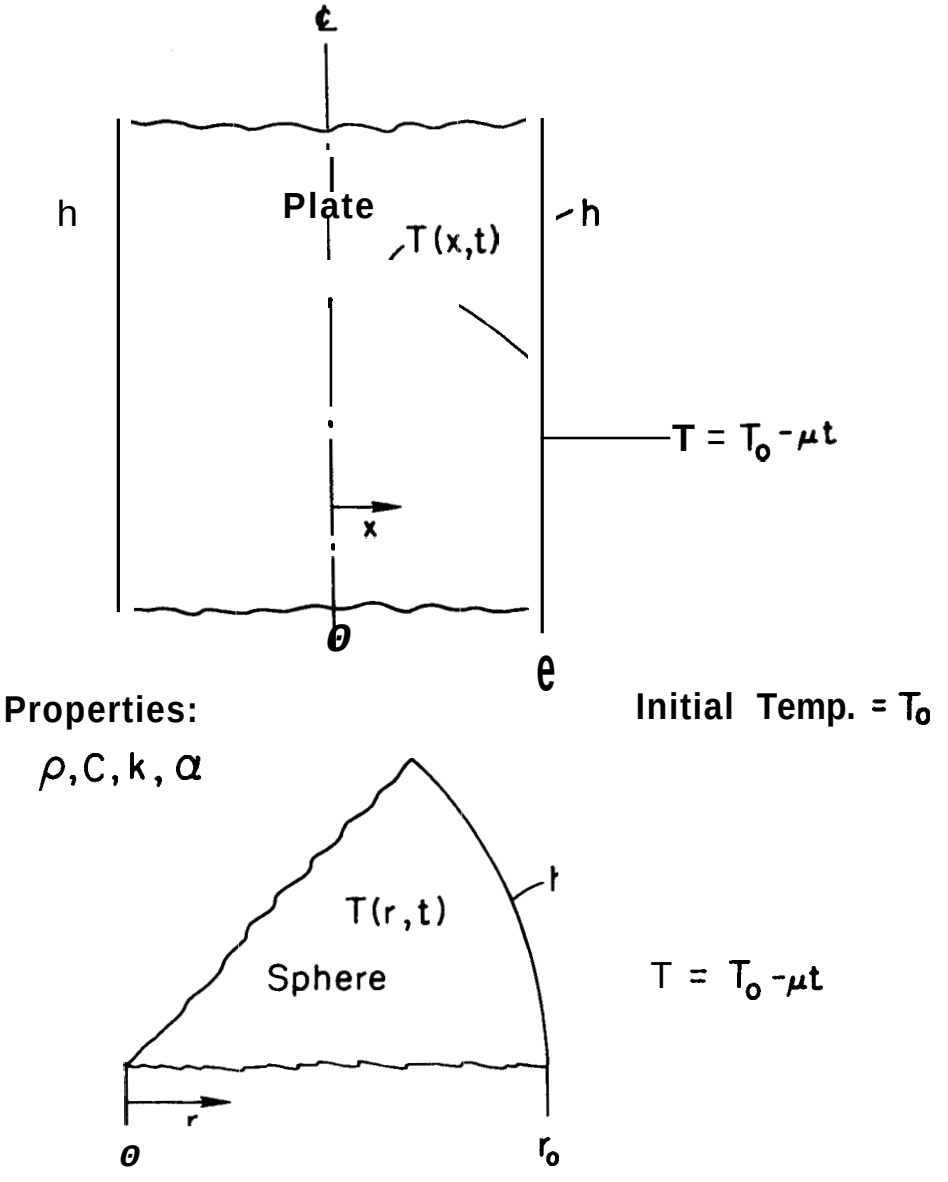

Figure C. 1 Notation for the Idealized Plate and Sphere Rocks Analyzed

The non-homogeneous boundary value problem is solved by superposing two different solutions. One solution satisfies the non-homogeneous boundary condition and the other satisfies the homogeneous boundary conditions, The solution to the above problem given by Carslaw and Jaeger (1947) is

$$u = -\mu t - \frac{\mu(Hx^2 - AH - 2\ell)}{2\alpha H} - \frac{2H\mu}{\alpha}\sum_{n=1}^{\infty}\frac{\cos\lambda_n x\, e^{-\alpha\lambda_n^2 t}}{\lambda_n^2[(H^2+\lambda_n^2)At H]\cos\ell\lambda_n} \qquad \text{(C. 2a)}$$

where the eignevalues λ_n are the roots of the transendental equation

$$\lambda\tan(\lambda\ell) = H \qquad \text{(C. 2b)}$$

The temperature at the center of the plate is obtained by setting x = 0. In presenting this result it is convenient to introduce the following non-dimensional parameters:

$$\frac{u\, t\, \mu t}{\mu\ell^2/\alpha} - \frac{T_r - T}{\mu\ell^2/\alpha} = \text{non-dimensional rock/steam temperature difference}$$

$$B \triangleq HA = \frac{h\ell}{k} = \text{Biot number} \qquad \text{(C. 3)}$$

$$F \triangleq \frac{\alpha t}{\ell^2} = \text{Fourier number}$$

$$\beta = \lambda\ell = \text{non-dimensional eigenvalue.}$$

The center temperature of the plate becomes in terms of these variables

$$\frac{T_{rc} - T}{\mu\ell^2/\alpha} = (1/2\ t\ 1/B) - \sum_{n=1}^{\infty}\frac{2Be^{-\beta_n^2 F}}{\beta_n^2[B(B+1)+\beta_n^2]\cos\beta_n} \qquad \text{(C. 4a)}$$

where the eigenvalues β_n are given by

$$\beta \tan \beta = B$$

The mean temperature of the plate is evaluated from

$$\bar{u} = \frac{1}{\ell} \int_o^{\ell} u dx \qquad (C.5)$$

Using Eq. (C.2a) for u in Eq. (C,5), the mean temperature in terms of the non-dimensional parameters defined above becomes

$$\frac{\bar{T}r - T}{pa^2/\alpha} = (1/3 \text{ t } 1/B) - \sum_{n=1}^{\infty} \frac{2 B^2 e^{-\beta_n^2 F}}{\beta_n^4 [B(B+1) + \beta_n^2]} \qquad (C.6)$$

C. 1.2 Exact Solution for Sphere

When the three orthogonal length dimensions of the rock do not differ by much, an approximate solution for the rock thermal behavior is obtained by considering a sphere of diameter $d = 2r_o$. The rock diameter used is the equivalent diameter defined as the diameter of a sphere having mass equal to that of the rock, Using the notation given in Fig. C. 1 for the sphere and $u = T - T_{\theta'}$ the one-dimensional boundary value problem becomes

PDE	$u_t - \frac{\alpha}{r^2}(r^2 u_r)_r = 0$	$0 \leq r \leq r_{\theta'}$, $t > O$
BC	$u_r = 0$	at $r = 0$, $t > 0$
	$u_r + Hu = -H\mu t$	at $r = r_o$, $t > 0$
IC	$u = o$	$0 \leq r \leq r_{\theta'}$, $t = 0$

The above problem cam be transformed into a form similar to that of the plate problem by introducing the new variable $U = ur$ which gives

PDE	$U_t - \alpha U_{rr} = 0$	$0 \leq r \leq r_o$, $t > 0$	(C. 7a)
BC	$U_r = 0$	at $r = 0$, $t > 0$	(C. 7b)
	$U_r + (H - \frac{1}{r_o})U = -H\mu r_o t$	at $r = r_o$, $t > 0$	(C. 7c)
IC	$u = 0$	$0 \leq r \leq r_o$, $t = 0$	(C. 7d)

The procedure for solving this problem is similar to that for the plate. The solution given by Carslaw and Jaeger (1947) is

$$u = \mu t - \frac{\mu(r_o H r^2 - r_o^2(2+r_o))}{6\alpha r_o H} - \frac{2r_o^2 H\mu}{\alpha} \sum_{n=1}^{\infty} \frac{\sin\lambda_n r\, e^{-\alpha\lambda_n^2 t}}{\lambda_n^2[r_o^2\lambda_n^2 + r_o H(r_o H - 1)]\sin\lambda n r_o} \tag{C. 8a}$$

where the eigenvalues λ_n are the roots of the transendental equation

$$r_o\lambda\cot(r_o\lambda) + (r_o H - 1) = 0 \tag{C. 8b}$$

The temperature at the center of the sphere is obtained by taking the limit as $r \to 0$ which gives in terms of non-dimensional parameters defined earlier

$$\frac{T_{rc} - T}{\mu r_o^2/\alpha} = (1/2 \text{ t } 1/B)/3 - \sum_{n=1} \frac{2Be^{-\beta_n^2 F}}{\beta_n[\beta_n^2 + B(B-1)]\sin\beta_n} \tag{C. 9a}$$

where the eigenvalues β_n are given by

$$\beta\cot\beta \text{ t } (B-1) = 0 \tag{C. 9b}$$

To evaluate the mean temperature of the sphere, it is necessary to evaluate the integral

$$\bar{u} = \frac{1}{V}\int_{o}^{r_o} u\,dV \qquad \text{(C. 10)}$$

where $V = 4/3\pi r^3$. Using Eq. (C. 8a) for u, the mean temperature becomes in terms of the non-dimensional parameters

$$\frac{\bar{T}_r - T}{\mu r_o^2/\alpha} = (1/5 + 1/B)/3 - \sum_{n=1} \frac{6B^2 e^{-\beta_n^2 F}}{\beta_n^4[\beta_n^2 + B(B-1)]} \qquad \text{(C. 11)}$$

C. 1. 3 One-Lump Parameter Solutions

The infinite sums in the exact solutions given above require considerable numerical evaluations. Approximate one-lump parameter solutions convenient for our purposes are derived by considering that the rock is at uniform temperature. The notation and the thermal circuit for the transient problem is given in Fig. C. 2. The first order linear differential equation for the mean rock temperature is obtained from an energy balance on the rock as

$$\frac{d\bar{T}_r}{dt} + \frac{\bar{T}_r}{RC} = \frac{T_o - \mu t}{RC} \qquad \text{(C. 12)}$$

where $R = R_i + R_s$ = total thermal resistance

$C = \rho V C_r$ = thermal capacitance (see Fig. C. 2).

The solution of the above equation with the initial condition $T_r = T_o$ is given by

$$\bar{T}_r = T_o e^{-t/RC} + \int_o^t e^{-(t-\delta)/RC}\left(\frac{T_o - \mu\delta}{RC}\right)d\delta$$

The solution reduces to

$$\bar{T}_r - T = \mu RC[1 - e^{-t/RC}] \qquad \text{(C. 13)}$$

Physical System

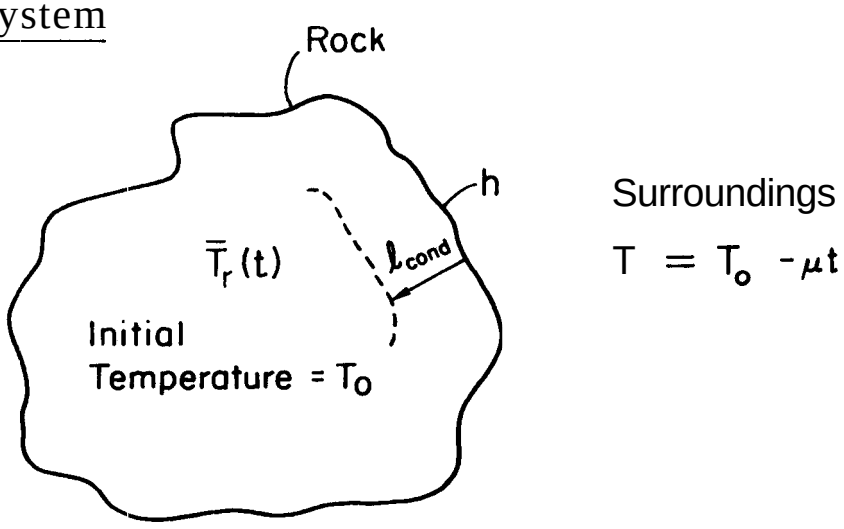

Thermal Circuit

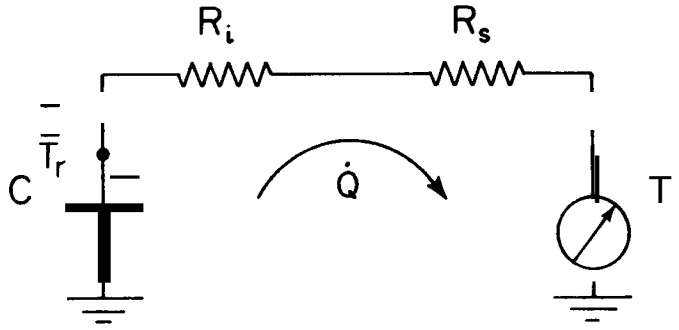

Figure C. 2 'Notation and Thermal Circuit for the One-Lump Parameter Analysis

It is necessary to evaluate the RC product in terms of the rock geometry and its properties. When the rock is approximated by a plate of half thickness ℓ, the total thermal resistance is given by

$$R = \frac{a_{cond}}{kA} \quad t \quad \frac{1}{hA}$$

and the thermal capacitance by

$$C = \rho \ell A \bar{C}_r .$$

The RC product becomes

$$RC = \rho \ell \bar{C}_r \left(\frac{\ell_{cond}}{k} + \frac{1}{h} \right) \qquad \text{(C. 14a)}$$

The RC product can be rewritten in terms of the following parameters

$\alpha = k/\rho \bar{C}_r$ = thermal diffusivity (ft^2/hr)

$B = h\ell/k$ = Biot number (dim.less)

$\delta_p = a_{cond}/\ell$ = normalized conduction path length (dim.less) (see Fig. C. 2)

as

$$RC = (\delta_p + 1/B)\ell^2/\alpha \qquad \text{(C. 14b)}$$

A similar expression can be derived for a spherical rock of radius r_o for which the total thermal resistance is given by (Holman, 1972)

$$R = \frac{\left(\frac{1}{r_o - \ell_{cond}} - \frac{1}{r_o}\right)}{4\pi k} + \frac{1}{hA_o}$$

The thermal capacitance of a sphere is

$$C = \rho \frac{4}{3} \pi r_o^3 \bar{C}_r$$

The RC product for the sphere becomes

$$RC = \frac{\rho \bar{C}_r r_o^2}{3k} \left(\frac{\ell_{cond}}{r_o - \ell_{cond}} + \frac{k}{r_o h} \right) \qquad \text{(C. 15a)}$$

Introducing the dimensionless parameter defined by

$$\delta_s = \frac{A}{} \frac{\ell_{cond}}{r_o - \ell_{cond}} \simeq \frac{\ell_{cond}}{r_o} = \text{normalized conduction path length,}$$

the Biot number, and the thermal diffusivity yields for the sphere

$$RC = (\delta_s \text{ t } 1/B) r_o^2 / 3\alpha \qquad \text{(C. 15b)}$$

With these expressions for RC, the approximate one-lump parameter solutions for the mean rock/steam temperature difference of the plate and the sphere are

Plate

$$\frac{T_r - T}{\mu \ell^2 / \alpha} = (\delta_p + 1/B) \left[1 - e^{-F/(\delta_p + 1/B)} \right] \qquad \text{(C. 16)}$$

Sphere

$$\frac{\bar{T}_r - T}{\mu r_o^2/\alpha} = \frac{(\delta_s + 1/B)}{3}\left[1 - e^{-3F/(\delta_s + 1/B)}\right] \qquad \text{(C. 17)}$$

The above derivations did not provide a range of the numerical values of δ. However, one would expect that δ is in the range $0 < \delta < 1$ and that it will change with time as the temperature profile in the solid develops. Also, it is likely that δ depends somewhat on the Biot number for moderately high values of this number such that $1/B$ is significant compared to δ. However, for large values of B (indicating negligible surface thermal resistance as compared to internal resistance) no effect is expected.

For the mean temperatures of the plate and the sphere, limiting values of 6 are obtained by compairing the exact solutions (Eqs. C. 6 and C. 11) to the lumped parameter solutions (Eqs. C. 16 and C. 17) for large times such that time dependent terms are negligible (quasi-steady state linear cooldown conditions). Such a comparison gives the data in the center column of Table C. 1.

TABLE; C. 1

Normalized Conduction Path Lengths for the Plate and the Sphere for Quasi-steady State Linear Cooldown Conditions

Geometry	Mean Temperature	Center Temperature
Sphere	$\delta_s = 1/5$	$6_{cs} = 1/2$
Plate	$\delta_p = 1/3$	$\delta_{cp} = 1/2$

Approximate expressions for the rock center/steam temperature differences are obtained by defining artificial conduction path lengths. These are obtained by comparing the exact solutions (Eqs. C. 4a and C. 9a) to the one-lump parameter solutions (Eqs. C. 16 and C. 17) in which $\bar{T}_r$ is replacedby T_{rc} and where the subscripts s and p are replaced by cs and cp. This comparison gives for quasi-steady state conditions the data in the right hand column of Table C. 1.

C. 1.4 Rock Time Constants

The time constant is a measure of how fast the rock attains equilibrium temperature following a step change in the ambient temperature. By definition, the time constant is the time required for the rock mean temperature to reach 63.2 percent of the step change. Thus, if a rock is at a uniform temperature of 200 ^{o}F and is suddenly exposed to a 100 ^{o}F environment, the time constant is the time required for the rock mean temperature to reach 136. 8 ^{o}F. A method for estimating the time constant for a rock when the shape factors equivalent diameter d, thickness c, and sphericity parameter + are given is outlined below.

The mean temperature transients of a sphere and a plate resulting from step changes in the surrounding temperatures were given by Jaeger and Clarke (1947), and by Schneider (1955). The results, presented graphically in terms of the Fourier and Biot numbers, may be used to obtain the time constant for the sphere and plate. However, the results may also be put into equation form convenient for numerical computations.

The RC product given by either Eq. (C. 14b) or Eq. (C. 15b) has the dimension of time. The time constant is obtained if δ is selected such that

$$RC = \tau = \text{time constant.}$$

These values of δ are computed for the plate and the sphere from

$$\delta_{p\tau} = \alpha\tau_p/\ell^2 - 1/B \qquad \text{(C. 18a)}$$

$$\delta_{s\tau} = 3\alpha\tau_s/r_o^2 - 1/B \qquad \text{(C. 18b)}$$

where τ_p and τ_s are obtained from the temperature charts.

The results of these evaluations are given in Fig. C. 3 where δ is plotted vs the Biot number for the plate and the sphere. It is observed that for Biot number greater than about 1, the values of δ are fairly constant. It is also noted that these constant values are only slightly lower (0. 31 vs 0. 33 for the plate and 0. 18 vs 0. 20 for the sphere) than the correspondirig asymptotic values for quasi-steady state linear cooldown $(t >> \tau)$. At early times in the transient $(t << \tau)$ δ is expected to be small. Thus, δ develops from zero at $t \sim 0$ to the asymptotic value at large times.

Equations (C. 18) solved for t'he time constants are

$$\tau_p = \frac{\ell^2}{\alpha}(\delta_{p\tau} + 1/B) \qquad \text{(C. 19a)}$$

$$\tau_s = \frac{r_o^2}{3\alpha}(\delta_{s\tau} + 1/B) \qquad \text{(C. 19b)}$$

These equations were used with the data in Fig, C. 3 to compute the time constants given in Figs. 3. 2 and 3. 3.

The above equations and Eq. (3, 7) were used to estimate the time constant for the mean size rock of each rock loading and for all instrumented rocks as explained in Chapter 3. The calculated time constants are given in Tables 3. 1 and C. 2.

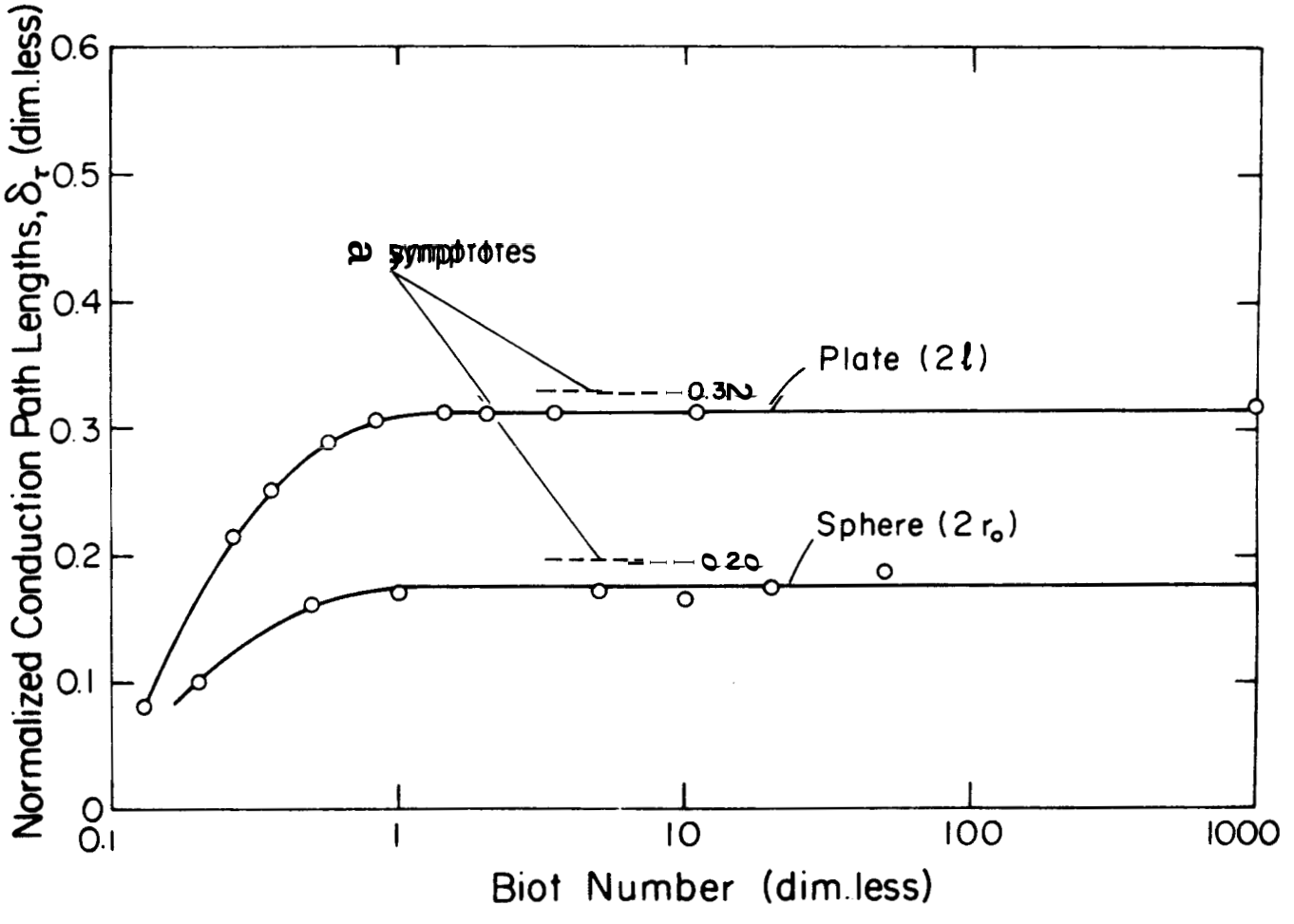

Figure C. 3 Mean Conduction Path Lengths for Evaluation of Time Constants for the Plate and the Sphere

TABLE C.2

Estimated Rock Time Constants in Vapor and Liquid Environments

Rock Loading	Rock Geometry	Time constants in vapor environment (h=3 Btu/hr ft^2 °F)*					
		τ_{sO} (Sr)	τ_{gO}	τ_O	τ_{sL}	τ_{gL}	τ_L
First (gabbro)	Mean	0.18	0.39	0.20	0.014	0.034	0.016
	Instrumented rock 1	0.28	0.53	0.30	0.025	0.048	0.027
	2	0.26	0.60	0.29	0.023	0.057	0.026
	3	0.28	0.69	0.31	0.024	0.071	0.028
	4	0.28	0.65	0.31	0.024	0.062	0.027
	5	0.29	0.65	0.32	0.026	0.062	0.029
	6	0.25	0.53	0.27	0.022	0.048	0.024
Second (granite)	Mean	0.46	0.92	0.49	0.044	0.085	0.048
	Instrumented rock 1	1.17	3.04	1.34	0.17	0.28	0.18
	2	1.09	2.67	1.24	0.15	0.24	0.16
	3	0.39	1.24	0.47	0.14	0.12	0.14
	4	1.17	3.04	1.34	0.17	0.28	0.18
	5	1.71	5.49	2.07	0.31	0.53	0.33
	6	1.09	3.04	1.27	0.15	0.28	0.17

*Biot numbers ranged between 0.10 to 0.17 and between 0.20 to 0.82 for instrumented rocks of the first and second rock loading, respectively.

**Biot numbers ranged between 1.7 to 2.7 and between 3.0 to 13.6 for instrumented rocks of the first and second rock loading, respectively.

C. 1. 5 Two-Lump Numerical Formulation

The basis for selecting three different size spheres each consisting of two equal thermal capacitance (equal volume) lumps to represent the rock loading was given in Chapter 3. The detailed geometry assumed for the two lumps in each sphere is shown in Fig. C. 4. The inner lump consists of a sphere of radius r_m. The outer lump consists of spherical shell of inner and outer radii r_m and r_o. The dividing radius, r_m is computed from

$$r_m = r_o / \sqrt[3]{2} = r_o / 1.26 \qquad \text{(C. 20)}$$

The magnitudes of the radii r_1 and r_2 where the mean temperatures T_{r1} and T_{r2} of the two lumps are located have been studied by Johnson (1955) for hollow spheres. In that analysis the normalized radii r_1^* and r_2^* were determined for the limiting case of a steady state temperature profile and no surface thermal resistance. It is proposed that Johnson's results for the largest outside to inside radii ratio be used as a first approximation. The numerical procedure is compared to the exact solution for the special case of linear cooldown to determine its adequacy.

The thermal circuit for a two-lump sphere is shown in Fig, 3. 7. Energy balances on each of the two lumps of the small size sphere (of the three sizes selected) together with heat transfer rate equations lead to the two first order, linear differential equations given below,

For the inner lump:

$$\frac{dT_{r1}}{dt} = \frac{T_{r2} - T_{r1}}{R_{1s} C_{1s}} \qquad \text{(C. 21a)}$$

For the outer lump:

$$\frac{dT_{r2}}{dt} = \frac{T_{r1} - T_{r2}}{R_{1s} C_{2s}} + \frac{T - T_{r2}}{C_{2s}(R_{2s} + R_{os})}, \qquad \text{(C. 21b)}$$

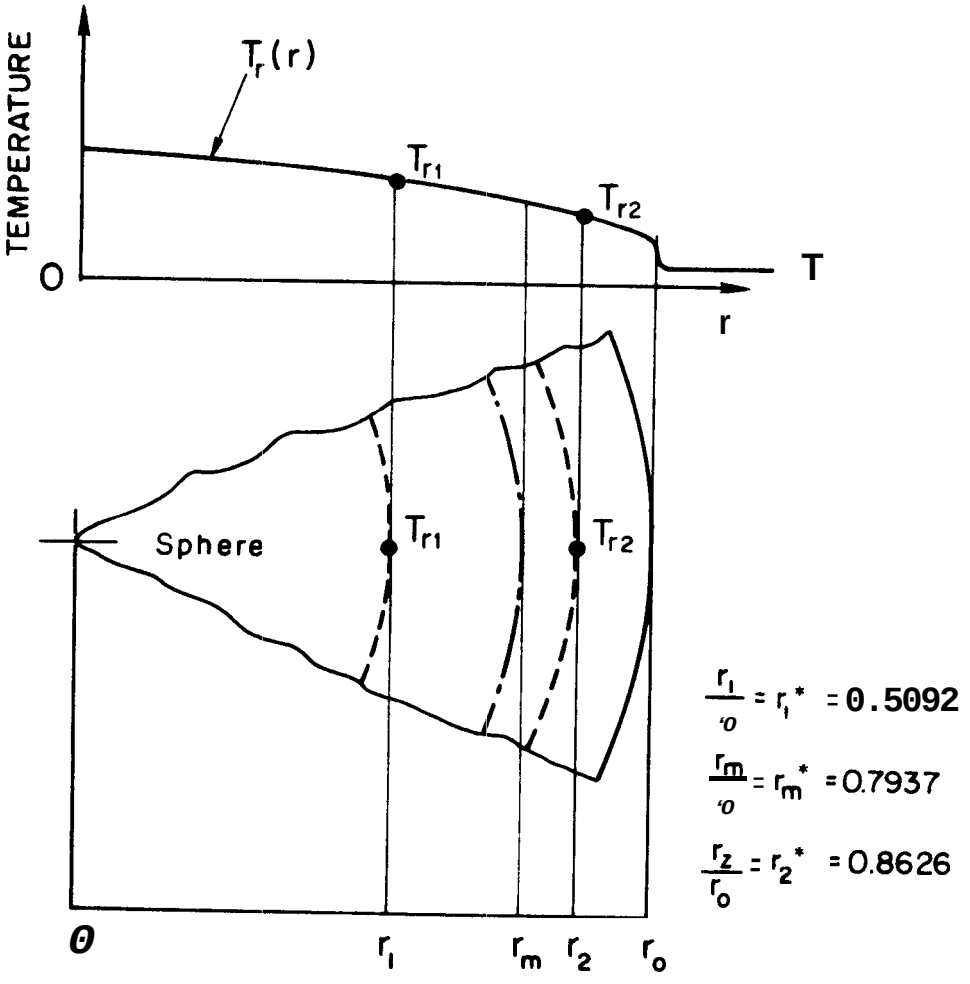

Figure C. 4 **Details of** Two-Lump **Sphere** Geometry

where the subscript "s" refers to small size sphere, T_{r1} and T_{r2} are the inner and outer lump temperatures, and where T (without subscript) is the surrounding steam temperature.

The conduction thermal resistances R_{1s} and R_{2s} for spherical shells are (see Holman, 1972)

$$R_{1s} = \left(\frac{1}{r_{1s}} - \frac{1}{r_{2s}} \right) \Big/ 4\pi k \qquad \text{(C. 22a)}$$

$$R_{2s} = \left(\frac{1}{r_{2s}} - \frac{1}{r_{os}} \right) \Big/ 4\pi k \qquad \text{(C. 22b)}$$

The convection thermal resistance at the surface is

$$R_{os} = 1/hA_{os} = 1/h4\pi r_{os}^2 \qquad \text{(C. 22c)}$$

the thermal capacitances of the two lumps are

$$C = C_{2s} = \rho_r \frac{1}{2}\left(\frac{4}{3}\pi r_o^3 \right)\bar{C}_r \ , \qquad \text{(C. 22d)}$$

where $\bar{C}_r$ is the rock specific heat.

Since there are a total of three rock sizes each with two lumps (see Figs. 3. 5 and C. 4), there are two more sets of equations and coefficients. The equations for the temperature of the six rock lumps, denoted by T_{ri} (i = 1, 2, . . ., 6), are given in standard form as

$$\begin{aligned} \frac{dT_{r1}}{dt} &= a'_{11}T_{r1} + a'_{12}T_{r2} + \cdots + a'_{16}T_{r6} + b'_1 T \\ &\vdots \\ \frac{dT_{r6}}{dt} &= a'_{61}T_{r1} + a'_{26}T_{r2} + \cdots + a'_{66}T_{r6} + b'_6 T \end{aligned} \qquad \text{(C. 23)}$$

The coefficients a'_{ij} and b'_j are determined for the small size sphere by comparison of these to Eqs. (C. 21) to be

$$
\begin{aligned}
a'_{11} &= -1/R_{1s}C_{1s} \\
a'_{12} &= a'_{11} \\
a'_{13} &= a'_{14} = a'_{15} = a'_{16} = b'_1 = 0 \\
a'_{21} &= 1/R_{is}C_{2s} \\
a'_{22} &= (1/R_{1s}C_{2s} - 1/C_{2s}(R_{2s} + R_{os})) \\
a'_{23} &= a'_{24} = a'_{25} = a'_{26} = 0 \\
b'_2 &= 1/C_{2s}(R_{2s} + R_{os})
\end{aligned}
\qquad \text{(C. 24)}
$$

Similar expressions are obtained for the coefficients of the **two** other pairs of equations.

The rock thermal properties--specific heat and thermal conductivities--varies with temperature a.s shown in Appendix D. These variations are neglected in the integration. The mean thermal property data in Table D. 1 were used to evaluate mean values of the coefficients.

C. 2 Derivations **for** Laboratory Model Reservoir Analysis

C. **2.** 1 Equations for Transient

The basis for considering the: idealized reservoir in Fig. **3.** 6 was given in Chapter **3.** If M is the mass of the two-phase steam mixture contained in the void space within the chimney control volume at time t, conservation of mass yields

$$\frac{dM}{dt} = \dot{M}_i - \dot{M}_P \qquad \text{(C. 25a)}$$

Integration of the above equation with respect to time with initial conditions

$$M = M_o \qquad \text{at } t = 0$$

$$M_i = M_P = 0 \qquad \text{at } t = O$$

gives M in terms of the cumulative fluid recharge M_i and cumulative steam production M_P as

$$M = M_o + M_i - M_P \tag{C. 25b}$$

If E is the internal energy of the two-phase steam mixture within the control volume at time t, conservation of energy gives

$$\frac{dE}{dt} = \dot{M}_i i_i - \dot{M}_p i_p + \dot{Q}_m + \dot{Q}_r \tag{C. 26}$$

where the boundary parameters $\dot{M}_i$, i_i, $\dot{M}_p$, i_p, $\dot{Q}_m$, and $\dot{Q}_r$ are all functions of time. The internal energy of the steam mixture (vapor and liquid) is given by

$$E = M_f e_f + M_g e_g \tag{C. 27}$$

where M_f = mass of saturated liquid
M_g = mass of saturated vapor
e_f = internal energy of saturated liquid
e_g = internal energy of saturated vapor

Equation (C. 27) can be rearranged to obtain an expression that is a function of pressure and M only using the following relationships between total mass and volume of the mixture and the masses and volumes of the two phases

$$M = M_f + M_g \tag{C. 28a}$$

$$V_v = V_f + V_g \qquad \text{(C.28b)}$$

Also, the mass of the liquid and vapor phases can be expressed in terms of the specific volumes as

$$M_f = V_f / v_f \qquad \text{(C.29a)}$$

$$M_g = V_g / v_g \qquad \text{(C.29b)}$$

Combining Eqs. (C.27) and (C.28a) gives

$$E = M\left[e_f + (e_g - e_f)\frac{M_g}{\cdot\cdot}\right] \qquad \text{(C.30)}$$

The mass of vapor can be expressed as

$$M_g = V_g / v_g = \frac{V_g}{v_g}\frac{(v_g - v_f)}{(v_g - v_f)} = \left(V_g - V_g\frac{v_f}{v_g}\right)\Big/(v_g - v_f)$$

$$= \left(V_g + V_f - V_f - V_g\frac{v_f}{v_g}\right)\Big/(v_g - v_f)$$

In the above expression it is noted that

$$V_g + V_f = V_v = V\phi$$

and

$$V_f + V_g\frac{v_f}{v_g} = \left(\frac{V_f}{v_f} + \frac{V_g}{v_g}\right)v_f = Mv_f$$

Writing $v_{fg} = v_g - v_f$ and $e_{fg} = e_g - e_f$, Eq. (C. 30) becomes

$$E = M\left[e_f + \frac{e_{fg}}{v_{fg}}\left(\frac{v\phi}{M} - \right.\right. \qquad (C.31)$$

The functional form of Eq. (C. **31**) is

$$E = E(P, M) = E(P(t), M(t))$$

The total derivative of E with respect to time is given by the chain rule as

$$\frac{dE}{dt} = \frac{\partial E}{\partial P}\frac{dP}{dt} + \frac{\partial E}{\partial M}\frac{dM}{dt}$$

$$= \left[M\frac{\partial e_f}{\partial P} + V\phi\frac{\partial}{\partial P}\left(\frac{e_{fg}}{v_{fg}}\right) - M\frac{\partial}{\partial P}\left(v_f\frac{e_{fg}}{v_{fg}}\right)\right]\frac{dP}{dt} + \left[e_f - v_f\frac{e_{fg}}{v_{fg}}\right]\frac{dM}{dt}$$

The partial derivative $\partial/\partial P$ is written as $(\ )^1$ in the above equation and the dM/dt multiplier in the last term is replaced by $\dot{M}_i - \dot{M}_p$ from Eq. (C. 25a). Combining the above equation and Eq. (C. *26)* gives

$$\left[M(e_f)' + V\phi\left(\frac{e_{fg}}{v_{fg}}\right)' - M\left(v_f\frac{e_{fg}}{v_{fg}}\right)'\right]\frac{dP}{dt} + \left[e_f - v_f\frac{e_{fg}}{v_{fg}}\right](\dot{M}_i - \dot{M}_p)$$

$$= \dot{M}_i i_i - \dot{M}_p i_p + \dot{Q}_m + \dot{Q}_r$$

This equation is solved for dP/dt which rearranted gives

$$\frac{dP}{dt} = \frac{\dot{Q}_m + \dot{Q}_r + \left(i_i + v_f \frac{e_{fg}}{v_{fg}} - e_f\right)\dot{M}_i - \left(i_p + v_f \frac{e_{fg}}{v_{fg}} - e_f\right)\dot{M}_p}{\left[(e_f)' + \frac{v\phi}{M}\left(\frac{e_{fg}}{v_{fg}}\right)' - \left(v_f \frac{e_{fg}}{v_{fg}}\right)'\right]M} \qquad \text{(C. 32)}$$

This equation provides a method for obtaining the reservoir pressure transient for given boundary parameters Q_m, $\dot{Q}_r$, $\dot{M}_i$, i_i, $\dot{M}_p$, i_p and M. The independent parameters $\dot{M}_i$, i_i and $\dot{M}_p$ are controled by the operator as functions of time. The parameters i_p, Q_m, $\dot{Q}_r$, M and P depend on the independent parameters, i.e., on time t. The boundary parameters used for the analysis were derived from experimental data as explained later.

An equation for the rate of external heat transfer Q_m is derived by considering the annular control volume enclosing the steel chimney with insulation. This control volume by definition excludes the water/rock system contained inside the chimney. The net energy transfer from the chimney wall to the water/rock system ("wall effect") involves the four energy terms:

1. Heat losses from the chimney to the surroundings of magnitude $UA\theta_m$ (Btu/hr).
2. Energy storage in the chimney metal of magnitude $M_m C_m \theta_m$ (Btu).
3. Net rate of energy transfer from the chimney system to the water/rock system denoted by $\dot{Q}_m$ (Btu/hr).
4. Electrical energy supply by the tape heaters on the chimney outside surface denoted by $\dot{Q}_E$ (Btu/hr).

An energy balance yields

$$\dot{Q}_m = \dot{Q}_E - M_m \frac{d(C_m \theta_m)}{dt} - UA\theta_m , \qquad \text{(C. 33)}$$

where $\theta_m = T_m - T_\infty$ is the average chimney metal temperature obtained experimentally from metal temperature measurements.

The electrical power input to the tape heaters was available from measurements. The mass of the chimney metal M_m and the heat loss conductance UA were determined from calibration tests as described previously (Hunsbeclt, Kruger and London, 1975). The numerical values and the standard deviations of these parameters are given in Table C. 3.

TABLE C. 3

Tabulation of Chimney Parameters

Effective chimney metal mass, M_m	3428 ± 240 lb_m
Effective chimney heat loss conductance, UA	32. 2 ± 1.2 Btu/hr F

The enthalpy of the recharged fluid i_i at the inlet of the chimney can be derived from inlet temperature measurements if the recharged fluid is subcooled. However, when the recharged fluid is preheated in the electric heater or by the tape heaters on the inlet line, the recharged fluid may be a two-phase mixture. In that case i_i is evaluated from measured temperature data at the electric heater exit where high pressures and subcooled water conditions were maintained by inlet valve regulation.

An energy balance on the inlet line assuming negligible energy storage effects in the steel line (see Fig. C. 5) gives

$$ii = iH\ t\ (\dot{Q}_i - \dot{Q}_{\ell i})/\dot{M}_i \qquad \text{(C. 34)}$$

where Q_i is the measured electrical energy supplied by the inlet line tape heaters. The free convection and radiation heat losses from the

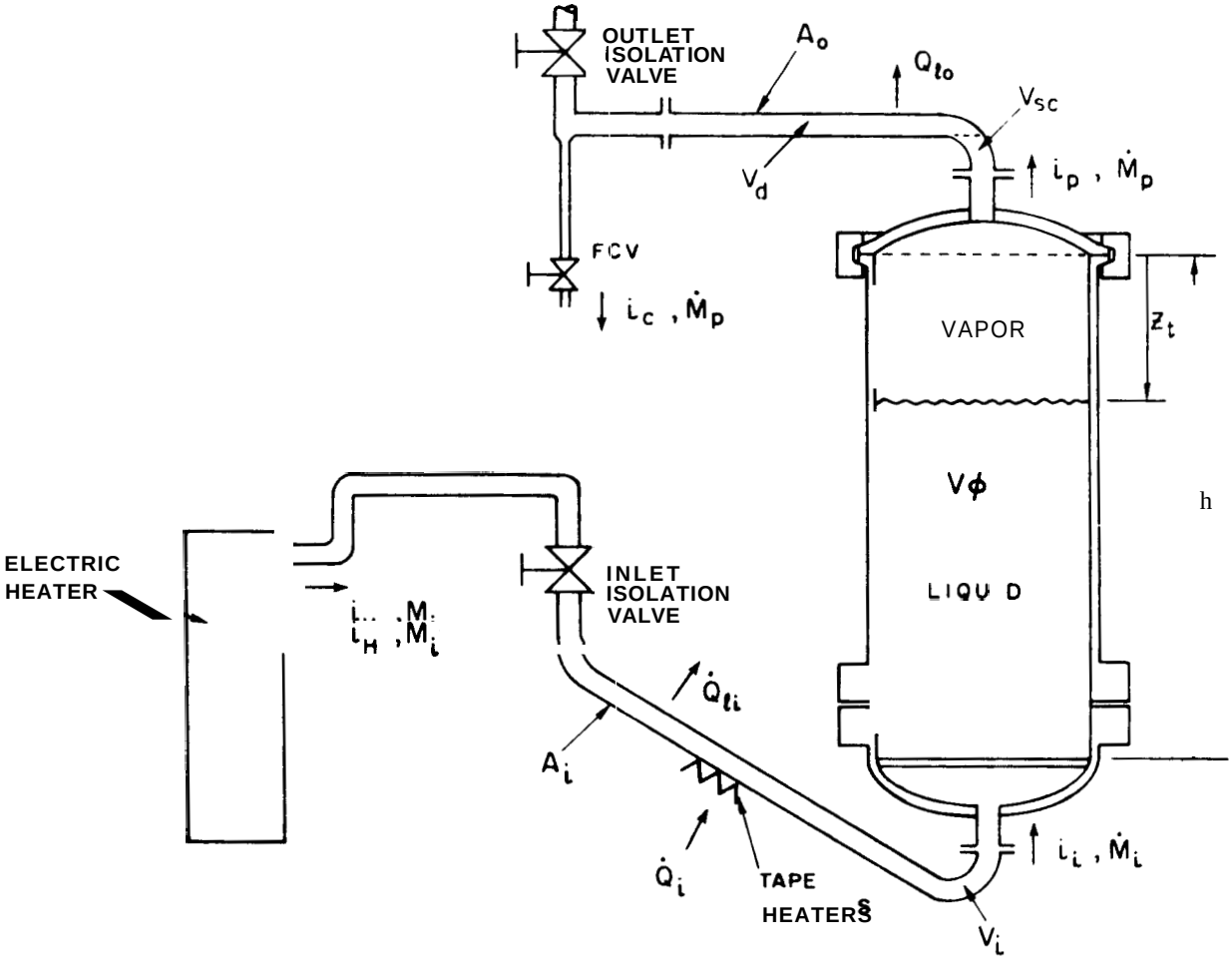

Figure C. 5 Notation for Line Heat Loss Analysis

inlet line were estimated using the following formula (from Fishender and Saunders, 1934')

$$Q_{\ell i} = A_i \{C_i (T_w - T_{a3})^{5/4} + \epsilon\, 0.17 \cdot 10^{-8} [(T_w + 460)^4 - (T_\infty + 460)^4]\} \quad \text{(C.35)}$$

The wall temperature T_w (insulation skin temperature) was measured as a function of time at one representative point. The constant C_i was evaluated experimentally ($C_i = 0.90$). The emissivity ϵ was taken to be 0.15 for this system.

The enthalpy of the produced steam was evaluated from temperature measurements at the chimney exit. Another independent method was based on a condenser heat balance which gives the steam enthalpy at the inlet of the condenser as (Hunsbedt, Kruger and London, 1975)

$$i_c = i_{H.\,out} + \frac{\dot{M}_c}{\dot{M}} \bar{C} (T_{c,\,out} - T_{c,\,in}) \quad \text{(C.36)}$$

where all quantities on the right are known from measurements. The steam enthalpy at the chimney exit is evaluated from an energy balance on the outlet line (see Fig. C.5) as

$$i_p = i_c - \dot{Q}_{\ell o} / \dot{M}_P \quad \text{(C.37)}$$

The heat losses from the outlet line are estimated from

$$Q_{\ell o} = A_o \{C_o (T_w - T_\infty)^{5/4} + \epsilon\, 0.17 \cdot 10^{-8} [(T_w + 460)^4 - (T_\infty + 460)^4]\} \quad \text{(C.38)}$$

where C_o was evaluated experimentally ($C_o = 0.80$).

C. 2. 2 Numerical Solution Procedure

The fourth order Runge-Kutta numerical integration scheme was used to solve the chimney transient problem governed by Eqs. (3.20a) through (3.20e). The time variable is written as

$$t_j^* = t_s^* + h^* j \qquad (C.39)$$

where t_s^* = starting time for integration (dim. less)

h^* = time step size (dim. less)

j = j^{th} time step (dim. less)

The variables are approximated as

$$\begin{aligned} T_{r1}^j &\simeq T_{r1}(t_j^*) \\ &\vdots \qquad\quad \vdots \\ T_{r6}^j &\simeq T_{r6}(t_j^*) \\ \bar{T}_r^j &\simeq \bar{T}_r(t_j^*) \\ P^{*j} &\simeq P^*(t_j^*) \end{aligned} \qquad (C.40)$$

A forward finite difference approximation was used for the time derivative of the mean rock temperature in Eq. (3.20c) as follows

$$-\left.\frac{d\bar{T}_r}{dt^*}\right|_j \cong \frac{\bar{T}_r^j - \bar{T}_r^{j-1}}{h^*} \qquad (C.41)$$

The maximum time step size h for stability is determined from considerations of the eigenvalues of the coefficient matrix which leads to the requirement that

$$h\lambda_{max} << 1$$

where λ_{max} is the maximum (absolute magnitude) eigenvalue. For the present system it was determined that the time step size was governed by the smallest rock lump time constant τ_{min}. The following formula was used to compute h*.

$$h^* \leq \frac{1}{5} \tau_{min}/t_c \qquad \text{(C. 42)}$$

Since experimental data to compute the boundary parameters $\dot{Q}_m$, i.e., i_i, i_p, M^*, $\dot{M}_i^*$, and $\dot{M}_P^*$ were available only at discrete points in time, approximations were required for intermediate points. The approximation scheme used for M^*, Q_m, i_i, and i_P is illustrated in the upper portion of Fig. C. 6 for M^*. Data are given at the discrete points n-1, n, and ntl. The mean value of M^* in the time interval t_n^* to t_{ntl}^* denotedby $\bar{M}_n^*$ is

$$\bar{M}_n^* = (M_n^* + M_{n+1}^*)/2 \qquad \text{(C. 43)}$$

The integration was carried out with constant parameters such as $\bar{M}_n^*$ when $t_n^* < t_j^* \leq t_{n+1}^*$. Checks were made to determine when $t_j^* > t_{ntl}^*$. When this occurred a new constant value denoted by $\bar{M}_{ntl}^*$ for the next time interval was used.

A similar procedure was used to approximate $\dot{M}_i^*$ and $\dot{M}_P^*$ as illustrated in Fig. C. 6 for $\dot{M}_P^*$. Data for M_P^* are given at points n-1, n, and ntl. The mean slope of the steam production characteristic in the interval is the mean. steam production rate given by

$$\dot{M}_{p,n}^* \cong (M_{p,n+1}^* - M_{p,n}^*)/(t_{n+1}^* - t_n^*) \qquad \text{(C. 44)}$$

The outlined procedure amounts to approximating continuous parameters by a series of step functions, An alternate procedure frequently used is the spline fit method which involves fitting continuous

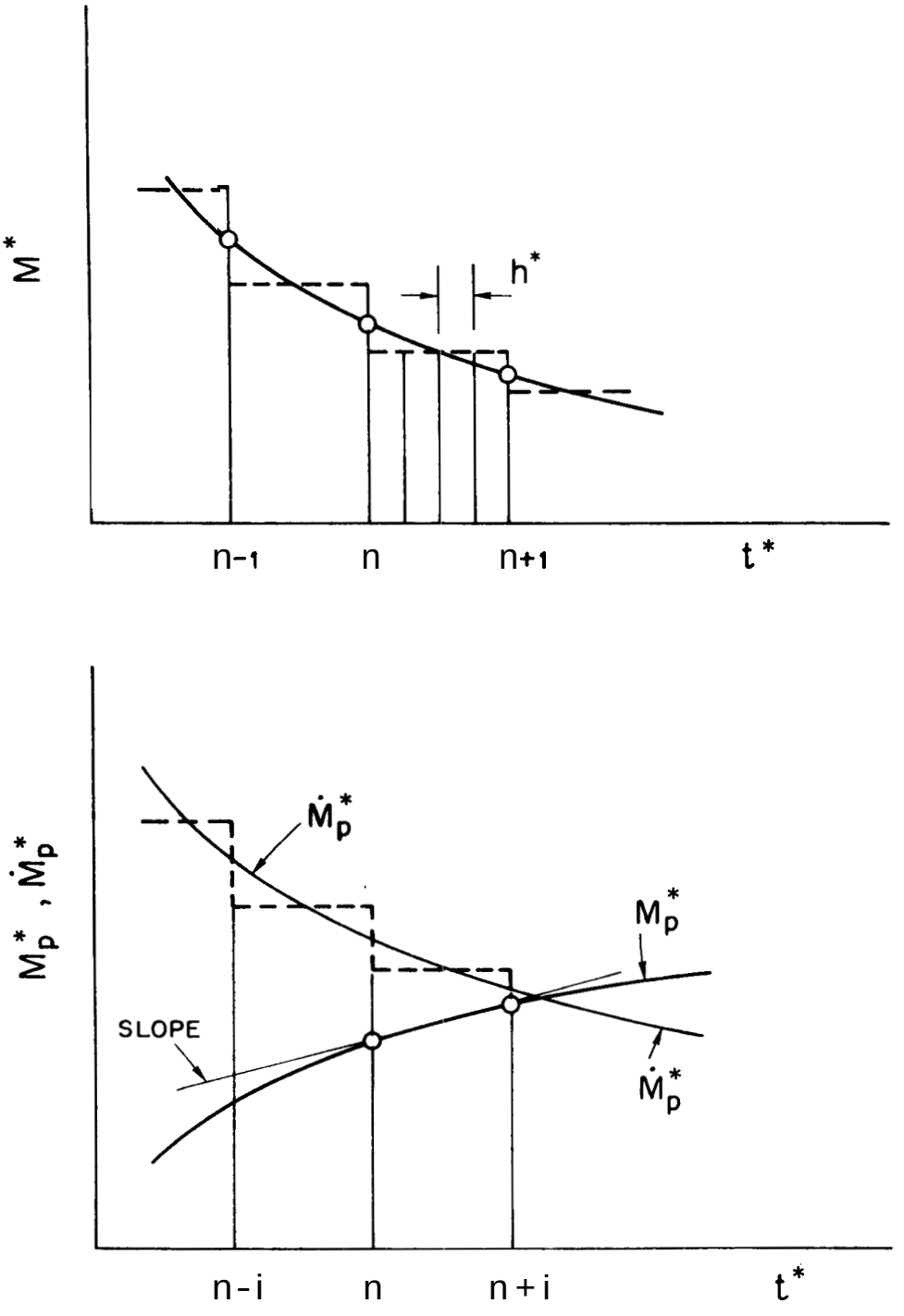

Figure C. 6 Numerical Approximations of **Mass** Fraction and Boundary Parameters

functions (usually polynomials) through the data points. This method is preferred when data are available only at a few points.

C. 2. 3 Time Interval Basis Analysis

In this section equations for the model reservoir analysis are derived on a time interval basis instead of on the previously considered rate basis. The major assumptions of the analysis are given in Chapter 3. Consider that during the period of time dt the mass δM_i enters and the mass δM_P leaves the control volume (see Fig. *3.6)* occupied by the two-phase mixture.* If the change in mass within the control volume is dM, conservation of mass gives

$$dM = \delta M_i - \delta M_P \qquad \text{(C.45a)}$$

Integration from the initial state denoted by subscript "o" to the end state denoted by subscript "e" gives

$$M_e = M_o + {}_oM_{ie} - {}_oM_{pe} \qquad \text{(C.45b)}$$

To simplify the notation the subscripts of M_i and M_P are dropped with the understanding that M_i represents the cumulative mass recharge and M_P represents the cumulative steam production from the initial to the end state. The above expression is then written

$$M_e = M_o + M_i - M_P \qquad \text{(C.45c)}$$

The mass associated energy outflow from the control volume during the time interval dt is $\delta M_P i_P$ and the inflow is $\delta M_i i_i$. The energy inflow

* The symbol δ is used here to denote inexact differentials.

to the control volume by heat transfer are δQ_m from the metal in the chimney and δQ_r from the rock media. If dE is the change in energy content of the two-phase mixture and if kinetic and potential energy terms are neglected, conservation of energy gives

$$dE = \delta Q_m + \delta Q_r + \delta M_i i_i - \delta M_p i_p \qquad \text{(C.46a)}$$

Integration from state "o" to state "e" gives

$$E_e - E_o = Q_{me} + Q_{re} + \int_o^e i_i \delta M_i - \int_o^e i_p \delta M_p \qquad \text{(C.46b)}$$

The two last integrations are carried out after defining appropriate mean values of i_i and i_p. The enthalpy of the produced steam in most cases is close to that of saturated vapor and therefore it does not vary significantly. The arithmetic mean value of the steam enthalpy may be sufficient. It is given by

$$i_p = (i_{po} + i_{pe})/2 \qquad \text{(C.47a)}$$

The enthalpy of the recharge fluid may vary significantly, but the arithmetic mean given below is used

$$i_i = (i_{io} + i_{ie})/2 \qquad \text{(C.47b)}$$

These approximations in Eq. (C.46b) give

$$E_e - E_o = Q_m + Q_r + M_i i_i - M_p i_p \qquad \text{(C.48a)}$$

The internal energy E of the two-phase mixture can be written in terms of the specific internal energy e and the mass M. The continuity equation

(Eq. (C.45c)) is solved for M_P and substituted into the above equation. The result is rearranged to give an expression for the mass in the system at the end state as

$$M_e = [(i_p - e_o)M_o + (i_p - i_i)M_i - Q_m - Q_r]/(i_p - e_e) \qquad \text{(C.48b)}$$

The maximum energy extraction from the rock is defined in terms of the measured initial temperature and the saturation temperature corresponding to the end pressure as*

$$Q_{r,max} = \rho_r V(1-\phi)\bar{C}_r(T_o - T_e) \qquad \text{(C.49)}$$

where $\bar{C}_r$ is the mean specific heat of the rock in the given temperature range. To account for the possibility that not all available energy is extracted at the end state, the rock extraction fraction η_e is introduced by defining

$$\eta_e \triangleq Q_r/Q_{r,max} \qquad \text{(C.50)}$$

Methods for extimating η_e for highly fractured systems are discussed in Chapter **4.** Equation (C.48b) is rewritten in terms of η_e and other parameters as

$$M_e = [(i_p - e_e)M_o + (i_p - i_i)M_i - \rho_r V(1-\phi)\bar{C}_r(T_o - T_e)\eta_e - Q_m]/(i_p - e_e) \qquad \text{(C.51)}$$

The interative procedure outlined in Chapter **3** is used to determine M_e and e_e.

To facilitate comparison of experimental and predicted chimney model reservoir behavior, Eq. (C.51) is rewritten in terms of the

*In cases with recharge of cool water at the bottom the rock energy extraction may be somewhat greater.

fraction produced FP and the fraction recharged FR. These fractions are, respectively, the cumulative steam production and the fluids recharged normalized to the initial system fluid mass. Equation (C. 51) becomes

$$FP_t = [(e_o - e_e) + (i_i - e_e)FR + q_m + \rho_r V(1 - \phi)\bar{C}_r (T_o - T_e)\eta_e / M_o]/(i_p - e_e) \qquad (C.52)$$

where the subscript "t" refers to predicted (from theory) fraction produced.

C. 3 Derivations for Liquid Level Analysis

C. 3. 1 Liquid Level Correction

The existence of a nominal liquid level z in the chimney was postulated in Chapter 3. It was assumed that the liquid in the upper portion of the chimney is saturated with no entrained vapor bubbles. The liquid in the partially insulated sight glass is cooler than the chimney liquid such that the nominal liquid level is higher than the observed. An equation for the nominal liquid level z in terms of the observed liquid level z' is defined using the notation in Fig. 3. 8. When flow friction pressure drop in the rock matrix is negligible, the pressure at point "1" due to the liquid column heads are equal. Equating these heads gives

$$\frac{H - z'}{v_{SG}} = \frac{H - z}{v_f} .$$

Solving for the nominal liquid level. gives

$$Z = \left(1 - \frac{v_f}{v_{SG}}\right) \frac{H}{h} + \frac{v_f}{v_{SG}} Z' , \qquad (C.53)$$

where Z' and Z are the observed and nominal liquid levels normalized to the chimney height h. The evaluations showed that Z/Z' ranged between 0.86 when the liquid level was at the top of the sight glass to unity for low liquid levels.

C.3.2 Void/Steam Quality Relationship

A diagram of the chimney and connecting inlet/outlet piping is shown in Fig. C.5. The notation used for the various volumes contained between the isolation valves are also indicated in the diagram. In the following analysis it is assumed that the chimney contains saturated liquid and saturated vapor. The total volume containing either vapor or liquid is

$$V_T = V_d + V_{sc} + V_\phi + V_i = V_g + V_f . \qquad (C.54)$$

The vapor volume space is

$$V_g = V_d + V_{sc} \int v\, dz . \qquad (C.55)$$

Substituting Eqs. (C.54) and (C.55) into the definition of the bulk void fraction given by Eq. (3.30), yields

$$\alpha = (V_d + V_{sc} + V_\phi Z)/V_T . \qquad (C.56)$$

The nominal liquid level is used in Eq. (C.56) to estimate the bulk void fraction with known system parameters. However, the nominal liquid level is not available during the early part of the experiment because the sight glass does not extend to the very top of the rock matrix (see Fig. 3.8). An equation for the liquid level in terms of the total chimney mass assuming saturated vapor and liquid phases is therefore derived for use in Eq. (C,56) such that α can be computed for the entire

experiment. Since liquid volume expansion due to entrained vapor bubbles in all chimney liquid is neglected, the computed liquid level is denoted by the effective liquid level z_t as opposed to the nominal liquid level z discussed earlier.

The effective liquid level is derived using the notation in Fig. C. 5. The total mass of fluids in the system (vapor and liquid) is expressed as

$$M = \frac{V_d}{v_g} + \frac{V_{sc}}{v_g} + \frac{V\phi}{v_g}\frac{z_t}{h} + \frac{V\phi}{v_f}\frac{h - z_t}{h} + \frac{V_i}{v_f}$$

Solving for $Z_t = z_t/h$ after introducing the mass fraction M^* gives

$$Z_t = \left[\left(\frac{V_d}{V\phi} + \frac{V_{sc}}{V\phi}\right)\frac{1}{v_g} + \left(1 + \frac{V_i}{V\phi}\right)\frac{1}{v_f} - \frac{M^*}{V\phi/M_o}\right]\frac{v_f}{1 - (v_f/v_g)} . \quad \text{(C. 57)}$$

The effective liquid level is computed for given M^* data available from steam production and fluid recharge measurements, known system parameters, and saturated steam properties. This level is used in Eq. (C. 56) to compute the bulk void fraction.

A relationship between the bulk void fraction and the bulk steam quality is derived such that the bulk steam quality also can be computed. The mass of liquid in the chimney is expressed as

$$M_f = V_f/v_f .$$

Substituting this expression into the definition of steam quality given by Eq. (3. 29) yields

$$X = 1 - \frac{v_f}{v_f M} ,$$

or

$$V_f = (1 - X)v_f M .$$

Substituting into the definition of the void fraction gives

$$\alpha = 1 - \frac{(1 - X)v_f M}{V_T}$$

Dividing through by the initial mass of water in the system M_o and redefining variables the void/ quality relationship is given by

$$X = 1 - \frac{V_T(1-\alpha)}{v_f M_o M^*} \qquad (C.58)$$

C.4 Details of Uncertainty Analysis

The techniques used for the uncertainty analysis were based on the methods given in Kline and McClintock (1953) as outlined in section 3.5. The first step in the analysis was to establish uncertainty intervals for each variable measured in the laboratory and for the system parameters such as the chimney mass, chimney geometry, and heat loss conductances.

The magnitudes of the uncertainty intervals were selected based on experience and engineering judgment as well as on calibration experiments. For example, the chimney steam pressure readings measured by the calibrated pressure gage and the pressure transmitter were found to be within ±5 psi of each other over a wide range of test conditions. This experience gave the uncertainty interval for pressure as ±5 psi. The odds that the actual pressure was within this range is estimated to be 20 to 1.

The uncertainties of the chimney steel mass and chimney heat loss conductance was determined from heatup and cooldown calibration experiments as described previously (Hunsbedt, Kruger, and London, 1975).

The uncertainty intervals for certain other variables and parameters could not be determined from direct experience or calibration. In these cases engineering judgment was used to arrive at conservative estimates as to what the uncertainties might be.

The uncertainty intervals and magnitudes for the variables required to estimate the uncertainties in the results as outlined below are given in Table C. **4.** The percentage uncertainty interval--or the uncertainty interval normalized to the magnitude expressed in percent--depends on the value of the variable. Often a variable change significantly from start to end of the transient. In these cases both percent uncertainty intervals are stated with the first interval corresponding to the start of the transient. The uncertainties in the results were estimated using Eq. **(3. 38)** and the functional relationships between the resulting quantities and the variables summarized in Table C. 5. The analysis procedure is outline in the following.

When the result is a linear function (a product or a ratio) of the variables, Eq. **(3. 38)** can be simplified. For example, consider the equation for the mass recharged given in Table C. 5 which is

$$M_i = \rho A \ell \qquad (C.59)$$

In this case Eq. **(3. 38)** simplifies to

$$\frac{w_{Mi}}{M_i} = \left[\left(\frac{w_\rho}{\rho}\right)^2 + \left(\frac{w_A}{A}\right)^2 + \left(\frac{w_\ell}{\ell}\right)^2\right]^{1/2} \qquad (C.60)$$

The above expression implies that when the function is linear, the percent uncertainty interval in the result is the square root of the sum of the percent uncertainty intervals of the variables squared. When the function is not linear such as the equation for the condenser cooling water flow rate given by

$$\dot{M}_c = C_F \sqrt{\Delta P} \tag{C.61}$$

the percent uncertainty interval for the result is

$$\frac{w_{\dot{M}_c}}{\dot{M}_c} = \left[\left(\frac{w_{C_F}}{C_F} \right)^2 + \left(\frac{1}{2} \frac{w_{\Delta P}}{\Delta P} \right)^2 \right]^{1/2} \tag{C.62}$$

Note that this case is similar to the linear case except for the factor of 1/2 for the term under the square root sign.

The resulting quantity can also be a sum or a difference of variables such as the mass of fluids in the system at time t given by

$$M = M_o + M_i - M_P \tag{C.63}$$

In this case the percent uncertainty in the result is

$$\frac{w_M}{M} = \frac{1}{M} \left(w_{M_o}^2 + w_{M_i}^2 + w_{M_p}^2 \right)^{1/2} \tag{C.64}$$

Note that the sum of the dimensional uncertainty intervals squared are required as opposed to the percent uncertainty intervals in the two previous cases. These dimensional uncertainty intervals were often intermediate results for more complicated expressions such as that for the effective liquid level shown as result (19) in Table C. 5.

The data given in Table C. 4 were used with Eqs. (C.60), (C.62), (C.64), and the functional relationships in Table C. 5 to compute the uncertainty intervals listed in Table 3. 3.

TABLE C.4

Estimated Uncertainty Intervals for Measured Variables and System Parameters

Quantity	Symbol	Magnitude ±w (20 to 1)	Units	Percent Uncertainty Interval (20 to 1)
Rock Matrix Void	V_v	7.3±0.2	ft^3	2.8
Volume of Chimney	V	16.6±0.2	ft^3	1.2
Total Volume of Chimney	V_T	17.7±0.4	ft^3	2.3
Volume of Rock	V_r	9.3±0.28	ft^3	3.0
Volume of Inlet Line	V_i	0.62±0.04	ft^3	6.5
Volume of Outlet Line	V_d	0.14±0.02	ft^3	14.4
Volume of Steam Cap	V_{sc}	0.19±0.10	ft^3	53.0
Mass of Rock	M_r	1640±20	lb_m	1.2
Chimney Metal Mass	M_m	3428±240	lb_m	7.0
Chimney Steam Pressure	P	600±5 to 50±5	psia	0.8 to 10.0
Steam Temperature	T	350±2	^oF	0.6
Chimney Metal Temperature	T_m	350±4	^oF	1.1
Mean Rock Temperature	T_r	470±2 to 300±5	^oF	0.4 to 1.7
Condenser Cooling Water Temperature	T_{cond}	70±1	^oF	1.4
Liquid Level in Head Tank	ℓ	10±0.25	inches	2.5
Observed Chimney Liquid Level	z	30±0.25	inches	0.8
Cumulative Fluid Production	M_p	20±1 to 150+1	lb_m	5.0 to 0.7
Orifice Flow Coefficient	C_F	700±30	$lb_m/hr\ inch^{1/2}$	4.3
Orifice Pressure Drop	ΔP	10±0.1	inches	1.0
Inlet Line Heater Tape Power	$\dot{Q}_i$	6800±350	Btu/hr	5.1
Chimney Heater Tape Power	$\dot{Q}_E$	6800±200	Btu/hr	3.0
Chimney Heat Loss Conductance	UA	32.2±1.2	Btu/hr ^oF	3.7
Inlet Line Heat Loss	$U_iA_i\theta_i$	3000±600	Btu/hr	20.0
Outlet Line Heat Loss	$U_oA_o\theta_o$	2000±400	Btu/hr	20.0

TABLE C.4 (Continued)

Quantity	Symbol	Magnitude ±w (20 to 1)	Units	Percent Uncertainty Interval (20 to 1)
Area of Injection Head Tank	A	1.8±0.08	ft^2	4.5
Density of Water in Injection Tank	ρ	62.4±0.4	lb_m/ft^3	0.9
Specific Volume of Chimney Water	v_o	0.02±0.0002	ft^3/lb_m	1.0
Specific Volume of Liquid Phase	v_L	0.018±0.00003	ft^3/lb_m	1.7
Specific Volume of Saturated Liquid	v_f	0.0787±0.00002	ft^3/lb_m	1.1
Specific Volume of Liquid in Sight Glass	v_{SG}	0.016±0.00002	ft^3/lb_m	1.2
Specific Volume of Vapor Phase	v_G	3.470±0.28	ft^3/lb_m	8.1
Specific Enthalpy of Saturated Liquid	i_f	0.4098±0.01	Btu/lb_m	2.4
Specific Heat of Rock	C_r	0.22±0.02	$Btu/lb_m\ ^oF$	10.
Specific Heat of Chimney Metal	C_m	0.117±0.001	$Btu/lb_m\ ^oF$	0.9
Rock Surface Heat Transfer Coefficient (Vapor)	h	3±1	$Btu/hr\ ft^2\ ^oF$	23
Rock Surface Heat Transfer Coefficient (Liquid)	h	50±20	$Btu/hr\ ft^2\ ^oF$	40
Rock Thermal Conductivity	k	1.4±0.2	$Btu/hr\ ft\ ^oF$	14
Rock Thermal Diffusivity	α	0.039±0.005	ft^2/hr	13
Rock Dimension	r_o	0.27±0.01	ft	4
Cooldown Rate	μ_ℓ	12±1	$^oF/hr$	8

TABLE C. 5

Functional Relationships Between Required Results and The Variables

Result	Equation	Units
(1) Rock Matrix Drainage Porosity	$\phi = V_v / V$	dim. less
(2) Rock Matrix Solid Density	$\rho_r = M_r / V - V_v)$	lb_m/ft^3
(3) Mass of Fluids Recharged	$M_i = \rho A \ell$	lb_m
(4) Rate of Mass Recharge	$\dot{M}_i = \Delta M_i / \Delta t$	lb_m/hr
(5) Rate of Mass Production	$\dot{M}_p = \Delta M_p / \Delta t$	lb_m/hr
(6) Condenser Cooling Water Flow Rate	$\dot{M}_c = C_F \sqrt{\Delta P}$	lb_m/hr
(7) Initial System Mass	$M_o = v_o V_T$	lb_m
(8) Fraction Recharged	$FR = M_i M_o$	dim. less
(9) Fraction Produced - Experimental	$FR = M_p M_o$	dim. less
(10) Fraction Produced - Theoretical	$FP_t = [(e_o - e_e) + (i_i - e_e) FR + q_m + M_r C_r (T_o \; T_e) \eta_e / M_o] / (i_p - e_e)$	dim. less
(11) Liquid and Vapor Mass in System	$M = M_o + M_i - M_p$	lb_m
(12) Mass Fraction	$M^* = M / M_o$	dim. less
(13) Normalized Chimney Steam Pressure	$P^* = P / P_{so}$	dim. less
(14) Recharge Fluid Enthalpy	$i_i = i_H + (\dot{Q}_i - U_i A_i \theta_i) / \dot{M}_i$	Btu/lb_m
(15) Produced Steam Enthalpy - at the PCV	$i_c = i_{H,\,out} + C\dot{M}_c (T_{c,\,out} - T_{c,\,in}) / \dot{M}_p$	Btu/lb_m
(16) Produced Steam Enthalpy - at Chimney Exit	$i_p = i_c + U_o A_o \theta_o / \dot{M}_p$	Btu/lb_m
(17) Rock Energy Extraction Fraction	$\eta_e = (T_{ro} - T'_{re}) / (T_o - T_e)$	dim. less
(18) Observed Chimney Liquid Level	$Z = (1 - v_L / v_{sG}) H / h + v_L / v_{sG} Z'$	dim. less
(19) Computed Chimney Liquid Level	$Z_t = [(V_d / V\phi + V_{sc} / V\phi) / v_g + (1 + V_i / \phi V) / v_f - M^* / (V\phi / M_o)] v_f / (1 - v_f / v_g)$	dim. less
(20) Chimney Bulk Steam Void Fraction	$\alpha = (V_d + V_{sc} + V\phi Z) / V_T$	dim. less
(21) Chimney Bulk Steam Quality	$X = 1 - v_o (1 - \alpha) / v_L M^*$	dim. less
(22) Chimney Bulk Steam Entropy	$i = i_f + i_{fg} X$	Btu/lb_m
(23) External Heat Transfer Parameter	$Q_m = [\dot{Q}_E t_e + M_m (C_m \theta_{mo} - C_m \theta_{me}) \cdot \theta_m t_e]$	Btu
(24) Specific Q	$q_m = Q_m / M_o$	Btu/lb_m
(25) Rock Center/Steam Temperature Difference	$T_{rc} - T = \mu_\ell r_o^2 (0.5 + 1/B) / 3\alpha$	^oF

APPENDIX D

THERMAL PROPERTIES OF ROCK

The rock thermal properties of interest are the specific heat capacity, the thermal conductivity, and the thermal diffusivity. Tests to determine these thermal properties on experiment rock samples were not made since adequate data were available in the literature for similar rocks.

Heat capacities and thermal conductivities of fluid saturated porous rocks were reported by Somerthon (1958) and by Ramey et al. (1974). The results show that these thermal properties depend significantly on temperature. The so-called Kopp's rule may be used to determine the thermal properties of an igneous rock from the thermal properties of the pure minerals in the rock. Extensive data on the thermal properties of pure minerals have been given by Kelley (1949). A compilation of experimental data on the thermal conductivity of granite and gabbro is given in the "Handbook of Physical Constants" by Clark (1966). Other general data on the thermal properties of solids are given by Gambill (March 1957, and June 1957).

The specific heat capacity, estimated using Kopp's rule and data from Kelley, are given in Fig. D. 1. Curve 1 is for granite, curve 2 is for gabbro and curve **3** is obtained from Gambill. The specific heat capacities of granite and gabbro do not appear to differ much. The variation with temperature is less than about 10 percent in the temperature range 300 to 500 $^{\circ}$F. The data from Gambill given by curve **3** are significantly lower than curves 1 and 2. Considerable uncertainties are associated with these data, For example, Gambill states that Kopp's rule may give results which are in error by ±20 percent. The uncertainty for the data given by curve **3** is also reported by Gambill to be ±20 percent. The average of all data in Fig. D. 1 was used for this study,

Thermal conductivity data from Clark are given in Fig. D. 2. It appears that considerable variation in the conductivity occurs from location to location, particularly for granite. Moreover, the conductivity depends on the temperature atlthough the dependence does not appear to be significant for gabbro. The uncertainties in these data were not reported. The average of the data from the various locations was used in this study.

The mean rock temperature was about 400 ^{o}F. The mean values of the thermal properties adapted based on the above data are given in Table D. 1. The estimated uncertainty intervals for the thermal properties are given in Table C. 4.

TABLE D. 1

Average Rock Thermal Properties at 400 ^{o}F

Rock	Specific Heat Capacity, C_r (Btu/lb$_m$ ^{o}F)	Thermal Conductivity, k (Btu/hr ^{o}F ft)	Thermal Diffusivity $\alpha = k/\bar{\rho}_r C_r$ (ft^2/hr)
Gabbro	0. 216	1.2	0. 032*
Granite	0.218	1.4	*0.039*

* The mean rock densities $\bar{\rho}_r$ (174. 1 lb$_m$/ft^3 for gabbro and 164.4 lb$_m$/ft^3 for granite) were used to compute the thermal diffusivities.

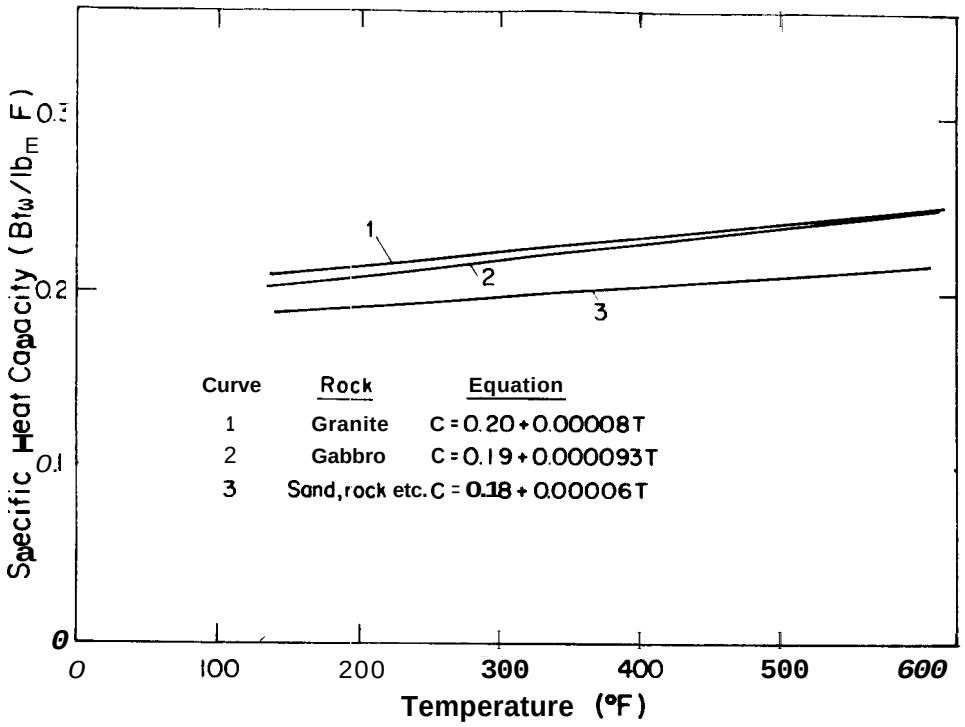

Figure D. 1 Specific Heat Capacity of **Rocks**

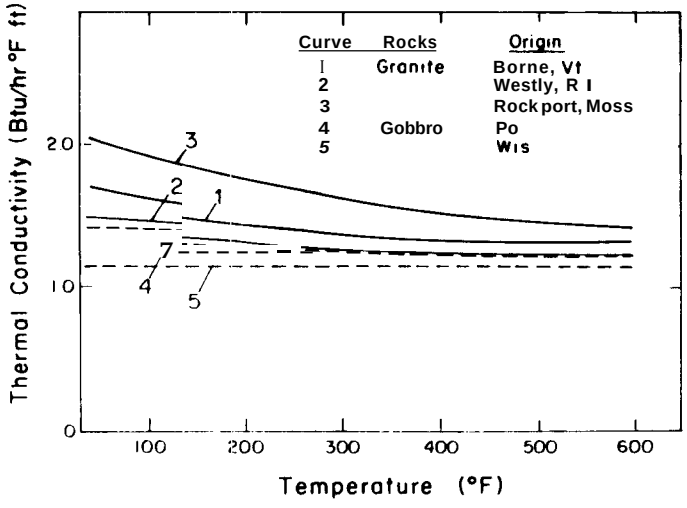

Figure D. 2 Thermal Conductivity of Rocks

REFERENCES

Arihara, N. , A Study of Non-Isothermal Single and Two-Phase Flow Through Consolidated Sandstones. Technical Report SGP-TR-2, Stanford University, Nov. 1974.

Boardman, C. R. , Some Characteristics of the Hardhat Chimney and Surrounding Wall Rock. Lawrence Radiation Laboratory, Livermore, UCRL 50177, Oct. 1966.

Boardman, C. R., Engineering Effects of Underground Nuclear Explosives, Proc. of Symposium on Engineering with Nuclear Explosives, Los Vegas, Nevada, Jan. 14-16, 1970.

Brigham, W. E. and Morrow, W. B., P/Z Behavior for Geothermal Steam Reservoirs, Paper No. SPE 4899, 44th Annual California Regional Meeting, SPE of AIME:, San Francisco, Calif. , April 4-5, 1974.

Cady, G. V. , Model Studies of Geothermal Fluid Production, Ph. D. Dissertation, Stanford University, Nov. 1969.

Carnahan, B., Luther, H. A. , and Wilkens, J. O., Applied Numerical Methods. John Wiley & Sons, Inc. , 1969.

Carlson, R. H., Utilizing Nuclear Explosives in the Construction of Geothermal Power Plants. Proc. Second Plowshare Symposium, UCRL-5677, 1959.

Carslaw, H. S. and Jaeger, J. C., Conduction of Heat in Solids. Oxford University Press, 1947.

Chicoine, S. D. , A Physical Model of a Geothermal System--Its Design and Construction and Its Application to Reservoir Engineering, Engineer Thesis, Stanford University, June 1975.

Clark, S. P. , Jr., Heat Transfer, 3rd ed. McGraw-Hill Book Company, 1972.

Diadkin, Yu. D. and Pariiskii, Yu. M., Theoretical and Experimental Grounds for Utilization of Dry Rock Geothermic Resources in Mining Industry. Second United Nations Symposium on the Development and Use of Geothermal Resources. San Francisco, California, 20-29 May, 1975.

Diadkin, Yu. D., Pariiskii, Yu. M., Vainblat, A. B., and Romanov, V. A., Research and Development of Efficient Systems of Extraction and Utilization of Heat, Accumulated within Deep Layers of the Earth's Crust in Extreme North and Northeast Regions of the USSR, Izuchenic i Ispol'zovanic Glubinnogo/Templa Zemli, Izdatel'stvo. Nauka Moscow, 1973.

Epstein, B. , The Mathematical Description of Certain Breakage Mechanisms Leading to the Logarithmico-Normal Distribution, J. Franklin Inst. , 244, 471-478 (1947).

Elder, J. W., Physical Processes in Geothermal Areas. In W. H. K. Lee, ed., Terrestrial Heat Flow, Am. Geophys. Union Mon., ser. 8, p. 211-239 (1965).

Fishender, M. and Saunders, O. A., The Calculation of Heat Transmissions. London, H. M. Stationary Off., 1934.

Gambill, W. R. , You Can Predict Heat Capacities, Chemical Engineering, June 1957.

Gambill, W. R. , Predict Thermal Conductivity - II, Chemical Engineering, March 1957.

Griffiths, J. C., Scientific Method in Analysis of Sediments. McGraw-Hill Book Co., 1967.

Grossling, B. F., An Appraisal of the Prospects of Geothermal Energy in the United States, Part 1, in An Initial Appraisal by the New Energy Forms Task Group 1971-1985. National Petroleum Council, 1972, p. 15-26.

Harlow, F. H. and Pracht, W. E., A Theoretical Study of Geothermal Energy Extraction, J. Geophys. Res., Dec. 1972.

Herdan, G., Small Particle Statistics. Elsevier Publishing Co. , Amsterdam, Houston, New York, Paris, 1953.

Holman, J. P., Heat Transfer, 3rd ed. McGraw-Hill Book Company, 1972.

Holzer, A., Gasbuggy in Perspective. Proc. of Symposium on Engineering with Nuclear Explosions, Las Vegas, Nevada, Jan. 14-16, 1970.

Howard, G. C. , and Fast, C. R., Hydraulic Fracturing, Monograph Volume 2, Henry L. Doherty Series, Published by the Society of Petroleum Engineers, 1970.

Hunsbedt, A., Kruger, P. and London, A. L., A Laboratory Model of Stimulated Geothermal Reservoirs, SGP-TR-7, Advanced Technology Dept. , RANN, National Science Foundation, Grant No. GI-34925, February 1975.

Hunsbedt, A., Kruger, P. and London, A. L., Laboratory Studies of Stimulated Geothermal Reservoirs, Second United Nations Symposium on the Development and Use of Geothermal Resources, San Francisco, Calif., May 20-29, 1975.

Jaeger, J. C. and Clarke, M., Numerical Results for Some Problems on Conduction of Heat in Slabs with Various Surface Conditions, Phil. Mag., 38(7), 504-515 (1947).

Johnson, A. L. , Lumped Parameter Solutions of One-Dimensional Transient Heat Conduction Problems. Engineer Thesis, Stanford University, August 1955.

Kelley, K. K., Contributions to the Data on Theoretical Metallurgy, Bull., USBM, 476 (1949).

Kennedy, G. C., A Proposal for a Nuclear Power Program- Proc. Third Plowshare Symposium, TID-7695, 1964.

Kilkenny, J. E. , Geothermal Energy, Part 11, General Appraisal of the Earth's Prospective Energy, in An Initial Appraisal by the New Energy Forms Task Group, 1971-1985. National Petroelum Council, 1972, p. 27-35.

Kline, S. J. and McClintock, F. A. , The Description of Uncertainties in Single Sample Experiments, Mechanical Engineering, 75, 1953, p. 3.

Kruger, P., Nuclear Civil Engineering, United States Atomic Energy Commission Report, TID-23748, 1966.

Kruger, Paul and Otte, Carel (eds.). , Geothermal Energy, Resources, Production. Stimulation. Stanford University Press, 1973.

Kruger, P., and Ramey, H. J., Stimulation of Geothermal Aquifers, Progress Report No. 1. Advanced Technology Dept., RANN, National Science Foundation, Grant No. GI-34925, March 1973.

Kruger, P., and Ramey, H. J., Stimulation and Reservoir Engineering of Geothermal Resources, SGP-TR-1. Advanced Technology Dept., RANN, National Science Foundation, Grant No. GI-34925, June 1974.

Krumbein, W. C., Measurement and Geological Significance of Shape and Roundness of Sedimentary Particles, J. Sediment Petrol., 11, 64-72 (1941).

McClintock, R. B. and Silvestri. G. J., Formulation and Iterative Procedures for Calculation of Properties of Steam, ASME Publication, 1968.

Meek, R. M. G., The Measurement of Heat Transfer Coefficients in Packed Beds by the Cyclic Method, Paper No. 93, International Developments in Heat Transfer, Part IV (ASME, 1961.

Meyer, C. A., McClintock, R. B., Silvestri. G. J., and Spencer, R. C., 1967 ASME Steam Tables - Thermodynamic and Transport Properties of Steam, An ASME Publication, 1967.

Miller, F. G., Steady Flow of Two-Phase Single Component Fluids Through Porous Media, Trans. AIME, 192, 205-216 (1951).

Muffler, L. J. P., and White, D. E., Geothermal Energy, Science Teacher, 39, 3, 40-43 (1972).

Pittijohn, F. J., Sedimentary Rocks, 2nd ed. Harper and Bros., 1951.

Rabb, D. D., Size-Distribution Study of Piledriver Particles, Lawrence Radiation Laboratory, Livermore, UCRL-50489, 1968.

Ramey, H. J., Brigham, W. E., Chen, H. K., Atkinson, P. G., and Arihara, N., Thermodynamic and Hydrodynamic Properties of Hydrothermal Systems, SGP-TR-6, Advanced Technology Dept., RANN, National Science Foundation, Grant No. GI-34925, April, 1974.

Rodean, H. C., The Particle Statistics of Rubble Produced by Underground Nuclear Explosions, Lawrence Radiation Laboratory, Livermore, UCRL-12129, 1964.

Schneider, P. J., Conduction Heat Transfer. Addison-Wesley Publ. Co., 1955.

Smith, M. C., Aamodt, R. L., Potter, R. M., and Brown, D. W., Man-Made Geothermal Reservoirs, Second United Nations Symposium on the Development and Use of Geothermal Resources, San Francisco, Calif., May 20-29, 1975.

Somerton, W. H., Some Thermal Characteristics of Porous Rocks, Trans. AIME, 213, 375-378 (1958).

Van Wylen, G. J., Thermodynamics. John Wiley & Sons, Inc., 6th printing, Sept. 1964, p. 94-97.

White, D. E., Geothermal Energy. U.S. Geol. Survey Circular 519, 1965, 17 p.

White, D. E., and Williams, D, L., Editors, Assessment of Geothermal Resources of the United States - 1975, U.S. Geol. Survey Circular 726, 1975.

Whiting, R. L. and Ramey, H. J., Jr., Application of Material and Energy Balances to Geothermal Steam Production, J. Pet. Tech., 893-900 (1969).

Wilson, W. A., Design of Power-Plant Tests to Insure Reliability of Results, Trans. ASME, Vol. 77, No. 4, May 1955.

Zingg, Th., Beitrag zur Schotteranalyse, Schweiz. Min. u. Pet. Mitt., 15, 39-140 (1935).